ATTACHMENT POINT CHARACTERISTICS AND MODELING OF SHEAR LAYER STABILIZED FLAMES IN AN ANNULAR, SWIRLING FLOWFIELD

A Thesis
Presented to
The Academic Faculty

by

Christopher W. Foley

In Partial Fulfillment
of the Requirements for the Degree
Doctor of Philosophy in the
School of Mechanical Engineering

Georgia Institute of Technology
December 2015

ATTACHMENT POINT CHARACTERISTICS AND MODELING OF SHEAR LAYER STABILIZED FLAMES IN AN ANNULAR, SWIRLING FLOWFIELD

Approved by:

Professor Tim Lieuwen,
Committee Chair
School of Mechanical Engineering
Georgia Institute of Technology

Professor Tim Lieuwen, Advisor
School of Mechanical Engineering
Georgia Institute of Technology

Professor Ben T. Zinn
School of Aerospace Engineering
Georgia Institute of Technology

Professor Jerry Seitzman
School of Aerospace Engineering
Georgia Institute of Technology

Professor Andrei Fedorov
School of Mechanical Engineering
Georgia Institute of Technology

Professor Michael Renfro
School of Mechanical Engineering
University of Kentucky

Date Approved: 21 August 2015

To my family, friends, and colleagues:

Thank you for your never ending support.

This journey was only possible with it.

To my beautiful wife, Melissa:

I am forever grateful having you in my life.

You have transformed this dream into a reality.

ACKNOWLEDGEMENTS

This has been an amazing journey and looking back there are certainly many people and memories that come to mind. For some who read this, you may question my recollection of the past, as I have been known to reminisce selectively. On the last day of AP Chemistry in high school, I told a friend how much I was going to miss going to class. He stared at me dumbfounded and quickly reminded me of my almost daily bellyaching. While my whining was undeniable, the truth was that I did miss AP Chemistry. While difficult in the moment, it was undeniable that I was better off as a result and any complaining was disproportionate to any hardship endured. Although the time scale, measured in years, of AP Chemistry and graduate school are considerably different, both endeavors were more than worthwhile. Through the support of friends, family, mentors, and colleagues, mountains were transformed into molehills which were ascended with the aid of a positive attitude.

The unwavering support of my parents, William and Christine, brings me to my knees in thanks. You provided me with what I needed and gave me everything I asked for. I look forward to celebrating this day with you both. To my brother Will: thank you for all those late night chats and for letting me talk your ear off. You continue to motivate me to make myself better every day. My sister Cat is an amazing person whose mastery of the kitchen and passion for life are to be admired. Thank you for being genuine and for your voice of reason. My other brother Joe, is more than just another brother. He's my other "bigger" brother. Thank you for your support, and Go Sox!

I am very grateful for my committee in their review of my dissertation work. I appreciate the time and attention that you have all put into this task. Thank you

Dr. Lieuwen, Dr. Seitzman, Dr. Zinn, Dr. Fedorov, and Dr. Renfro.

I deeply grateful for guidance and support from my advisor, Tim Lieuwen. I agreed to join Tim's group as a graduate student because of his genuine excitement and passion for the field of combustion. Early on in the lab, it became clear that this was no gimmick or Sunday stroll. His drive to succeed and perform high quality work pushed me to accomplish beyond my expectations. I am grateful for the care, time, and effort that Tim put forth to ensure my success as a person and the opportunities which he has opened up for me.

I would also like to recognize Jerry Seitzman, for his guidance and assistance over the years. Your insightful questions have greatly improved my research at Georgia Tech and will assist in the future as I strive to think as Seitzman would.

There have been so many colleagues at the combustion lab which have made a difference in my time here. From the start, it become clear that the combustion lab was comprised of a very unique group of people. The dynamic duo of Andrew Marshall and Prabhakar Venkateswaran quickly became close friends. I should have known that Andrew being the quieter of the two, that I should always have kept a close eye on him at all times. Luckily, I was more often in cohorts with Andrew than not, and that led to a very special and entertaining year and a half. Yes, a whole year and a half. Luckily Prabhakar was always a good sport with our shenanigans but always blamed solely me. Evil Switzerland escapes yet again. It was truly an honor to have met you both and I am appreciative for our friendship.

For a large part of my time in the lab, I shared a cubicle with Jacqueline O'Connor. This was comforting as Jackie and I were part of a small representation of students who knew what a snowy winter was like. Quite fortuitously, we are both Red Sox fans as well and shared a love for Jason Varitek, a Georgia Tech graduate. I'm pretty sure things would not have gone as well if I had to sit next to a Yankees fan. Speaking for myself, I learned a lot from Jackie on how to lead and organize group efforts both

in and outside of the lab. We shared music, good recipes, and our references of swirl literature with each other, and did our best to keep the wheels of the lab turning.

I came to know Matt Quinlan only after at least a year passed since he joined the lab. How could I have predicted that our love for mustaches would bring us together? There are many good times that we shared together over the years but it was the support that we provided for each other during our thesis writing that I am especially grateful for. Thanks for providing that extra push and motivation Mr. Quinlan.

I am very grateful for the support from Ianko Chterev. Ianko took over the experimental lead for the gaseous swirl rig as I went off to focus on the analysis and reduced–order modeling approaches that would compliment the experimental efforts. Without Ianko's expertise in PIV and PLIF diagnostics, my thesis work would have been impossible. Thank you for dedication and support over the years and especially in the last few months of my time here.

Thanks to Bobby Noble as well who was an integral part of the design, build, and operation of the test facility used for these studies, and his efforts on the project planning side ensuring that we had everything we needed to get the job done.

Many thanks go out to the AE Machine shop, Scott Elliot, Scott Moseley, and Henry "Red" Russell, for their tireless efforts in creating and aiding in the design of our test facility.

For the rest of the lot in no particular order: Ben Wilde, Jack Crawford, Nick Magina, Ben Emerson, Jordan Blimblaum, Yash Kochar, Brandon Sforzo, Ben Knox, Gina Sforzo, Sasha Bibik, Shane Getchell, Karthik Periagaram, Michael Malanoski, Nishant Jain, Travis Smith, Luke Humphrey, Sai Kumar Thumuluru, David Scarborough, and Sampath Adusumilli. It has been a pleasure working with you and I consider myself lucky to have gotten to know each and every one of you.

Last, but certainly not least, I would like to pay special thanks to my wife, Melissa. You've given me support beyond what is expected and shown patience throughout it

all. Thanks for all that you've done and do to keep me in one piece. I couldn't have made it here without you.

TABLE OF CONTENTS

LIST OF TABLES

LIST OF FIGURES

NOMENCLATURE

$\vec{n}_f$	Flame normal vector.
$A_{annulus}$	Cross-sectional area of annulus.
A_{comb}	Cross-sectional area of combustor.
D_T	Thermal diffusivity.
d_{cb}	Centerbody diameter.
d_{comb}	Combustor diameter.
$d_{exhaust}$	Exhaust exit diameter.
d_{outer}	Outer diameter of premixer annulus.
Da	Damkoehler number.
Ka	Karlovitz number.
l	Integral length scale.
l_D	Diffusive length scale.
l_{comb}	Combustor length.
Le	Lewis number.
p_{rms}	Root-mean square of acoustic pressure.
Q_{bl}	Boundary layer heat addition.
Q_{cb}	Recirculation zone heat loss to combustor.
r_{edge}	Radial location of flame leading edge.
r_f	Radial flame location.
R_{min}	Minimum absolute curvature measured along CH-layer centerline.
Re	Reynolds number.
Re_t	Turbulent Reynolds number.
S_{c,CH_4}	Methane consumption based flame speed.
$S_{d,CH}$	Laminar, displacement flame speed relative to the location of maximum χ_{CH}.

$S_{d,ph}$	Laminar, displacement flame speed relative to the initiation of the preheat zone.
S_d	Laminar, displacement flame speed.
S_d^o	Unstretched laminar, displacement flame speed.
$S_{i,j}$	Symmetric strain rate tensor.
S_m	Swirl number.
T_{RZ}	Recirculation zone temperature.
T_{bhd}	Combustor bulkhead temperature.
T_{ext}^{ad}	Adiabatic, stretched flame, extinction temperature calculated using the symmetric opposed jet configuration.
T_{ph}	Preheat temperature.
T_{ref}	Reference temperature correction for κ_{ext} blowoff scaling.
T_r	Ratio of product side temperature, T_{prod} to adiabatic, stretched flame, extinction temperature, T_{ext}^{ad}.
$u^{'}$	Integral velocity scale.
u^N	Flow velocity normal to flame.
u^T	Flow velocity tangent to flame.
u_i	Velocity component in direction i.
u_o	Characteristic bulk flow velocity.
u_{pm}	Premixer velocity.
u_{rms}	Room mean square of velocity.
v_f	Edge flame speed.
Y_{EGR}	Mass fraction of reactant stream dilution by recirculated products.
Y_i	Mass fraction of species i.
χ_i	Mole fraction of species i.
Δ_{CH}	CH-PLIF image pixel spacing.
Δ_{IW}	Size of PIV interrogation window sizes.
Δ_{PIV}	PIV vector spacing.

δ_R	Reaction zone thickness.
$\delta_R^{CH,FWHM}$	CH based, FWHM reaction zone thickness.
δ_f	Flame thickness.
δ_f^T	Temperature based flame thickness.
δ_{image}	Experimentally determined CH-layer thickness.
Δ_{offset}	Offset distance between CH-layer centerline and edge of Mie-scattering image.
η	Kolmogorov length scale.
κ	Total flame stretch.
κ_{curv}	Curvature induced flame stretch.
κ_{ext}	Extinction stretch rate.
$\kappa_{s,norm}$	Hydrodynamic normal strain induced flame stretch.
$\kappa_{s,shear}$	Hydrodynamic shear strain induced flame stretch.
κ_s	Hydrodynamic strain induced flame stretch.
κ_s^{CH}	Hydrodynamic strain induced flame stretch at the location of maximum χ_{CH}.
κ_s^{ph}	Hydrodynamic strain induced flame stretch at the initiation of the flame preheat zone.
ν	Kinematic viscosity.
ϕ	Equivalence ratio.
ρ	Density.
σ_i	Standard deviation or uncertainty of parameter i.
τ_{chem}	Characteristic chemical time.
τ_{flow}	Characteristic flow time.
τ_{pf}	Premixed flame characteristic chemical time.
τ_{res}	Characteristic residence time.
τ_{wsr}	Critical chemical time of a well-stirred reactor.
$\theta_{\vec{u}}$	Flow angle.

θ_f	Flame angle.
θ_{rel}	Relative angle between flame, θ_f, and flow, $\theta_{\vec{u}}$.
θ_{vane}	Swirler vane angle.
EGR	Exhaust gas recirculation.
IRZ	Inner recirculation zone.
ISL	Inner Shear Layer.
ORZ	Outer Recirculation Zone.
OSL	Outer Shear Layer.
PIV	Particle image velocimetry.
PLIF	Planar laser induced fluorescence.
VBB	Vortex Breakdown Bubble.
WSR	Well-stirred reactor.

SUMMARY

Many practical combustor technologies, such as natural gas turbines, operate under lean premixed conditions. Premixed systems are attractive from an emissions standpoint with the ability to directly control combustor temperature through changes in the fuel to air mixture ratio. In addition, when operated under lean conditions, they are highly efficient in their consumption of fuel as well. However, lean premixed systems are highly susceptible and responsive to fluctuations in flow and mixture properties. This coupled with operator requirements for gas turbines to operate over a range of power outputs, provides challenges for the gas turbine designer and operator. For instance, the question of what flow rate and equivalence ratio should one operate at in order to double the thermal power output, while meeting emissions, can be non-trivial. In this simple example, assuming emission requirements drive the range of equivalence ratios allowable, and therefore combustor temperatures, total flow rate would control the thermal output of the combustor. With an increase in flow rate at a fixed equivalence ratio, the flame may extinguish or blowoff. However, an increase in equivalence ratio may prevent flame out. The question for designers and operators is how much should equivalence ratio change to maintain flame stability?

In order to answer this question, an understanding of the mechanisms and physics of flame stabilization of premixed flames is required. Due to the high bulk flow velocities typical of practical combustors, the flame anchors in the shear layers where the local flow velocities are much lower. Thus, our discussion is focused on shear layer stabilized flames. Within the shear layer, the flame is subject to strain induced flame stretch which can alter the burning of the flame. At a fixed equivalence ratio, operation of these combustors is limited by an upper limit in bulk flow velocity for

which stable combustion is attainable. This bulk flow velocity limit is presumably the result of flame stretch induced extinction caused by increasing fluid strain rates with increases in bulk flow velocity.

Through experimental studies of a shear layer stabilized flame, a deeper understanding of the mechanisms of flame stabilization and extinction for shear layer stabilized, premixed flames was obtained. Measurements were performed in the most upstream region where the flame was observed in the inner shear layer of an annular swirling combustor. Through high resolution, planar, and simultaneous PIV and CH-PLIF measurements, the instantaneous flow field and flame position was captured enabling calculations of 2D flame stretch in the flame attachment region. These flame stretch rates, calculated relative to the CH reaction layer location, were compared with steady extinction stretch rates calculated using the opposed jet model, OPPDIF, of CHEMKIN, a model widely used to study the effect of fluid strain rates on flames. In addition, comparisons between model and experiment were made to interpret the experimental observations of the flame response to changes in combustor operational parameters such as equivalence ratio and premixer velocity. The CH-PLIF data obtained also directly elucidated the unsteady behavior of the flame in the near field, as observed through the location and orientation of the CH reaction layer within the shear layer.

Most notably, these studies show that as lean blowoff conditions are approached by decreasing equivalence ratio, ϕ, the mean stretch rates near the attachment point decrease but remain positive throughout the measurement domain, from the dump plane to $\approx$ $10mm$ downstream. In fact, compared to extinction stretch rates calculated using a reduced–order opposed–jet model, the flame apparently becomes less critically stretched as ϕ is decreased. Also, investigation of the flame structure at the leading edge of the flame showed strong evidence that the flame is edge flame stabilized. This was supported by inspection of the CH-PLIF images, which showed

the CH-layer oriented tangent to the flow field and terminating abruptly at the leading edge, and not curved and oriented perpendicular to the flow at the leading edge. Lastly, the flame anchoring was observed to be highly robust as the flame edge flow conditions and location of leading edge of the flame were insensitive to ϕ remaining nearly constant for $0.9 \leq \phi \leq 1.1$. However, at the leanest test condition, $\phi = 0.8$, the flame leading edge was located farther downstream and subjected to much higher flow velocities. These results thus suggest that blowoff is the result of a kinematic balance and not directly from stretch induced flame extinction.

CHAPTER I

MOTIVATION AND BACKGROUND

Practical combustors are driven to operate at high velocity conditions in order to produce the largest amount of power for a fixed combustor size. In addition, dry low NOx technology operates on the lean operability limit where flames have low temperatures and are highly sensitive to fluctuations. In order to maintain flame stability at these high flow rates and lean mixtures, these combustors often rely on low velocity regions and recirculation zones in order to anchor the flame. These flow features can easily be created through the use of bluff bodies which obstruct the flow and produce recirculation zones in their wakes, and low velocity regions in the free shear layers, which form as the flow separates from the surface of the bluff body. The addition of a swirling component to the incoming flow is commonly used in practical combustors because of the higher achievable thermal power output compared to other combustor technologies of comparable size. High power density combustion is directly linked to swirling flow fluid mechanics and the resulting structure of the flow field. Very simply, increases in thermal power density are essentially driven by rapid increases in flame area progressing downstream, making swirl flames more compact than a bluff body stabilized flame of equal size, and thus, a more attractive combustor technology from an energy density standpoint.

The structure of the swirling flow field which leads to these high power density flames is shown in Figure 1.1 for a swirling flow field with and without a centerbody at the dump plane. The two configurations shown in 1.1 share many of the same fluid mechanic features including an annular jet, an outer recirculation zone (ORZ), an inner recirculation zone (IRZ), and inner and outer shear layers (ISL & OSL)

separating the jet from the IRZ and ORZ respectively. When a bluff centerbody is present, the IRZ can consist of a wake feature associated with the centerbody and the vortex breakdown bubble (VBB). These two features can exist independently or as a single merged recirculation zone structure. When there is no centerbody, or a recessed centerbody, the inner recirculation is comprised of only the VBB. Note the rapid spreading of the jet radially outward downstream of the dump plane. Flames that are able to stabilize along the jet, either in the ISL or OSL, will have rapidly increasing areas progressing downstream ($A_f \propto r_f^2$) thus resulting in compact, efficient flames.

In addition, flame stability is enhanced by the inner recirculation zone associated with the VBB. The VBB is larger and extends further into the downstream flowfield after expansion than any wake recirculation zone caused by inner flow obstruction. This enhancement in the inner recirculation zone increases flame stability, enabling the combustion of leaner mixtures. This is of particular importance in the design of dry low NOx combustors which rely on being able to operate at very lean mixtures to reduce flame temperature and achieve low NOx emissions. The challenge for these devices is to operate at conditions which produce ultra-low NOx emissions while maintaining a highly efficient, stable, and clean burning flame. It is also important to note that the VBB provides a product recirculation pathway even in the absence of any bluff body. In the presence of an outer wall, as shown in this schematic, the resulting ORZ will enhance OSL flame stability. Practical flames of interest in these combustors tend to stabilize in at least one of the shear layers present where the flame is subject to high rates of fluid strain. It is presumed that the operation of these combustors is limited by the limit in fluid strain rate which the flame can withstand before extinguishing or locally blowing off. The interaction between flame and strain is a complex phenomenon but fundamental topic that to our benefit has been studied extensively by the combustion community. There are several fundamental combustor

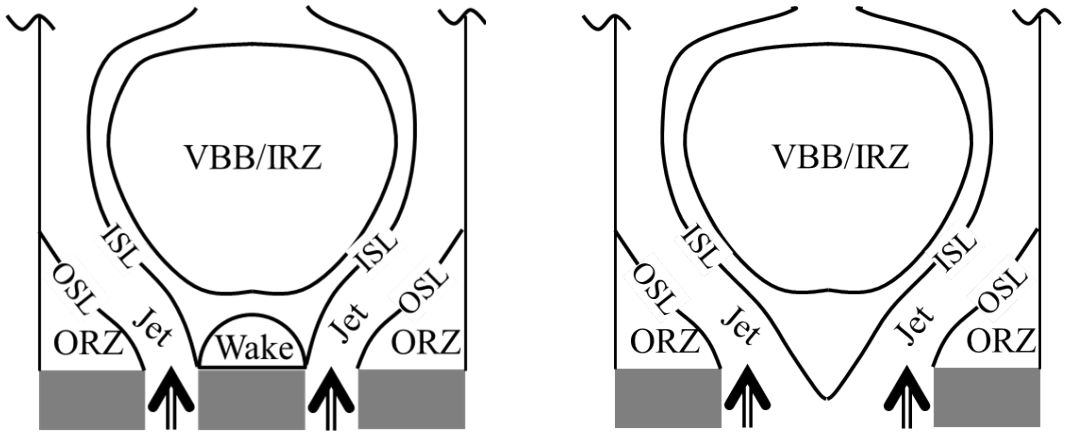

(a) With centerbody **(b)** Without centerbody

Figure 1.1: Fluid mechanic structures for typical representative annular swirl combustor geometries with a bluff center body (left) and a recessed or absent centerbody (right).

configurations that have been developed to study the flame's response to flame strain. These combustors provide well defined strain and flow fields lending themselves to numerical, analytical, and experimental approaches. Most notably, the opposed jet model has been widely used to study the stability of stretched flames under laminar, steady conditions by many investigators over the years [66, 67, 45, 44]. In fact, the use of the opposed jet model to characterize the steady extinction stretch limits is common and widespread amongst researchers and combustor designers. The tubular and opposed tubular flame configurations have also been used to study flame stretch response experimentally and numerically in steady, laminar stretch rate calculations [50]. The distinguishing features between these configurations are discussed in detail within this chapter.

In reality, flames are subject to additional physics which will alter their response to stretch. Additional considerations relevant to practical combustors include heat loss, unsteadiness, and turbulence. For example, the opposed jet model has been used by investigators to study a non-adiabatic flame's response to stretch [121, 27, 28, 25].

These studies are of particular interest in understanding the effect of heat loss on the operational limit of shear layer stabilized combustors. Flow and mixture unsteadiness are additional factors relevant to practical combustors which operate under turbulent flow conditions and with finite time for mixing. Unsteady laminar studies of the opposed jet model addressing these concerns have been carried out through harmonically time dependent jet velocities as well as through harmonically time dependent equivalence ratios [37, 110, 111, 53, 117]. The results of these unsteady studies provide insight on the unique way in which harmonic fluctuating stretch conditions influence the burning properties of the flame as a precursor to discussing turbulent opposed jet configurations. Finally, turbulent studies of the opposed jet configuration are discussed [64, 19, 49, 18, 17, 8, 26].

In addition to understanding flame interaction with stretch, studies of edge flame behavior are discussed. While there have been extensive fundamental studies of edge flames, [11, 13, 119, 74, 29, 32], edge flames have not been discussed as the relevant set of physics in the context of practical combustor flame stability. Based on the observations from the current studies, the physics of flame stability may in fact be edge flame controlled for the studies in question.

Finally, studies of practical burners relevant to the test geometry of this work which investigate stabilization mechanisms and or flame stretch are discussed. The focus is on bluff body and swirl stabilized combustors and include studies which report observations on the flame as blowoff is approached as well as studies which provide detailed measurements on the kinematic and stretch conditions experienced.

1.1 Fundamental Stretch Burners

As a central part of this work is the measurement of flame stretch in a practical combustor, it is pertinent to discuss the wide range of work that has been completed studying premixed flame response to flame stretch, and the experimental and model

geometry used to do so. There are several fundamental burner configurations which provide well defined strain and flow fields making them ideal burners to study the effects of flame stretch. These various burner geometries are introduced, with specific focus directed towards discussing the opposed jet configuration, which was the configuration used for the numerical modeling studies of this work. Our discussion of the opposed jet model in detail is first restricted to steady state results; in particular, studies which have characterized the extinction stretch limits for adiabatic, premixed flames.

Unsteadiness is another key parameter of interest which has been investigated through single frequency harmonically unsteady variations in a single input parameter of the opposed jet stream, namely jet exit velocity or equivalence ratio. In addition turbulent, opposed jet studies have been performed to characterize turbulence effects on flame structure. Other models, which are inherently unsteady, such as the spherically expanding flame are introduced as well.

1.1.1 Opposed Jet Combustor

The opposed jet combustor is perhaps the most common configuration used in the study of flame stretch. In its most basic form, it consists of a premixed jet directed normal to a wall. This wall jet configuration produces a flat flame, parallel to the wall. The thermal boundary conditions at the wall can strongly influence the stretched flame response, especially for conditions which result in a flame stabilized in close proximity to the wall. A stagnation plane configuration can also be produced by directly opposing two jets with a stagnation plane forming between the two jets.

The opposed jet configuration has several variations with the added jet. When both jets are premixed mixtures which have the same thermodynamic state, composition, and velocity at the exit, it is considered *symmetric*. A symmetric opposed jet configuration results in the *twin flame* configuration with flames stabilizing on both

sides of the stagnation plane. When the streams are not of the same thermodynamic state, composition, or have unequal exit velocities, the configuration is considered *asymmetric*.

Typical asymmetric configurations that have been studied include a premixed reactant stream opposed by: hot products, hot inert gases, or premixed mixtures of a different fuel and or equivalence ratio [33, 27, 78]. In a fundamental sense, asymmetric configurations allow for flame stretch to be studied in the presence of diffusional transport of heat and or species across the stagnation plane which, depending on the composition and state of the non-reactant, can enhance or degrade the stretch limits of the flame, which is discussed in Chapter 5. The opposed jet model can also be used to study the effect of stretch on non-premixed flames by opposing a fuel jet with an oxidizer jet. These stagnation plane configurations are shown in Figure 1.2. The flames for all three opposed jet configurations are flat and stationary resulting in flames which are stretched only by hydrodynamic strain sources:

$$\kappa = \kappa_s = \frac{\partial u_y}{\partial y} = -\frac{\partial u_z}{\partial z} \tag{1.1}$$

where the equation above is for a 2D, planar, opposed jet configuration and incompressible flow was assumed.

Figure 1.3 shows a representative non-reacting velocity and strain field for the opposed jet configuration. Note, due to the similarity conditions within the jet, axial velocity is only dependent upon axial location. Thus, the profiles along the jet centerline are valid throughout the jet domain. Likewise, the transverse velocity is only dependent upon the transverse location.

In the absence of a flame, the axial velocity decreases monotonically towards the stagnation plane resulting in negative axial strain field. From equation 1.1, negative axial strain results in a positive stretch field throughout the non-reacting domain, which increases monotonically towards the stagnation surface and results in a maximum stretch rate at the stagnation plane. While it is the local stretch in reference to

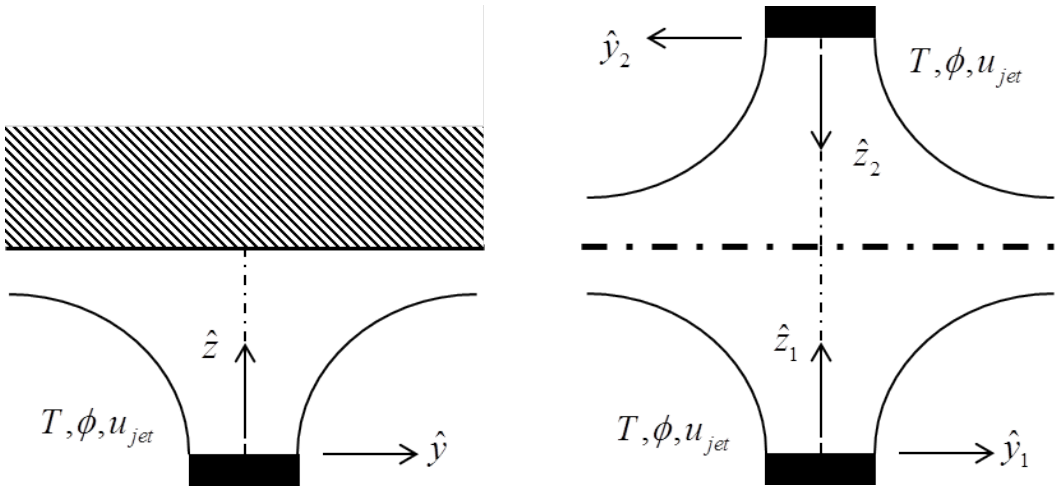

(a) Wall stagnation jet

(b) Symmetric opposed jet

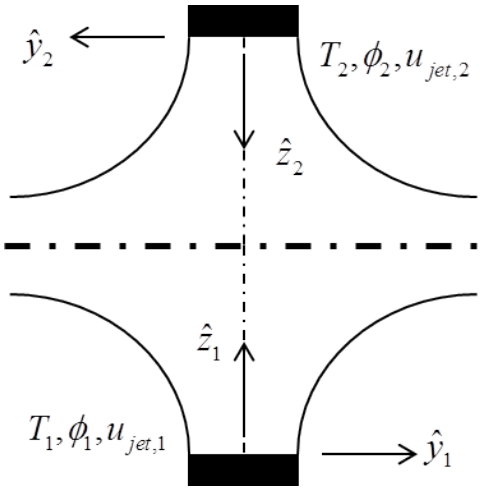

(c) Asymmetric opposed jet

Figure 1.2: Various configurations for the stagnation flame model: a)single jet, b)symmetric opposed jets, and c)asymmetric opposed jets

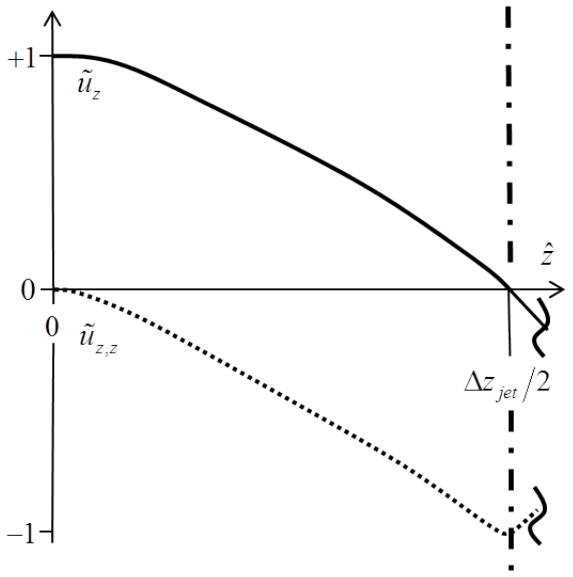

Figure 1.3: Normalized axial velocity, $\tilde{u}_z$, and normalized normal strain field, $\tilde{u}_{z,z}$, for a non-reacting, opposed jet configuration shown from jet exit, $z = 0$, to stagnation plane, $z = \Delta z_{jet}/2$

.

the onset of the preheat zone of the flame which is physically relevant, the following is a commonly used approximations of the flame stretch based on bulk scaling when local stretch measurements are not available:

$$\kappa_{bulk} = \frac{U^o_{jet}}{\Delta z_{jet}/2} \tag{1.2}$$

where U^o_{jet} is the flow velocity at the exit of the jet and $\Delta z_{jet}/2$ is the distance from the exit of the jet to the location of the stagnation plane. The opposed jet configuration is available in commercial codes such as CHEMKIN [1] and open source codes such as Cantera [47].

There has been extensive work done using the symmetric opposed jet configuration under steady operating conditions to study the response of flames to stretch. Law *et al.* [110, 66] provides a review of the experimental, analytical, and numerical work which has been carried out studying opposed jet flames.

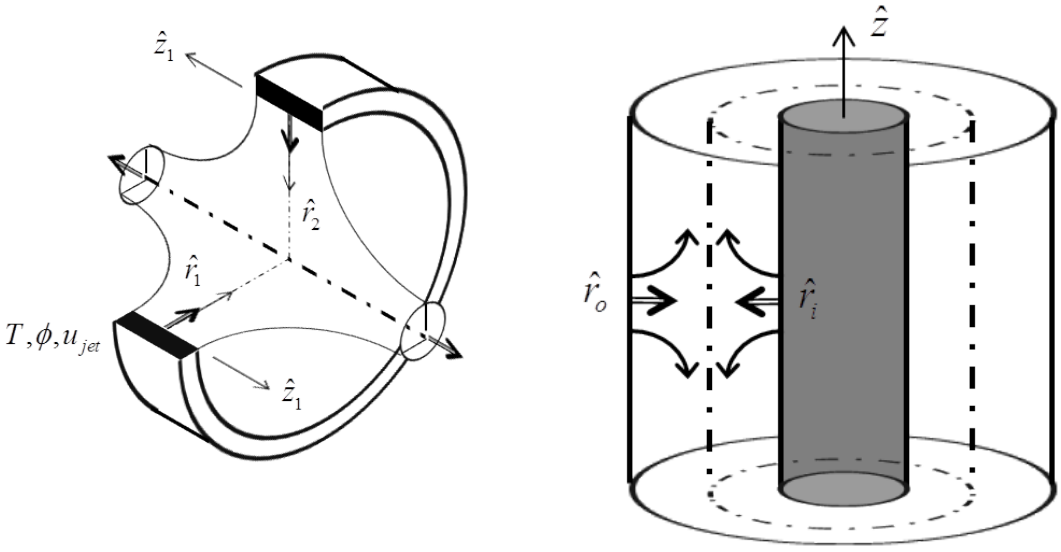

(a) Tubular burner

(b) Opposed Tubular burner

Figure 1.4: Tubular(left) and opposed tubular (right) burner schematics

1.1.2 Tubular and Opposed Tubular Flame

The tubular flame and opposed tubular flame combustors are similar configurations to the planar opposed jet burner in many respects. Both of these configurations provide well defined fluid strain fields which allow for flame-stretch interaction to be studied. Kinematic and strain conditions are changed through bulk velocity variations. However, because of the axisymmetric nature of the flow field, the flames supported by the tubular and opposed tubular burner configurations are cylindrical sheets and therefore are curved flames subject to strain–induced stretch. Hu *et al.* [50] and Wang *et al.* [120] have studied these configurations analytically, numerically, and experimentally. Investigations of this configuration have shown an additional sensitivity of the flame to curvature induced stretch when subject to equivalent strain induced flame stretch [125]. A brief summary of these models and their respective flow and strain field characteristics based on the above reference work is presented.

First, the tubular burner shown on the left hand side of Figure 1.4 is described. This configuration consists of axisymmetric, inwardly directed, radial jets. Along the

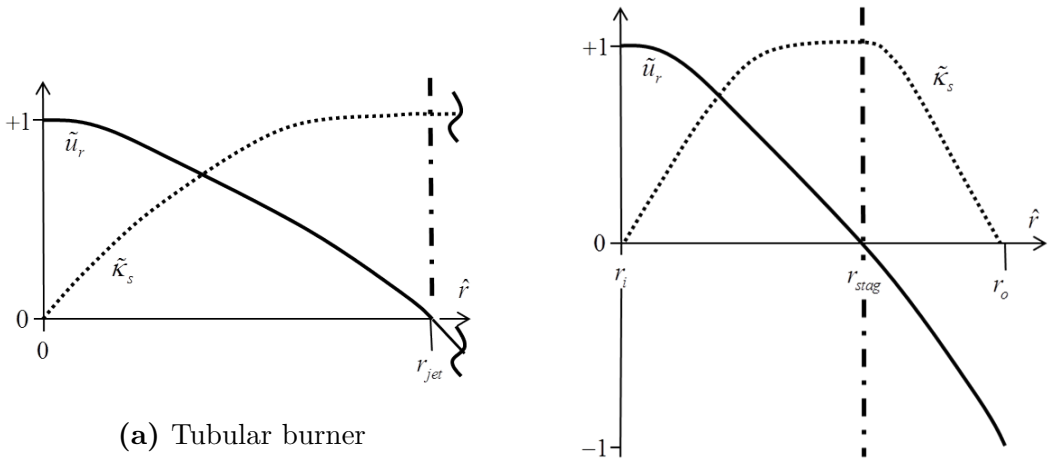

(a) Tubular burner

(b) Opposed tubular burner

Figure 1.5: Non-reacting tubular (1.5a) and opposed tubular (1.5b) representative flow, $\tilde{u}_r = u_r/U^o_{jet}$, and stretch fields, $\tilde{\kappa}_s = \kappa_s/max\left(\kappa_s\right)$ based on analytical solutions provided by Wang *et. al* [120].

axis of symmetry of the jets, radial velocity stagnation conditions exist and a single, connected, cylindrical flame is supported by this combustor with a radius less than the location of the exit of the radial jets. Due to the axisymmetric conditions of this geometry, and the similarity conditions, the radial velocity depends only on the radial location, while the z-component of the velocity field only depends on the z coordinate.

The opposed tubular flame configuration (right image of Figure 1.4) has outwardly directed radial jets which oppose the inwardly directed radial jets. This results in a cylindrical stagnation surface of radial velocity which separates the jets. If both jets are comprised of combustible reactant streams, two cylindrical flame sheets can be supported by this configuration with opposite signs of flame surface curvature for the inner and outer flame. Representative velocity fields and stretch fields for these two configurations are shown in Figure 1.5 where quantities have been normalized by the maximum value observed in the field: For both cases, we show local stretch rates

rather than local strain rates where the incompressible equation for stretch is:

$$\kappa_s^{tubular} = \frac{\partial u_z}{\partial z} = -\frac{\partial u_r}{\partial r} \tag{1.3}$$

For the tubular burner, radial velocity monotonically decreases along the jet axis as the hydrodynamic stretch rate becomes increasingly positive (1.5a), similar to the behavior noted for the planar opposed jet configuration under non-reacting conditions. Maximum stretch rates occur at the axis of symmetry, where the radial flow stagnates. Analytical solutions of the non-reacting flow field for the tubular burner done by Wang *et al.* [120], provide the following expression for local surface stretch throughout the burner domain:

$$\kappa_s^{tubular} = +\frac{\pi U_{jet}^o}{r_{jet}} \cos(0.5\pi\tilde{r}^2) \tag{1.4}$$

where $\tilde{r} = r/R_{jet}$.

For the opposed tubular burner, the non-reacting, hydrodynamic stretch field, $\kappa_s^{tubular}$, is positive throughout the domain and maximum at the stagnation plane (1.5b). Away from the stagnation plane, $\kappa_s^{tubular}$ decreases monotonically in either direction towards the inner or outer jet. Wang *et al.*[120] also provide non-reacting, analytical solutions for the hydrodynamic stretch field of the opposed tubular burner [120]. The solution below is for a simplified set of conditions where the velocity and density of both the inward and outward jets are equal [120] ($U_{jet}^o = U_{jet}^i$, and $\rho^o = \rho^i$):

$$\underline{\tilde{r}_s < \tilde{r} < 1:}$$

$$\kappa_s^{tubular,opposed} = -\frac{U_{jet}^o}{R_{jet}^o} Q^{0.5} cos\left(0.5Q^{0.5}\tilde{r}^2 + \pi/2 - 0.5Q^{0.5}\right) \tag{1.5}$$

$$\underline{R_{jet}^i/R_{jet}^o < \tilde{r} < \tilde{r}_s:}$$

$$\kappa_s^{tubular,opposed} = -\frac{U_{jet}^o}{R_{jet}^o} Q^{0.5} cos\left(0.5\frac{R_{jet}^o}{R_{jet}^i} Q^{0.5}\tilde{r}^2 + \pi/2 - 0.5\frac{R_{jet}^i}{R_{jet}^o} Q^{0.5}\right) \tag{1.6}$$

where the radial location, r, has been normalized as $\tilde{r} = r/R_{jet}^o$ and the location of the stagnation plane, R_s, has been normalized as $\tilde{r}_s = R_s/R_{jet}^o$. Expressions for the

location of the stagnation plane, and Q are as follows [120]:

$$R_s = \left(R^o_{jet} R^i_{jet}\right)^{0.5} \tag{1.7}$$

$$Q = \frac{\pi^2}{\left(1 - R^i_{jet}/R^o_{jet}\right)^2} \tag{1.8}$$

While the strain and flow field of the tubular, or cylindrical, flame configuration are seemingly very similar to the opposed jet configuration, as pointed out earlier, studies have shown the response of flames to this configuration to be sensitive to the radius of curvature of the flame[125, 5]. In fact, Yokomori *et al.* have recommended the use of this configuration in assessing the sensitivity of flames to curvature [125].

1.1.3 Unsteady Stretch Configurations

There are multiple pathways through which unsteady effects on a stretched flame can be studied, which are discussed in this section. For instance, unsteadiness can be introduced simply by varying the input parameters of the model with time. This can be achieved for the opposed jet model through a time varying outlet velocity introducing flow and strain unsteadiness to the flame. Likewise, varying the equivalence ratio of the jet with time introduces mixtures with time varying stretch sensitivities into the flow field. Both of these forms of harmonic unsteadiness in the velocity and mixture composition at the jet exit for the opposed jet model are discussed [95, 53, 117, 111]
.

There are also models for which the flame and stretch conditions are inherently unsteady, such as the expanding spherical or cylindrical flames. As the flame progresses in these configurations, the radius of the flame front changes with time causing a change in the curvature induced stretch. Lastly, studies of the opposed jet configuration subject to turbulent flow conditions are introduced [36, 64].

1.1.3.1 Harmonically Forced Opposed Jet

In this section, we are interested in discussing the response of the flame stabilized in an opposed jet combustor when subject to unsteadiness in the local flow field conditions and in the local mixture composition. First, studies are highlighted which have investigated harmonically unsteady flow effects on flame response in a strained flow field. Then, studies which have investigated the effect of equivalence ratio oscillations are discussed.

For instance, Sung *et al.* [111] performed symmetric opposed jet calculations for a premixed flame subject to mono-frequency harmonic oscillations in the jet exit velocity. The results of these studies are reproduced in Figure 1.6. They found for $Le \leq 1$ mixtures that low frequency velocity oscillations, $f < 100Hz$, the dynamic flame response was pseudo-steady state and that extinction boundaries were not affected by the unsteadiness. The pseudo-steady state flame behavior in this case is due to the time scale of the velocity fluctuations being larger than the chemical time scale.

As the frequency of the velocity oscillations was increased above 100 Hz, Sung *et al.* noted that the flame response deviated from a pseudo-steady state response for $Le \leq 1$ and $Le > 1$ mixtures. In fact, for inlet velocity oscillations having a frequency on the order of $10kHz$, the flame response loop is bi-modal, having a lower and upper value that is stretch invariant with small deviation from the steady state response at the mean stretch value. This behavior is result of the period of oscillations becoming on the order of and then smaller than the chemical time scale at which point the flame is insensitive to these oscillations. In other words, the lifetime of the unsteady strain caused by the velocity oscillations is too small to allow for non-equidiffusion to manifest and cause burning rate fluctuations.

In addition to numerical studies of the opposed jet configuration to harmonic inlet velocity, there have been experimental studies as well [98, 97, 62, 77]. For example, Sardi and Whitelaw [97] characterized the extinction limits of premixed flames subject

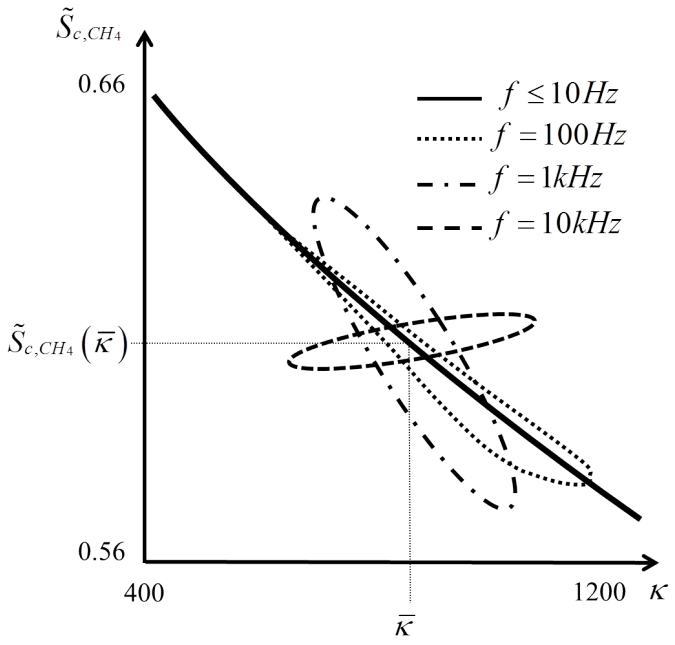

Figure 1.6: Flame stretch response of flame consumption speed to harmonic fluctuations in inlet velocity for an opposed jet configuration, reproduced from studies performed by Sung *et al.* [111] with author permission.

to periodic velocity oscillations. Their experiments also demonstrated the dependence of the flame response on disturbance frequency as well as disturbance amplitude and duration as they noted the ability of the flame to withstand instantaneous strain rates higher than the extinction strain rates of unforced cases.

Lastly, similar studies have been performed on the opposed jet model subject to harmonic variations in the equivalence ratio of the mixture at the jet exit [93, 95]. Richardson *et al.* [93] explored the effect of mixture stratification resulting from harmonically varying mixture composition at the jet exit with specific focus on the effect on flame structure. Sankaran *et al.* [95] performed studies on a similar configuration but focused on the effect on flammability limits, establishing a *dynamic flammability limit*. Similar to the unsteady strain field studies, the response of the flame was observed to decrease with increasing frequency of mixture composition variations.

1.1.3.2 Turbulent Opposed Jet

The opposed jet configuration lends itself to the study of turbulence-flame interaction within a strained flow field. It has been used to study the effect of turbulence on flame structure and the phenomenon of stretch induced extinction. There have been various experimental studies investigating turbulent flame structure using this configuration [126, 63, 20]. Within these studies, observations of turbulence induced flame structure changes has important implications on modeling flame extinction using flamelet concepts. Extinction studies have captured the progression of the flame as it progresses towards blowoff [64] and have also studied the sensitivity of bulk extinction stretch rates to geometric parameters, such as nozzle separation, chemical kinetic parameters, such as equivalence ratio, and flow parameters, such as bulk nozzle velocity [77, 62].

1.1.3.3 Spherically/Cylindrically Expanding Flame Configurations

Non-stationary flames, or expanding flames, occur when there is a kinematic imbalance along the flame front where the flame speed does not equal the flame normal flow velocity. The most basic non-stationary flames involve the flame propagating freely into a field with no bulk flow velocity. Two such geometric configurations are the spherically and cylindrically expanding flames which originate from point source or line source ignition events respectively (Figure 1.7). As a result of the non-stationary nature of these configurations, there is a time dependence on the speed of the advancing flame front. This unsteadiness is the result of expansion effects on the product side of the flame displacing the flame front to which corrections can be applied in order to extract meaningful flame speeds. Another source of unsteadiness is caused by the changing flame radius as the flame expands outward, $r_{flame}(t)$ thereby causing a change in the curvature induced stretch, $\kappa_{curv}(t)$. Depending on the mixture's Le number, this will either result in a flame that is more or less critically stretched as

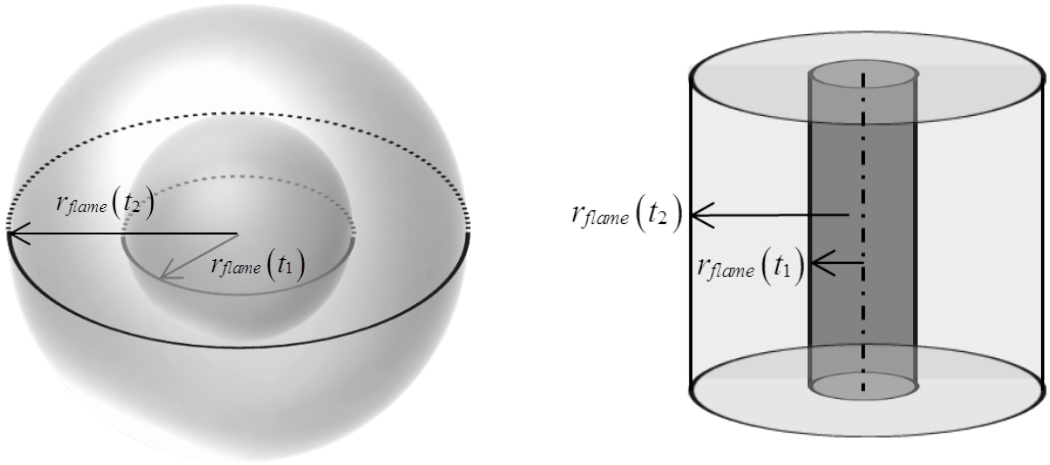

(a) Spherically Expanding

(b) Cylindrically Expanding

Figure 1.7: a) Spherically and b) cylindrically expanding flame geometric configurations.

time passes.

1.2 Angled Opposed Jet Burners

These burners are similar in appearance to the opposed jet burners but differ with respect to the relative orientation of the opposing jets. As its name would suggest, the centerlines of the opposed jets are angled relative to each other by angle α, as shown in Figure 1.8. This produces a flow field distinguished from that of the opposed jet configuration. Most importantly, it results in a strain and velocity field that is no longer collapsed by a single similarity variable but highly dependent upon y and z. Non-reacting studies by Besbes *et al.* [7] demonstrate the unique flow field characteristics of the angled opposed jet configuration. For reference, results of their work are reproduced in Figure 1.9 which shows the transverse velocity profile along the stagnation plane between the two jets. For the angled case, $\alpha = 45°$, the velocity profile is no longer symmetric about the jet centerline, producing higher velocities on one side and lower velocities on the other side of the jet centerline compared to the directly opposed jet case, $\alpha = 0°$. In addition, note that due to the distance between

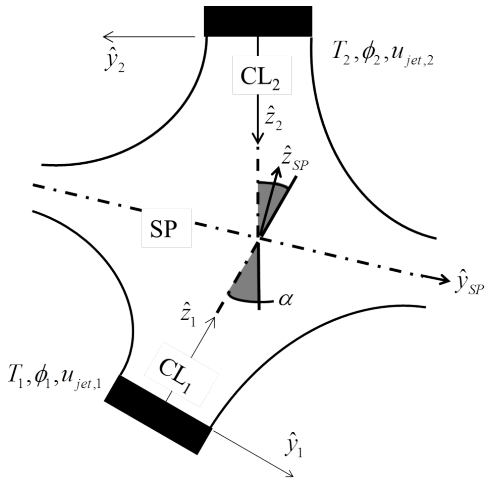

Figure 1.8: Angled opposed jet burner configuration.

the burners being dependent upon y, evident in Figure 1.8, it is expected for the local strain to be dependent upon y as well.

Liu and Ronney [74] have experimentally characterized flames in the angled slot burner, showing that flames stabilized in this configuration are horizontal relative to the burner exit, but curve towards and terminate at the stagnation plane marking the edge of the flame. It is the point where the two flames meet which is the "edge" of the flame and for this reason that flames supported by the angled burner configuration are referred to as "edge flames." Figure 1.10 shows select images from Liu *et al.* and their experimental studies of the angled burner for several configurations. Note that when both jets are premixed streams, as is the case for the middle and bottom image of the figure, the two flames on either side of the stagnation plane do in fact connect at a single location on the stagnation plane. We presume that away from the flame edge, based on Besbes *et al.* [7], that there are normal and tangential flow velocity components relative to the flame surface. Thus, it is the edge of the flame, located on the stagnation surface, which likely anchors the flame as it lacks a tangential flow velocity component along its surface and is oriented such that the direction of flame propagation aligns with the flow direction. Numerical studies have been performed

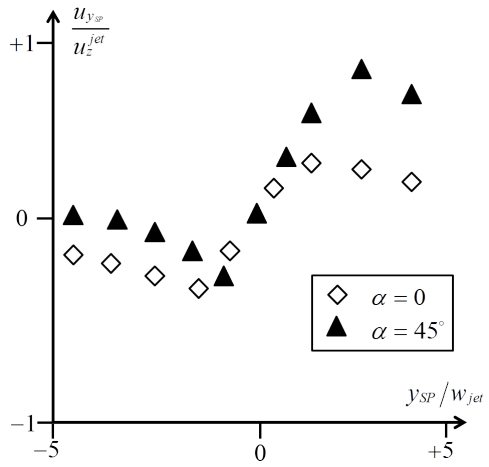

Figure 1.9: Reproduced figure of non-reacting angled opposed jet transverse velocity profile along center stagnation plane from Besbes *et al.* [7]

.

on the angled opposed jet configuration calculating the burning rates of edge flames [30].

In summary, the characteristics of the angled burner are compared to opposed jet burner. Contrary to the opposed jet burner, in addition to spatially varying strain rates along its surface, the angled burner flame likely has non-constant flame speeds along the flame surface as well. In addition, similar to the opposed jet configuration, there is a tangential velocity component along the flame surface throughout the domain except where the flame is anchored by the edge of the flame residing on the stagnation plane. Studies of angled opposed jet flames or, more generally, edge flames, are of relevance as practical flames are stabilized in developing shear layers with highly spatially dependent strain and velocity fields, and the flame structure at the anchoring location has been observed to resemble that of an edge flame, as is discussed further in Chapter 6. This has important implications on modeling of flame stabilization as the physics of edge flames are different from idealized, 1D flames.

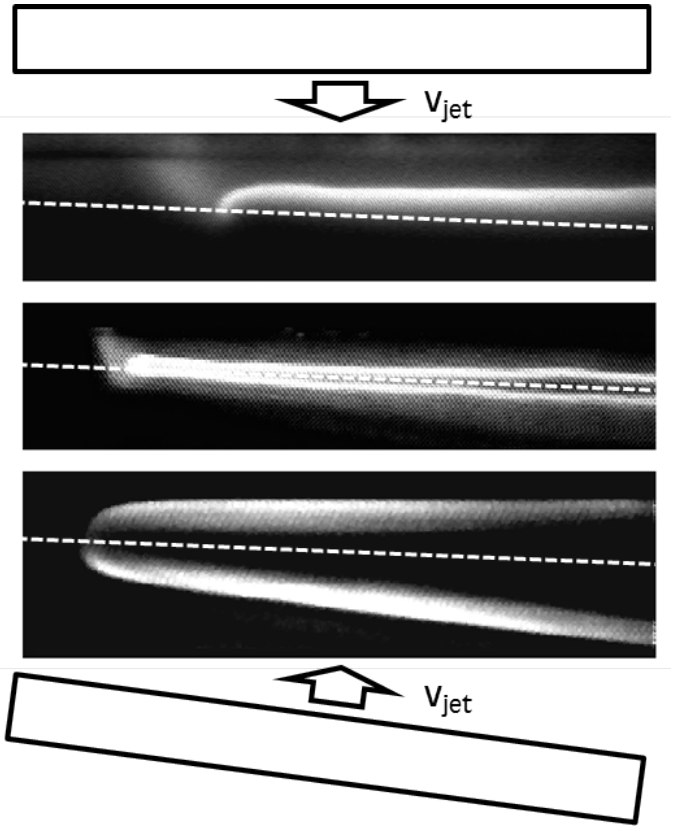

Figure 1.10: Figure reproduced from Liu *et al.* [74] with author permission, showing chemiluminescence flame images of angled opposed jet flames produced from CH_4/Air (top), $CH_4/O_2/CO_2$ (middle), and $C_3H_8/O_2/He$ (bottom) mixtures. Note: Top condition is for a reacting top jet opposed by a non-reacting bottom stream.

1.3 Experimental Studies of Practical Combustors

In this section we discuss and highlight notable and relevant studies of bluff body and swirl stabilized flames. Bluff body stabilized flames are included in this discussion because the geometry of interest in this work, although a swirling flowfield, includes a centerbody. As a result of this common geometric feature, these two combustor configurations share similar flow features of a separating shear layer and wake in the near field of the combustor in and by which flames are stabilized for both configurations. A selection of the many studies exploring the sensitivity to geometrical and operational parameters, as well as reduced–order scaling of blowoff events using Da number, is discussed. The inability for a single reduced–order scaling parameter to capture blowoff events is a strong indicator of the complex physics which control flame stabilization. This has motivated studies focused on observing the flame as it progresses towards blowoff [84, 16]. These studies aid greatly in elucidating the phenomenon of blowoff and controlling physics from a macro field perspective. Finally, studies measuring local conditions and properties related to blowoff, such as flame stretch, are discussed for swirl stabilized combustors.

1.3.1 Bluff body stabilized flames

1.3.1.1 Blowoff sensitivities of bluff body flames

There have been many studies of bluff body combustors investigating operational limits, namely blowoff, and the sensitivity of blowoff events to operational and geometric parameters [104, 22]. These studies have demonstrated the complexity in developing scaling parameters which collapse the observed operational and geometric parameter dependencies. For example, Shanbhogue *et al.* [104] applied a Da number approach to scaling blowoff using bulk flow parameters for bluff body stabilized flames. Da number scaling approaches reduce the physics of blowoff to a competition between

fluid mechanic and chemical time scales:

$$Da = \frac{\tau_{flow}}{\tau_{chem}} \tag{1.9}$$

A classic example of Da scaling is the well-stirred reactor (WSR) for which τ_{flow} is the combustor residence time, $\tau_{res} = V/\left(u_o \times A_o\right)$, and τ_{chem} is the critical chemical time, defined by the minimum residence time for which a reaction occurs. Flame extinction occurs when $Da \leq 1$, or when the residence time is less than the critical chemical time. In this very simple example, the key characteristic times are easily identified and quantified, which results in the success of Da as a scaling parameter. Thus, once τ_{chem} is determined, the extinction velocity can be determined for a given WSR volume, V, and inlet cross sectional area,A_o , by setting $Da = 1$. However, for practical combustors, the relevant time scales are not as easily defined.

Classical Da approaches to capture blowoff of bluff body stabilized flames have based τ_{flow} on observable mean features of the flowfield such as the bluff body wake. For instance, Zukoski [128] hypothesized the critical physics of flame stability to be the ignition of the incoming flow by the products in the bluff body wake. In this model, blowoff occurs when the ignition time is larger than the time which the incoming reactant stream is in contact with the wake, which is defined as:

$$\tau_{flow} = L_{wake}/u_o \tag{1.10}$$

While seemingly simple, the length of the wake, L_{wake}, is a function of u_o as well as the equivalence ratio. In addition to the size of the wake, the entire structure of the wake can change as well. In fact, as discussed by Nair [83], the structure of the wake has been observed to be a strong function of Reynolds number [70], as well as the temperature jump across the flame. Thus as operational and geometrical space is explored, the relevant chemical and fluid mechanical parameters governing flame stability can change as well.

More recent studies have benefited from the ability to calculate fundamental chemical times using chemical kinetic codes such as CHEMKIN [1]. For instance, critical chemical times from the WSR can be calculated *a priori*, allowing for the form of τ_{flow} to be directly evaluated from experimental blowoff data. Shanbhogue *et al.* [104] assembled blowoff data from multiple experimental investigations reporting blowoff conditions, and evaluated several formulations for $\tau_{flow} = D_{ref}/U_{ref}$, using different reference lengths, D_{ref}, and reference velocities, U_{ref}. In addition, Shanbhogue *et al.* evaluated three different chemical times: the extinction time of a WSR, τ_{WSR}, the inverse of the extinction stretch rate, τ_{ext}, and the unstretched, laminar flame time, τ_{pf}, defined as δ_f/S_d^o. They observed an additional Re dependence on Da for all variations of τ_{flow} and τ_{chem} combinations. Irrespective of the definition of Da chosen, when the data was grouped by axisymmetric and two-dimensional bluff bodies, the two groupings had different power dependencies on Re when fit to:

$$Da = b\ Re_D^a \tag{1.11}$$

Note however, that within each grouping of data, there were systematic differences between the subset of axisymmetric and two-dimensional bluff bodies as observed by differences in the values of b. Although Shanbhogue *et al.* [104] demonstrated the ability of Da scaling to reduce blowoff data, it falls short in capturing the physics which distinguishes axi-symmetric and two-dimensional bluff bodies, explaining the additional velocity dependence, and accounting for the systematic differences amongst data sets. If anything, this work reaffirms the difficulties in Da scaling approaches due to the complexities of the physics which cause blowoff.

1.3.1.2 Observations of near extinction bluff body flames

In this section, we describe the blowoff process for a bluff body stabilized flame, as commonly observed by experimental studies.

As near extinction conditions are approached by decreasing equivalence ratio towards the lean limit, for instance, there is a noticeable change in the spatial and temporal characteristics of the flame. Experimental studies of a bluff body stabilized flame performed by Nair *et al.* [84] observed extinction events occurring downstream of the bluff body, resulting in the formation of flame pockets at near blowoff conditions. As equivalence ratio was further decreased towards the lean limit, the extinction events occurred more frequently and initiated at distances closer to the bluff body. A representative sketch of blowoff progression from Nair *et al.* [84] is reproduced in Figure 1.11. Experimental work by Chaudhuri *et al.* [16] confirmed the observations above, capturing near blowoff conditions of a bluff body stabilized flame through OH-PLIF flame imaging. Their results show a planar sequence of blowoff very similar to that observed by Nair *et al.* [84], as shown in Figure 1.12, where extinction events initially occur downstream of the wake, increase in frequency, and eventually lead to extinction of the flame in the wake region at blowoff conditions. Similar studies performed by Kariuki *et al.* [58] focus on the progression towards blowoff in the wake region of the flow field. As a precursor to blowoff, regions void of OH-PLIF signal in the center regions of the recirculation zone are observed, also leading to increased OH-PLIF intensity on the interior boundary of OH-PLIF within the wake region. All in all, these studies suggest that absolute extinction is preceded by changes in flame stability downstream of the anchoring or attachment region of the flowfield.

1.3.2 Swirl stabilized flames

1.3.2.1 Swirling flame behavior

There have been many studies examining the behavior of swirl stabilized combustors, both experimental and computational [112, 73]. In fact, due to the complexity of the swirling flow field, there have been numerous studies of non-reacting, swirling flows [76]. These studies identified the main structures of a swirling flowfield and sought to map out the various flowfield topologies which exist across a range of reduced–order

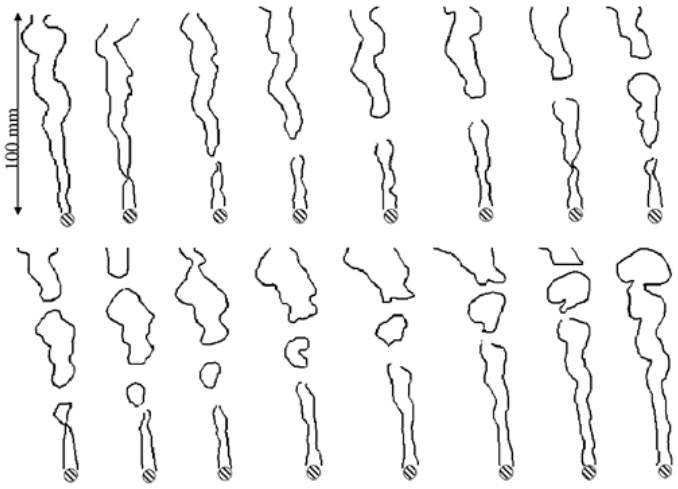

Figure 1.11: Blowoff progression for a bluff body stabilized flame reproduced from Nair *et al.* [84] with author permission.

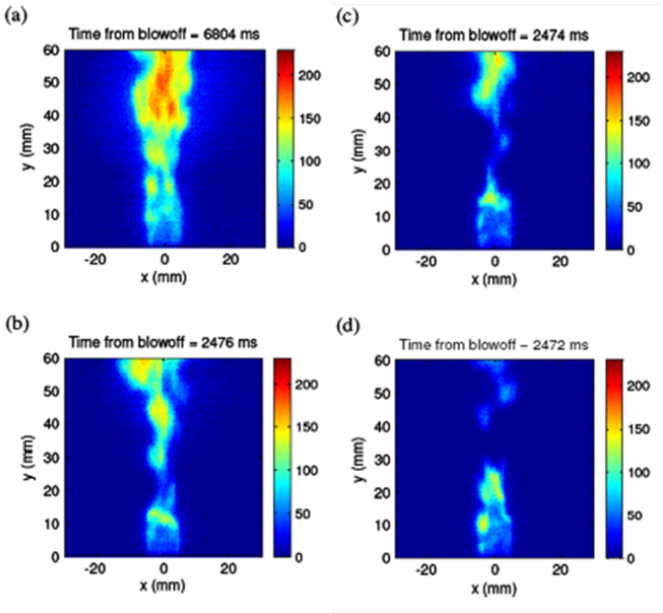

Figure 1.12: OH-PLIF images of flame sequence at near blowout conditions reproduced from Chaudhuri *et al.* [15] with author permission.

parameters. For example, Emara *et al.* [38] studied the effect of contraction ratio on the vortex breakdown structure. Others have systematically explored the sensitivity of the flow field structure of annular swirling flows in Reynolds and swirl number space [105, 51]. Understanding swirling flowfields is important since, to a large extent, the stabilization locations are directly related to the structure of the flow field. In addition, the presence of heat release can alter the flowfield on a local and macro scale as demonstrated by Chterev *et al.* [22].

Within a particular swirling combustor, reacting studies have addressed questions relating to the flame shapes which can be supported by swirling flowfields. These questions ultimately are where does the flame stabilize and how do the flame stabilization locations change as operational limits are approached. For example, Chterev's study of an annular swirl stabilized combustor demonstrated the ability of the combustor to support four unique flame shapes [22]. Additionally, studies by Fritsche *et al.* [43] have mapped the flame shapes as a function of preheat temperature and equivalence ratio at thermally steady state conditions, also showing the existence of multiple flame shapes. For all the various flame shapes observed, the stability of each flame is either governed by the dynamics of a shear layer or the vortex breakdown bubble of the flow field. In some cases, flame shapes have been observed which are stabilized in multiple shear layers or some combination of shear layer and VBB stabilization. Also, as was noted by Chterev *et al.* [22] the transition from one stabilization region or from one flame shape to another occurs abruptly resulting in drastic changes in combustor performance. In addition, these studies by Chterev *et al.* [22] of an annular swirl combustor observed the lean operational limit for some cases to be governed by ISL flame extinction.

1.3.2.2 Flame stretch measurements

While there have been many macro scale studies on swirling flames, there are fewer investigations into the flow conditions in the regions where the flame stabilizes. Thus, the physics limiting the operation of these combustors is not yet fully understood. That being said, studies have been performed characterizing the strain conditions experienced by flames in swirling combustors. For example, Zhang *et al.* [127] obtained such measurements for the inner shear layer of a swirl stabilized facility reporting the conditions of stretch in the attachment point region using the mean flow field and assuming a mean flame position and orientation. Zhang's measurements demonstrated the high fluid strain rates present in the near field and the potential for high flame stretch conditions to be present. Other studies measuring the stretch along a flame were completed by Filatyev *et al.* [41] and Sinibaldi *et al.* [106] for a premixed flames, and Donbar *et al.* [34] for a non-premixed flame. Their results also demonstrated the high mean stretch conditions present in the shear layer as well as wide range of stretch, made possible by the time-resolved flow and flame field measurements that were made using PIV and PLIF respectively.

CHAPTER II

PREMIXED FLAME STABILIZATION

This chapter discusses the concepts of premixed flame stabilization relevant to these studies. A pivotal precursor to this discussion is the establishment of an understanding of turbulent combustion regimes. The various combustion regimes are unique in the degree to which the flow field can interact with the flame, which depends on the flow field turbulence, and the structure and propagation speed of laminar flames. The various regimes of turbulent combustion defined by a comparison of velocity and length scales of the flow and flame are briefly discussed based on work done by Peters [88, 89]. In addition to the traditional turbulent combustion regimes established by Peters, a spectral turbulent combustion regime diagram incorporating the range of turbulent scales developed by Poinsot *et al.* [90] is introduced and discussed as well. As demonstrated by a more detailed discussion of turbulent combustion regimes, the regime of combustion strongly influences the physics included in modeling and interpretation of experiments related to flame stabilization.

In addition, because the flame is anchored in the shear layers of the flow field, as observed experimentally and expected with bulk flow velocities being much greater than the laminar flame speed of the incoming reactant mixture, the physics of shear layer flame stabilization is also discussed. First and foremost, shear layer stabilized flames are subject to a high degree of fluid strain, especially at the attachment point. The behavior of premixed flames subject to fluid strain is well documented from opposed jet experiments and models as discussed in Chapter 1. As such, this section focuses on a discussion of the strain contributions to stretch for a swirling flowfield with a brief discussion on the manner through which flame stretch effects manifest

themselves. Second, recirculation zone physics and the various pathways through which the flame burning rate is affected by heat transfer or mixing are discussed. Lastly, the concept of flame anchoring, a requirement for flame stability, is discussed and distinguished between *normal propagation* and *edge flame* anchoring.

2.1 Turbulent Combustion Regimes

This section discusses approaches to characterize the manner in which turbulence interacts with the flame. First we consider approaches which compare length and velocity scales of the flame and velocity field in order to establish the regimes of turbulent combustion. Within this framework, we discuss the various regimes established and the distinguishing characteristics of each of the regimes. Second, we introduce a modified turbulent combustion regime approach which incorporates the range of length and time scales present in a turbulent flow field.

2.1.1 Time and length scale parametrization

There have been several proposed combustion regime diagrams based on length and velocity based scalings of flame and turbulence parameters [9, 87, 2, 90, 89]. These approaches aim to describe how turbulent eddies can interact with a propagating flame. The spectrum of interaction ranges from the laminar regime, where there is an absence of turbulence such that a laminar flame structure and burning properties are observed, to highly turbulent flow fields that are able to break up any flame structure resulting in *distributed* or *broken reaction zones*. In between these two extremes, there is a progression towards increased interaction between flame and flow as turbulence is increased. We next present a summary of Peters' description of turbulent combustion regimes [89], describing the criteria establishing the various regimes and characteristics of each.

Central to Peters' approach are two questions: are velocity fluctuations large enough to locally displace the flame front and are the turbulent scales small enough

to disrupt the flame structure. As such, two parameters are defined, a velocity ratio comparing the turbulence intensity and laminar flame speed, u'/S_d, and a length scale ratio comparing the integral length scale and flame thickness, l/δ_f. Peters uses these two parameters to define various combustion regimes as shown in Figure 2.1. We briefly describe the nature of burning in each of the combustion regimes and the physical meaning behind the boundaries, and reference Peters [89] for a complete derivation of the turbulent regime boundaries.

We begin in the *laminar flames* regime characterized as the region where the turbulent Reynolds' number is less than one, $Re_t < 1$. The $Re_t = 1$ line in the plot marks the boundary between laminar and turbulent flames and thus, the turbulent combustion regimes are all characterized by $Re_t > 1$. However, the degree to which turbulence interacts with the flame is quite different between each turbulent flame regime. In the weakest turbulent flame regime, the *wrinkled flamelets* regime, the turbulence intensity is not strong enough to cause significant unsteadiness in the flame front location ($u' < S_d$). It is only when $u' > S_d$ that the turbulence is able to effectively displace the flame front. The $S_d = u'$ line represents that boundary between weakly *wrinkled flamelets* and *corrugated flamelets* where strongly wrinkled flames are expected. Note however, that for the *wrinkled flamelets* and *corrugated flamelets* regimes that the smallest scale of turbulence, the Kolmogorov scale of turbulence, η, is larger than the laminar flame thickness and thus laminar flame structure is preserved. Also, since the laminar flame structure is preserved within these regions, flame propagation can be modeled using laminar flame concepts.

The remaining two combustion regimes are distinguished by the degree to which the flame structure is affected by the Kolmogorov length scale, η. Above the $\eta = \delta_F$ line, the Kolmogorov turbulent length scale is smaller than the laminar flame thickness and able to alter the preheat zone of the flame. If however, $\eta > \delta_R$, a structured reaction layer is preserved within the *thin reactions* regime. Once η is able

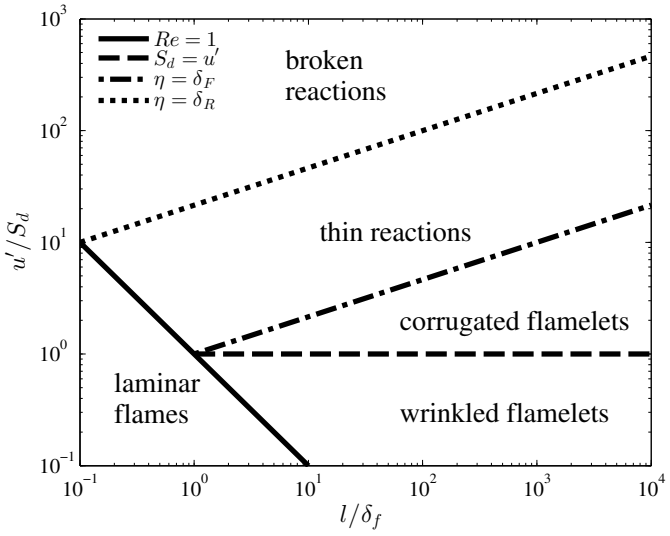

Figure 2.1: Turbulent combustion diagram reproduced from Peters [89].

to penetrate the reaction layer, burning is no longer structured as a thin reaction region dividing products from reactants, but occurs as *broken reactions*.

2.1.2 Spectral diagrams

There are several shortcomings in the derived turbulent combustion regime diagram presented in Figure 2.1. Besides the order of magnitude assumptions and the difficulty in obtaining turbulence properties such as the integral length scale velocity fluctuations, u', there are additional physics which must be included in establishing turbulent combustion regimes. For example, in turbulent combustion, there is not a single length scale but a range of length scales, from the integral to the Kolmogorov length scale, interacting with the flame. Large and small length scales interact with the flame in very different manners, and evaluated separately, could lie in different regimes of the combustion diagram shown in Figure 2.1. The destruction of turbulence by viscous dissipation is another important set of physics which alters the lower limit of length scales potentially interacting with the flame. In fact, with increases in viscous dissipation within the flame due to temperature driven increases in viscosity, the Kolmogorov length scale is expected to increase within the flame. Finally, in

addition to length and velocity scales of the turbulence, the lifetime of a vortex will influence its ability to interact significantly with the flame.

This motivated the development of a modified turbulent combustion regime diagram by Poinsot *et al.* [90] shown in Figure 2.2. Note the inclusion of the *Turbulence Line* representing the range of velocity and length scales from integral to Kolmogorov, with the Kolmogorov end of the line terminating on the $Re_\eta = 1$ line. The $Re_\eta = 1$ line is also the demarcation between turbulent and laminar flame regimes. In addition, the critical time-scale based Karlovitz number criteria for flame quenching, was generalized for all turbulence scales in the following expression:

$$Ka(r) = \left(\frac{u'(r)}{S_d}\right)\left(\frac{r}{\delta_f}\right)^{-1} \tag{2.1}$$

For turbulent scales with $Ka(r) < 1$, flame quenching is not predicted. Only scales with $Ka(r) > 1$ are predicted to induce flame quenching. Thus for the *Turbulence Line* shown in Figure 2.2, one would conclude that the flame would be quenched by the turbulence scales in the range $\eta < r <\approx 10^1\ \delta_f$. Normalized turbulent length scales greater than $\approx 10^1$ fall below the $Ka(r) = 1$ line and therefore would not quench the flame. It should be pointed out that if any scale quenches the flame, then distributed reactions would be expected. In their work, Poinsot *et al.* [90], evaluated the interaction of a vortex pair with a flame through numerical computations. By varying the size and characteristic velocity of the vortex pair, the turbulent regime diagram was evaluated point by point. These simulations resulted in two modifications to regime diagram: a lower cut-off limit and a modified quenching limit. The lower cut-off limit is the result of small scales of turbulence being destroyed by viscous dissipation in the flame such that the flame position and structure is unaffected. This lower cut-off limit establishes a lower range of scales along the *Turbulence Line*, $\eta < r < r_{cutoff}$, which have *no effect* on the flame. Above r_{cutoff}, there is a small range of scales which lie slightly above the $Ka(r) = 1$ line, however simulations showed that flame quenching

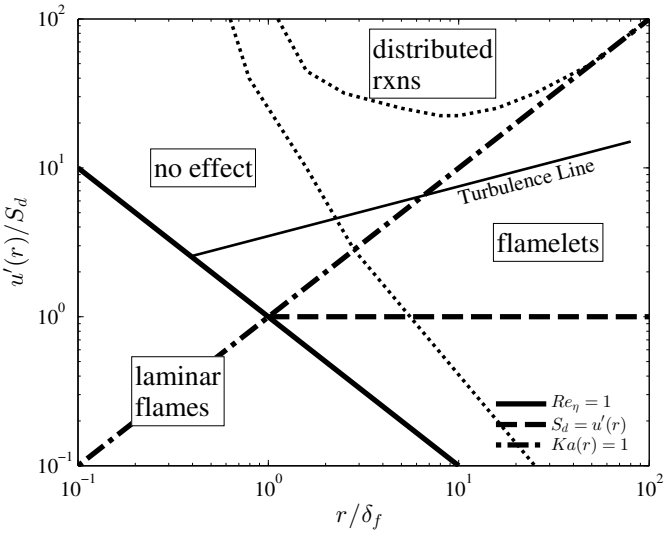

Figure 2.2: Modified turbulent combustion diagram reproduced from Poinsot *et al.* [91].

did not always occur when $Ka(r) > 1$. The line which defines the *distributed reactions* regime, was defined by simulation cases which caused flame quenching. Note that for large enough length scales, $r/\delta_f > \approx 10^{1.6}$, that $Ka(r) = 1$ does capture the boundary between *distributed reactions* and *flamelets*. With decreasing length scales, the deviation between the *distributed reactions* boundary and the $Ka(r) = 1$ line becomes increasingly large. In other words, smaller length scales require larger levels of turbulence, $u'(r)$, in order to effectively quench the flame. These findings by Poinsot *et al.* [90] were corroborated by experimental vortex-flame studies performed by Roberts *et al.* [94]. All in all, there is still much to be understood in defining combustion regimes for turbulent flames and the appropriate physics required to appropriately model turbulent flames.

2.2 Shear Layer Flamelet Stabilization Physics

There are several sets of physics of interest that could act to alter the local burning characteristics of the flame at the attachment point, as shown in Figure 2.9. As discussed, the local strain conditions at the attachment point can alter the flame

through flame stretch, κ_s, causing flame extinction as κ_s approaches the extinction stretch rate, κ_{ext}. The stability of shear layer stabilized flames is also sensitive to the composition and temperature of the recirculation zone. Experimental and numerical studies of counterflow flames have demonstrated the enhanced stability achieved through higher backside, product stream temperatures [21, 78]. Mixing between the recirculation zone and the incoming reactants is another pathway through which the local burning characteristics at the attachment point can altered. Although this pathway will result in dilution of reactants, the heat added to the mixture can overcome any decrease in reactant concentrations and enhance local flame stability. Finally, in order for the flame to maintain attachment in the shear layer, it must match the local flow velocity magnitude and direction at an anchoring location. For this discussion we assume that this experiment is within the corrugated flamelets regime. This assumption is supported by estimates of u'/S_d and l/δ_f on the order of ≈ 5 and $\approx 10^1$ respectively as well as by the behavior noted in CH-PLIF images of the flame where the high intensity regions of CH-PLIF in the shear layer occur as a continuous feature.

2.2.1 Stretched, Premixed Flames

Flames which are stabilized in shear layers are subject to high degrees of flame stretch that alters burning rates, flame speeds, edge velocities, and can ultimately lead to flame extinction [66, 68]. The underlying physics of flame stretch which engender these changes in flame speed and flame temperature are discussed in detail by Law [68] and later in this section. First, the stretch equations are presented for hydrodynamic strain sources for a swirling flowfield. These equations describe the manner in which fluid strain contributes to flame stretch. A separating shear layer is examined and used to demonstrate how normal and shear strain contribute to flame stretch. Lastly, the effect of flame stretch on important flame parameters influencing flame stability, such

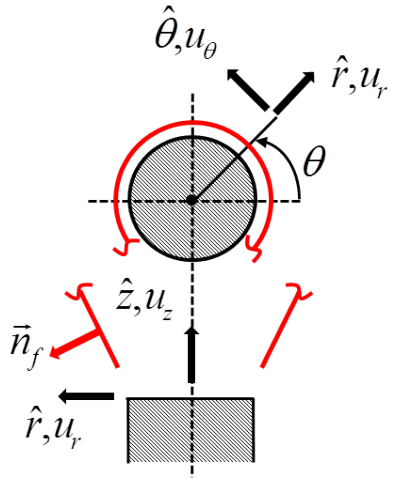

Figure 2.3: Flow and flame coordinate system for a centerbody stabilized, axisymmetric flame in cylindrical polar coordinates.

as displacement flame speed, S_d, and the extinction stretch limit, κ_{ext}, is discussed using results from opposed jet flame calculations.

2.2.1.1 Fluid Strain Rate Contributions to Flame Stretch

As discussed in the previous sections, flames are limited by a maximum stretch which they can withstand. Therefore, in order to stabilize in shear layers, the local flame stretch must be less than this limit. Although, the fluid mechanic strain rates in shear layers can be much larger than the extinction stretch rate, flames are still capable of existing. This is explained by analyzing how fluid mechanic strain rates contribute to flame stretch. As is be demonstrated below, the magnitude of the shear and normal strain rate components of the symmetric strain rate tensor, $S_{i,j}$, are quite different from the flame stretch rate, κ. Roll up of the shear layer, caused by the Kelvin-Helmholtz instability, can result in curvature induced flame stretch, κ_{curv}, and flame stretch caused by unsteady effects. The coordinate system used for this discussion is shown in Figure 2.3, which illustrates a flame anchored upon a bluff body. This discussion closely follows a related analysis of flame stretch rates in Zhang *et al.* [127]. In order to understand the relationship between the components of flow strain rate,

$S_{i,j}$, and flame stretch rate, κ, it is useful to first write the equation for flame stretch in its most general form:

$$\kappa = \frac{1}{A_f}\frac{dA_f}{dt} \tag{2.2}$$

Fundamentally defined, flame stretch is the area normalized, time rate of change of the flame material surface. Very simply, as is evident in eq. 2.2, positive stretch rates results from an increase in the area of the flame material surface and negative stretch rates from a decrease. Concealed in this simple representation of flame stretch are the fluid mechanical strain and flame curvature sources of flame stretch. This expression can be related to these quantities as follows [91]:

$$\kappa = \underbrace{-n_i n_j \frac{\partial u_i}{\partial x_j} + \frac{\partial u_i}{\partial x_i}}_{\kappa_s} + \underbrace{S_L\left(\frac{\partial n_i}{\partial x_i}\right)}_{\kappa_{curv}} \tag{2.3}$$

$$\kappa = \underbrace{-\vec{n}_f\vec{n}_f : \nabla\vec{u} + \nabla\cdot\vec{u}}_{\kappa_s} + \underbrace{S_d\left(\nabla\cdot\vec{n}_f\right)}_{\kappa_{curv}} \tag{2.4}$$

Note that equations 2.3 and 2.4 are identical in form but shown in index and Gibb's notation respectively. For both equations, the dependence of flame stretch on the orientation of the flame, fluid strain rates, the local flame speed, and the curvature of the flame is clearly evident. The terms have been grouped by contributions arising from hydrodynamic strain rate sources, κ_s, and from flame curvature, κ_{curv}. κ_s is non-zero only if the flow has spatial gradients, where as κ_{curv} contributes to flame stretch only if $\nabla\cdot\vec{n}_f$ is non-zero. For this analysis, we focus on flame stretch due to hydrodynamic strain for a two dimensional, steady flame in cylindrical polar coordinates and compressible flow upstream of the flame sheet as observed in the $r-z$ plane, $\kappa_{s,r-z}$. Although far upstream of the flame front, we expect the flow to be incompressible in the absence of temperature induced density gradients, the compressible flow equations derived are valid throughout the measurement domain. Under these assumptions, the $\kappa_{s,r-z}$ term may be written as:

$$\kappa_{s,r-z} = \frac{u_r}{r} + \frac{\partial u_r}{\partial r}\left(1 - n_r^2\right) + \frac{\partial u_z}{\partial z}\left(1 - n_z^2\right) - n_r n_z \left(\frac{\partial u_z}{\partial r} + \frac{\partial u_r}{\partial z}\right) \tag{2.5}$$

From eq.(2.5), we can explicitly identify the flame stretch due to normal (symmetric) and shear (anti-symmetric) flow strain as:

$$\kappa_{s,r-z}^{normal} = \frac{u_r}{r} + \frac{\partial u_r}{\partial r}\left(1 - n_r^2\right) + \frac{\partial u_z}{\partial z}\left(1 - n_z^2\right) \tag{2.6}$$

$$\kappa_{s,r-z}^{shear} = -n_r n_z \left(\frac{\partial u_z}{\partial r} + \frac{\partial u_r}{\partial z}\right) \tag{2.7}$$

The $\kappa_{s,r-z}^{normal}$ term describes the impact of flow acceleration and deceleration, while $\kappa_{s,r-z}^{shear}$ quantifies the manner in which shearing flow strain translates into flame stretch. Both terms are clearly nonzero in regions of high shear in flame stabilization regions, as the approach flow boundary layer separates into a significant change in cross sectional flow area. Equations (2.6) and (2.7) represent the two-dimensional fluid strain contributions to flame stretch that are resolved from the combined PIV and CH-PLIF planar measurements. Although these measurements will not resolve the out of plane contributions, it is argued that they are small in comparison to the measured quantities due to the flame being axisymmetric in the nearfield [127]. The contributions of strain terms not observable in the $r - z$ plane to stretch are presented and discussed later in this section.

The manner in which these flow strain terms lead to flame stretch is illustrated in Figure 2.4. A flame is shown in flowfields representative of positively sheared and decelerating flows with the flow velocity at the flame front projected into the flame tangential and normal directions. In both cases, flame stretch occurs due to variations in tangential flow velocity along the flame sheet. The contributions of shear and normal strain to flame stretch are discussed in detail next.

Figure 2.4b depicts the manner in which shear strain, manifested through positive, transverse gradients in axial velocity, $\frac{\partial u_z}{\partial r} > 0$, causes positive stretching of the flame, $\kappa_s > 0$. This is evident by the positive gradient of flow velocity tangential to the flame

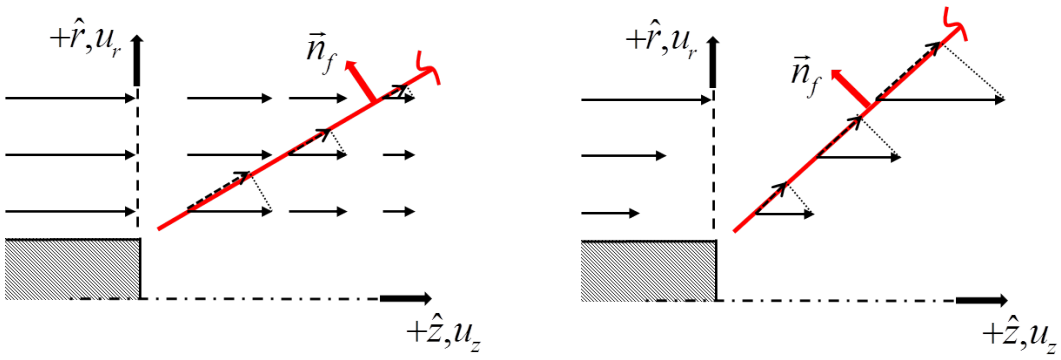

(a) Normal Strain, $\frac{\partial u_z}{\partial z} < 0$ **(b)** Shear Strain, $\frac{\partial u_z}{\partial r} > 0$

Figure 2.4: Illustration of the manner in which flow normal strain (2.4a)and flow shear strain (2.4b) cause flame stretch through variation in tangential flow velocity along the flame sheet.

front, which effectively acts to increase the flame front area. Figure 2.4a demonstrates the isolated effect of normal strain contributions to flame stretch. For this example we have illustrated this effect assuming that the axial flow is decelerating, $\frac{\partial u_z}{\partial z} < 0$, demonstrating the negative stretching or compression of the flame, $\kappa_s < 0$. Again, this effect is manifested through a variation of tangential velocity along the flame front, which in the illustration shows a negative gradient of tangential velocity.

Note that the effect of normal strain on flame stretch in this example is the opposite for flow fields which exhibit flow acceleration, however for our flow field of interest, we assume that the flow is locally decelerating. This can be justified by bulk flow arguments of flow deceleration caused by the abrupt increase in flow cross-sectional area at the point of flame attachment. However, as is demonstrated in the results section, a bulk flow argument overlooks the details of the strain field within the structure of the shear layer.

The equations for hydrodynamic stretch observed in the $r-\theta$ plane, $\kappa_{r-\theta}$, representing the potential out of plane strain contributions to flame stretch not captured

in this study are presented next:

$$\kappa_{s,r-\theta} = \frac{1}{r}\frac{\partial u_\theta}{\partial \theta}\left(1-n_\theta^2\right) - n_\theta n_r\left(\frac{\partial u_\theta}{\partial r}+\frac{1}{r}\frac{\partial u_r}{\partial \theta}-\frac{u_\theta}{r}\right) - n_z n_\theta\left(\frac{\partial u_\theta}{\partial z}+\frac{1}{r}\frac{\partial u_z}{\partial \theta}\right) - n_\theta^2\frac{u_r}{r} \tag{2.8}$$

The strain terms in eq. 2.8 could be measured by performing planar, stereo-PIV measurements in the $r-\theta$ plane. However, the 3D orientation of the flame must be captured completely in order to resolve all strain contributions to stretch. Using a two planar approach, one $r-z$ and one $r-\theta$, to capture the flame orientation, this would limit the resolution of the complete hydrodynamic stretch conditions to a point. We next consider the impact of the potential out of plane contributions in the $r-\theta$ plane on our interpretation of stretch conditions measured in the $r-z$ plane. We argue that these terms are small relative to resolved terms because of the axisymmetric nature of the flame in the nearfield close to the centerbody [127]. For reference, Figure 2.5 shows example OH-PLIF images taken in the $r-\theta$ plane, showing that while there is some fine scale wrinkling, the flame is nearly axisymmetric.

Revisiting eq. 2.8 note that the products of the time averages of each individual term is zero, as for instance, $\partial u_\theta/\partial\theta$ or $\bar{n_\theta}$. As such, these terms only can lead to time averaged contributions to flame stretch if the fluctuations are correlated. In contrast, the time average of resolved quantities such as $\partial u_z/\partial z$ and $\partial u_z/\partial r$ are strongly non-zero.

While extensive measurements and analysis exist for the maximum stretch rates that flames can withstand [3, 67], less is known about the extinction conditions for the edge flames that occur near the point of initiation of reaction. In addition, very little data or analysis is available on the actual stretch rates that flames see. Moreover, scalings for these stretch rates is not straightforward. For example, a hydrodynamic strain rate of the flow in a shear layer of thickness, δ, and velocity, u, can be estimated to scale as u/δ. However, *fluid mechanic strain* and *flame stretch* values can be quite

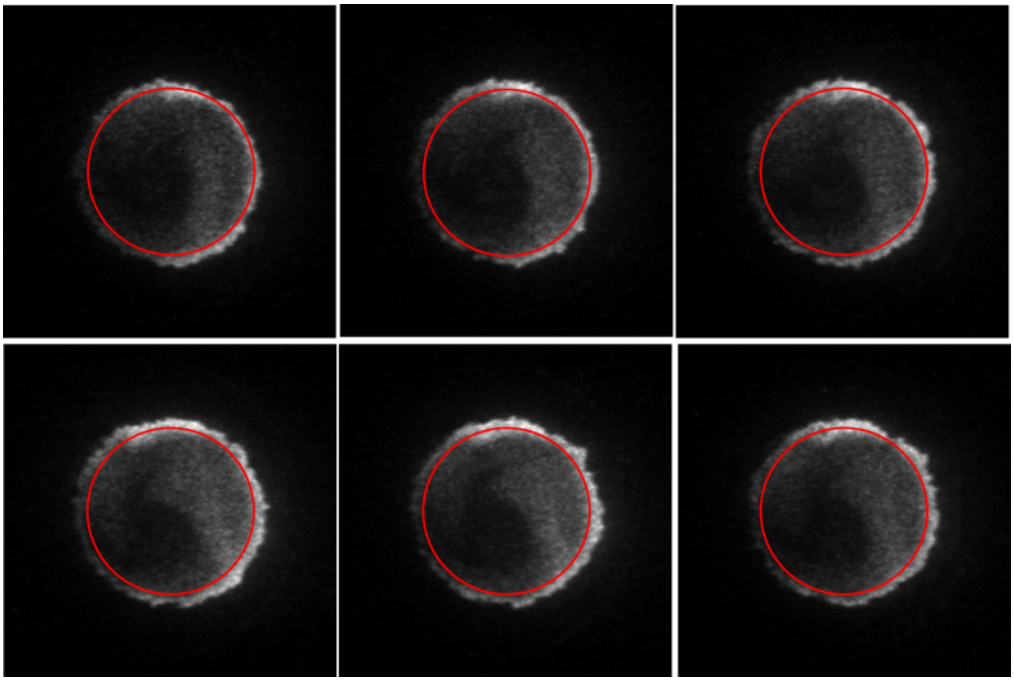

Figure 2.5: Typical OH-PLIF images in the $r-\theta$ plane 4 mm downstream of the dump plane for an inner shear layer (ISL) stabilized flame ($u_{pm} = 35\ m/s$ at $T_{ph} = 366\ K$, $\phi = 0.65$, 1.42" centerbody, 4.2" combustor, $S_m = 0.8$). Red line indicates location of centerbody relative to flame.

different [127], and their relationship is a very sensitive function of the flame angle with respect to the flow, among other parameters. In addition, it has been shown that the sensitivity of flame stretch to the velocity is not straightforward, which may explain the complex velocity scalings often observed for blowoff [104].

2.2.1.2 Premixed Flame Response to Stretch

The fundamental pathway through which stretch influences the flame is through an imbalance of heat and species diffusion, or *non-equidiffusion* effects. Diffusional imbalances of heat and species occurs as a result of the size of the material surface parallel to the flame front changing within the flame. These material surface area changes can result from the strain induced or curvature induced sources introduced in the previous section. The contributions from a single source of flame stretch can be visualized through representative control masses as shown in Figure 2.6 for normal strain and shear strain induced flame stretch. Shown is the deformation of a fluid element from the onset of the preheat zone to the product side of the flame along with the representative pathways for species diffusion and heat diffusion. For simplicity, we show the competing fluxes of heat and species diffusion within the context of a non-unity Lewis number mixture.

These examples clearly show in both cases how the presence of stretch can alter the pathways of heat and species diffusion, potentially altering the local burning properties. This can be observed by examining the diffusional pathways, identifying where heat produced by the control mass, and reactants initially within the control mass diffuse to. For example, let us examine the case of positive flame stretch induced by an axially decelerating, or negative normal strain, flow field (Figure 2.6a). Shown in this schematic is a control mass of reactants just upstream of the flame front, the location of the flame, and the control mass post flame. The dashed lines connecting the two control masses represent streamlines and thus no mass is convected across

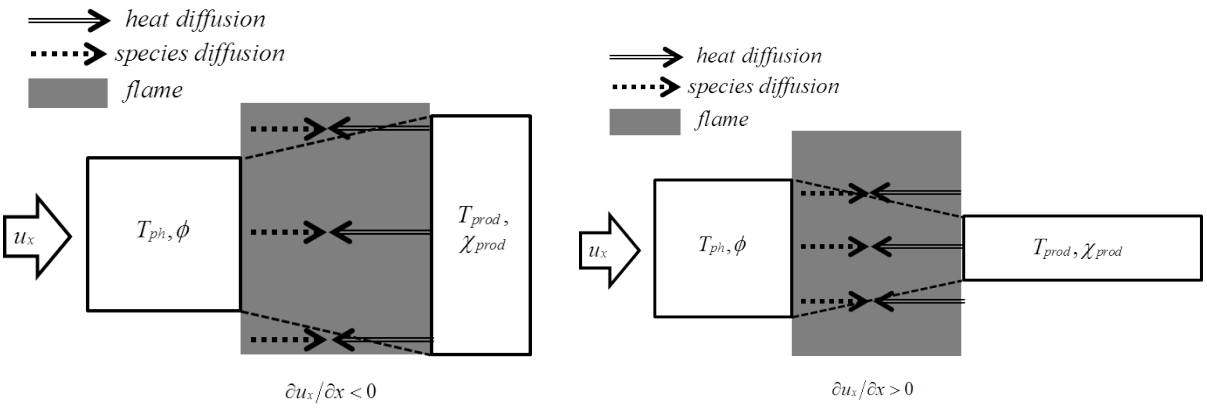

(a) Normal strain induced positive stretch

(b) Normal strain induced negative stretch

Figure 2.6: Schematic representation of the manifestation of non-unity Lewis number stretch effects for examples of positive (2.6a) and negative flame stretch (2.6b).

these lines. However, mass and heat can diffuse normal to the flame and across these streamlines. For the control mass in this example, species diffusion from neighboring control mass alters the reactant concentration locally while heat produced by the control mass diffuses to preheat the control mass as well as to neighboring control mass. For the former case, flame reactivity could potentially increase through increases in deficient reactant concentration while for the latter case, flame reactivity could potentially decrease as a result of heat losses. The net effect that stretch has on this flame is dependent upon the relative strength of these two opposing pathways as evaluated through a Lewis number defined as follows:

$$Le = \frac{\alpha}{D_{deficient}} \tag{2.9}$$

where α is the thermal diffusivity of the products and $D_{deficient}$ is the mass diffusivity of the deficient reactant species. For mixtures with $Le > 1$, and with positive stretch ($\kappa > 0$), heat losses are dominant causing flame reactivity to decrease which results in lower flame temperatures and decreased flame speeds. Note the opposite is true for $Le < 1$ mixtures because mass diffusivity of the deficient species is dominant.

As can be deduced from the representative schematic for negative stretch ($\kappa < 0$), non-equidiffusion pathways have the opposite effect on a given non-unity Le number mixture when the stretch rate changes sign.

Because of the aforementioned non-equidiffusion effects, the burning characteristics of stretched flames are vastly different than their 1D counterparts. As an example, the response of a premixed methane-air flame to stretch is shown in terms of its flame speed defined by the local displacement speed just upstream of the flame preheat zone, $S_{d,ph}$, in Figure 2.7. These results were captured using the OPPDIF module of CHEMKIN using GRI Mech 3.0 [107]. Compared to unstretched laminar flame speeds, $S^{\circ}_{d,ph}$, the flame speed of stretched flames for the test cases shown are $2-4$ times faster. In this case, flame speed is enhanced by flame stretch until an upper limit, marked by the turning point in the flame speed curve. The maximum stretch rate which the flame can withstand, the extinction stretch rate, κ_{ext}, is defined as the maximum flame stretch at the turning point. Note that the response of the flame to stretch is different for each of the methane-air mixtures and that κ_{ext} is also dependent upon the ϕ of the mixture as well.

For example, Figure 2.8 plots calculated extinction stretch rates of methane-air mixtures as a function of reactant temperature for several lean equivalence ratios. κ_{ext} increases with ϕ for these lean mixtures and has an exponential dependence on T_{reac}. Thus one might reason that lean blowoff of a shear stabilized flame to be the result of the mixture's κ_{ext} dropping below some critical limit. The evaluation of κ_{ext} as a fundamental parameter requires an understanding of the stretch rates that practical flames experience, as well as the extinction stretch rates numerically modeled or experimentally measured using fundamental combustors. This comparison is critical is critical to understanding and modeling shear layer flame stabilization.

Lastly, radiative heat losses can potentially alter the burning properties and limits of stretched flames. We briefly mention numerical studies which have investigated the

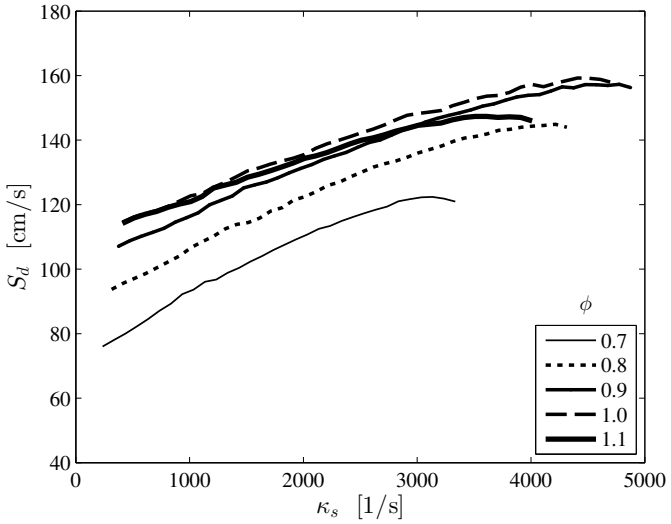

Figure 2.7: Laminar flame speed sensitivity, S_d, to hydrodynamic flame stretch, κ_s, for methane-air mixtures of varying ϕ at a preheat temperature of $533K$.

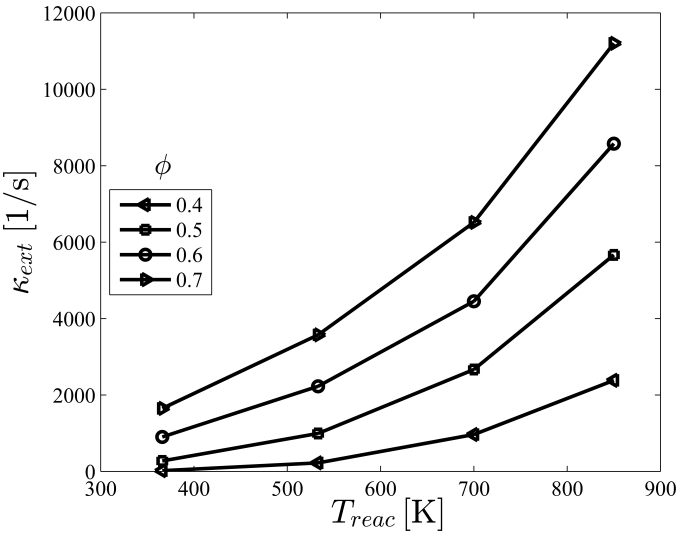

Figure 2.8: κ_{ext} dependence upon reactant temperature, T_{reac}, for lean mixtures of methane-air.

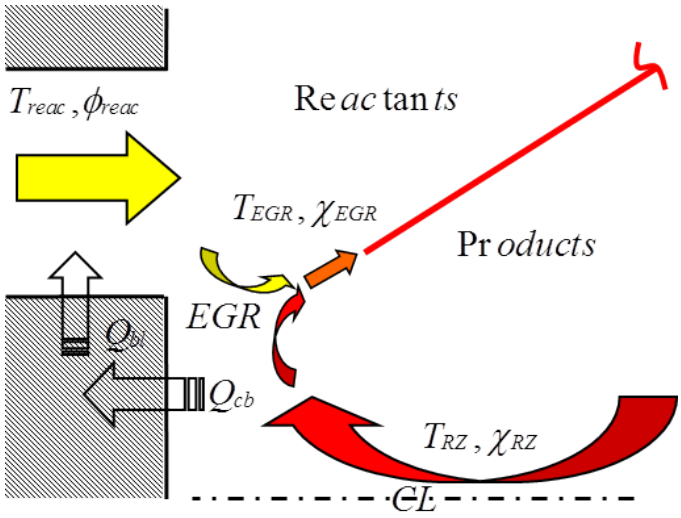

Figure 2.9: Schematic of recirculation zone physics affecting flame stabilization through compositional and thermal changes in reactant composition and heat loss across the flame.

effect of radiative heat transfer on the extinction limits and flame speeds of premixed stretched flames [85, 55, 56, 57, 54]. For example, studies performed by Ju *et al.* on lean, premixed, methane-air mixtures, using the opposed jet configuration, showed decreasing radiative heat loss with stretch. In fact, at the extinction limit, radiative heat losses were insignificant compared to the heat produced by the flame.

2.2.2 Recirculation zone physics

The enhancement of flame stability brought about by the presence of a recirculation zone has been implemented in practical combustor geometries. Enhanced flame stability is the result of both favorable kinematic conditions in the region of the recirculation zone and enhanced mixture reactivity caused by the recirculation of hot products to the incoming reactant stream. It is the pathway of the recirculated products which we are most interested in discussing related to this work. There are several processes which are represented in Figure 2.9 which can potentially alter the effectiveness of the recirculation zone feedback loop.

First, downstream of the flame attachment point, in regions where the flame separates the reactants from the products, the temperature and composition of the recirculation zone, T_{RZ} and χ_{RZ}, affects the flame through diffusional transport of heat and radicals to or from the product side. Depending on the composition and temperature of the recirculation zone, it can result in either enhancement or degradation of the flame with increasing or decreasing reactivity of the mixture upstream of the flame front. As a simple example, if the recirculation zone temperature is less than the flame temperature, the flame will incur diffusional losses of heat to the recirculation zone side of the flame resulting in decreased flame temperatures and flame speeds.

Next, focusing our attention on the region upstream of the flame attachment point in Figure 2.9, there is another pathway which could alter the burning properties of the reactant mixture. With the flame stood off from the edge of the centerbody, there is a region in which the recirculation zone can mix with the reactant stream. This dilutes the reactant mixture locally, decreasing the local equivalence ratio for lean mixtures, but ultimately increases mixture reactivity through an increase in reactant temperature. This set of physics is similar to exhaust gas recirculation (EGR) techniques and are referred to as such. We expect as well that increasing mixing between reactants and recirculated products through EGR, will result in higher extinction stretch rates. The sensitivity of flames to recirculation zone temperature, T_{RZ}, and EGR are considered to be the dominant physical pathways and are assessed in the numerical modeling section. While heat losses from the recirculation zone to combustor hardware, Q_{cb}, could potentially alter T_{RZ}, and boundary layer heating, Q_{bl}, could alter T_{ph}, these secondary pathways are not considered in this study.

2.2.3 Anchoring Mechanisms

Flamelet flame stabilization requires that flame displacement speed, S_d, must match flow velocity magnitude and direction at at least one point in the flow, which will act to anchor the flame throughout the combustor. This classical explanation of flame stabilization, where the flame is propagating normal to its surface, would envision a flame orienting itself perpendicular to the flow at the attachment point to meet the requirement for flame anchoring. We will refer to flames stabilized in this way as *normal propagation stabilized*. However, real flames may terminate at a point resulting in a flame edge at the anchoring location. Flame anchoring would require the propagation of flame at the edge, or the edge flame speed, v_f, and not S_d, to match local flow velocity. Although edge flame stabilization in practical combustors has not been extensively discussed in the literature, it is also a possible means for flame anchoring [12, 74, 31]. We will refer to flames stabilized in this manner as *edge flame stabilized*.

These topology of flame and flow field in the attachment point region is shown in Figure 2.10 for *normal propagation* and *edge flame* stabilized conditions. We note that the flame orientation at the most upstream location is perpendicular to the flow when normal propagation stabilized and tangential to the flow when edge flame stabilized. Thus we expect to be able to infer the physics controlling flame anchoring based on the orientation of the flame relative to the flow. Distinguishing between these two modes of stabilization is important because edge velocities can be significantly higher than displacement speeds of 1D flames [31, 29, 4]. It is therefore possible that the edge flame stabilization process may be preferred in high velocity flows, as opposed to normal flame propagation.

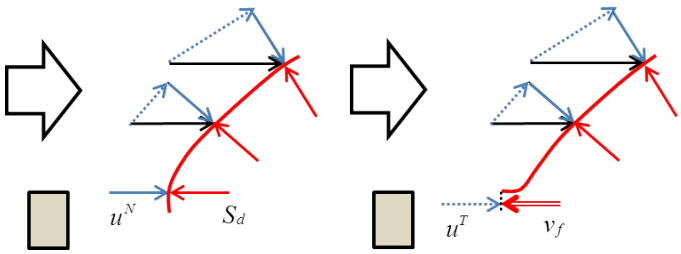

Figure 2.10: Illustration of a normal propagation stabilized flame (*left*) and an edge flame stabilized flame (*right*) in the flame anchoring region.

CHAPTER III

TEST FACILITY AND DIAGNOSTIC TECHNIQUES

This chapter provides the relevant details of the experimental facility and diagnostic techniques used in these studies. First the details of the annular swirl combustor experimental facility is described, followed by the details of the diagnostic techniques utilized to study the flow field and the flame.

3.1 Test Facility

The nominal experimental facility is sketched in Figure 3.1 and can be divided into the following sections: a reactant supply system, flow conditioning and fuel/air mixing (A), premixer (B), combustor (C), and exhaust (D). First the supply of air and fuel upstream of their entry into the schematic shown is described. We begin with a discussion of the air and natural gas supply to the test facility. The air and natural gas lines supplied are regulated to upstream supply pressures of $\approx 60\ psi$ and $\approx 25\ psi$ respectively. The composition of the natural gas supplied to the lab does vary slightly but not considerably as shown in Table 3.1. Shown in the table is the composition of the natural gas supplied to the lab over the period of a month in terms of mean and standard deviation of the molar percentages of the major constituents of the mixture. The natural gas supplied to the lab is $\approx 97.5\%$ methane on average but also includes small quantities of nitrogen, carbon dioxide, and higher order hydro-carbons.

The fuel and air mass flow rates are separately measured using sub-critical, calibrated orifice plates, installed in a flange union. The pressure sensors were installed in the pressure taps located in the flanges of the union. For reference, Table 3.2 shows the model of the pressure sensors used in the measurements of static and differential pressure for the calculation of flow rates fuel and air mass flow rates.

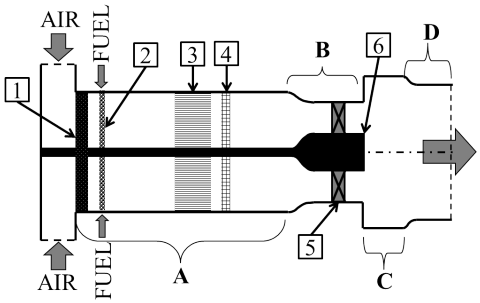

(a) Test facility schematic

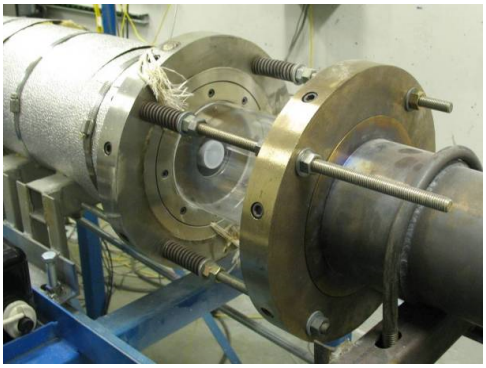

(b) Picture of combustor section

Figure 3.1: Left: Schematic of the test facility showing *flow conditioning and fuel/air mixing* (A), *premixer* (B), *combustor* (C), and *exhaust* (D) sections. Right: Picture of combustor section of test facility.

Table 3.1: Natural gas supply composition as determined from reported composition from 4/1/2007-4/29/2007

	CH_4	N_2	CO_2	C_2H_6	C_3H_8
Mean %	97.5494	1.0875	0.4273	0.6875	0.1309
Standard Deviation %	0.7026	0.0987	0.2046	0.4036	0.0875

	n-C_4H_{10}	C_5H_{12}	Iso-C_5H_{12}	Neo-C_5H_{12}	C_6H_{14}
Mean %	0.0377	0.0004	0.0156	0.0105	0.0218
Standard Deviation %	0.0238	0.0006	0.0103	0.0071	0.0142

Table 3.2: Pressure sensors for orifice plate measured mass flow rates

	Static Pressure Sensor	Differential Pressure Sensor
Fuel Orifice Plate	Omegadyne PX409-100GI	Omega PX771-300WCDI
Air Orifice Plate	Omegadyne PX409-050GI	Rosemount 3051CD1A22A1AB4

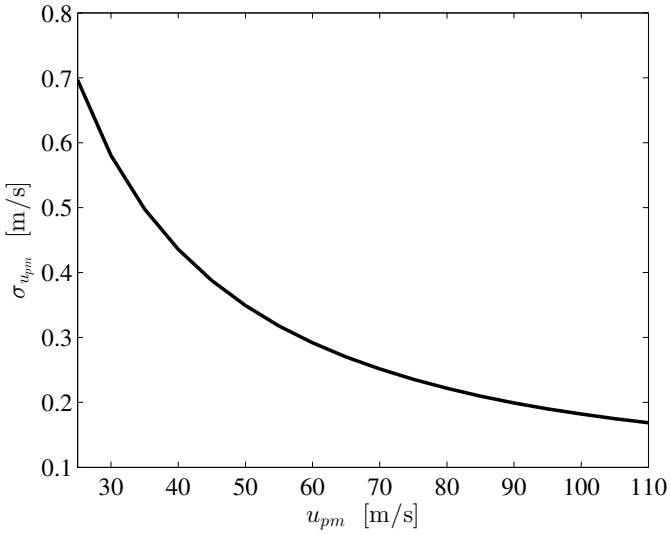

Figure 3.2: Uncertainty in u_{pm}, $\sigma_{u_{pm}}$, as a function of u_{pm} for a T_{ph} of $533K$.

The error in the flow velocity in the premixer section, $\sigma_{u_{pm}}$, resulting from uncertainties in the measured static and differential pressure across the orifice plate, is calculated to be 0.50 m/s and 0.25 m/s for nominal premixer velocities, u_{pm}, of 35 m/s and 70 m/s at reactant temperatures of 533 K and for the smaller centerbody test configuration. For these uncertainties, no uncertainty in cross-section area or mixture density was assumed. Uncertainty in the reported velocity over a range of premixer flow velocities is shown in Figure 3.2. For the test space shown, the absolute and relative uncertainty in flow velocity decreases with increasing premixer velocities.

Next, the uncertainty in the reported equivalence ratio is shown as a function of ϕ for both velocities in Figure 3.3. Uncertainty in ϕ, σ_ϕ, is dominated by uncertainty in the mass flow rate of fuel, $\dot{m}_f$, with a local minimum in uncertainty, occurring near $\phi = 0.9$, of $\sigma_\phi = 0.018$ for $u_{pm} = 35\ m/s$ and $\sigma_\phi = 0.005$ for $u_{pm} = 70\ m/s$ test cases. Note that uncertainties in ϕ are considerably less for the higher premixer velocity test case.

After flow rate measurement, the air supply then enters a 50 kW WATLOW heater raising the air to a preheat temperature of $533K$. The air enters the test section as

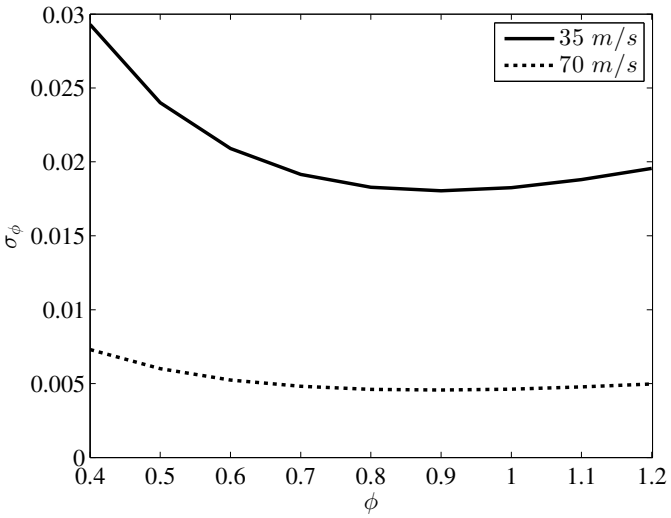

Figure 3.3: Uncertainty in ϕ, σ_ϕ, as a function of ϕ for premixer velocities, u_{pm}, of $35m/s$ and $70m/s$.

shown in Figure 3.1a from two sides of a pipe T-junction. It then passes through a perforated plate with a blockage ratio $\approx 53\%$ (Item 1 of Figure 3.1a), and into the preconditioning section (A). This blockage plate was created using a 4" schedule 40 blind pipe flange by drilling the hole pattern as shown in Figure 3.4.

Approximately 3.3" downstream of the blockage plate, natural gas is injected into the flow through eight equally spaced radial fuel injectors (Item 2 of Figure 3.1a) as shown schematically in Figure 3.5. These fuel injectors were built using 1/4" stainless tubing. The end of the tube was welded shut and holes along the tube were drilled through the tube. Table 3.3 provides the radial location of the holes relative to the flow center, r_c, and relative to the end of the fuel injector, l_c, and the diameter of the drill bit used to machine the through holes at each location, d_{hole}. The fuel injectors are oriented such that the through holes are perpendicular to the bulk flow.

After fuel injection, there is a settling length of ≈ 39" to allow for the fuel and air to mix before passing through a honeycomb flow straightener and a wire mesh (Items 3 and 4 of Figure 3.1a) to straighten the flow and reduce turbulence [100]. The model of the honeycomb flow straightener is shown in Figure 3.6. The honeycomb

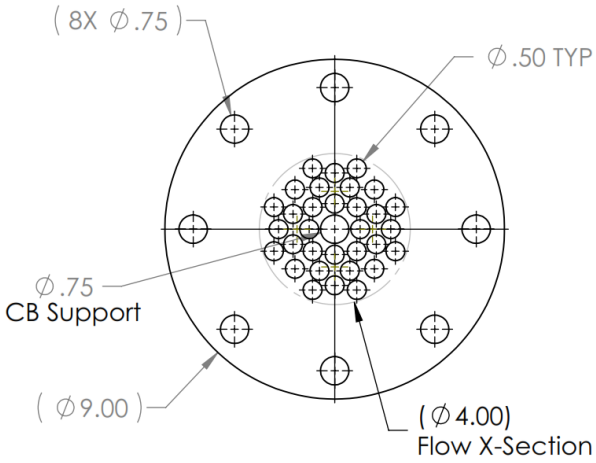

Figure 3.4: Drawing of blockage plate hole pattern, Item 1 in Figure 3.1, manufactured from a 4"⌀ schedule 40 blind pipe flange. Hole pattern results in an area blockage of $\approx 53\%$.

Table 3.3: Fuel injector hole locations and sizes. Hole locations are indicated relative to flow center, r_c, and the end of the fuel injector, l_c.

r_c [inches]	l_c [inches]	d_{hole} [inches]
0.63	.25	0.0550
0.98	.60	0.0550
1.23	0.85	0.0595
1.44	1.06	0.0595
1.62	1.25	0.0635

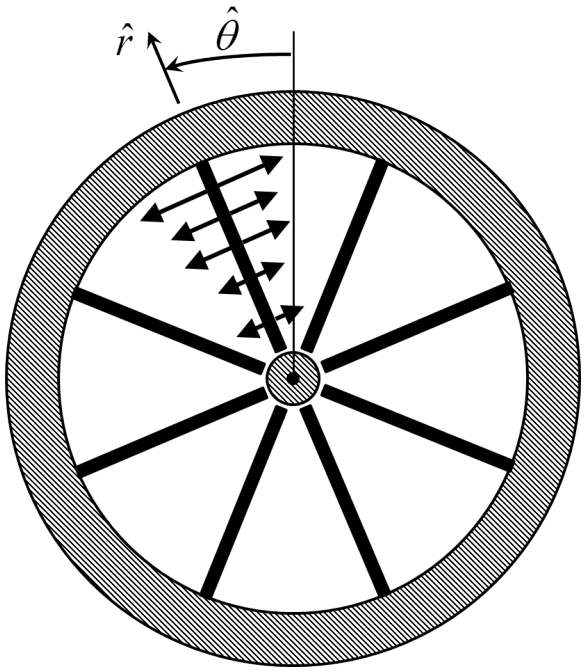

Figure 3.5: Schematic of fuel injector arrangement shown from a plane transverse to the flow direction. Shown are the outer wall of the premixer section, 8 fuel injectors, the fuel injection path for a single injector, and the center obstruction from the centerbody feature.

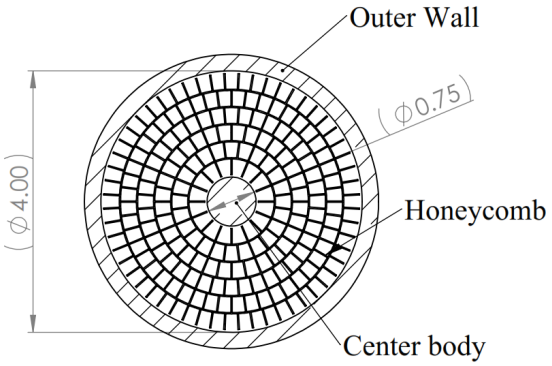

Figure 3.6: Cross-section of honeycomb flow straightener showing axisymmetric cell pattern of honeycomb as well as the outer wall and centerbody of the annular flow section. The honeycomb is 2" in length, has cell wall thicknesses of 0.020" throughout with a typical cell widths of 0.14" to 0.173" and a radial cell height of ≈ 0.30".

is 2 *inches* long, with a constant wall thickness of 0.020" throughout. The cell size of the honeycomb varies, increasing in cell width radially outward. Cell width values range from 0.14" to 0.173" with radial cell heights of ≈ 0.30". Overall, this results in an area blockage of $\approx 14\%$. The wire mesh is installed ≈ 1.75" downstream of the end of the honeycomb, made of 1/16" diameter wire in 0.3" $\times$ 0.3" mesh sizes.

Upon entering the premixer section (Section B of Figure 3.1a) the outer and inner diameter of the test section are smoothly transitioned to match the dimensions of the annular cross-section at the dump plane ($d_{outer} = 2.44$", $d_{inner} = d_{cb}$"). This transition occurs over a length of 6.75", the profile of which is determined by the hyperbolic tangent function. For reference, Figure 3.7 shows the key geometric dimensions and details of the premixer section. Note the location of the "Swirler Mid-Plane" at which the swirler inlet conditions were characterized, as well as the "Dump Plane" marking the beginning of the combustor and plane at which the premixedness of the flow was characterized as described in more detail in the following text.

In order to provide boundary conditions for computational efforts and to verify

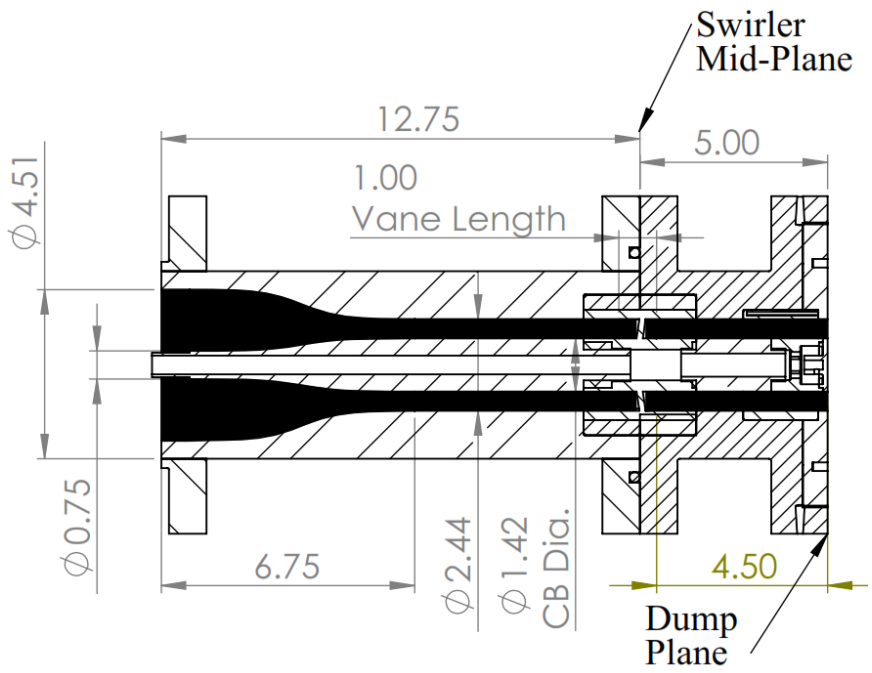

Figure 3.7: Cross-section of premixer section of test facility showing key dimensions of the contraction section, swirler, and dump plane.

the effectiveness of the flow conditioning measures, the axial flow conditions at the mid-plane of the swirler, were characterized using laser Doppler velocimetry (LDV) measurements which are presented in Table 3.4 and Figure 3.8 for $u_{pm} = 35\ m/s$, and Table 3.5 and Figure 3.9 for bulk flow for $u_{pm} = 70\ m/s$. Figure 3.10 defines the relative locations at which the velocity measurements were taken. Two points follow regarding the velocity conditions at the this location, which are representative of the swirler inflow conditions, for both premixer velocities. The velocity profile is a top hat profile, with velocities uniform in the bulk of the cross-section, and there are low levels of turbulence away from the shear layers.

The flow then passes through a 16 blade, aerodynamically designed swirler (Item 5 of Figure 3.1a) with the trailing edge of the vanes at fixed angles of either 45° or 37° relative to the oncoming flow. Due to the proprietary design of the swirler, there are limited details that can be provided on the exact airfoil profile of the swirler

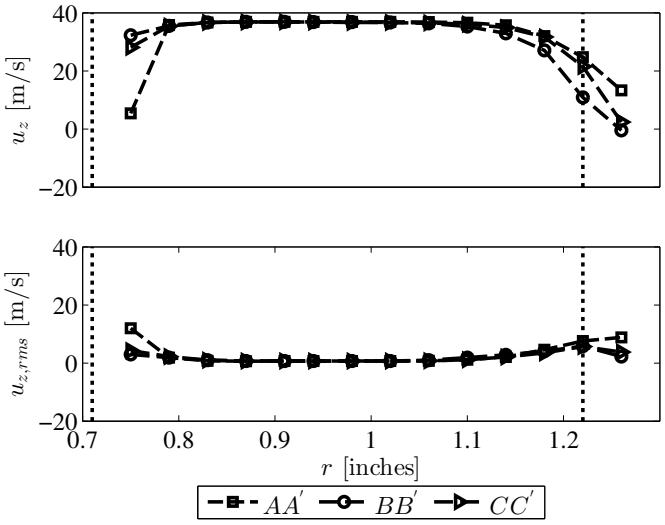

Figure 3.8: Swirler inlet axial velocity profile measured at swirler inlet plane where $r_{outer} = 1.22$" and $r_{inner} = r_{cb} = 0.71$", for a bulk premixer velocity of $u_{pm} = 35\ m/s$.

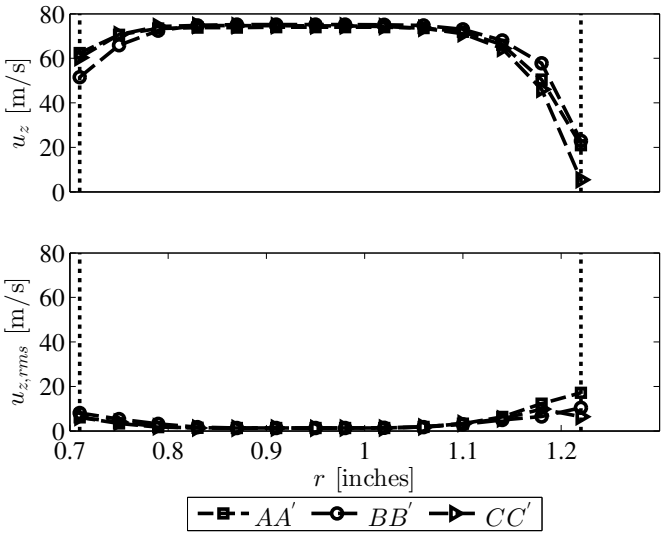

Figure 3.9: Swirler inlet axial velocity profile measured at swirler inlet plane where $r_{outer} = 1.22$" and $r_{inner} = r_{cb} = 0.71$", for a bulk premixer velocity of $u_{pm} = 70\ m/s$.

Table 3.4: Mean and RMS Axial Velocity Profiles at Swirler Inlet for $u_{pm} = 35\ m/s$.

	$\bar{u}_z$ [m/s]			$u_{z,rms}$ [m/s]		
r [inches]	AA'	BB'	CC'	AA'	BB'	CC'
0.75	5.4	32.3	28.1	12.0	3.0	4.3
0.79	35.8	35.5	35.4	1.9	1.9	2.2
0.83	36.7	36.7	36.7	0.8	1.0	1.0
0.87	36.9	36.9	36.8	0.6	0.7	0.7
0.91	36.9	36.9	36.9	0.7	0.7	0.7
0.94	36.9	36.8	36.8	0.7	0.7	0.7
0.98	36.9	36.8	36.7	0.7	0.7	0.7
1.02	36.9	36.7	36.7	0.7	0.7	0.7
1.06	36.8	36.4	36.5	0.8	1.0	0.8
1.10	36.6	35.3	36.1	1.1	1.9	1.1
1.14	35.7	32.9	34.9	2.1	2.8	2.1
1.18	32.0	27.1	31.7	4.6	4.1	3.5
1.22	24.7	10.9	21.5	7.6	5.8	5.7
1.26	13.3	-0.5	2.4	8.8	2.2	3.8

blades. Approximately 4.5 *inches* downstream of the trailing edge of the swirler blades, the annular cross-section abruptly transitions to a circular cross-section at the dump plane.

For reference, the fuel concentration at the dump plane was measured using a gas analyzer that collected local samples from a tube directed upstream while positioned at discreet locations at the dump plane. From these measurements, the uniformity of the fuel-mixedness was characterized at the dump plane. The gas probe was moved from location to location with local concentrations of natural gas recorded after allowing enough time for the measurement value to stabilize. These measurements

Table 3.5: Mean and RMS Axial Velocity Profiles at Swirler Inlet for $u_{pm} = 70\ m/s$.

	$\bar{u}_z$ [m/s]			$u_{z,rms}$ [m/s]		
r [inches]	AA'	BB'	CC'	AA'	BB'	CC'
0.71	62.4	51.5	60.3	6.1	8.1	6.1
0.75	70.6	65.9	70.7	3.4	5.3	4.0
0.79	73.4	72.4	74.3	1.7	3.2	1.9
0.83	73.8	74.8	74.8	1.4	1.7	1.3
0.87	73.8	75.2	74.7	1.3	1.3	1.2
0.91	74.0	75.2	74.7	1.3	1.3	1.3
0.95	74.0	75.2	74.6	1.3	1.3	1.2
0.98	74.0	75.2	74.6	1.3	1.3	1.3
1.02	74.0	75.1	74.3	1.3	1.4	1.3
1.06	73.6	74.8	73.5	1.8	1.7	1.8
1.10	71.9	73.0	71.1	3.3	3.0	3.4
1.14	66.1	68.0	64.4	6.3	4.9	5.4
1.18	50.5	57.8	46.1	12.3	6.5	9.8
1.22	21.0	22.9	5.4	17.1	10.4	6.4

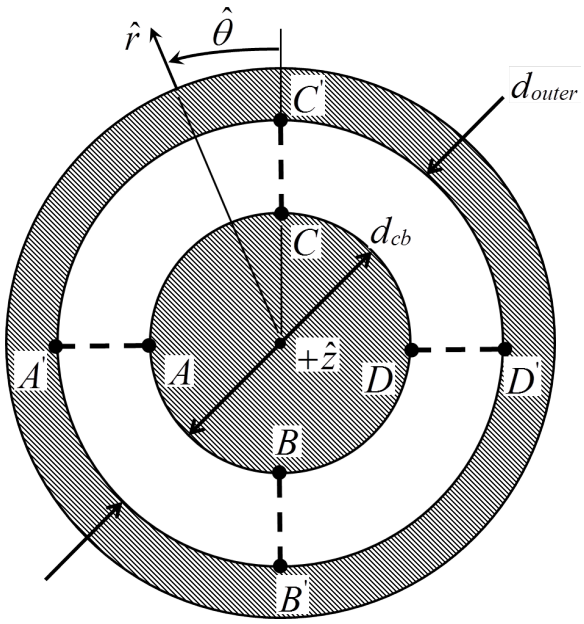

Figure 3.10: Schematic of an annular cross-section of the premixer region showing the locations where flow and mixture characterization measurements were performed along radial profiles.

were performed along four radial arms, 90° apart as shown in Figure 3.10. The radial dependence of equivalence ratio at these four locations is shown in Figure 3.11 for premixer velocities of $u_{pm} = 35\ m/s$ and $u_{pm} = 70\ m/s$ and summarized in Table 3.6. Note that for the most part the spatial variance of ϕ is within $\pm 5\%$ of the radially averaged equivalence ratio, $\bar{\phi}$.

In addition to equivalence ratio measurements performed along radial arms at fixed θ, measurements were also performed circumferentially at a fixed radius of $r = 0.88$" and for both premixer velocities. These results are summarized in Table 3.7 and Figure 3.12. Similar to the radial distribution of ϕ, the circumferential variation in local equivalence ratio is less than $\pm 5\%$ of the azimuthally averaged ϕ at that fixed radius.

The combustor section, Section C of Figure 3.1a, is a cylindrical quartz tube. The face plate of the combustor is replaceable, allowing for different diameter quartz

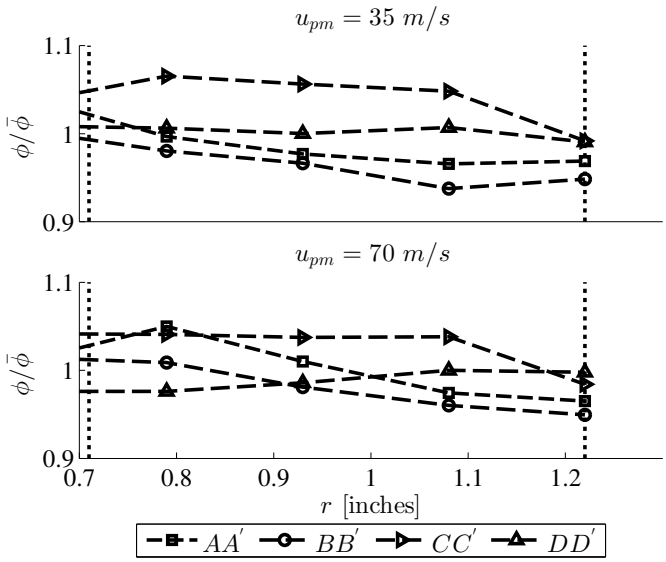

Figure 3.11: Measurements of normalized equivalence ratio taken at the combustor dump plane for premixer velocities of $u_{pm} = 35\ m/s$ and $u_{pm} = 70\ m/s$ at a nominal equivalence ratio of $\phi = 0.50$. Local values of ϕ were normalized by the mean value of all measured ϕ.

tubes to be used, which changes the combustor diameter as well as the dump ratio, $A_{annulus}/A_{comb}$. In addition, the test facility could accommodate variations in quartz tube length. For reference, the baseline combustor geometry for this facility was $d_{comb} = 135\ mm$ and $l_{comb} = 202.5\ mm$.

Normally, there would be a contracting exhaust section at the end of the combustor, providing a nominal area contraction of 30%, as was the case for general studies of flame stabilization in this facility. However, in order to obtain PIV and CH-PLIF measurements over a long enough time, the quartz tube and corresponding exhaust contraction were removed for this testing effort, thereby eliminating the issue of seeding particles collecting on the quartz tube. While this limited our detailed studies to the inner shear, as the flame does not stabilize in the outer shear layer for this unconfined case, this resulted in much longer run times. In addition to changing the nature of the ORZ, the removal of the contraction certainly changes the structure of

Table 3.6: Normalized equivalence ratio, $\phi/\bar{\phi}$, measured along radial arms at the dump plane as shown in Figure 3.10.

	u_{pm} = 35m/s				u_{pm} = 70m/s			
r	A-A	B-B	C-C	D-D	A-A	B-B	C-C	D-D
0.64”	1.044	1.004	1.034	1.009	1.009	1.015	1.042	0.976
0.79”	0.997	0.980	1.065	1.006	1.050	1.009	1.041	0.976
0.93”	0.977	0.967	1.056	1.000	1.010	0.981	1.037	0.986
1.08”	0.966	0.938	1.048	1.007	0.974	0.960	1.038	1.000
1.22”	0.969	0.949	0.992	0.991	0.965	0.949	0.984	0.998

the vortex breakdown region of the flow field as well [38, 39]. In order to monitor the thermal state of the combustor during operation, the bulkhead and the centerbody are instrumented with thermocouples. Typical flow rates that the test facility was operated at have Reynolds numbers on the order of $\approx 10^4 - 10^5$ where $Re = \frac{d_{outer}\, u_{pm}}{\nu}$.

3.2 Diagnostic Techniques

For these studies, Planar Laser Induced Fluorescence of CH radicals (CH-PLIF) and Particle Image Velocimetry (PIV) were used to characterize the 2D, planar behavior of the flame and flow field. These measurements were performed simultaneously enabling the study of flame-flow interaction. The details of the CH-PLIF and PIV laser systems and optical setup are described in the following sections.

3.2.1 CH-PLIF flame measurements

CH-PLIF measurements were obtained using a Light Age PAL 101 frequency-doubled alexandrite laser system tuned with an intercavity birefringent filter. The broadband, long pulse laser was tuned to the R-bandhead of the B-X(0,0) transition at a wavelength of 387.2 nm, with a linewidth of $\approx$ 0.01 nm (0.7 cm^{-1}) and pulsewidth of

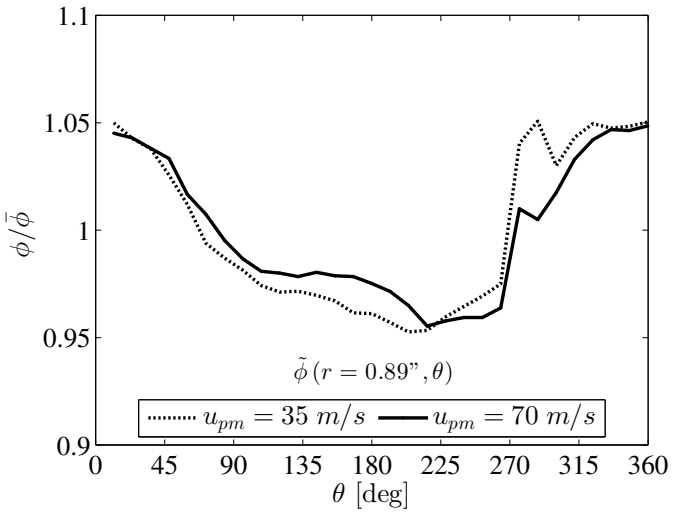

Figure 3.12: Measurements of normalized equivalence ratio taken at the combustor dump plane for premixer velocities of $u_{pm} = 35\ m/s$ and $u_{pm} = 70\ m/s$ at a nominal equivalence ratio of $\phi = 0.50$. Circumferential measurements of ϕ were normalized by the mean value of all measured ϕ at $r = 0.89"$.

$\approx 70\ ns$. By exciting multiple CH transitions with a long pulse length, strong fluorescence signals are obtained within the linear excitation limit [86]. While capable of double-pulse operation, the laser was operated in single pulse mode with energies of approximately 15 mJ, with the pulse timed to occur between the two pulses of the PIV laser system. A laser sheet approximately 100 μm thick and $9-10\ mm$ wide was created using uncoated fused silica lenses. Images of the resulting fluorescence from A-X transitions near 430 nm were captured with an intensified (Gen III HB filmless) CCD camera (PI-Acton 512×512) with a quantum efficiency of 45% in the spectral region of interest. The intensifier was gated to 300 ns to minimize chemiluminescence pollution and to avoid irising. A series of O.D. 6 band pass filters were used in order to reject elastic scattering.

3.2.2 PIV velocity measurements

A dual head, frequency doubled, flash-lamp pumped Nd:YAG laser, with measured pulse energy of approximately 200 mJ was used for 10 Hz PIV measurements. The PIV beam was optically conditioned to produce a collimated laser sheet of approximately 9 mm in width and 1 mm in thickness sharing sheet optics with the CH-PLIF laser. Figure 6.12a shows a representative image of the location of the interrogation region where these measurements were performed. The laser thickness was chosen based on loss-of-pairs considerations due to the high out of plane motion expected for this swirling flowfield. Given the swirler vane angle, θ_{vane}, out of plane velocities were assumed to be on the order of the mean bulk flow velocity, $u_{pm} = 35\ m/s$. The laser sheet thickness was set at 1 mm, requiring a shot separation time of $5\mu s$ to mitigate the effect of loss of pairs, expected to be less than 20% for these conditions. For the higher velocity test case, $u_{pm} = 70\ m/s$, the shot separation time was set to $2\mu s$ for similar concerns of loss of pairs. A 532 nm interference bandpass filter was used to reject other sources of light. Imaging was performed with a PCO CCD camera, equipped with a Nikon Nikor $f = 55\ mm$ Macro lens with a combination of extension rings. The flow was seeded with $1 - 2\ \mu m$ alumina particles. The seeding system consisted of a passive agitation, swirling seeder, which operated with about 5% of total air flow after preheating. The seeding particles were injected 10 cm upstream of the fuel injection, to ensure uniform seeding density. Particle flow following error and frequency response is discussed in a previous paper [22] and in more detail in the Appendix section.

3.2.3 Measurement resolution of flame and flow

This section discusses the ability of the raw data obtained to resolve relevant features of the flow field, as well as relevant characteristics of the flame. Most importantly, the ability to resolve the location and orientation of the CH-layer is critical to providing

meaningful flow and stretch characteristics of the flame. In addition, special attention is paid to the ability of these measurements to resolve the orientation of the CH-layer at the leading edge. This is particularly important in this study's evaluation of the stabilization mechanism at the leading edge as the flame orientation is expected to be different for normal propagation stabilized and edge flame stabilized flames, as discussed in Section 2.2.3.

PIV interrogation windows of $32 \times 32\ pixels^2$ with 50% overlap resulted in a velocity field vector spacing of $\Delta_{PIV} = 0.11\ mm$ where the equivalent camera pixel spacing of the CH-PLIF images with magnification was $\Delta_{CH} \approx 0.16\ mm$. For reference, a stoichiometric methane-air mixture at a reactant temperature of $533K$ has an unstretched flame thickness of $\approx 0.35\ mm$ and minimum stretched flame thickness of $\approx 0.26\ mm$ where flame thickness is defined as:

$$\delta_f^T = \frac{T_b - Tu}{max(\partial T/\partial x)} \tag{3.1}$$

with T_b as the "burned" or flame temperature, and T_u as the "unburned" or reactant temperature. In addition, a minimum full width at half maximum (FWHM) CH-layer flame thickness, $\delta_R^{CH,FWHM}$, was determined to be $\approx 0.1mm$ from OPPDIF calculations.

The ability to resolve flow conditions in the shear layer and CH-layer are discussed next. The boundary layer thickness, defined by the location where the axial velocity is 90% of the bulk flow velocity, is approximately 1.5 mm at the dump plane. This shows that the PIV measurements are able to resolve the boundary layer with $\approx$ 6 uncorrelated velocity measurements within the the boundary layer. Each data set consisted of approximately 500 simultaneous CH-PLIF and PIV measurements. Example images of instantaneous PIV fields with CH-PLIF are shown in Figure 3.13 for the $\phi = 1.0$, $u_{pm} = 35m/s$ test case. Note that the PIV vector field has been drastically down-sampled in the figure for visualization purposes. Given that average values of the CH-layer thickness observed, δ_{image}, were $\approx 0.6mm$, there are $\approx 4 - 5$

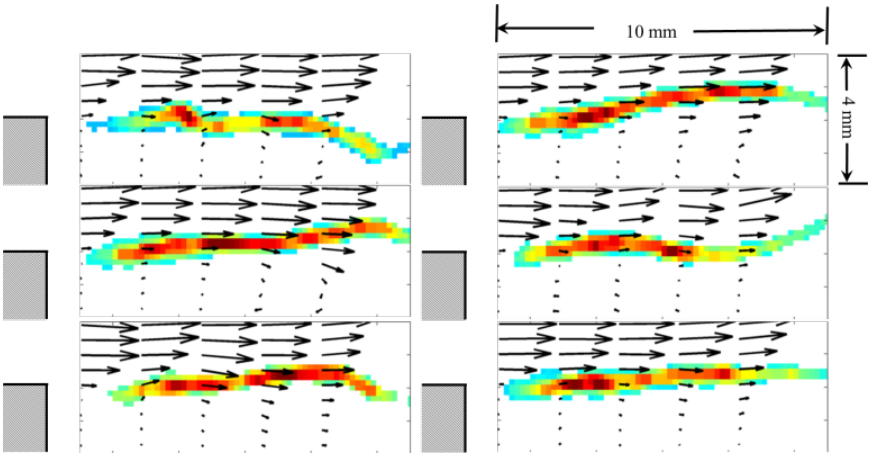

Figure 3.13: Sample instantaneous images of CH-PLIF and velocity vectors for $\phi = 1.0$, $u_{pm} = 35m/s$.

PIV velocity vectors within the observed CH-layer.

Next, the ability of these measurements to resolve the orientation of the flame at its leading edge is discussed. Calculations of both flame thicknesses are shown for high stretch rates in Figure 3.14 for $\phi = 1.0$ methane-air mixtures at $T_{ph} = 533K$. Other relevant parameters, such as the CH-PLIF image pixel spacing, Δ_{CH}, the average thickness of the CH-layer, δ_{image}, and minimum radius of curvature along the CH-layer, R_{min}, are shown as well. Note that the experimentally observed thickness of the CH-layer, δ_{image}, is roughly twice the value determined from OPDIFF calculations, $\delta_R^{CH,FWHM}$. This "thickening" of the CH-layer is the likely the result of un-focused or blurred CH-PLIF images as the pixel to pixel spacing, Δ_{CH}, is small enough such that the experimentally observed CH-layer thickness is $\approx 3-4$ pixels thick. Based on the observed flame thickness, the minimum wrinkle scale along the CH-layer was defined as $R_{min} = 2 \times \delta_{image}$. R_{min} represents a physical limit of the smallest wrinkle scale that is possible. These parameters will have a direct influence on the ability to resolve the orientation and curvature of the flame at the leading edge.

Figure 3.15 shows a representative to scale schematic of the CH-layer extracted from CH-PLIF images at the leading edge. This image assumes that the flame "hooks"

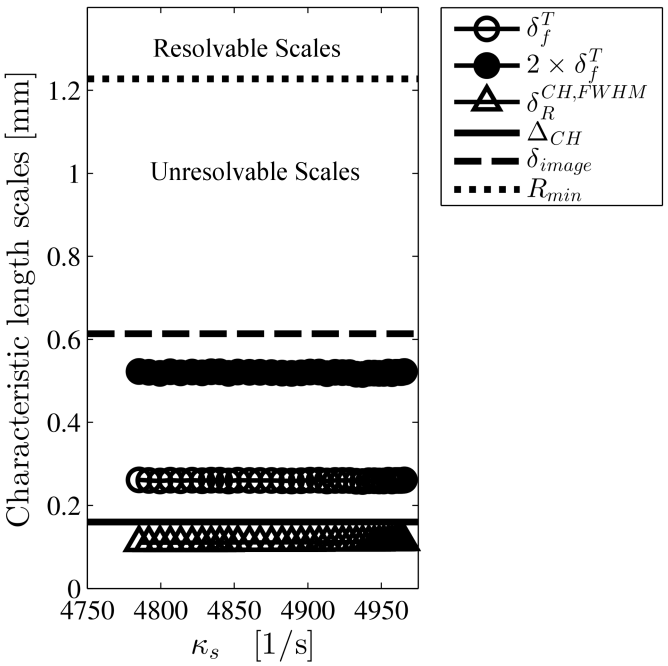

Figure 3.14: Comparison of temperature based flame thickness, δ_f^T, and CH based reaction layer thickness, $\delta_R^{CH,FWHM}$, as a function of stretch, computed for a stoichiometric methane-air mixture at a $T_{ph} = 533K$. For reference, the CH-PLIF image pixel spacing, Δ_{CH}, the observed CH-layer thickness, δ_{image}, and minimum flame curvature, R_{min}, are shown as well.

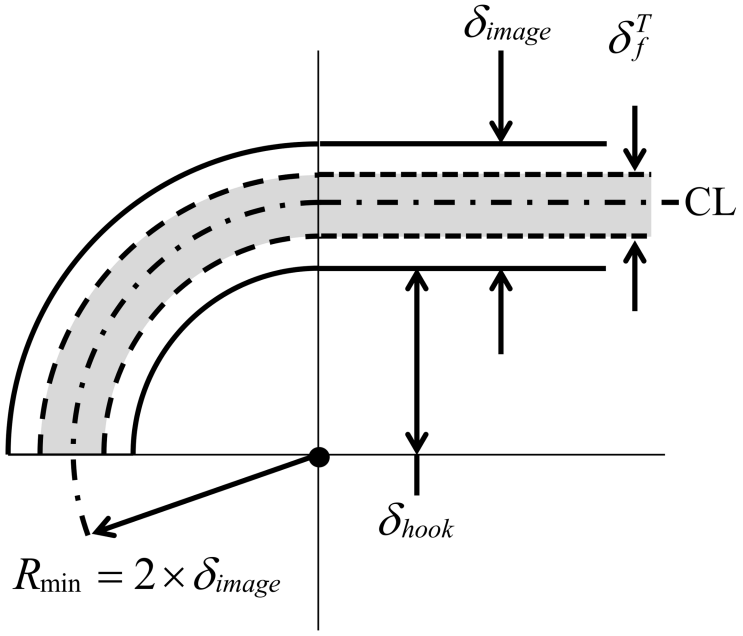

Figure 3.15: Schematic of representative flame hook feature with characteristic length scales of interest as follows: δ_{image}, observed thickness of CH-layer, δ_f^T, temperature based flame thickness, CL, centerline of CH-layer, R_{min}, minimum flame curvature based on observed flame thickness, and δ_{hook}, minimum standoff distance required for complete flame hook.

at the leading edge, the curvature of the hook is the minimum possible, R_{min}, the flame thickness remains relatively uniform along the flame, and that the experimentally observed flame thickness is physical. Under these assumptions, in order for a complete "hook" feature to exist, it would require for the edge of the flame to extend a minimum distance below the flat section of the flame, $\delta_{hook} = 1.5 \times \delta_{image}$. Provided the observed CH-layer thicknesses, this would result in $\delta_{hook} \approx 0.9mm$. Such a feature was not observed in the experimental images of CH-PLIF, and from this analysis one would conclude that a complete "hook" feature at the leading edge of the flame does not exist.

Next, we examine the orientation of the leading edge of the flame taking into account that partial hooking of the flame is potentially unresolvable due to blurring

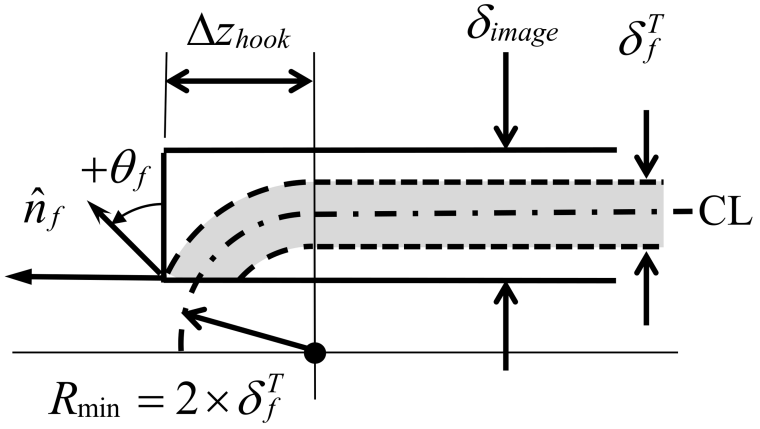

Figure 3.16: Schematic of representative flame hook feature within a horizontal and rectangular region of CH-PLIF with characteristic length scales of interest as follows: δ_{image}, observed thickness of CH-layer, δ_f^T, temperature based flame thickness, CL, centerline of CH-layer, R_{min}, minimum flame curvature based on δ_f^T, Δz_{hook}, axial length of hook feature, $\hat{n}_f$, flame normal at leading edge of flame, and θ_f, flame angle at leading edge.

of the CH-PLIF images. This is shown schematically in Figure 3.16 assuming that artificial thickening of the CH-layer in the images occurs. The gray region represents the "real" thickness of the CH-layer, δ_f^T, as determined from OPPDIF calculations, with the observed boundary of the CH-layer thickness, δ_{image}, represented by the solid black lines. Within the boundaries of the CH-layer, a partial hooking of the flame is possible as shown for $R_{min} = 2 \times \delta_f^T$. At this minimum flame curvature, the hook feature would extend an axial distance of $\delta z_{hook} \approx 0.57mm$. In other words, these hook features, even at the minimum flame curvature, would occur over $\approx 3.5 pixels$ in the CH-PLIF images. In addition, the orientation of the flame at the leading edge, $\hat{n}_f$, would result in a flame angle of $\theta_f \approx 66.4°$. Thus, if a flame were to orient itself normal to the flow field, it would be reflected both in the observable orientation at the leading edge and in the form of a hook feature. As is discussed in more detail in Section 6.2.1, the experimentally observed flame angles at the leading edge are near

horizontal, $\theta_f \approx 0°$, and lack any hook feature. Thus, the leading edge of the flame is concluded to be edge flame stabilized.

Table 3.7: Circumferential equivalence ratio measurements for a fixed radius, $r =$ 0.88", normalized by the circumferentially averaged equivalence ratio, $\bar{\phi}$.

	$r = 0.88$"			$r = 0.88$" inches	
θ	$u_{pm} = 35$m/s	$u_{pm} = 70$m/s	θ	$u_{pm} = 35$m/s	$u_{pm} = 70$m/s
11.9°	1.050	1.045	191.9°	0.957	0.971
23.9°	1.043	1.043	203.9°	0.953	0.965
35.8°	1.038	1.038	216.0°	0.953	0.955
47.8°	1.026	1.033	228.0°	0.960	0.958
59.8°	1.012	1.017	240.0°	0.965	0.959
71.8°	0.994	1.007	252.0°	0.969	0.959
84.0°	0.987	0.995	264.0°	0.975	0.964
96.0°	0.981	0.987	276.2°	1.040	1.010
108.0°	0.974	0.981	288.2°	1.051	1.005
120.0°	0.971	0.980	300.2°	1.030	1.018
132.0°	0.972	0.978	312.2°	1.043	1.033
144.0°	0.970	0.980	324.2°	1.050	1.042
156.0°	0.967	0.979	335.9°	1.048	1.047
168.0°	0.962	0.978	347.9°	1.048	1.046
180.0°	0.961	0.975	359.9°	1.050	1.049

CHAPTER IV

SWIRLING FLAME SHAPES AND REDUCED–ORDER MODELING

This section presents the flame shapes observed in the experimental facility, the fluid mechanic features of the flow field responsible for the flame shapes, and the sensitivities of these flames to combustor operational, geometrical, and thermal parameters. In addition, a stretch based reduced–order modeling technique for flame attachment and blowoff from shear layer stabilized flames is presented. As is demonstrated later in detail, this stretch based approach captures combustor temperature, and preheat temperature sensitivity for outer shear layer flames but fails to collapse the transition sensitivity to premixer velocity.

4.1 Observed flame shapes

The test configuration shown in Figure 3.1, is a common geometry for both commercial low NOx combustor hardware [69, 118] and in fundamental studies of swirling flows [52, 99]. The time averaged flow field of this geometry, consists of four main regions [48, 75, 122], which are highlighted in Figure 4.1: the outer recirculation zone (ORZ), the inner recirculation zone (IRZ), the annular swirling jet, and the inner and outer shear layers (ISL & OSL). These features are discussed again briefly in this chapter as a more detailed discussion can be found in Chapter 1. The ORZ is generated by the sudden area expansion resulting in a toroidal recirculation zone. The IRZ is comprised of the wake behind the centerbody and the vortex breakdown bubble (VBB), the latter a result of swirling incoming flow experiencing vortex breakdown. Depending on the swirl number, size of the centerbody and Reynolds number, the

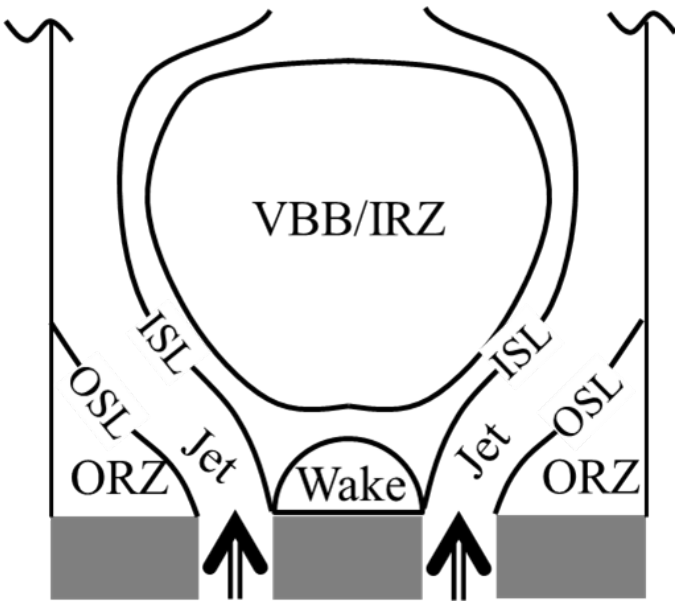

Figure 4.1: Illustration of the key fluid mechanical features of an annular, swirling, dump combustor.

center body wake and VBB can exist individually or as a single, merged IRZ structure [105]. The two shear layers which separate the high velocity annular jet from their associated recirculation zones, are referred to as the outer shear layer (OSL) and the inner shear layer (ISL) based on their relative location to the axis of symmetry.

Consider Figure 4.2, which illustrates several flame configurations which have been observed for this geometry [22]. Note that within this complex flow field, there are three basic flame holding locations: the outer shear layer, OSL, the inner shear layer, ISL, and the vortex breakdown bubble, VBB. The various combinations of potential flame stabilization location results in four unique flame shapes observed, shown in Figure 4.2.

Note, that although four flame shapes are shown, not all are observed for a given set of geometric and operational parameters within ϕ space, and due to hysteresis, flames observed at lean ignition may not be observed at lean blowout. These four flame shapes are anchored by the VBB (I), the VBB and ISL (II), the ISL (III),

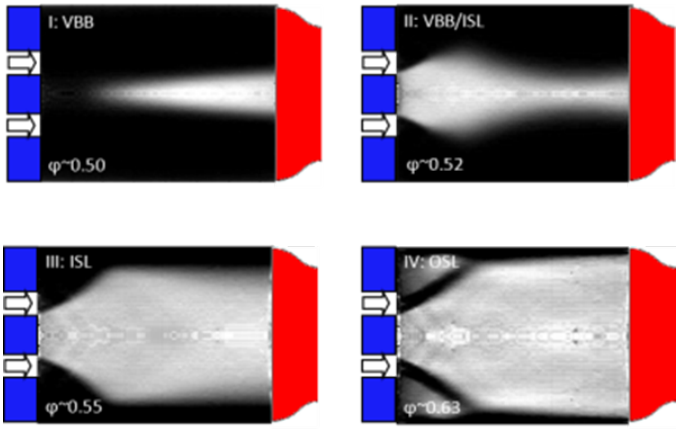

Figure 4.2: Time averaged chemiluminescence of basic flame configurations possible for geometry of interest, reproduced from Chterev *et al.* [22].

and the ISL and OSL (IV). The change in flame location between these flame shapes is a fundamental problem that has important ramifications on combustor operability, durability, and emissions. It can be seen that flame stabilization location has very strong influences upon flame shape that, in turn influences heat loadings to combustor hardware (e.g., centerbody, walls, dome plate). For example, the heat transfer to the centerbody is fundamentally different in configurations III and IV than in I. This, in turn, has direct implications on centerbody design and life. Similarly, the degree of flame spreading to combustor walls will vary between, for example, configurations III and II.

Flame location also has an important influence on combustion instability boundaries [71]. In short, combustor stability limits are controlled by the time delay between when a fuel/air ratio disturbance or vortex is created and when it reaches the flame. This time delay will certainly vary between, for example, configurations I and III. This also illustrates that discontinuous changes in combustor stability behavior may occur when the flame abruptly bifurcates from one stabilization location to another.

Additionally, stabilization locations influence the blowoff limits of the system. In reality, shifts in flame location can be thought of as a sequence of local blowoff events

(e.g., a flame nominally looking like configuration III will bifurcate to configuration I due to local blowoff of the flame from the ISL). In previous work, the flame shapes which are supported by this combustor geometry were explored [42].

How the flame is stabilized plays a crucial role in which physical processes control its dynamics. For example, configuration IV shown in Figure 4.2 is clearly affected by the dynamics of both shear layers, while that of configuration I may be lesser affected by the centerbody shear layer. Similarly, the dynamics of the central portion of the flame in configurations I and II are strongly influenced by vortex breakdown bubble dynamics, while configurations IV and III are presumably less affected. Furthermore, the time averaged stabilization location can vary with perturbation amplitude during combustion dynamics, implying that one set of fluid mechanic processes is important at low amplitudes, and another at higher amplitudes.

We focus our attention on the flame stabilization behavior at the attachment point of a flame stabilized in the inner shear layer. Whether the flame stabilizes in the low velocity regions of the shear layers, or near the stagnation region ahead of the vortex breakdown bubble, the transition from one flame shape to another can be described as a local extinction event leading to a large scale change in flame shape. It is hypothesized that the cause of local extinction is caused by aerodynamic straining on the flame [66], which alters the local temperature and burning rate [68]. If the shear rate and consequent flame strain rate is too large, the flame will locally extinguish and either blow out of the combustor completely, or stabilize at another location, such as transitioning from configuration IV to III or from configuration II to I.

The significance of aerodynamic straining of the flame sheet in the shear layer near the attachment point is discussed by Karlovitz *et al.* [59]. They noted that holes appeared in the side of the flame as flow velocity increased, apparently due to local extinction. Similar observations of such holes in flames near blowoff are detailed in a review by Shanbhogue *et al.* [104] and by Khosla *et al.* [61]. A discussion of the

Table 4.1: Swirling Flame Independent Test Parameters

Geometric	Fluid Mechanic	Thermo-kinetic
θ_{vane}	u_{pm}	T_{ph}
d_{cb}		ϕ
d_{comb}		
$d_{exhaust}$		
l_{comb}		

behavior of flames subjected to aerodynamic straining can be found in the textbook by Law [68]. In addition to strain effects, heat loss is also important to consider as it has a significant effect on the laminar consumption speed and therefore on the ability of the flame to stabilize in a shear layer [21].

4.2 Parameter Space

The test facility used in this study of swirling flames allowed for geometric, fluid mechanic, and thermo-kinetic parameters to easily be changed. This allowed for a diverse parameter space to be tested as shown in Table 4.1, which lists the various parameters changed in these swirling flame shape studies. Note that the geometric parameters listed, such as swirler vane angle, θ_{vane}, will have direct impacts on the fluid mechanic structure of the flow field.

These parameters represent the design space which can be directly changed from case to case. However, as fundamental groupings of these parameters are defined, like dump ratio, $A_{annulus}/A_{comb}$, a change in either centerbody diameter, or combustor diameter will change this ratio. Also, a change in a single parameter in Table 4.1 may cause a change in more than one fundamental parameter. For instance, holding all other parameters constant, a change in centerbody diameter will change the dump ratio as well as the swirl number, as defined in Equation 4.1. These considerations

are not unique to this test facility and are common to any experimental investigation of complex systems.

$$S_m = \frac{\int_{r^i}^{r^o} u_z u_\theta r^2 dr}{r_o \int_{r^i}^{r^o} u_z^2 r dr} \tag{4.1}$$

There are various parameter groupings which lend themselves to describing a swirling, annular, dump combustor. For swirling flows it is common to define it by the swirl number, S. There are many definitions for swirl number but the one used in these studies, S_m, is defined by the ratio of the angular momentum flux to the axial momentum flux. The sensitivity of the structure of a swirling flow field to swirl number is complex as for certain ranges of S_m, there are bifurcations in the structure with small changes in S_m. In addition to S_m, the structure of the non-reacting, swirling flowfield is sensitive to the ratio of the exhaust to the combustor cross-sectional area, $A_{exhaust}/A_{comb}$. This has been reported by other investigations as well [39, 38]. Our studies were conducted with a small enough exhaust section such that the flow at the exhaust exit was positive for non-reacting conditions. Finally, the ratio of the length of the combustor to its diameter, $(l/d)_{comb}$, captured the change in combustor length relative to its diameter, a parameter which alters the fundamental natural longitudinal acoustics of the combustor.

Table 4.2 displays the various combinations of geometric and operational test parameters explored in our work. Note, that the test space was created by varying each of the parameters listed in Table 4.1 between a high and low value. Geometric parameters are shown in column space, with the exception of θ_{vane}, which is shown in row space along with the operational parameters. Data has been obtained over a wide range of this test space, as shown in Table 4.2, but in some cases the presence of thermo-acoustic instabilities prevented flame stabilization studies to be performed. Enough space was explored allowing for the sensitivity to single parameters, shown in Table 4.3 and 4.4, and independent parameter groupings, such as $(l/d)_{comb}$, to be

Table 4.2: Geometric and operational test space

Data

X Unstable

			Swirler Vane Angle							
			37°				45°			
			Premixer Velocity [m/s]							
			70		35		70		35	
			Preheat Temperature [K]							
D_{CB} [mm]	D_{comb} [mm]	L/D	533	366	533	366	533	366	533	366
36	105	1.5		X						
	135	1.0		X				X		
		1.5	X	X		X	X	X		X
46	105	1.5					X			

assessed. Key sensitivities are further discussed in the analysis section of this chapter.

4.3 Experimental Procedure: Flame Configuration Mapping

We next describe how the flame transition data were taken. The mixture stoichiometry, ϕ, was swept up or down to cause a flame transition at a fixed set of operating conditions. While the bulkhead temperature could not be directly controlled, the time required for the system to reach thermal equilibrium was long enough ($\approx$ 1 hour) to allow us to also measure the influence of T_{bhd} on the transition ϕ value by varying the dwell time between transitions. For example, the steady state value of T_{bhd} differs by about $200K$ when a flame in the OSL is present (III) and not present (IV). By varying ϕ up and down between configurations III and IV while the system is approaching thermal equilibrium, the sensitivity to T_{bhd} was systematically explored. In this manner, flame configuration maps were created which marked the transition lines for OSL attachment and OSL blowoff in equivalence ratio and bulkhead temperature space.

Figure 4.3 plots a typical flame configuration map obtained for a single test case at conditions with low thermoacoustic levels. For this analysis, only the OSL attachment

Table 4.3: List of case studies investigating flame stabilization sensitivity to variations in geometric parameters.

Case #	*L/D*	D_{comb} [mm]	D_{CB} [mm]	θ_v [deg]	T_{ph} [K]	U_{pm} [m/s]	a_{attach}	$a_{blowoff}$	*Parameter Study*
1 A/B	1.5	105	***36 / 46***	37	533	70	0.60 / 0.40	0.90 / 0.20	D_{CB}
2 A/B	1.5	105	***36 / 46***	37	533	35	0.25 / 0.55	1.00 / 0.95	
3 A/B	1.5	105	***36 / 46***	37	366	35	0.00 / 0.05	0.25 / 0.70	
4 A/B	1.5	***105 / 135***	36	37	533	35	0.25 / 0.45	1.00 / 0.50	D_{comb}
5 A/B	1.5	***105 / 135***	36	37	366	35	0.00 / 0.10	0.25 / 0.05	
6 A/B	***1 / 1.5***	135	36	37	533	35	0.55 / 0.45	0.45 / 0.45	L/D
7 A/B	***1 / 1.5***	135	36	37	366	35	0.35 / 0.10	0.45 / 0.05	
8 A/B	***1 / 1.5***	135	36	45	533	35	0.50 / 0.40	0.50 / 0.40	
9 A/B	***1 / 1.5***	135	36	45	366	35	0.35 / 0.50	0.30 / 0.20	
10 A/B	1	135	36	***37 / 45***	533	70	0.30 / 0.25	0.35 / 0.30	θ_v
11 A/B	1	135	36	***37 / 45***	533	35	0.55 / 0.50	0.45 / 0.50	
12 A/B	1	135	36	***37 / 45***	366	35	0.35 / 0.35	0.45 / 0.30	
13 A/B	1.5	135	36	***37 / 45***	533	35	0.45 / 0.40	0.45 / 0.40	
14 A/B	1.5	135	36	***37 / 45***	366	35	0.10 / 0.50	0.05 / 0.20	
15 A/B	1.5	105	46	***37 / 45***	366	70	0.05 / 0.05	0.80 / 0.35	
16 A/B	1.5	105	46	***37 / 45***	533	35	0.55 / 0.55	1.00 / 0.60	
17 A/B	1.5	105	46	***37 / 45***	366	35	0.00 / 0.30	0.65 / 0.60	

Table 4.4: List of case studies investigating flame stabilization sensitivity to variations in operational parameters (Cases 18-31) and combustion dynamics (Cases 32 & 33).

Case #	*L/D*	D_{comb} [mm]	D_{CB} [mm]	θ_v [deg]	T_{ph} [K]	U_{pm} [m/s]	a_{attach}	$a_{blowoff}$	*Parameter Study*
18 A/B	1.5	105	46	37	***366 / 533***	70	0.05 / 0.40	0.80 / 0.50	T_{ph}
19 A/B	1.5	105	46	37	***366 / 533***	35	0.00 / 0.55	0.65 / 1.00	
20 A/B	1.5	105	46	45	***366 / 533***	35	0.30 / 0.55	0.60 / 0.60	
21 A/B	1.5	135	36	37	***366 / 533***	35	0.10 / 0.45	0.05 / 0.45	
22 A/B	1.5	135	36	45	***366 / 533***	35	0.50 / 0.40	0.20 / 0.40	
23 A/B	1	135	36	37	***366 / 533***	35	0.35 / 0.55	0.45 / 0.45	
24 A/B	1	135	36	45	***366 / 533***	35	0.35 / 0.50	0.30 / 0.50	
25 A/B	1.5	105	36	37	***366 / 533***	35	0.00 / 0.35	0.50 / 1.00	
26 A/B	1.5	105	46	37	533	***35 / 70***	0.55 / 0.40	1.00 / 0.50	U_{pm}
27 A/B	1.5	105	46	37	366	***35 / 70***	0.00 / 0.05	0.65 / 0.80	
28 A/B	1.5	105	46	45	366	***35 / 70***	0.25 / 0.05	0.55 / 0.35	
29 A/B	1	135	36	37	533	***35 / 70***	0.55 / 0.30	0.45 / 0.35	
30 A/B	1	135	36	45	533	***35 / 70***	0.50 / 0.25	0.50 / 0.30	
31 A/B	1.5	105	36	37	533	***35 / 70***	0.35 / 0.55	1.00 / 0.70	
32 A/B	***1 / 1.5***	135	36	37	366	35	0.35 / 0.10	0.45 / 0.05	p_{RMS}
33 A/B	***1 / 1.5***	135	36	45	366	35	0.35 / 0.50	0.30 / 0.20	

and OSL blowoff transitions are studied in detail. The upper line represents flame attachment in the OSL ($III - IV$ transition), above which the flame is stabilized in the OSL (OSL Stabilized Zone). Note the decrease in required equivalence ratio for OSL flame attachment with bulkhead temperature as ϕ goes from 0.65 to 0.58 with T_{bhd} correspondingly increasing from $350K$ to $575K$. In other words, as combustor temperature increased, OSL flame attachment became easier, occurring at lower ϕ. The lower line represents the lean OSL flame blowoff limit ($IV - III$ transition) which also shows a dependence on bulkhead temperature. Note that with OSL attachment occurring at higher ϕ than OSL blowoff, there is region where the flame can exist in either configuration III or IV, depending on the path taken. Thus there is a zone of hysteresis in the OSL stability map where the flame shape is not uniquely defined by ϕ and T_{bhd} alone. For example, suppose a flame transitions from configuration III to IV at $\phi = \phi_1$. Once a flame is stabilized in the OSL, ϕ must be decreased to a value of $\phi < \phi_1$, in order to cause extinction in the OSL. Data obtained from multiple test runs at the same set of operating and geometric conditions were used to determine the transition lines, for which there is relatively good agreement between the lines and the raw data points for both OSL attachment and blowoff as shown in the example figure.

Flame configuration maps were obtained for the highlighted test space shown in Table 4.2, or organized by geometric parameter and operational parameter sensitivities in Table 4.3 and Table 4.4, and are discussed in detail in the following section.

4.4 Reduced–Order Modeling

4.4.1 Stretch Based Scaling

Flames stabilized in the shear layers are likely to experience changes in burning properties, such as flame temperature and burning velocity [68], as a result of hydrodynamic flame stretch [66]. Since there is a limit to the degree of stretch which a flame

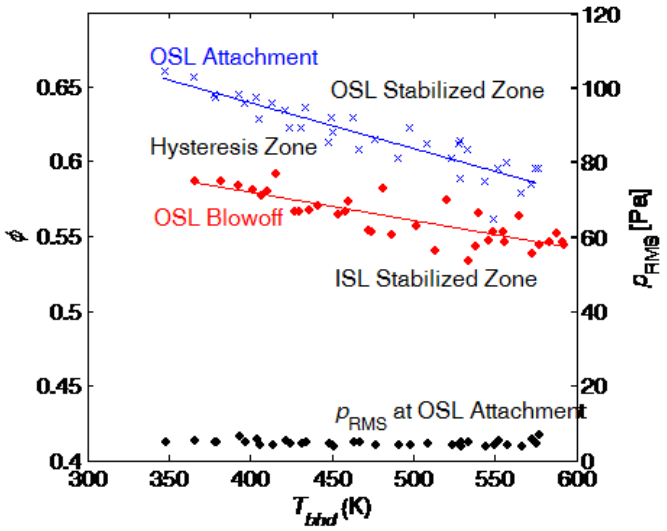

Figure 4.3: Typical flame configuration mapping results for test case 9*A*.

can withstand before extinguishing, it is likely that global changes in flame configuration are brought about by local extinction events within the shear layers. We define the following Karlovitz number as the ratio of the stretch rate imposed on the flame, κ, to the extinction stretch rate, κ_{ext}:

$$Ka = \frac{\kappa}{\kappa_{ext}} \tag{4.2}$$

As these extinction events are local, and with multiple stabilization locations present, global extinction does not necessarily happen with a single extinction event. For example, the flame shape can transition from being stabilized in both shear layers to solely the inner shear layer, or from ISL to VBB stabilized as a result of local extinction events. In fact, recall that for this combustor, four unique flame shapes were observed, each with a unique combination of stabilization locations. The primary directive of the reduced–order model was to develop a stretch based scaling to characterize and capture the sensitivity of flame extinction and attachment events in the OSL to key design parameters.

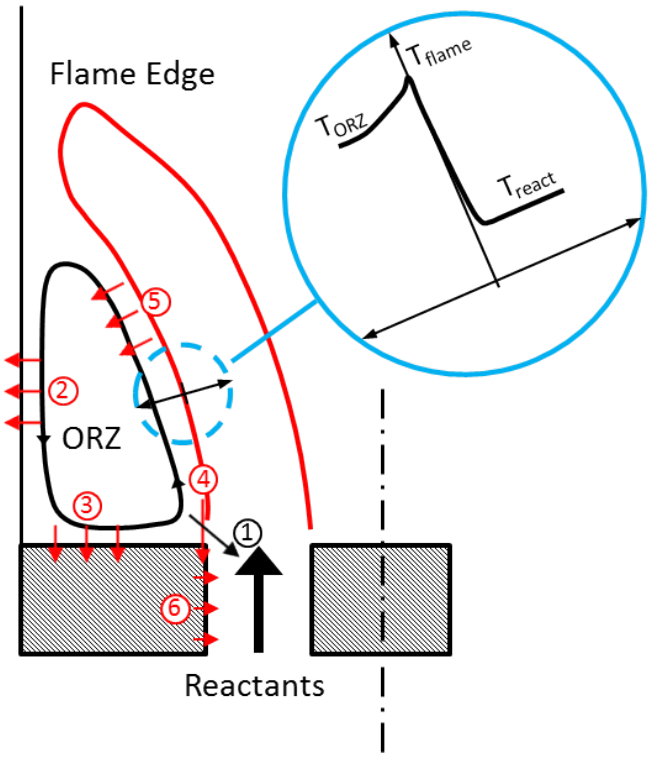

Figure 4.4: Physical processes for shear layer flame stabilization in a swirl stabilized combustor. Image courtesy of I. Chterev [23].

Figure 4.4 illustrates three key physical processes influencing flame stabilization in the outer shear layer: flame stretch, product recirculation, and combustor heat transfer. These are discussed next, beginning with flame stretch. Previous studies of shear layer stabilized flames noted that holes appeared in the flame as flow velocity increased due to local extinction [83]. Similar observations of such holes in flames near blowoff are described by Chaudhuri *et al.* [16] and in a review by Shanbhogue *et al.* [104]. Given the high strain rates present it is presumed that flame stretch induced extinction could be the cause of flame holes. In order to analyze the factors influencing the stretch rate imposed on the flame, consider the following equation for flame stretch:

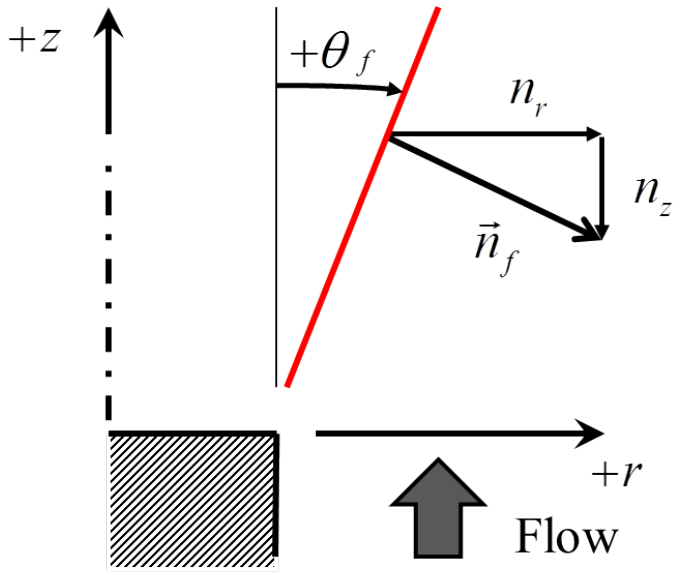

Figure 4.5: Flow and flame coordinate system for a centerbody stabilized, 2-D flame.

$$\kappa = \underbrace{-n_i n_j \frac{\partial u_i}{\partial x_j} + \frac{\partial u_i}{\partial x_i}}_{\kappa_S} + \underbrace{S_d \left(\frac{\partial n_i}{\partial x_i} \right)}_{\kappa_{curv}} \tag{4.3}$$

where we have written the stretch as the sum of three terms. The sum of the first two terms, κ_s, is a result of hydrodynamic strain and is non-zero only if the flow has spatial gradients. The third term, κ_{curv}, describes the contribution of flame curvature to flame stretch.

For this analysis, we focus on flame stretch due to hydrodynamic strain for a two dimensional, steady flame and an incompressible flow upstream of the flame sheet. The coordinate system and reference geometry for this analysis are shown in Figure 4.5. Following references [72, 127], the κ_s term may be written as:

$$\kappa_s = \kappa_{s,shear} + \kappa_{s,normal} \tag{4.4}$$

where assuming an incompressible approach flow, that the largest velocity gradients

are due to transverse shearing of the axial flow(ie., $\partial u_r/\partial z << \partial u_z/\partial r$), and that the flow speed is much greater than the flame speed (i.e., $\theta_f << 1$), then:

$$\kappa_{s,normal} \approx \frac{\partial u_z}{\partial z} \tag{4.5}$$

$$\kappa_{s,shear} \approx \theta_f \frac{\partial u_z}{\partial r} \tag{4.6}$$

The $\kappa_{s,shear}$ term quantifies the manner in which shearing flow strain translates into flame stretch, showing that they are related by the flame angle, θ_f. Similarly, the $\kappa_{s,normal}$ term describes the impact of flow acceleration and deceleration. Both terms are clearly nonzero in regions of high shear in flame stabilization regions, as the approach flow boundary layer separates into a change in cross sectional flow area. As is demonstrated later, the experimental results in Chapter 6 support this reduced form of strain induced flame stretch in the near field. Shanbhogue *et al.* [104] scaled flame stretch introduced by flow shear as:

$$\kappa_{s,shear} \sim S_d \left(\frac{u_o}{L_{shear}\, \nu} \right)^{1/2} \tag{4.7}$$

and axial acceleration/deceleration induced stretch term in Equation 4.5 as:

$$\kappa_{s,normal} \sim \frac{u_o}{L_{norm}} \tag{4.8}$$

where L_{norm} and L_{shear} denote characteristic length scales associated with normal and shear strain, respectively. Combining the scalings for $\kappa_{s,shear}$ and $\kappa_{s,normal}$ with Eq. 4.4 shows that there are two relevant Karlovitz numbers:

$$Ka_{s,shear} = \frac{\kappa_{s,shear}}{\kappa_{ext}} \sim \frac{S_d}{\kappa_{ext}} \left(\frac{u_o}{L_{shear}\, \nu} \right)^{1/2} \tag{4.9}$$

$$Ka_{s,normal} = \frac{\kappa_{s,normal}}{\kappa_{ext}} \sim \frac{u_o}{L_{norm} \kappa_{ext}} \tag{4.10}$$

Since eq. 4.9 has both S_d and κ_{ext}, it is worthwhile to relate these two quantities. As shown by Chung [24], κ_{ext} is related to the flame thickness and burning velocity

at extinction conditions by $\kappa_{ext} = S_{d,ext}/\delta_{f,ext}$, leading to:

$$\kappa_{ext} \sim S_{d,ext}^2/\alpha \tag{4.11}$$

Solving for $S_{L,ext}$ in Equation 4.11, substituting into Equation 4.9, and assuming $Pr \equiv \nu/\alpha = 1$, results in the following Ka number scaling for shear induced extinction:

$$Ka_{s,shear} \sim \left(\frac{u_o}{L_{shear}\kappa_{ext}}\right)^{1/2} \tag{4.12}$$

Comparing equations 4.10 & 4.12, if one assumes that the relevant length scales are the same ($L_{shear} = L_{norm}$), then the appropriate scaling parameter is the same for normal and shear strain contributions to flame stretch with power dependencies of 1 and 1/2, respectively. Furthermore, this would suggest that two fundamentally different flame stabilization scalings may exist, depending upon which term dominates. However, stretch is the sum of contributions from normal and shear strain contributions such that power dependence of total stretch on velocity is not constant. An appropriate scaling must be derived based on the sum of these contributions to total stretch as shown below:

$$Ka_s = \frac{\kappa_{s,normal} + \kappa_{s,shear}}{\kappa_{ext}} \tag{4.13}$$

Thus, although the power dependence of Ka_s on velocity varies in stretch space, the conditions at which blowoff occur are at $u_o/(L\kappa_{ext}) = const.$

Second, as we have implicitly done in the derivation of equations 4.9 and 4.10, the sign of the strain terms must be known or assumed *a priori*. Also, as noted above, there are two length scales as well that are unknown. Granted, based on our assumed laminar boundary scaling of boundary layer thickness, one would assume L_{shear} to be the boundary layer development length. Appropriate length and velocity selection, multiple strain sources of flame stretch, and the high spatial dependence on the local velocity and strain conditions within the shear layer complicate the derivation of a reduced–order scaling approach to capture flame blowoff.

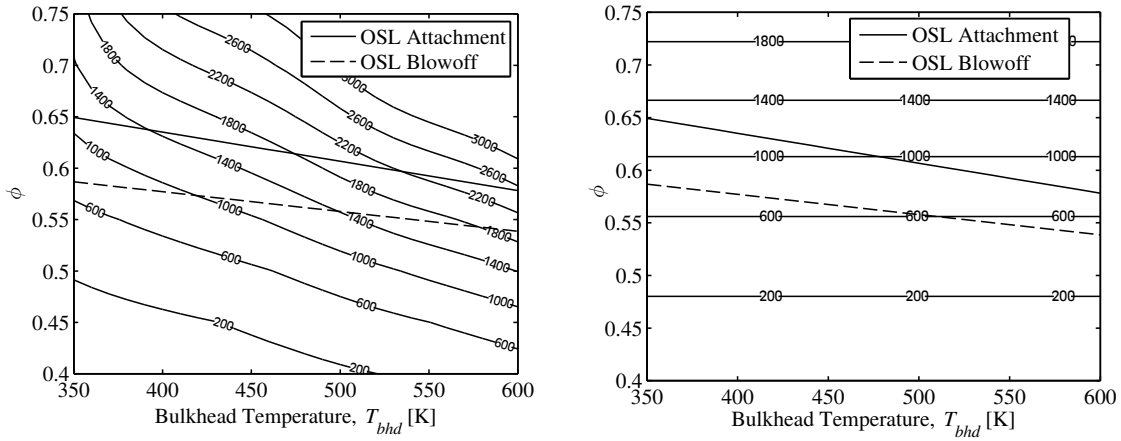

(a) Flame map with $\kappa_{ext}\,(\phi, T_{bhd})$.

(b) Flame map with $\kappa_{ext}\,(\phi, T_{ph})$

Figure 4.6: Example flame configuration mapping of OSL attachment and blowoff with $\kappa_{ext}\,(\phi, T_{bhd})$ isolines overlaid (left) and $\kappa_{ext}\,(\phi, T_{ph})$ isolines overlaid (right) for test case 24A.

4.4.2 Chemical Kinetic Sensitivities

This section considers fuel/air ratio and temperature effects on flame transitions. Returning to Figure 4.4, these data clearly show that the transition ϕ is a function of T_{bhd}. This indicates that understanding the heat transfer between the edge flame stabilized in the shear layer and the combustor walls is needed in order to predict flame stabilization. As was outlined above, κ_{ext} is used as a more fundamental indicator of reactant kinetics, and so operating conditions at the measured transitions are used to calculate its value. κ_{ext} values are also directly related to the critical chemical time of stretched flames as $\tau_{ext} = 1/\kappa_{ext}$. However, note that there are at least two reference temperatures that can be used as in input to such a calculation: the free-stream reactant preheat temperature, T_{ph}, and the bulkhead or combustor wall temperature, T_{bhd}. Figure 4.6 shows the OSL attachment and blowoff lines for a single test case with isolines of $\kappa_{ext}\,(\phi, T_{bhd})$ on the left, and isolines of $\kappa_{ext}\,(\phi, T_{ph})$ on the right.

Neither of the above approaches collapses a transition line onto an isoline of κ_{ext}.

Using the bulkhead temperature as the input to the calculated κ_{ext} shows a stronger sensitivity to T_{bhd} than experimentally observed, while using a fixed value of T_{ph} shows a weaker sensitivity (indeed, no sensitivity) than measured. These results make sense, as it seems likely that the reactants in the separating boundary layer are preheated to some intermediate temperature value, $T_{ph} < T_{reac} < T_{bhd}$. These results suggest defining an intermediate reference temperature, which we do through the relation:

$$T_{ref} = T_{ph} + a\,(T_{bhd} - T_{ph}) \tag{4.14}$$

The coefficient a is empirically determined so that flame transitions occur at fixed κ_{ext} values. To illustrate, Figure 4.7 replots the iso-κ_{ext} lines using this reference temperature; note that the best fit value of a differs for OSL attachment and OSL blowoff, and so two plots are needed. Repeating a point made above – the clear implication of these results is the importance of heat transfer between the flame and the combustor hardware on flame shapes and therefore computations of blowoff or flame shape transitions must capture this heat transfer; adiabatic boundary conditions will not work. The values of a are tabulated in Table 4.3 and Table 4.4 for OSL blowoff, $a_{blowoff}$, and attachment, a_{attach}. This scaling restricts the a coefficient to lie between $0 \leq a \leq 1$ and values lie anywhere within this range as shown in the tables. There is no apparent correlation with the a coefficient values with any of the parameters explored.

We next consider results from different preheat temperatures. Figure 4.8 compares the OSL transition points for test cases at T_{ph} of $366K$ and $533K$. Note that from this point forward we only show the linear least squares fit line of the transition data. The OSL transition lines at the lower preheat temperature (solid lines of Figure 4.8), occur at higher ϕ than the higher preheat temperature test case (dashed line of Figure 4.8). In fact, all preheat temperature sensitivity test cases completed indicated a decrease in ϕ at the transition point with increasing T_{ph}. This result was expected as increasing the preheat temperature increases the resistance of the flame to stretch.

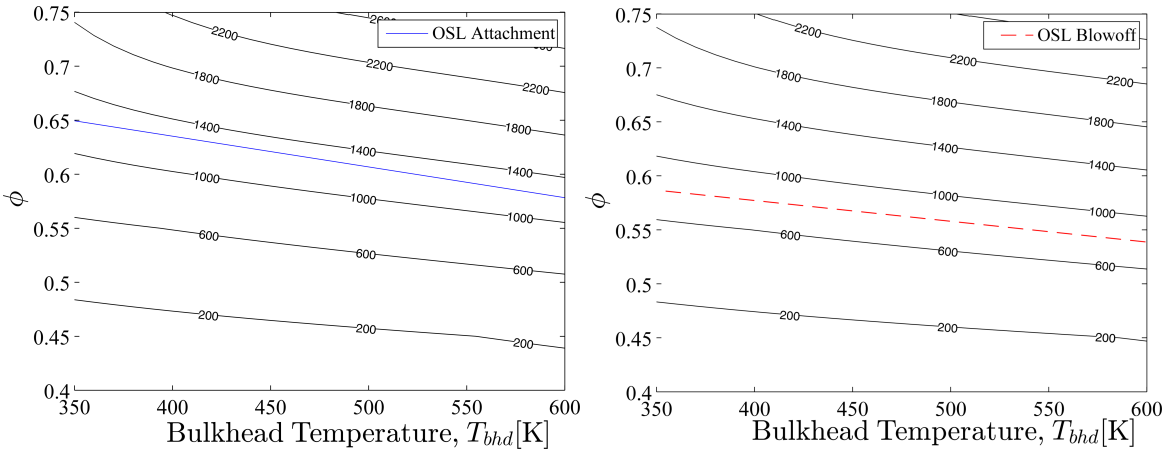

(a) OSL Attachment **(b)** OSL Blowoff

Figure 4.7: Flame transition maps for attachment (left) and blowoff (right) with isolines of extinction stretch rate calculated using reference temperature correction from Equation 4.14 for test case 24A.

Note also that while significant hysteresis is observed for $T_{ph} = 366K$, very little occurs at $533K$. While increasing T_{ph} did generally decrease the region of hysteresis in $\phi - T_{bhd}$ space, it did not always result in the complete elimination of hysteresis. As is discussed further in later sections, the presence and degree to which hysteresis exists is sensitive to both operational and geometrical parameters.

These general preheat sensitivities can be approximately captured with detailed kinetics calculations of the extinction stretch rates of the different mixtures. To illustrate, Figure 4.9 plots the relationship between the computed extinction stretch rates of OSL attachment and blowoff for T_{ph} cases of $366K$ and $533K$. The extinction stretch rates are calculated using the measured ϕ value for a given transition, and the preheat temperature, T_{ph}, as $\kappa_{ext}(\phi, T_{ph})$. Extinction stretch rates for the two T_{ph} test cases are compared at the same T_{bhd} as $\phi(T_{bhd})$. For example, for the OSL attachment data in Figure 4.9 at a $T_{bhd} = 500K$, extinction stretch rates would be compared at $\phi = 0.61$ and $\phi = 0.50$ for the $T_{ph} = 366K$ and $T_{ph} = 533K$ test cases, respectively.

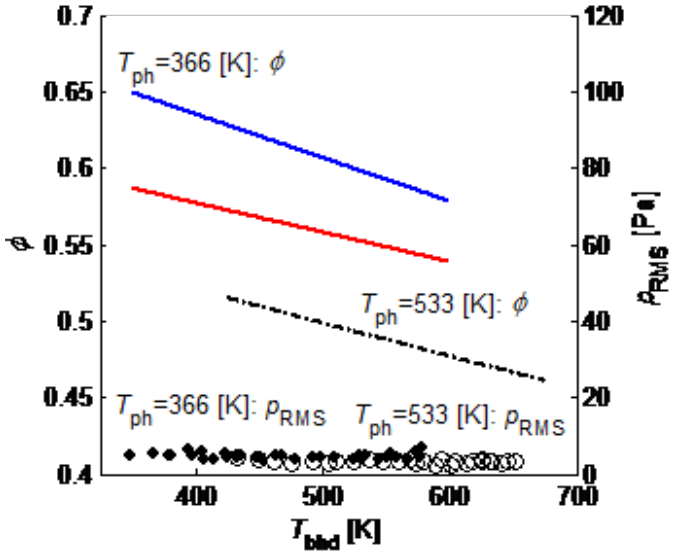

Figure 4.8: Preheat temperature sensitivity of OSL stabilization/blowoff for $l/d = 1$, $d_{comb} = 5.26$", $d_{cb} = 1.42$", 45° vane swirler, $u_{pm} = 35\ m/s$.

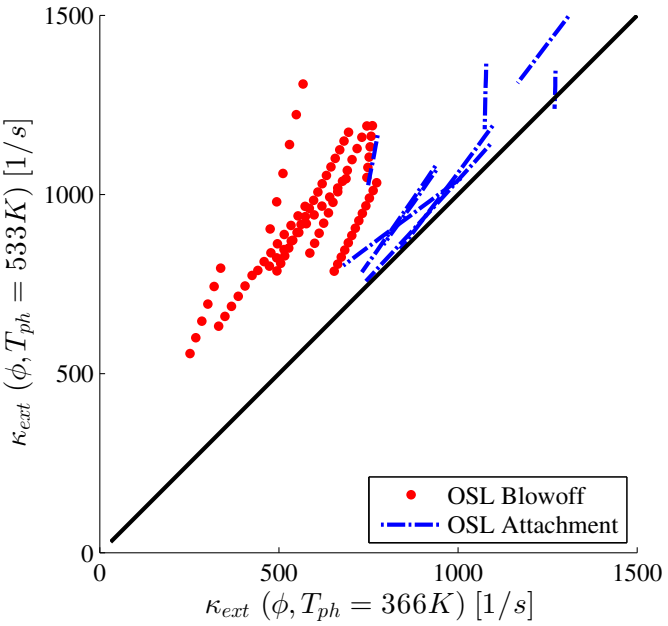

Figure 4.9: Comparisons of extinction stretch rate at two different T_{ph} for OSL attachment and blowoff transitions (Test cases 19-25, A & B).

Figure 4.9 plots the calculated extinction stretch rate values at the measured transition points for a range of T_{bhd}, for both the $IV - III$ (OSL blowoff) and $III - IV$ (OSL attachment) transitions. The figure shows that OSL attachment for both preheat temperatures occur at nearly the same extinction stretch rate throughout the bulkhead temperature space explored. In other words, from a measurement of the transition value at one preheat temperature, one could use kinetics calculations to predict the OSL attachment point at another preheat temperature. However, this is not the case for the OSL blowoff transition. Rather, the higher preheat temperature case transition occurs at a systematically higher extinction stretch rates. Thus, bulk mixture values of T_{ph} and ϕ can be used to capture transition associated with OSL attachment, but not OSL blowoff.

We can make a similar comparison of sensitivity of OSL blowoff and attachment to T_{ph} using the new reference temperature, T_{ref}, defined in Eq. 4.14. Because the κ_{ext} value line is by definition parallel to the measured T_{bhd} sensitivities, the blowoff line shown in Figure 4.6b is replaced by a single point, which corresponds to the iso-κ_{ext} value, represented as $\kappa_{ext,a}$. The same OSL blowoff data shown in Figure 4.9, are plotted in Figure 4.10, where we used the calculated $\kappa_{ext,a}\left(\phi, T_{ref}\right)$ value obtained. The figure clearly shows that the sensitivity of OSL blowoff to preheat temperature is captured using this approach.

A key conclusion from these results is the significance of two reference temperatures for capturing shear layer flame transitions, T_{ph} for attachment and T_{ref} for blowoff. This result is physically intuitive. For a flame that is stabilized in the shear layer, the extinction conditions which will cause OSL blowoff are a strong function of the local reference temperature, T_{ref}. For the flame to reattach, these results show that the bulk approach flow temperature is the more significant. For the rest of this paper, we use T_{ph} and T_{ref} for calculations of κ_{ext} for interpreting the sensitivity of OSL attachment and blowoff, respectively.

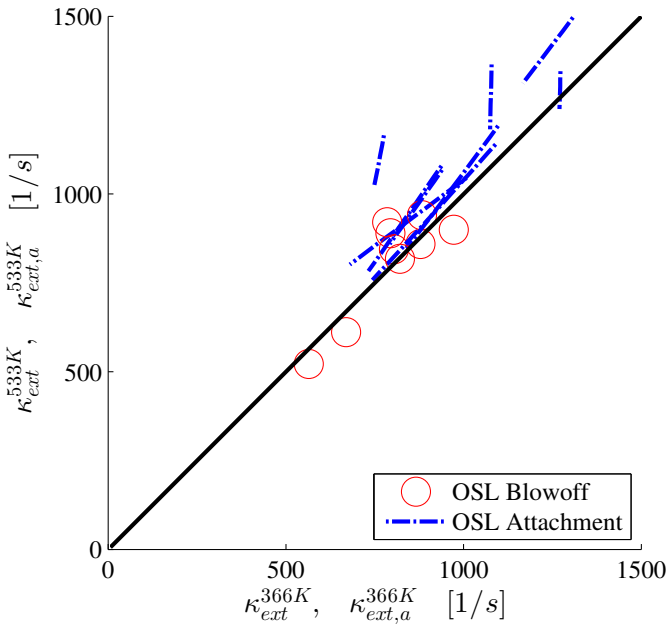

Figure 4.10: Comparisons of extinction stretch rate at two different T_{ph} for OSL attachment and blowoff transitions using $\kappa_{ext}(\phi, T_{ph})$ and $\kappa_{ext,a}(\phi, T_{ref})$, respectively (Test cases 19-25, A & B).

Finally, the hysteresis between OSL attachment and blowoff shown in terms of equivalence ratio, $\Delta\phi$, is shown in Figure 4.11. Note that the largest hysteresis is for $T_{ph} = 366K$ test cases, however, there are test cases where the level of hysteresis are comparable between the two preheat temperatures.

4.4.3 Fluid Mechanic Sensitivities

The parameters of u_{pm} and S_m have strong impacts on the fluid mechanic features of the combustor, as well as the stretch rate, κ_s, that the flame is subject to. For example, we expect higher u_{pm} to be destabilizing to flame holding as flame stretch increases, as shown by equations 4.7 and 4.8. The flow swirl number influences the pressure gradients that the separating boundary layers are subjected to, and therefore the separating shear layer thickness. It certainly also influences the character of the flow recirculation regions, particularly in the IRZ.

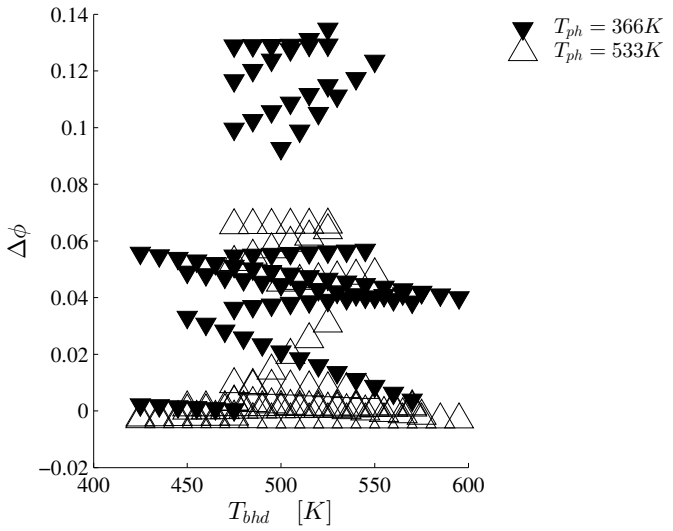

Figure 4.11: Hysteresis between OSL attachment and blowoff identified by T_{ph} (Test cases 19-25, A & B).

Figure 4.12 demonstrates the effect of u_{pm} on the flame transitions by showing the stability maps of the OSL for a low velocity and high velocity test case. As is clear from the figure, doubling the bulk flow velocity increases the equivalence ratio for attachment and blowoff transitions, thus making flame stabilization in the OSL more difficult with the increase in velocity. In this particular case, significant hysteresis is observed for both the low and high velocity test cases, although the hysteresis zone is wider for the higher velocity case. For the most part (but not always), hysteresis is greater for the higher velocity condition.

Using the Karlovitz number approach described above, we revisit the velocity dependence of blowoff. Assuming that transition events occur at a constant Ka, then the extinction stretch rate at blowoff should increases linearly with velocity. If the appropriate physical scaling is used in the definition of Ka, this also implies that the ratio of Karlovitz numbers at the two velocities should be constant. We define the following two ratios of Karlovitz numbers at the transition point:

$$R \equiv \frac{Ka^{35m/s}}{Ka^{70m/s}} = \frac{\kappa_{ext}^{70m/s}\left(\phi, T_{ph}\right)}{\kappa_{ext}^{35m/s}\left(\phi, T_{ph}\right)} \frac{35m/s\ /L_o}{70m/s\ /L_o} \tag{4.15}$$

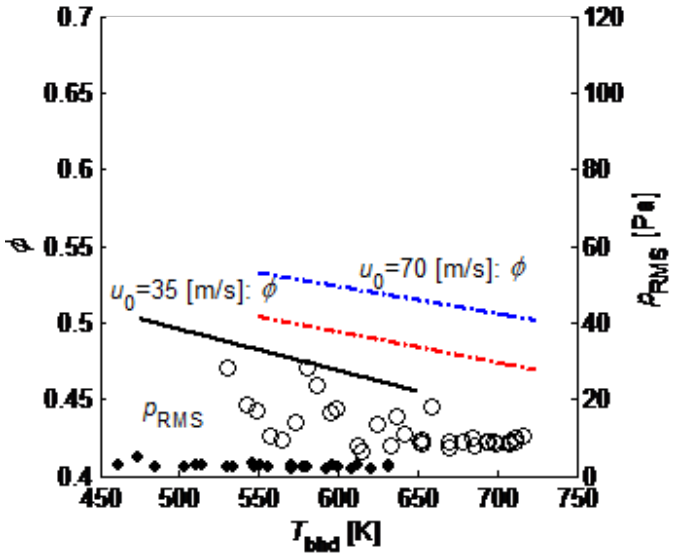

Figure 4.12: Nozzle exit velocity sensitivity for test case 28.

$$R_a \equiv \frac{Ka_a^{35m/s}}{Ka_a^{70m/s}} = \frac{\kappa_{ext,a}^{70m/s}(\phi, T_{ph})}{\kappa_{ext,a}^{35m/s}(\phi, T_{ph})} \frac{35m/s\ /L_o}{70m/s\ /L_o} \tag{4.16}$$

using Ka for scaling OSL attachment events and Ka_a for scaling OSL blowoff events, consistent with our discussion at the end of Subsection 4.4.2.

Figure 4.13 plots these ratios, R and R_a, at the two velocities as a function of T_{bhd}. If Eqns. 4.15 and 4.16 correctly capture the velocity sensitivity, then R and R_a should equal unity. The figure shows that these ratios always exceed 1/2, implying that increasing premixer velocity decreases flame stability for all of the test cases, as expected. However, the majority of the OSL attachment and blowoff data fall below one, suggesting that the sensitivity of flame stabilization to velocity is less than would be expected. For example, a value of 0.8 implies that the extinction stretch rate increases by 60% when the velocity is doubled. The reasons for this deviation from unity are unknown although these results are consistent with blowoff analysis of other data sets [104], and show the shortcomings in current abilities to scale velocity sensitivities for flame anchoring. The discussion of the flame stretch scaling in the context of Eq. 4.3 provides some hints of the complexity of this matter.

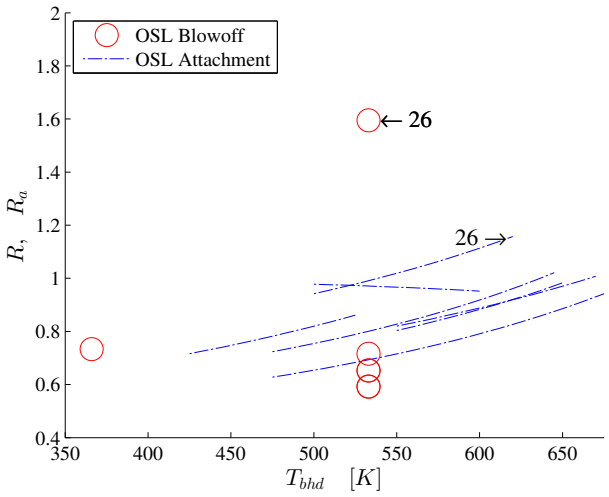

Figure 4.13: Dependence of extinction stretch rate ratios, R and R_a, at two premixer velocities, $35m/s$ and $70m/s$, on T_{bhd} (Test cases 26, 28-31).

Put differently, the prior section showed that changes in flame transitions driven by kinetic parameters could be well captured by constant Ka scalings, while this section shows that flame transitions driven by fluid mechanic parameter variations are much more complex. For the most part, R and R_a also increase as a function of bulkhead temperature itself for attachment events. Finally, there is one outlier, test case 26, for which OSL blowoff shows a much greater velocity sensitivity (i.e., values greater than unity) for unknown reasons.

Lastly, the hysteresis between OSL attachment and blowoff is characterized in terms of difference in equivalence ratio for the velocity sensitivity test cases as shown in Figure 4.14. The largest hysteresis was observed for $u_{pm} = 70m/s$ test cases, while negligible hysteresis was observed for several $u_{pm} = 35m/s$ test cases.

We next consider swirl number effects through changes in the swirler vane angle, θ_{vane}. The effect of θ_{vane} on flame stability were minimal and did not significantly influence OSL flames as only slight changes in transition equivalence ratio were observed, on the order of $0.01 - 0.02$. Generally it was found that increases in swirl number degraded stability by inhibiting flame attachment in the OSL. For example,

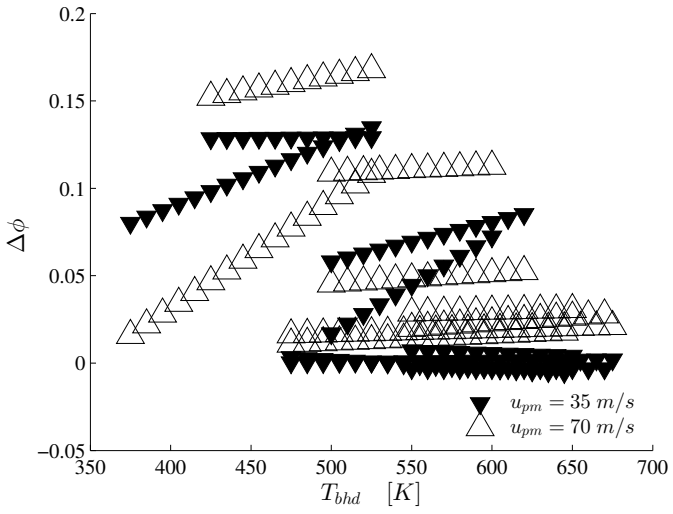

Figure 4.14: Hysteresis between OSL attachment and blowoff identified by premixer velocity, u_{pm} (Test cases 26 and 28-31, A & B).

Figure 4.15 presents a flame configuration map for a representative θ_{vane} sensitivity test case where no hysteresis was observed for either swirler. In this example, flame stability is degraded only slightly with an increase in swirl as the OSL stability line for the 45° swirler is slightly higher than the 37° swirler for all bulkhead temperatures. Figure 4.16 summarizes these findings for all θ_{vane} sensitivity cases performed, comparing conditions of OSL attachment using $\kappa_{ext}\left(\phi, T_{ph}\right)$ and OSL blowoff using $\kappa_{ext,a}\left(\phi, T_{ref}\right)$, for the two swirl vane angles. With the exception of one test case, OSL flame attachment lines are above the $1-1$ line shown (black line) thus indicating that flame attachment is degraded for the higher swirl condition. However, there is not a clear systematic effect of swirl vane angle on OSL blowoff as data points are scattered about the $1-1$ line.

The effect of swirler vane angle on the observed hysteresis between OSL attachment and blowoff is shown in Figure 4.17. While there is a grouping of data sets in the region $\Delta\phi \leq 0.02$, where hysteresis is similar in magnitude and dependence on bulkhead temperature, outside of that region, there is less agreement in the hysteresis for the two swirler vane angles.

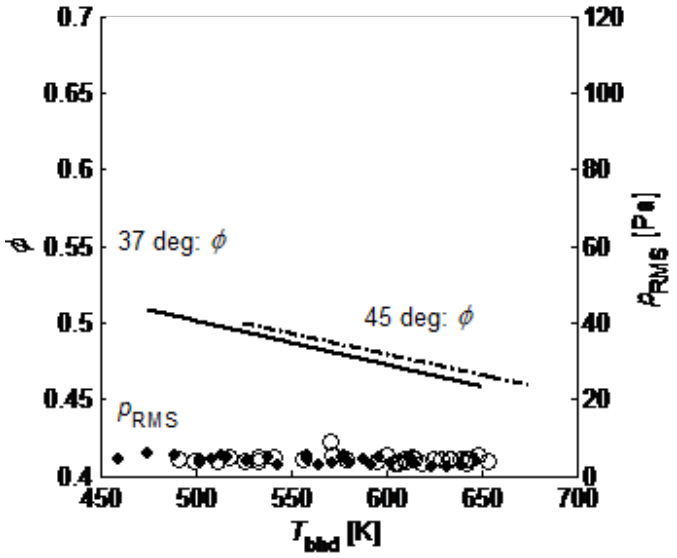

Figure 4.15: Swirler vane angle sensitivity for test case 14, A & B.

Note that it is important to differentiate the effects on global stability of the flame and its anchoring in the OSL. Increasing swirl clearly has a positive influence on ISL flame stability as shown in previous work [23] as well as on flames stabilized by the vortex breakdown bubble, but has a degrading influence on flame stability in the OSL, as shown here. It is likely that this is a manifestation of its influence on shear characteristics in the separating boundary layer.

Similarly, very modest changes in blowoff conditions were observed at the two combustor lengths, $l/d = 1.0$ and $l/d = 1.5$, as indicated in Figure 4.18. This result would be expected, as the combustor length should not have a strong impact on the OSL.

4.4.4 Hysteresis and Thermoacoustics

Thermoacoustic oscillations was observed to have significant impact on hysteresis levels. Acoustic measurements confirmed that when significant levels of acoustics were present, the region of hysteresis decreased. Similarly, high levels of acoustics were associated with independence of the OSL transition to bulkhead temperature. An

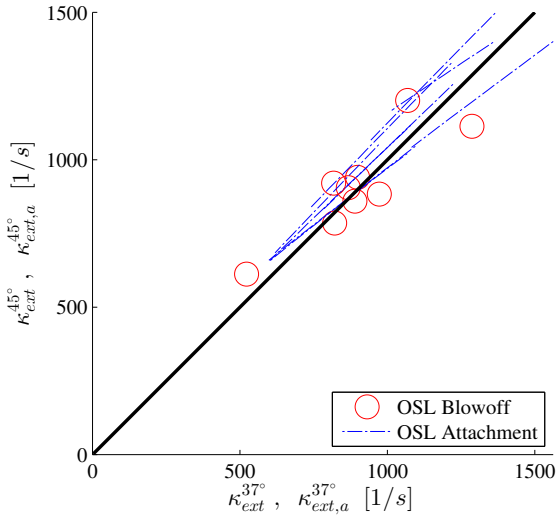

Figure 4.16: Comparison of extinction stretch rate for two θ_{vane}, 45° (y-axis) and 37° (x-axis), at $T_{bhd} = const$ (Test cases 10-17, A & B).

example result is shown in Figure 4.19, which compares the flame configuration maps for a test case which exhibits a thermoacoustic instability during OSL attachment and one which does not.

These test cases are identical in operational and geometric parameter space with the exception of combustion length, l_{comb}, which is 50% longer for the test case which is thermoacoustically unstable during OSL attachment (prior planar flow field measurements have shown that such a change in l_{comb} has negligible influence on the time averaged flowfield and flame attachment behavior near the dump plane). Thus, this result isolates the effect of thermoacoustics.

The solid lines in Figure 4.19 represent the low acoustics or $(l/d)_{comb} = 1.0$ test case with the OSL attachment line above the blowoff line. Also shown as the black dots corresponding to the right axis, are the acoustic measurements. There is a noticeable change in the OSL attachment line for the thermoacoustically unstable test case, shown as the dashed lines in Figure 4.19. Note the nearly horizontal OSL attachment line; i.e. flame attachment is a weak function of bulkhead temperature; in fact, the

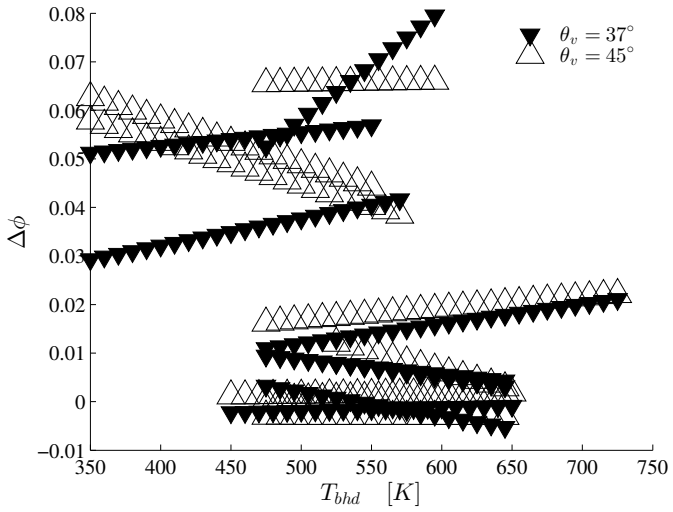

Figure 4.17: Hysteresis between OSL attachment and blowoff identified by swirler vane angle, θ_{vane} (Test cases 10-17, A & B).

slight bulkhead temperature sensitivity is inverted! The acoustic measurements for the unstable case are shown as the open circles on the plot and interestingly enough, decrease in value with bulkhead temperature as hysteresis increases.

Another important result is the fact that acoustics levels affect OSL attachment, but hardly affect OSL blowoff. Hysteresis fundamentally occurs because the flame in configuration III cannot propagate upstream in the high velocity flow in order to attach in the low velocity shear layer. This is believed to be caused by the oscillatory flow field leading to time instants where the low flow velocity allows for upstream flame propagation, whereupon it can lock onto the shear layer for the high velocity instants of the cycle. As such, acoustic levels have significant influences on OSL attachment. Acoustic levels have little effect on OSL blowoff as once the flame attaches to the OSL the ORZ is close enough to adiabatic temperature so ISL flame gases have negligible influence.

It is expected for the effect of acoustics on hysteresis to be correlated to the ratio of acoustic velocity to nozzle exit velocity, given by u_{rms}/u_o. A reference acoustic velocity is given by $u_{rms} = p_{rms}/\left(\rho c\right)_{avg}$. Figure 4.20 shows this trend by plotting

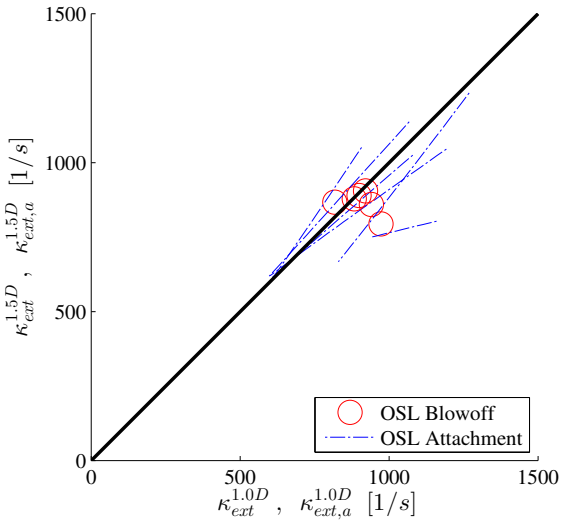

Figure 4.18: Sensitivity of outer shear layer flame stabilization to combustor length for test cases 6-9, A & B.

hysteresis against u_{rms}/u_o for a particular set of conditions.

Hysteresis levels also exhibit additional sensitivities to flow velocity and preheat temperature that are not fully capture simply by this u_{rms}/u_o parameter. As noted above, we find that increasing flow velocity or decreasing preheat temperature will increase hysteresis. We have observed, however, that for any given operating conditions, hysteresis decreases monotonically with increases in thermoacoustic amplitudes.

Finally, although for test case 32, l_{comb} did separate the stable case from the unstable case in Figure 4.19, this was not always the case.

4.4.5 Inner shear layer blowoff

In order to further analyze flame stabilization sensitivities to S_m, measurements of the ISL blowoff transition were also obtained over a broader range of u_{pm} from $35 - 115$ m/s for both swirlers. Note that thermoacoustic levels here were very low and are not shown. These results are indicated in Figure 4.21, showing that the $S_m = 0.8$ case generally blows off at ϕ values of about 0.02 lower than the $S_m = 0.6$ case. However, it is also clear that the sensitivity of the different S_m cases to u_{pm} is different. It is much

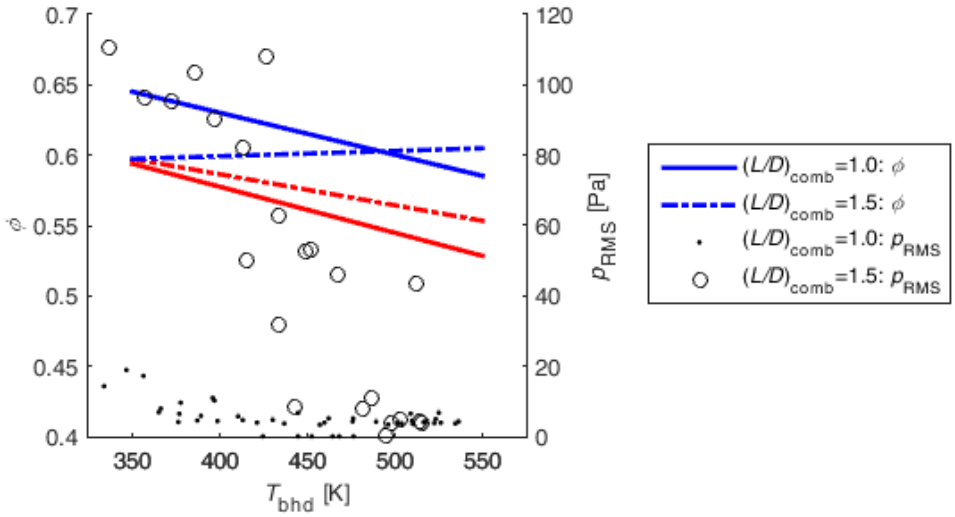

Figure 4.19: Thermoacoustic fluctuation amplitude sensitivity for test case 32, A & B.

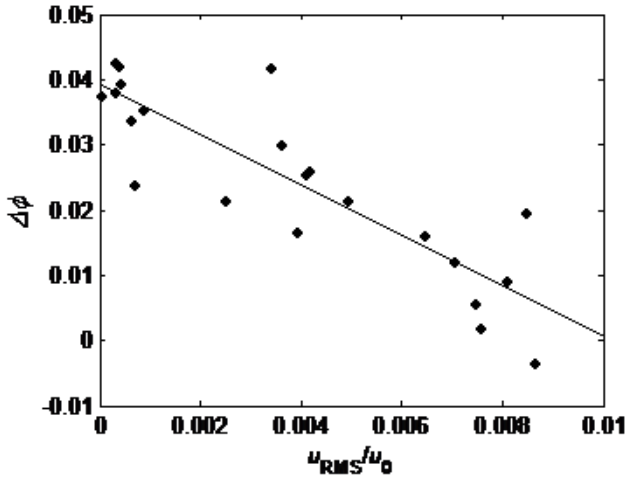

Figure 4.20: Hysteresis sensitivity to normalized acoustic velocity at attachment point condition for test case 32B.

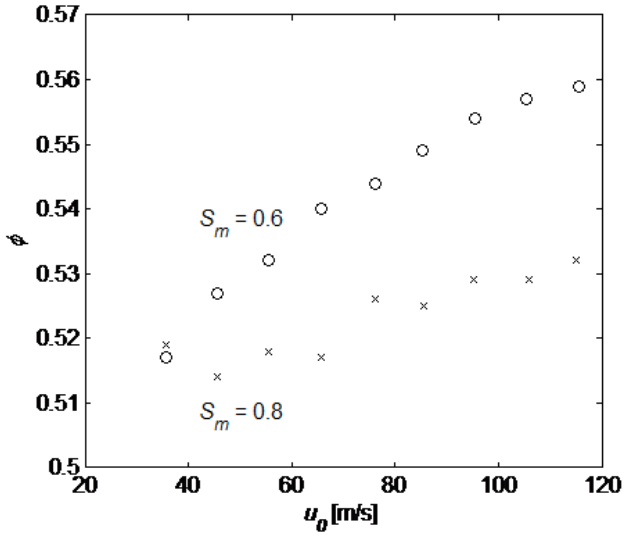

Figure 4.21: Measurements of ISL blowoff transition point, corresponding to flame lean blowoff limit. ($d_{comb} = 5.26$", $d_{cb} = 1.42$", and $T_{ph} = 533K$).

stronger for the weaker swirl case, and that the sensitivity to velocity is different at low and high velocities for the stronger swirl case. The curves seem to either converge or cross at a premixer velocity near 35 m/s. In reference to the previous premixer velocities of 35 and 70 m/s, looking at the open circle symbol, we note that near 70 m/s the $S_m = 0.8$ data blows off at lower ϕ than the $S_m = 0.6$ data.

CHAPTER V

NUMERICAL MODELING OF RECIRCULATION ZONE PHYSICS

As a companion to the experimental studies performed in this work, numerical model studies were carried out as well. Numerical models are powerful tools which allow for the sensitivities of flames to parameters of interest to be explored without the costly and time intensive setup changes associated with experiments. Numerical models can range from highly detailed and computational intensive approaches such as direct numerical simulations (DNS) to simplified physics models or reduced–order models which calculate fundamental parameters. Reduced–order models are attractive because of their numerical simplicity lending themselves to design of experiments (DOE) where the sensitivity to a wide range of parameters can be determined. For example, chemical kinetic software such as CHEMKIN offers models for fundamental parameters such as the unstretched, laminar flame speed, S_d^o, the stretched flame speed, $S_d(\kappa_s)$, and the extinction stretch rate, κ_{ext}. One can then chose a reduced–order model based on the physics which one expects to be most relevant. For the experimental studies in question, where the flame is stabilized within the inner shear layer, it is assumed that flame stability is strongly related to the response of the flame to stretch. As such, CHEMKIN's opposed jet model, OPPDIF, was used to determine stretched flame properties of interest such as $S_d(\kappa_s)$ and κ_{ext}. These parameters are of particular interest for interpreting the experimentally measured flame stretch, κ_s, and velocity conditions along the flame as compared to numerically calculated values. These parameters are calculated using the symmetric opposed jet model. The details of the symmetric opposed jet model are described in detail, including the importance

of the reference location within the flame structure to which they are reported.

In addition to providing reference values of stretched flame parameters of interest using the symmetric model, the opposed jet model is modified to include and assess the sensitivity of stretched flames to additional physics. For instance, heat loss with the combustor boundaries, such as the centerbody, will result in a non-adiabatic, stretched flame. With heat losses to the centerbody, the recirculation zone temperature, which supports the flame at the attachment point, will drop. A decrease in recirculation zone temperature, in turn, will result in heat losses from the flame to the recirculation zone. A modified opposed jet model is presented which simulates the effects of recirculation zone temperature changes. Finally, an asymmetric variation of the opposed jet model is proposed which simulates product/reactant mixing as well as non-adiabaticity. Mixing could potentially alter the burning composition of the flame at times when the flame is stood off from the edge of the centerbody.

5.1 Symmetric Opposed Jet Calculations

This section first describes the model details and parameters of CHEMKIN's opposed jet solver, OPPDIF. This will include a detailed list of parameter values chosen in the OPPDIF used to calculate stretched flame parameters of interest for these studies. Then, each of the flame parameters of interest are defined in reference to an OPPDIF calculation and the sensitivities of these parameters to reference location, equivalence ratio, and flame stretch, is discussed. For reference, a schematic of the opposed jet configuration is shown in Figure 5.1.

5.1.1 CHEMKIN OPPDIF Model Details

The OPPDIF model of CHEMKIN, is a reduced–order approach to simulating the behavior of flames resulting from the opposed jet configuration consisting of two concentric jets directed towards each other at some fixed distance apart as shown

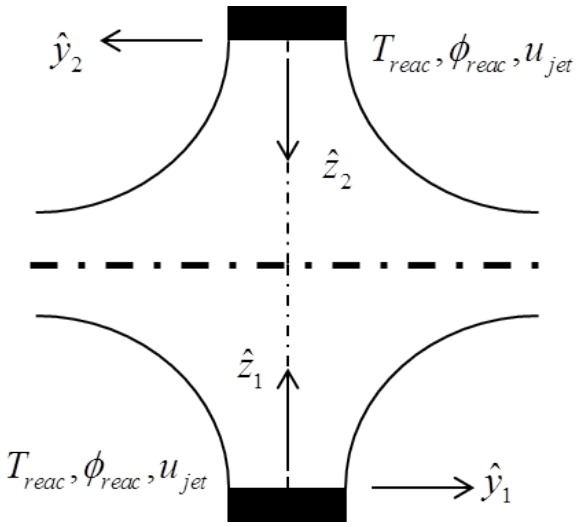

Figure 5.1: Schematic of symmetric opposed-jet extinction model using undiluted reactant properties for both streams and equal jet exit velocities.

schematically in Figure 5.1. The OPPDIF model was developed based on work completed by Kee *et al.* [60]. Through a similarity solution approach based on the work of von Karman [65], which is also documented by Schlichting [101], the governing equations derived by Kee *et al.* [60] are reduced from a multi-dimensional system to a one-dimensional system. The major assumption facilitating this simplification to a one-dimensional system is the linear dependence of velocity in the direction transverse to the jet centerline, $\hat{y}$. In effect, this model determines the jet properties in the core flow region as a function of axial distance, $\hat{z}$. Note as well, that these solutions are restricted to the core regions of the jets as edge or boundary effects are neglected.

5.1.2 CHEMKIN OPPDIF Model Parameters

The stretch sensitivities of the mixtures used in these measurements were calculated from using the opposed jet model of CHEMKIN, OPPDIF. Many of the parameter values described here were used for both the symmetric and asymmetric modeling approaches. Those OPPDIF model parameters which are different for the asymmetric model are described in a later section.

For all OPPDIF calculations, the radial, axisymmetric model (AXIS) with a domain size (XEND) of 1.4 *cm* was used. The spreading rate of the radial velocity (AINL) at both jet exits was set to zero with equal jet exit velocities at both jets. Natural gas mixtures were assumed to be pure methane and air was assumed to be comprised of oxygen and nitrogen in relative molar proportions of 21% and 79% respectively. Multicomponent thermal and species diffusion coefficients and thermally induced species diffusion, or the Soret effect (TDIF), were included in these calculations. A typical maximum number of grid points of 2000 was used for an individual OPPDIF run, with adaptive grid control based on profile curvature and gradient set to equal values of 0.1 (CURV & GRAD). When using CHEMKIN's *Flame Extinction Simulator* to capture the turning point in the flame response curve, *two-point control* was selected. Finally, GRI Mech 3.0 [107] was the chemical kinetics mechanism used.

5.1.3 Flame Parameter Definitions

Figure 5.2 displays the 1D structure of a stretched flame obtained from an opposed jet calculation. Shown are the profiles of normalized axial velocity, $\tilde{u}_z$, and normalized temperature, $\tilde{T}$, from the jet exit at $\tilde{z} = 0$ to the stagnation plane at $\tilde{z} = 1$. In this case, the flow rates are high enough such that the flame is forced to stabilize very close to the stagnation plane, as noted by the location of steep temperature rise beginning near $\tilde{z} \approx 0.9$. Note as well the non-monotonic behavior in the axial velocity profile, with an increase in axial velocity occurring near the location of steep temperature rise, demonstrating the influence of the flame on the flow field in this region, as a non-reacting flow field lacks this feature. From these calculations, the local flame speed and local stretch rate are determined. To aid in this discussion, Figure 5.3 provides a zoomed in view of Figure 5.2 with the addition of the profile of normalized CH mole fraction, $\tilde{\chi}_{CH}$. First, the displacement flame speed is defined for the opposed jet configuration in relation to the preheat zone, $S_{d,ph}$. It should be noted that this

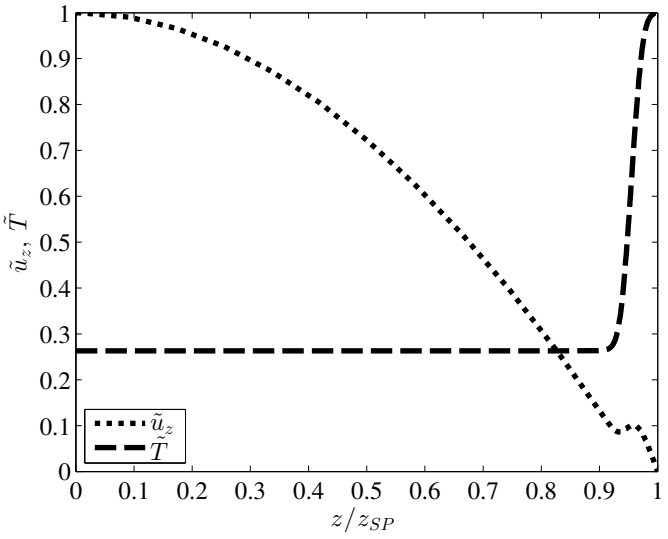

Figure 5.2: Normalized axial velocity, $\tilde{u}_z = u_z/max(u_z)$, and temperature, $\tilde{T} = T/max(T)$, profiles of an opposed jet flame obtained from OPPDIF module in CHEMKIN for a $CH_4 - air$ mixture (ϕ=1.0, T_{reac}=533 K). Profiles are shown from the jet exit, $z = 0$, to the stagnation plane, $z = z_{SP}$.

definition of flame speed is the one typically reported for these calculations and is defined by the local minimum in axial velocity between the jet exit and stagnation plane, $0 \leq \tilde{z} < 1$, when the axial velocity profile is non-monotonic. Thus for highly stretched, weakly burning flames, a displacement based flame speed may not exist based on this definition and a consumption based flame speed or some other flame metric must be used to track flame response. In this example case, $S_{d,ph}$ is marked in Figure 5.3 accordingly. Also shown in this example case is $S_{d,ch}$, which represents a displacement flame speed in reference to the location of peak CH mole fraction, $\tilde{\chi}_{CH} = 1$. This definition of flame speed was created in order to compare calculated displacement flame speeds with experimental flow velocities obtained in reference to the flame location defined by CH-PLIF flame imaging. Although in the example case shown, $S_{d,ph}$ and $S_{d,CH}$ are fairly similar, this is not always the case as is demonstrated later.

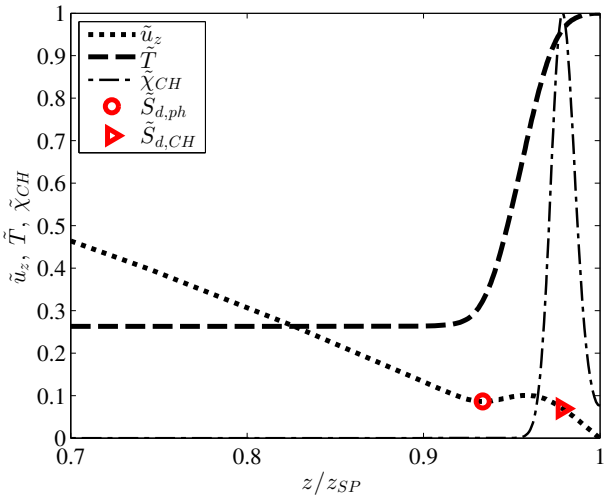

Figure 5.3: Zoomed in region of Figure 5.2 with normalized CH mole fraction added, $\tilde{\chi}_{CH} = \chi_{CH}/max(\chi_{CH})$, as well as local flame speeds defined relative to the preheat and CH-layer of the flame, $\tilde{S}_{d,ph}$ and $\tilde{S}_{d,CH}$.

Next, flame stretch is defined for the opposed jet configuration. Previously, the following expression for calculating flame stretch for the opposed jet configuration was introduced:

$$\kappa_{s,incomp} = -\frac{\partial u_z}{\partial z} \tag{5.1}$$

Note, that $\tilde{\kappa}_{s,incomp}$ assumes the flow to be incompressible and although shown throughout the computational domain, the value of interest is the local maximum on the reactant side of the flame, as shown in Figure 5.4 as $\tilde{\kappa}_s^{ph}$. Again, since the experimental calculations of flame stretch are conditioned on the CH-reaction layer, incompressible flow cannot be assumed. Using continuity, the following correction to flame stretch calculated numerically is obtained which is valid through the entire domain:

$$\kappa_s = -\frac{\partial u_z}{\partial z} - \frac{u_z}{\rho}\frac{\partial \rho}{\partial z} \tag{5.2}$$

This allows for flame stretch rates calculated using the opposed jet model and conditioned on the location of $\tilde{\chi}_{CH} = 1$, $\tilde{\kappa}_s^{CH}$, to be compared with experimentally calculated flame stretch rates conditioned on the CH-reaction layer. Note in Figure

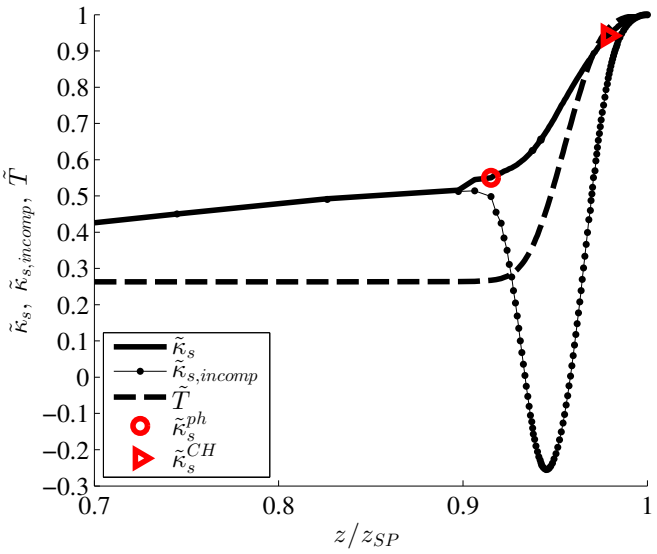

Figure 5.4: Zoomed in region of Figure 5.2 ($\tilde{u}_z$ removed) with normalized profiles of compressible and incompressible surface stretch rates shown, $\tilde{\kappa}_s = \kappa_s/\kappa_s^{max}$ and $\tilde{\kappa}_{s,incomp} = \kappa_{s,incomp}/\kappa_s^{max}$, as well as local flame stretch defined relative to the preheat and CH-layer of the flame, $\tilde{\kappa}_s^{ph}$ and $\tilde{\kappa}_s^{CH}$.

5.4, that flame stretch varies greatly within the flame. Also take note that the differences between $\tilde{\kappa_s}$ and $\tilde{\kappa}_{s,incomp}$ could potentially result in reported flame stretches of opposite signs within the flame thus demonstrating the importance of using the appropriate equation for flame stretch, and the sensitivity to the flame reference location to which the calculations are made.

With the stretched flame parameters of interest defined, the response of each of these flame parameters to stretch is discussed beginning with flame speed. Figure 5.5 plots the dependence of the displacement speed defined relative to the onset of the preheat zone, $S_{d,ph}$, and relative to the CH-reaction layer, $S_{d,CH}$ as a function of flame stretch at the preheat zone, κ_s^{ph}, for methane-air mixtures at a preheat temperature of 533K and equivalence ratios of $\phi = 0.8$ and $\phi = 1.0$. For these particular conditions, $S_{d,ph}$, increases with positive stretch, however the opposite behavior is observed for $S_{d,CH}$ which decreases with stretch such that the two flame speeds are roughly the

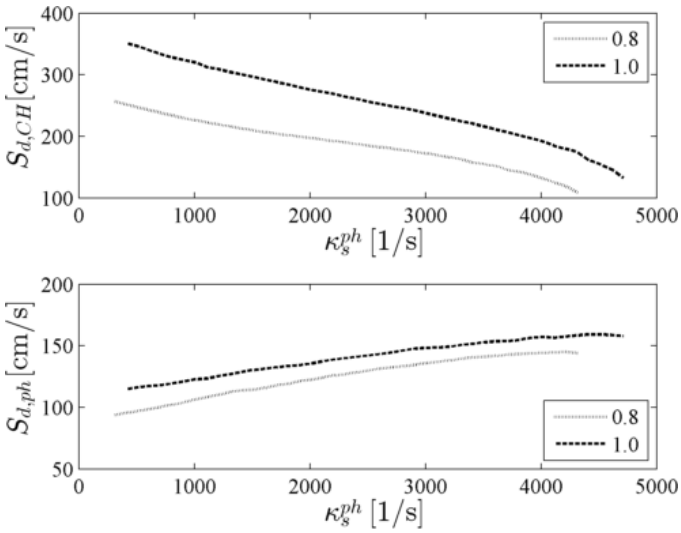

Figure 5.5: Laminar flame speed sensitivity to flame stretch for $CH_4 - air$ mixtures defined at preheat zone (bottom) and location of Y_{CH}^{max} (top) for $T_{ph} = 533K$ and ϕ=0.8 and ϕ=1.0.

same at high stretch rates, near flame extinction. At low stretch rates, these two flame speeds are much different as a result of gas expansion within the flame causing $S_{d,CH} > S_{d,ph}$. Clearly, the difference between $S_{d,ph}$ and $S_{d,CH}$ is highly dependent upon stretch and whether the flame burning is enhanced or degraded by stretch. Lastly, the terminating point in flame response marks the extinction of the flame at the extinction stretch rate, κ_{ext}.

While it is clear from Figure 5.4 that the value of flame stretch is dependent upon the reference location chosen, and surely this difference changes throughout the range of stretched flames, it is the value of κ_{ext} that is relevant to these studies. Figure 5.6 plots calculated extinction stretch rates of methane-air blends as a function of equivalence ratio for a given pressure and preheat temperature showing κ_{ext} values of $10^3 - 10^4\ s^{-1}$, depending on the reference location chosen. κ_{ext} at the preheat zone, κ_{ext}^{ph}, is consistently lower than the value at $max(\chi_{CH})$, κ_{ext}^{CH}. This is due to the induced strain caused by gas expansion within the flame, or the $-u_z/\rho \times \partial\rho/\partial z$ term in equation 5.2. Again, because the experimental measurements were conditioned

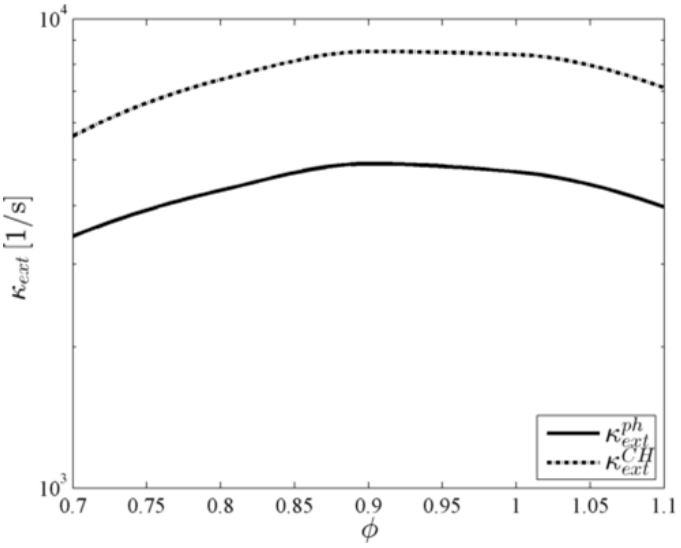

Figure 5.6: Calculated dependence of κ_{ext}^{ph} (solid line) and κ_{ext}^{CH} (dashed line) upon ϕ for $CH_4 - air$ mixtures with a preheat temperature of 533K.

upon the CH-reaction layer of the flame, flame stretch measurements are compared to κ_{ext}^{CH} and not κ_{ext}^{ph}.

5.2 Modeling Recirculation Zone Physics

Recalling from the earlier discussion on recirculation zone physics presented in Figure 2.9, there are multiple pathways through which the flame burning properties can be modified. Two pathways which are investigated are non-adiabatic effects and reactant dilution. Extinction limits and extinction behavior are evaluated for varying degrees of heat losses and reactant dilution using the opposed jet model. The opposed jet, counterflow model can be adapted to study the additional physics identified in Section 2.2.2. Modifications to the counterflow model are proposed below, that enable the study of the effect of non-adiabatic conditions, causing lower recirculation zone temperatures, on flame stability. A second model is proposed to study the effect of reactant dilution, occurring as a result of mixing with the recirculation zone upstream of the flame attachment point. The goal of these approaches is to be able to understand the sensitivity of flame stability to these physical pathways, by quantifying the

extinction limit of these flames subject to varying degrees of heat loss and reactant dilution.

5.2.1 Modifications to CHEMKIN Parameters

There were slight modifications to the CHEMKIN OPPDIF model parameters from those outlined in Section 5.1.2. These modifications are required in order to perform the proposed *Non-Adiabatic* and *Attachment Point Mixing* studies described in the following sub-sections. For these calculations, the density of the two opposing jets are no longer equal. This is due to differences in the temperature and composition at the exit of the two opposing jets. In order to perform opposed jet calculations which maintain the stagnation plane near the center of the domain, such that the flame is likely to remain near the center of the flame, the mass flux of each jet was set to have equal momentum fluxes:

$$\rho_{reac}\ u_{jet,reac}^2 = \rho_{RZ}\ u_{jet,RZ}^2 \tag{5.3}$$

5.2.2 Non-Adiabatic Effects

In addition to the role that strain plays in affecting the burning characteristics of the flame by contributing to flame stretch, shear layer flames which are supported by recirculation zones are subject to additional factors. It is widely accepted that the regions of recirculation aid in flame stabilization by transporting hot products back to the location of flame attachment. Previous computational and experimental studies have emulated the back-heating effect of recirculation zones through the study of asymmetric opposed jet flames [78, 33]. This opposed jet configuration directs a jet of premixed methane-air against a jet of hot products as shown in Figure 5.7. In this configuration, the hot products jet is representative of the recirculation zone composition and temperature as determined from adiabatic equilibrium calculations. By varying the temperature of the product side jet, the effect of combustor heat loss can be simulated. Lower product jet temperatures represent conditions of greater heat

Table 5.1: Non-adiabatic opposed jet test cases

T_{reac}	ϕ	T_{RZ}/T_{ext}^{ad}
533K	0.7 to 1.1	0.8, 1.0, & 1.05

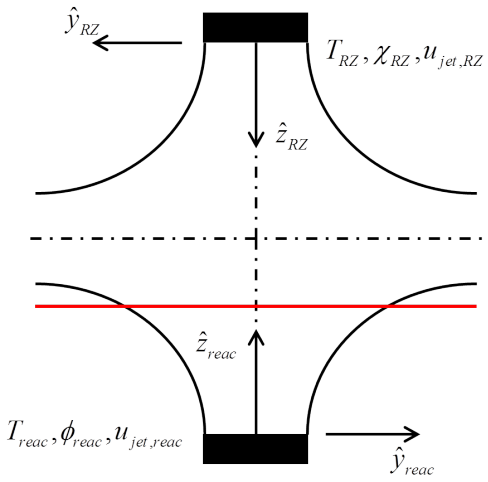

(a) Opposed jet, non-adiabatic configuration

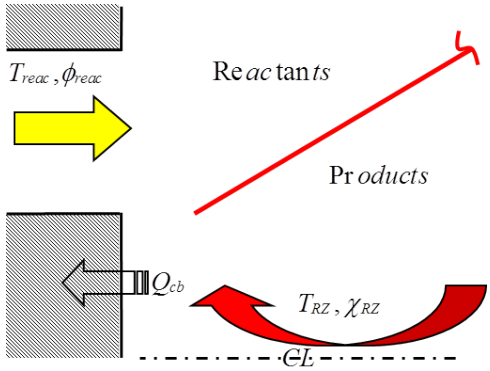

(b) Non-adiabatic, recirculation zone physics

Figure 5.7: Non-adiabatic asymmetric opposed-jet extinction model (*left*), and corresponding physical pathways in experimental combustor(*right*).

loss, which will potentially decrease the reactivity of the flame. These calculations are be performed holding T_{RZ} at fixed value for a given test run. Values of T_{RZ} are defined at varying degrees of heat loss specified relative to the extinction temperature for an adiabatic, symmetric flame stretch calculation (T_{RZ}/T_{ext}^{ad}). Table 5.1 outlines the test cases for this study of non-adiabatic effects using the asymmetric opposed jet configuration.

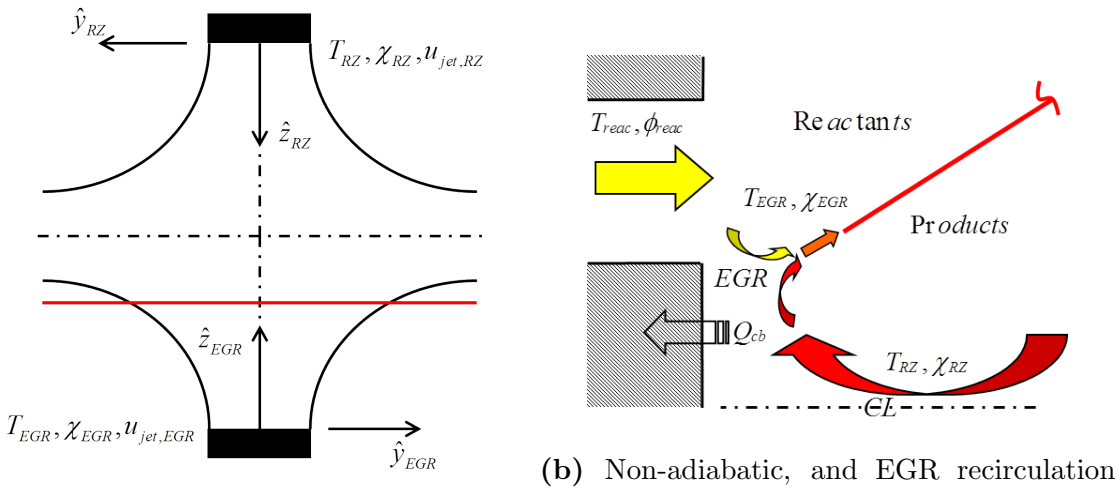

(a) Non-Adiabatic and EGR mixing, opposed jet model

(b) Non-adiabatic, and EGR recirculation zone physics

Figure 5.8: Non-adiabatic, and EGR mixing, asymmetric opposed-jet extinction model (*left*), and corresponding physical pathways in experimental combustor(*right*).

5.2.3 Attachment Point Mixing

Another factor of interest near the attachment point is mixing between the reactant stream and the product stream. During points of flame detachment from the bulk-head, there is the opportunity for the reactant stream to mix with the recirculating products thereby changing the characteristics of the reactant stream upstream of the flame front. The reactant stream is altered by products mixing with it, raising its temperature and introducing product species into it. Thus the reactant stream is altered from its freestream properties, T_{reac} and ϕ_{reac}. A schematic of opposed jet model and the corresponding physics modeled by this approach is shown in Figure 5.8a. In addition to mixing of the reactant stream, non-adiabatic effects are included in this study for a fixed value of $T_{RZ}/T_{ext}^{ad} = 0.8$. In this manner, flame stability is a competition between the increase in the reactant stream temperature and the dilution of the reactant concentrations as a result of product/reactant mixing subject to non-adiabatic conditions. These studies are performed for various degrees of EGR

Table 5.2: Non-adiabatic, EGR, opposed jet test cases

T_{reac}	T_{RZ}/T_{ext}^{ad}	ϕ	Y_{EGR}
533K	0.8	0.7 to 1.1	0 to 0.3

as defined by the mass fraction of products mixed with the reactants, Y_{EGR}:

$$Y_{EGR} = \frac{m_{RZ}}{m_{reac} + m_{RZ}} \tag{5.4}$$

The complete test space that was explored for these studies is shown in Table 5.2.

CHAPTER VI

RESULTS: EXPERIMENTS

The purpose of the experimental studies was to characterize the flow field and flame behavior near the attachment point for a swirl–stabilized combustor elucidating the physics governing flame stabilization. This chapter outlines the approach taken to characterize the flame and flow field experimentally. It provides details on the experimental techniques chosen. Then, the details of the quantities and parameters to be calculated relative to the flame location and specifically to the edge of the flame are provided. In addition, the approach to characterize the mixing between the incoming reactant stream and recirculation zone is described. These experiments and calculations were carried out at several sets of conditions outlined in Table 6.1. The space outlined explores the sensitivity of the mean flame stretch characteristics to flow field changes by altering flow velocity, and to reactivity changes, through equivalence ratio variations.

The goal of this work was to better understand the stabilization of flames in swirl stabilized shear layers. To achieve this, experimental studies were performed on a swirl stabilized combustor to both quantitatively and qualitatively describe the attachment point behavior of shear layer stabilized flames. The analysis of these experimental data sets comprise the main effort of this work. Extinction stretch rates

Table 6.1: Operational space of experiments

Equivalence Ratios	*Premixer Velocity [m/s]*
{0.7,0.8,0.9,1.0,1.1}	{35, 70}

calculated using the symmetric opposed jet model are compared to the experimentally determined flame stretch rates. The details of the experimental tasks are outlined below in the following sections.

6.1 Shear Layer Characteristics

In this section, we present the measurements of the flow and strain fields obtained from 2D-PIV measurements. We also examine the behavior of the dominant strain terms expected in the shear layer. Lastly, the turbulence of the flow field is characterized and the unsteadiness of the strain field is discussed.

6.1.1 Flow and Strain Field

We begin by discussing the mean flow conditions as captured by the PIV measurements obtained as shown in Figure 6.1. The mean axial velocity field, $\bar{u}_z$, is shown on the left and the mean transverse velocity field, $\bar{u}_r$, is shown on the right. Bulk flow is from left to right in both images and roughly centered about the separating shear layer, most notable from the structure of the $\bar{u}_z$ field, with the jet region above and wake region located below. There is a distinct structure of the $\bar{u}_r$ field within the shear layer, located roughly between $-0.5mm < r < 2mm$ over the range of axial distances in the field of view. Note the demarcation in the direction of $\bar{u}_r$ occurring in the upper half of the shear layer with negative values in the lower section of the shear layer.

Strong strain rates are expected within the shear layer and upon inspection of the $\bar{u}_z$ field, the strain field is expected to be dominated by shear strain from $\frac{\partial u_z}{\partial r}$. Noting the spreading of the axial velocity contours with axial distance, and the large expansion in cross-sectional area at the dump plane exit, significant normal strain is expected as well, $\frac{\partial u_z}{\partial z}$, but at a much smaller magnitude. Figure 6.2 plots the time averaged strain fields of $\overline{\frac{\partial u_z}{\partial r}}$ on the left, and $\overline{\frac{\partial u_z}{\partial z}}$ on the right. The peak values of mean shear strain are much larger than the peak normal strain values within the

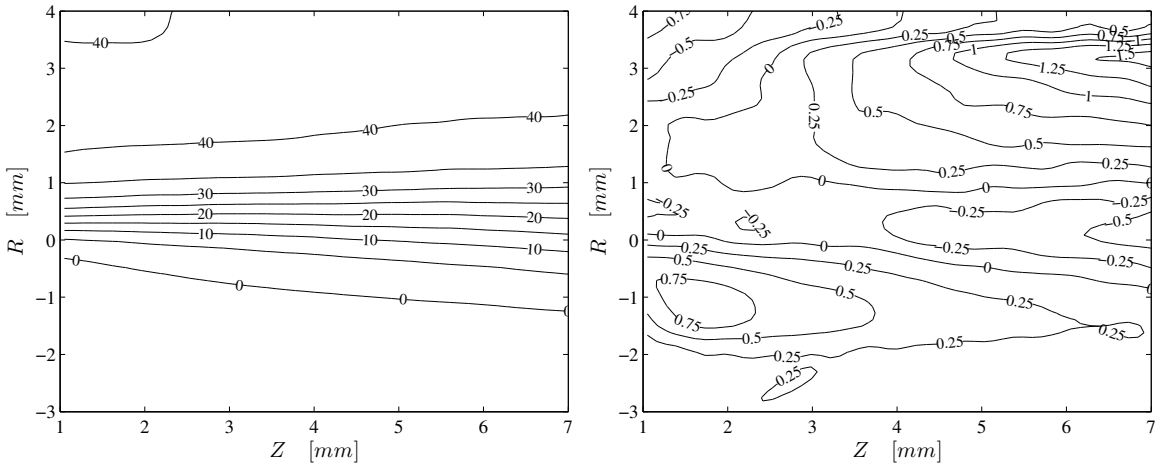

(a) $\bar{u}_z$ [m/s] **(b)** $\bar{u}_r$ [m/s]

Figure 6.1: Mean axial velocity field, $\bar{u}_z$ (left), and mean transverse velocity field, $\bar{u}_r$ (right), for $\phi = 1.0$, $u_{pm} = 35\ m/s$ test case.

shear layer and on average are positive throughout the shear layer. Like the mean transverse velocity field, $\bar{u}_r$, there is a demarcation in the sign of normal strain from $\overline{\frac{\partial u_z}{\partial z}}$ within the shear layer with positive values in the lower half and negative in the upper half of the shear layer.

6.1.2 Turbulence

Turbulence within the shear layer will result in time fluctuations in the local velocity conditions along the flame front, and if the fluctuations are large enough, $u' > S_d$, they will also displace the flame front causing flame wrinkling. Velocity fluctuations will also introduce strain field fluctuations as well. Figure 6.3 shows that the fluctuations in velocity are largest within the region of the flow field where the shear layer exists. Peak RMS velocities compared to the laminar flame speed of a stoichiometric methane-air flame at a $T_{ph} = 533K$ are $\frac{u_{z,rms}}{S_d} \approx 5$ and $\frac{u_{r,rms}}{S_d} \approx 2$. Thus, given the flame orientation within this flowfield, displacement of the leading edge of the flame and flame wrinkling within the shear layer is expected, and observed, for these test cases.

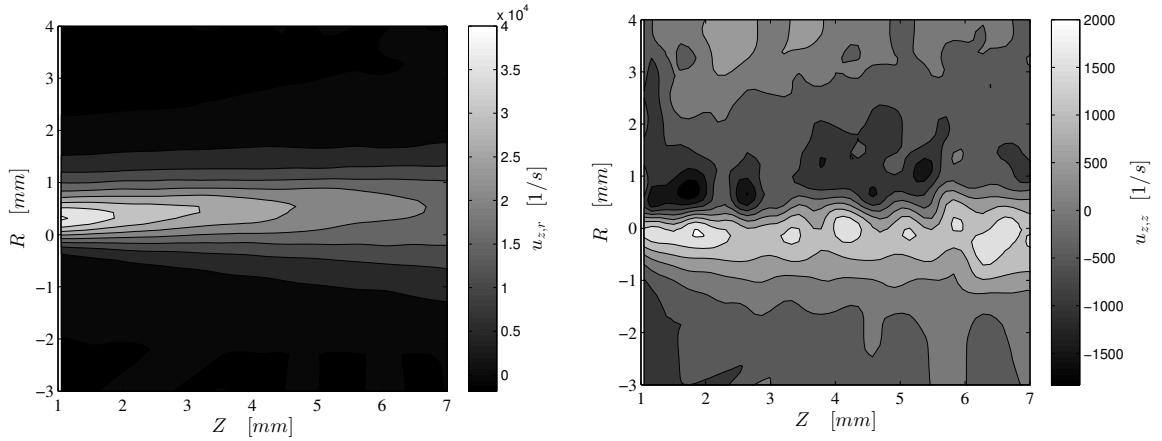

(a) $\overline{\frac{\partial u_z}{\partial r}}$ [1/s] **(b)** $\overline{\frac{\partial u_z}{\partial z}}$ [1/s]

Figure 6.2: Mean shear strain field, $\overline{\frac{\partial u_z}{\partial r}}$ (left), and mean normal strain field, $\overline{\frac{\partial u_z}{\partial z}}$ (right), for $\phi = 1.0$, $u_{pm} = 35\ m/s$ test case.

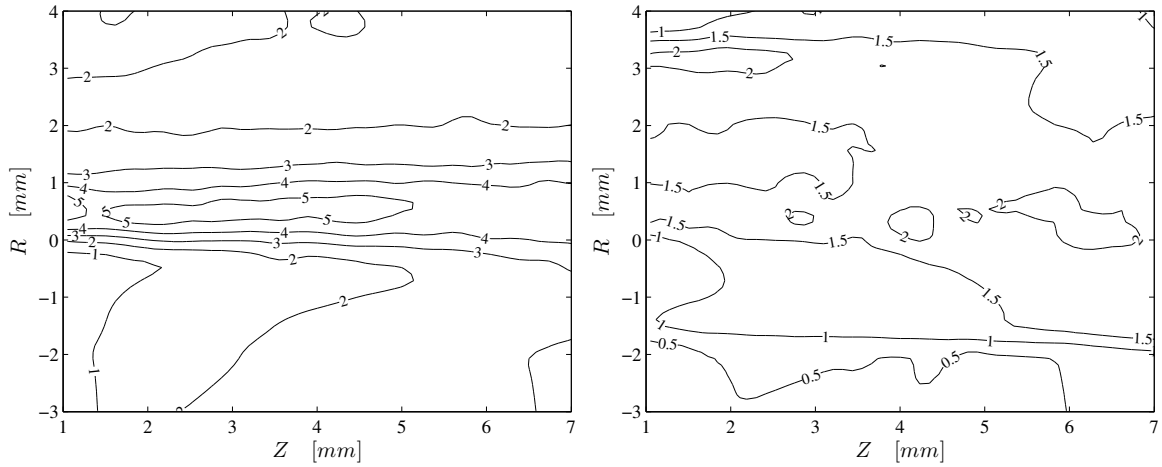

(a) $u_{z,rms}$ [m/s] **(b)** $u_{r,rms}$ [m/s]

Figure 6.3: RMS axial velocity field, $u_{z,rms}$ (left), and RMS transverse velocity field, $u_{r,rms}$ (right), for $\phi = 1.0$, $u_{pm} = 35\ m/s$ test case.

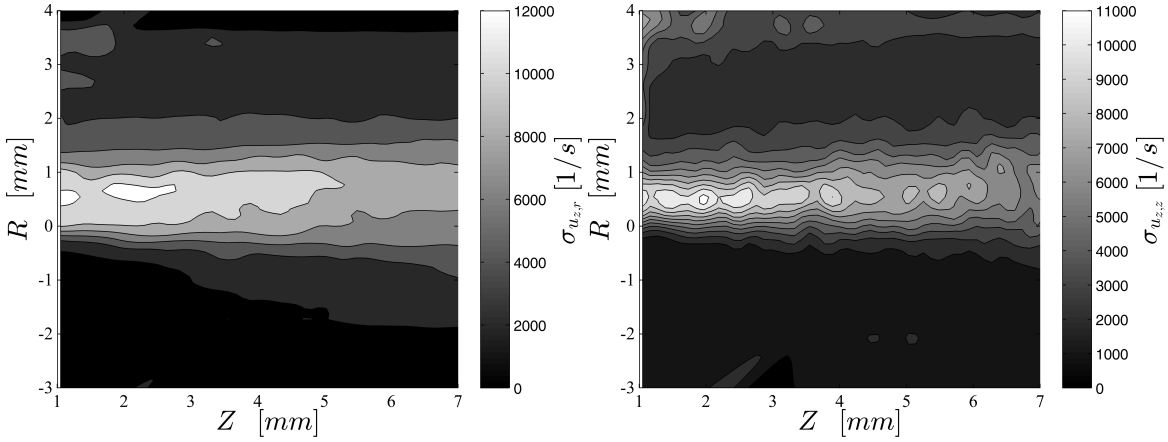

(a) $\sigma_{u_{z,r}}$ [1/s] **(b)** $\sigma_{u_{z,z}}$ [1/s]

Figure 6.4: Standard deviation of fluid strain components $\partial u_z/\partial r$, $\sigma_{u_{z,r}}$ (left), and $\partial u_z/\partial z$, $\sigma_{u_{z,z}}$ (right), for $\phi = 1.0$, $u_{pm} = 35\ m/s$ test case.

Although for average quantities within the shear layer region of the flow field, $\overline{\frac{\partial u_z}{\partial z}}$ is much less than $\overline{\frac{\partial u_z}{\partial r}}$, the maximum magnitude of the standard deviation of these strain terms are the same order of magnitude, $\approx 10^4$, as shown in Figure 6.4. Thus, although $\overline{\frac{\partial u_z}{\partial r}} >> \overline{\frac{\partial u_z}{\partial z}}$, the variations in both strain terms are large enough that either term could be locally dominant.

6.2 Flame Measurements

In this section, we present a summary of the CH-PLIF data obtained and discuss notable characteristics of the CH-reaction layer. We present the metrics that we can track from the CH-PLIF images including location of the CH-reaction layer, orientation of the reaction layer, and from these metrics we can track the location of the leading edge of the reaction layer. These metrics of the flame location are defined relative to the centerpoints of the CH-layer as determined by a local minimum search algorithm of the magnitude of the gradient of the intensity field. This is done only after first performing a background subtraction and then median filtering the raw CH-PLIF intensity images. In addition, the stretch and velocity conditions in reference

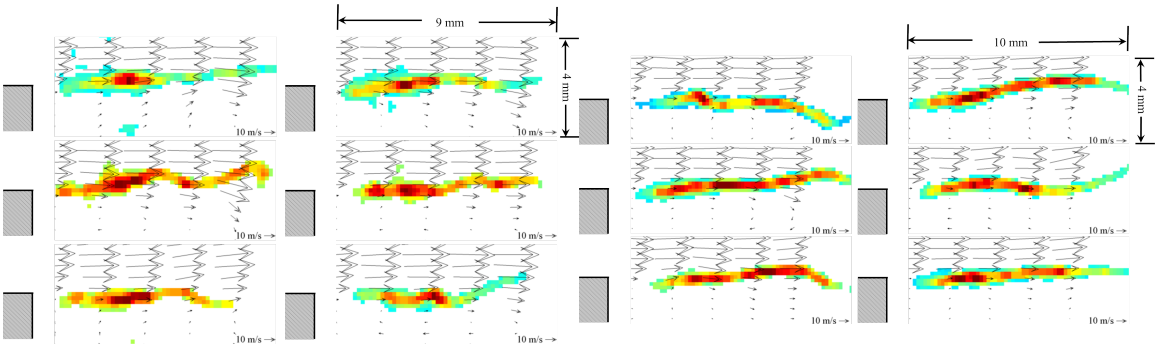

(a) $\phi = 0.8$ **(b)** $\phi = 1.0$

Figure 6.5: Sample instantaneous images of CH-PLIF and velocity vectors for $\phi =$ 1.0, 6.5b, and $\phi = 0.8$, 6.5a ($u_{pm} = 35 m/s$)

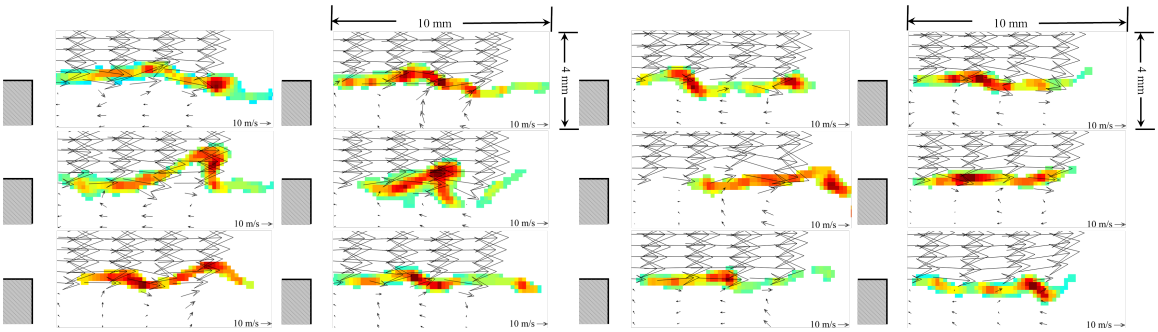

(a) $\phi = 0.8$ **(b)** $\phi = 1.0$

Figure 6.6: Sample instantaneous images of CH-PLIF and velocity vectors for $\phi =$ 0.8, 6.6a, and $\phi = 1.0$, 6.6b ($u_{pm} = 70 m/s$)

to the CH-reaction layer are discussed. As a demonstration of the simultaneous PIV and CH-PLIF data obtained in order to extract these quantities, a series of example CH-PLIF intensity images are shown in Figure 6.5 with down-sampled field of instantaneous PIV vectors overlaid.

6.2.1 CH-Layer Characteristics

First, the nature of the CH-Layer as observed from CH-PLIF images is discussed. Typical signal to noise levels of the CH-PLIF images are 7 to 1 and 3 to 1 for the $\phi = 1.0$ (Figure 6.5b) and $\phi = 0.8$ (Figure 6.5a) mixtures, respectively, with minimum

signal to noise ratios on the order of 4 to 1 and 2 to 1 respectively. An additional data set was taken at $\phi = 0.7$ but the low signal to noise made it difficult to track the CH-layer. These trends were expected based on the results discussed later in Figure 6.13, showing decreasing peak mass fractions of CH away from stoichiometric conditions.

Several observations follow from these images. First, the leading edge of the CH-layer lies within $1-3\ mm$ of the corner of the centerbody and its transverse coordinate does not vary significantly for either velocity condition. For reference, a characteristic axial diffusive length scale is $l_D = D_T/u_{ref}$, where D_T denotes the thermal diffusivity and u_{ref} denotes a reference axial velocity. Assuming a D_T of $2.76 \times 10^{-4}\ m^2/s$ based on the average of reactant temperature and flame temperature of 2340 K, and u_{ref} ranging from $5 - 10\ m/s$, based on typical tangential flame edge velocities for test cases with bulk flow velocity of $u_{pm} = 35\ m/s$ (measured edge velocities discussed in Section 6.2.3.2), results in values of l_D ranging from 0.02-0.05 mm. With standoff distances ranging from 1-3 mm, this suggests that the leading edge of the flame is not quenched by heat losses to flow boundaries. Note that the reference velocity values chosen from the $u_{pm} = 35\ m/s$ case are conservative in their estimate of l_D as reference edge velocities for the $u_{pm} = 70\ m/s$ are much higher ranging from $20 - 45\ m/s$.

The degree of flame wrinkling and transverse flapping grows monotonically with downstream distance, as would be expected, but the flame is still quite laminar in appearance. In the $\phi = 0.8$ case, the flame is clearly being rolled up over length scales of 1-2 mm, presumably due to the shear layer structures. The $\approx 30\%$ higher flame speed in the $\phi = 1.0$ case is presumably the reason that less significant roll-up of the flame occurs for the higher fuel-air ratio. These observations are further confirmed from overlays of the instantaneous center points of the CH-layer as shown in Figure 6.7a for the 35 m/s test case. The CH-brush thickness clearly grows as a

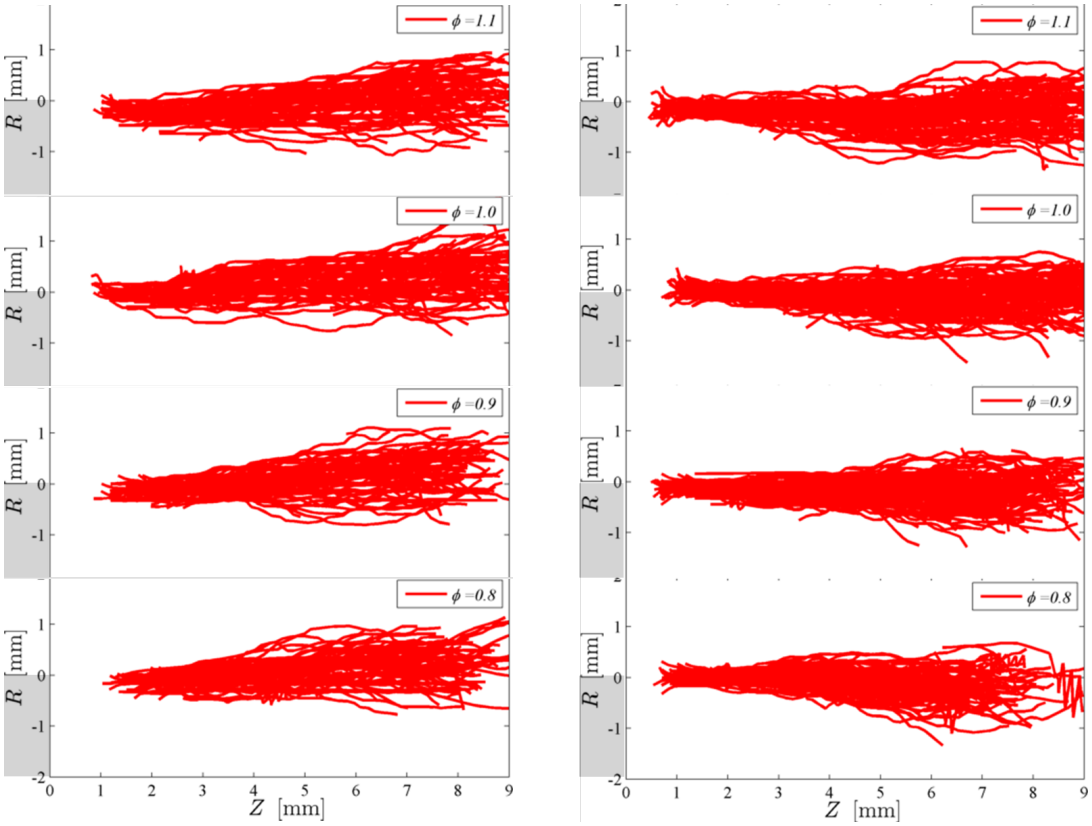

(a) $u_{pm} = 35m/s$ **(b)** $u_{pm} = 70m/s$

Figure 6.7: CH-layer centerline flame brush images as a function of $\phi = 0.8 - 1.1$ for $u_{pm} = 35m/s$ (left) and $u_{pm} = 70m/s$ (right). Centerbody location shown as gray box with bulk flow going from left to right.

function of downstream distance and extends into the jet side of the shear layer with many instances downstream where the radial flame location, r_f, is greater than zero. While these characteristics in flame brush are similar for all 35 m/s test cases with varying equivalence ratio, there is a distinct change in the flame brush behavior for the 70 m/s case, shown in Figure 6.7b. First of all, there are fewer instances where $r_f > 0$ resulting in a downward shift in the flame brush. Second, this shift seems to result in flames that are horizontal or more aligned with the bulk flow direction.

The observations on the effect of flow velocity on flame position and orientation are confirmed by analysis of the mean flame location and orientation. Figure 6.8 shows the mean radial flame location as a function of downstream distance for the 35 m/s and 70 m/s test cases. The tendency of the flame to extend into the reactant jet is clearly observed for the low velocity test case (Figure 6.8a) whereas for the high velocity case, the mean radial flame location turns down towards the recirculation zone (Figure 6.8b). Thus, as one would expect, premixer velocity has a major effect on the ability of the flame to propagate into the reactant stream. Assuming a fixed flame location, fixed flame speed, and a kinematic balance argument, higher flow velocities would result in shallower flame angles. While the orientation of the mean flame position would suggest a difference in flame angles between the two cases, a more thorough analysis based on the instantaneous orientation of the flame is presented.

The orientation of the flame is characterized, where a positive flame angle , θ_f, is defined as into the reactant side of the shear layer and negative into the product side, as illustrated in Figure 6.12b. The mean flame angle was determined by calculating instantaneous realizations of the flame angle along the entire length of the flame, binning the data by axial location, and time averaging the data for $1mm$ axial bins. The axial profiles of mean flame angle are quite similar for the $35m/s$ test cases as shown in Figure 6.9a. $\bar{\theta}_f(Z)$ is not a strong function of equivalence ratio and is always positive; i.e., into the reactant stream. Again, the adverse effect of increasing

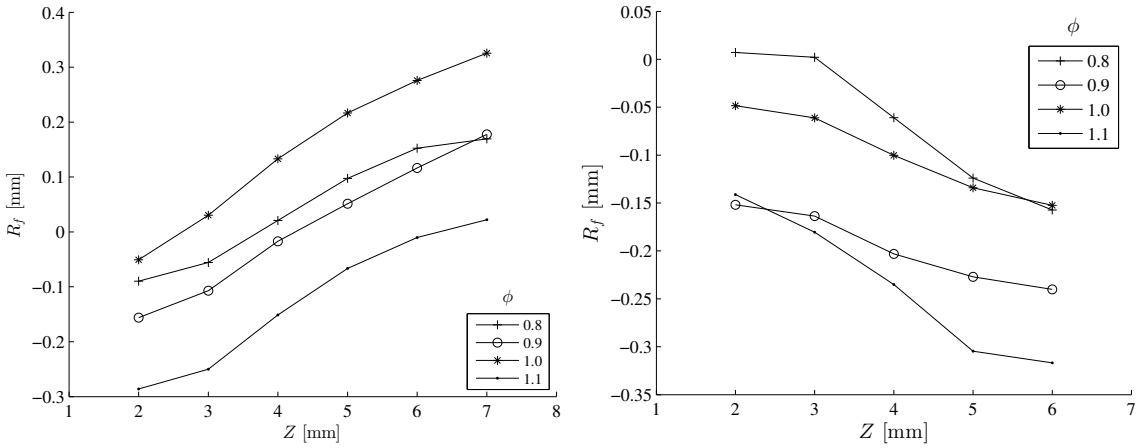

(a) $u_{pm} = 35m/s$ **(b)** $u_{pm} = 70m/s$

Figure 6.8: Mean flame radial location, $\bar{R}_f$, as a function of axial location, Z, using $1mm$ axial bins shown for $\phi = 0.8 - 1.1$ at $u_{pm} = 35m/s$ (left) and $u_{pm} = 70m/s$ (right).

premixer velocity on flame stability is observed in Figure 6.9b. This effect is so drastic for the $u_{pm} = 70m/s$ test case that the mean flame angle is non-positive for all axial locations.

6.2.2 Flame Stretch and Velocity Along CH-Layer

In this section we present the measured stretch rates as well as the velocity conditions along the CH-reaction layer centerline. Both of these parameters are interpreted in terms of their implications on flame stability. The former being related to stretch induced flame blowoff and the latter related to the kinematic stability of the flame. In addition, the sensitivity of these parameters to operational conditions are discussed.

6.2.2.1 Flame Stretch

From the PIV and CH-PLIF measurements, characteristics of the flow field relative to the flame location were feasible (Figures 6.5 and 6.6). In order to resolve the shear layer, a fine spatial resolution was required, which was achieved by zooming into a small region of interest in the combustor where the attachment point is likely

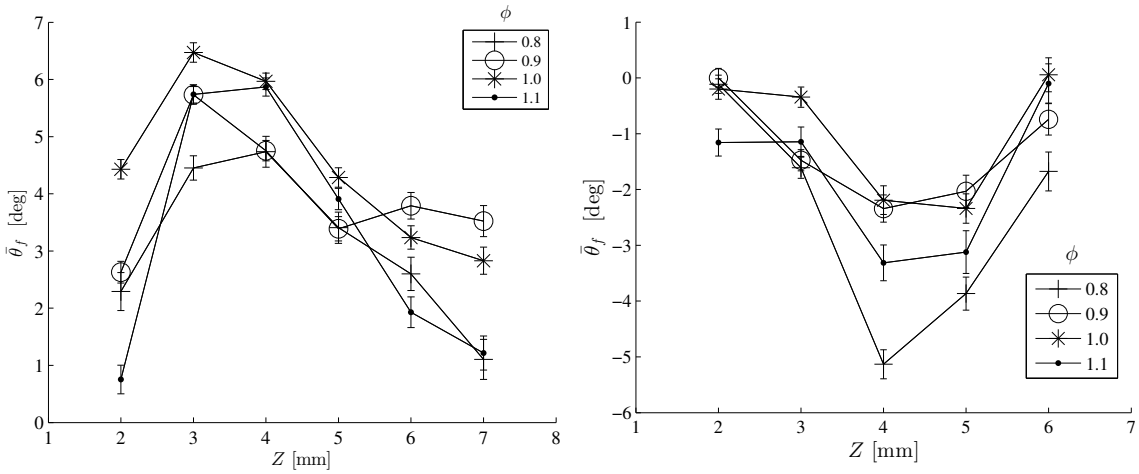

(a) $u_{pm}=35m/s$ **(b)** $u_{pm}=70m/s$

Figure 6.9: Mean flame angle, $\bar{\theta}_f$, as a function of axial location, Z, using $1mm$ axial bins shown for $\phi=0.8-1.1$ at $u_{pm}=35m/s$ (left) and $u_{pm}=70m/s$ (right).with error bars in the mean value shown for one standard deviation.

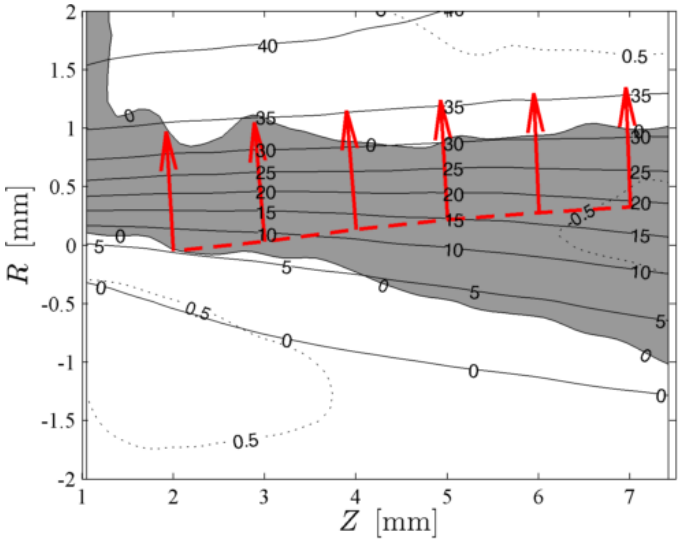

Figure 6.10: Mean flame position (dashed red line) and flame normal (red arrows) overlaid on top of $\bar{u}_z$ contours (solid lines) and $\bar{u}_r$ contours (dashed lines) with regions of $\bar{u}_r>0$ and $\bar{u}_r\leq 0$ shown in white and gray respectively ($\phi=1.0$, $u_{pm}=35\ m/s$).

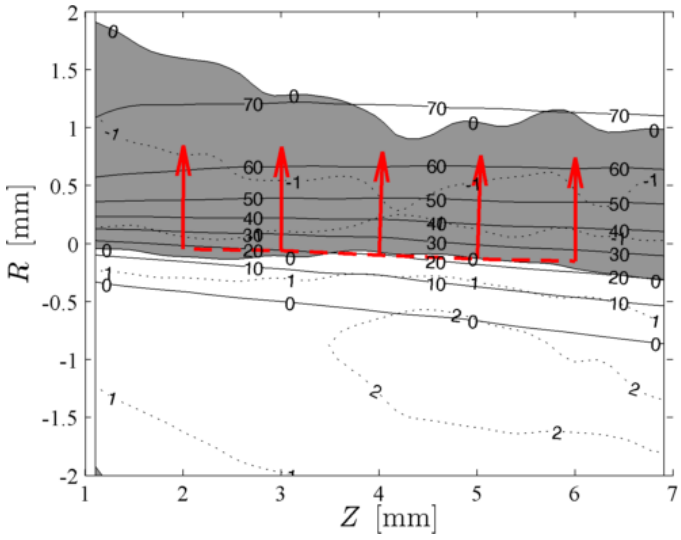

Figure 6.11: Mean flame position (dashed red line) and flame normal (red arrows) overlaid on top of $\bar{u}_z$ contours (solid lines) and $\bar{u}_r$ contours (dashed lines) with regions of $\bar{u}_r > 0$ and $\bar{u}_r \leq 0$ shown in white and gray respectively ($\phi = 1.0$, $u_{pm} = 70\ m/s$).

to be (Figure 6.12a). From the CH-PLIF images, the flame position was defined by the isoline of local peaks of CH-PLIF image intensity in the region of signal (See Figure 6.28). This provides both a well defined location within the flame to perform calculations in reference to as well as a means of determining the local orientation of the flame, $\vec{n}_f$. Given the velocity field, flame position, and flame orientation, the flame stretch along the flame can be quantified using Eq.2.5 in reference to the flame reaction layer. This is carried out at every instant in time, enabling for the reaction layer conditioned stretch characteristics of the flame in the near field region to be captured. From this data, various flame stretch rate statistics are determined. Namely, mean stretch rates are reported with estimates in the error in the reported mean.

Periagaram [86] demonstrated the feasibility of performing CH-PLIF on stretched flames using broad frequency excitation. A pivotal requirement for CH-PLIF to be a relevant diagnostic technique of stretched methane-air flames, is the presence of CH radicals within the flame throughout stretch space. The opposed jet model was used

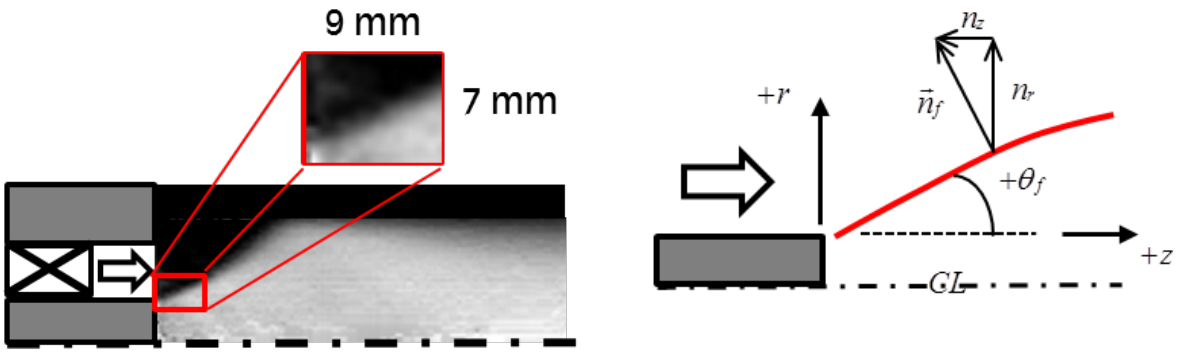

(a) Measurements' Field of View **(b)** Flame Coordinate System

Figure 6.12: Time averaged chemiluminescence image of inner shear layer stabilized flame with interrogation region for stretch measurements shown in red (left) and corresponding coordinate system, flame angle, and flame normal definitions (right).

in calculations of the peak CH value, Y_{CH}^{max}, as a function of flame stretch, the results of which are shown in Figure 6.13. Two points immediately follow. First, Y_{CH}^{max}, varies only slightly with stretch rate until extinction suggesting that the edge of the measured CH layer coincides with the edge of the flame itself (i.e., an exothermic flame is not existing upstream of the CH layer). For this reason, we will refer to the upstream edge of the measured CH profiles as the flame edge. Second, CH levels are an exponential function of fuel/air ratio. This is the reason why these measurements were performed at relatively high fuel/air ratios, $0.8 < \phi < 1.1$. For reference, the approximate blowoff condition of the inner shear layer stabilized flame is somewhere below $\phi < 0.7$ (its confined value is equal to ≈ 0.50, but this was not measured for the unconfined case).

At each instance in time, the instantaneous stretch rate is calculated along the CH-layer centerline as shown in Figure 6.14 for the $\phi = 0.9$, $u_{pm} = 35\ m/s$ test case. The net flame stretch is shown as well as the sources of flame stretch by each strain term. As is evident in the plot of instantaneous flame stretch, there are large variations in both the total flame stretch along the reaction layer as well as the dominant sources

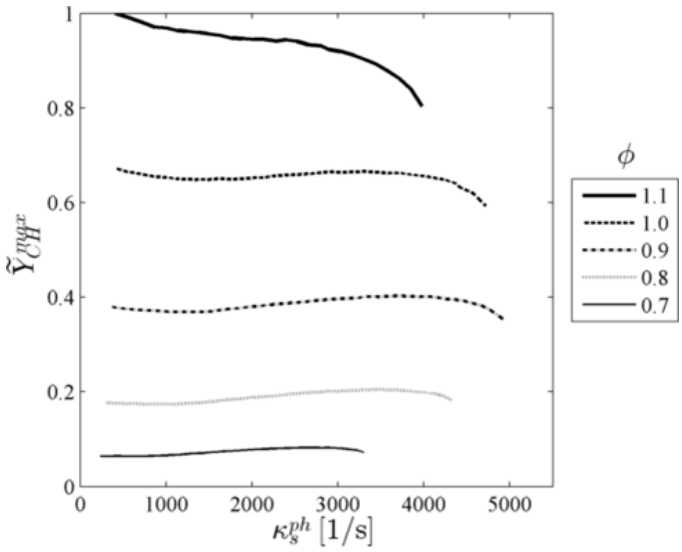

Figure 6.13: Maximum CH mass fraction, with all cases normalized by maximum of $Y_{CH}^{max}\left(\kappa_s^{ph}\right)$ for $\phi = 1.1$, as a function of stretch at atmospheric conditions and a preheat temperature of 533K.

of flame stretch. Large temporal and spatial fluctuations in the fluid strain rate are not unexpected for a turbulent shear layer like the one in this study and have been observed in other studies measuring the stretch rate along the CH-layer in a turbulent flow field [41]. We have chosen to characterize the response of the flame to changes in equivalence ratio by the mean stretch rate observed at the CH-layer (i..e, not at a fixed spatial location, but conditioned on the flame) as a function of axial location. A change in the mean value would signify a shift in the distribution of the stretch rates. We utilize a spatial moving average to compute time averaged stretch rates over axial lengths of 1 mm, equivalent to six interrogation volumes.

First, the time averaged distribution of stretch is plotted in Figure 6.15a for the $u_{pm} = 35\ m/s$ and $\phi = 0.9$ test case. It shows, as expected, that the mean stretch is dominated by contributions from a normal and a shear strain term: $\partial u_z/\partial z$ and $\partial u_z/\partial r$ respectively. Note that these terms are indicated as $u_{z,z}$ and $u_{z,r}$ in Figure

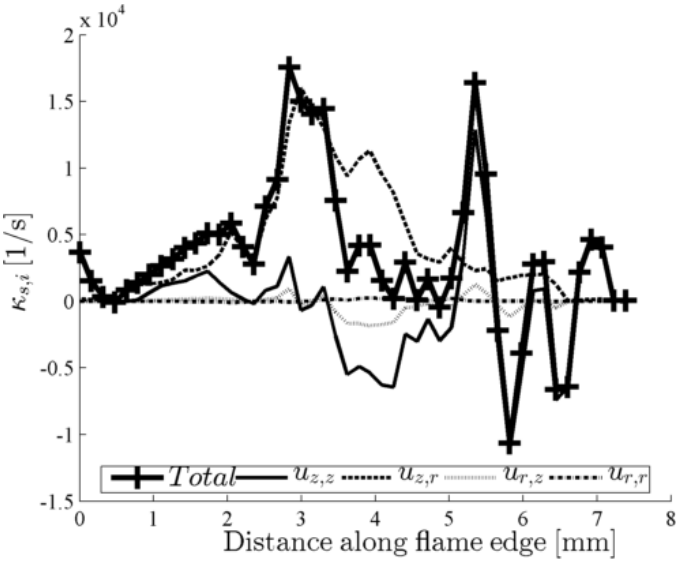

Figure 6.14: Instantaneous flame stretch profile along CH-layer centerline as a function of flame arc length by source (ϕ=0.9, u_{pm}=35m/s).

6.15a, respectively. In addition, contributions from both terms are positive throughout the entire domain. These observations are typical for all of the $u_{pm} = 35\ m/s$ test cases. However, while the dominant strain sources are the same for the higher velocity test cases, $u_{pm} = 70\ m/s$, mean contributions from $u_{z,r}$ are negative as shown in Figure 6.15b. This point is discussed later as we further analyze and compare results between the two velocity conditions.

From these observations, we can simplify the expression for stretch, leaving these two dominant sources:

$$\kappa_s \approx \frac{\partial u_z}{\partial z} + \theta_f \frac{\partial u_z}{\partial r} \tag{6.1}$$

These terms are uncorrelated as evident in the joint PDF of the contributions of $u_{z,r}$ and $u_{z,z}$ to flame stretch, Figure 6.16, where $\kappa_s\left(u_{z,r}\right) \approx \theta_f \partial u_z/\partial r$ and $\kappa_s\left(u_{z,z}\right) \approx \partial u_z/\partial z$.

Given this simplified expression for flame stretch in equation 6.1, and the structure of the strain fields, the trends in flame stretch can be explained. The mean spatial distribution of the shearing and normal strain terms, $\partial u_z/\partial r$ and $\partial u_z/\partial z$, are plotted

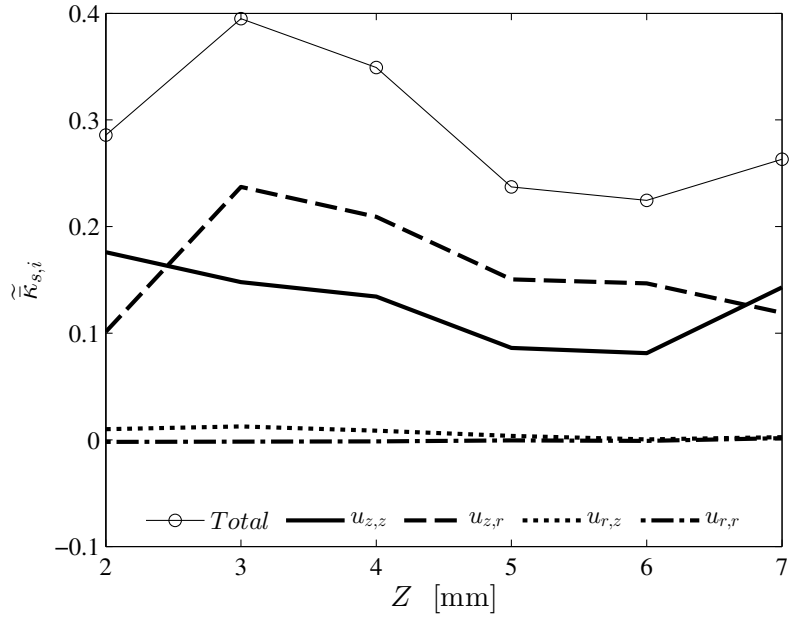

(a) u_{pm}=35m/s

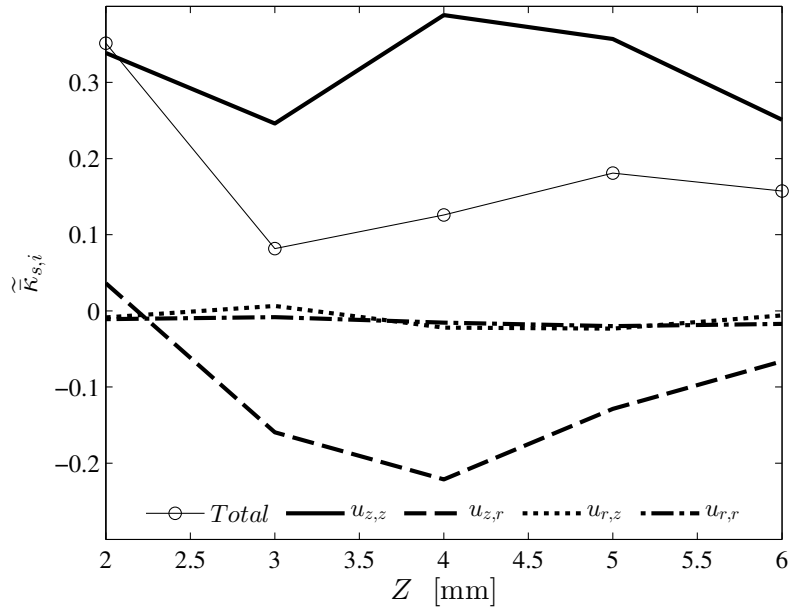

(b) u_{pm}=70m/s

Figure 6.15: Mean flame stretch axial dependence by source, normalized by the extinction stretch rate, for a ϕ=0.9 and u_{pm} of 35m/s (top) and 70m/s (bottom).

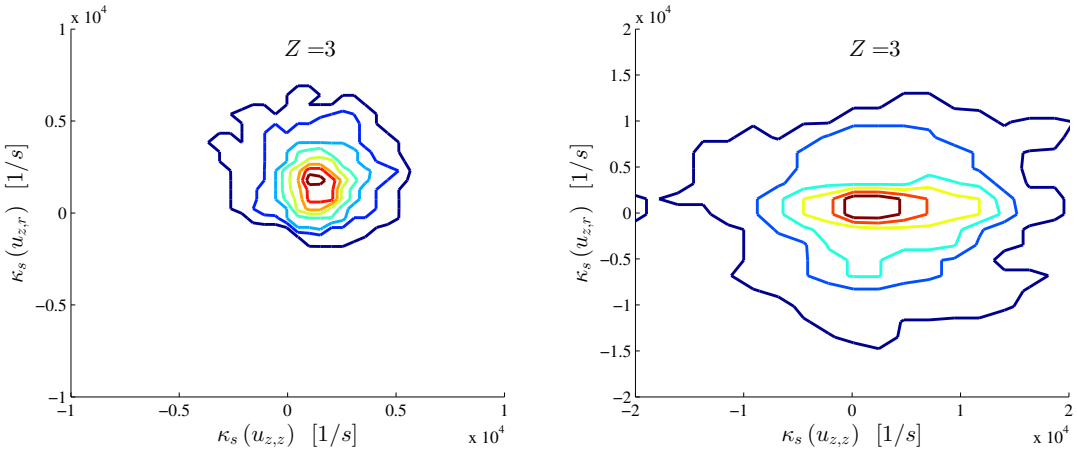

(a) $u_{pm} = 35\ m/s$ **(b)** $u_{pm} = 70\ m/s$

Figure 6.16: Joint PDF of flame stretch by dominant shear and normal strain sources of $u_{z,r}$ and $u_{z,z}$, respectively, shown for $u_{pm} = 35\ m/s$ (left) and $u_{pm} = 70\ m/s$ (right), at an axial location 3 mm downstream of the dump plane and $\phi = 1.0$.

in Figure 6.17 and Figure 6.18, respectively, for both velocity conditions at a fixed equivalence ratio. These show how the flame lies in regions where the shear strain values range from about 20,000-30,000 1/s and normal strain values of 1000 1/s at $\phi = 1.0$ and $u_{pm} = 35 m/s$. Several observations from the $u_{pm} = 35\ m/s$ test case follow. First, even though the two flow strain values differ by a factor of 20, Figures 6.17a and 6.18a, their relative contributions to flame stretch are nearly equal, as shown in Figure 6.15a. This follows from the fact that the flame angle determines the relative contributions from shear and normal strain terms flame to stretch (Eqn. 6.1). Second, although the mean shear strain field, $\overline{\partial u_z/\partial r}$, is clearly positive as shown in Figure 6.17a, the resulting shear strain contributions to flame stretch can be either positive or negative depending on the flame angle sign. Recalling from Figures 6.9a and 6.9b, the mean flame angle changes from positive to negative for the higher premixer velocity test cases, and thus explains the change in sign of shear strain contributions (Figure 6.15b). Third, normal strain also leads to positive flame stretch, since $\partial u_z/\partial z > 0$ as indicated in Figure 6.18.

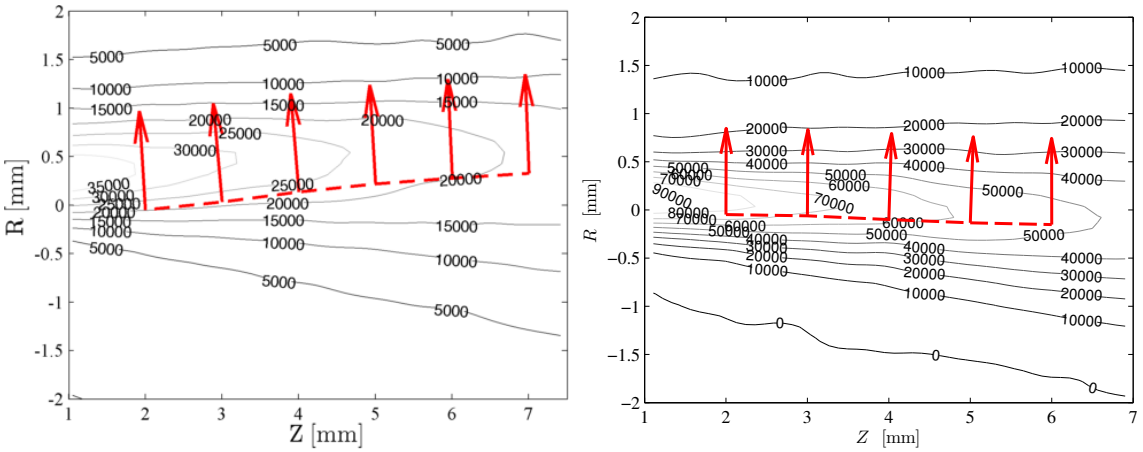

(a) $\bar{u}_{z,r}$ $[1/s]$ $(u_{pm} = 35\ m/s)$

(b) $\bar{u}_{z,r}$ $[1/s]$ $(u_{pm} = 70\ m/s)$

Figure 6.17: $\bar{u}_{z,r}$ strain field $[1/s]$ with mean CH-layer center line position (dashed red line) and flame normal (red arrows) overlaid for $\phi = 1.0$ at $u_{pm} = 35\ m/s$ (left) and $u_{pm} = 70\ m/s$(right).

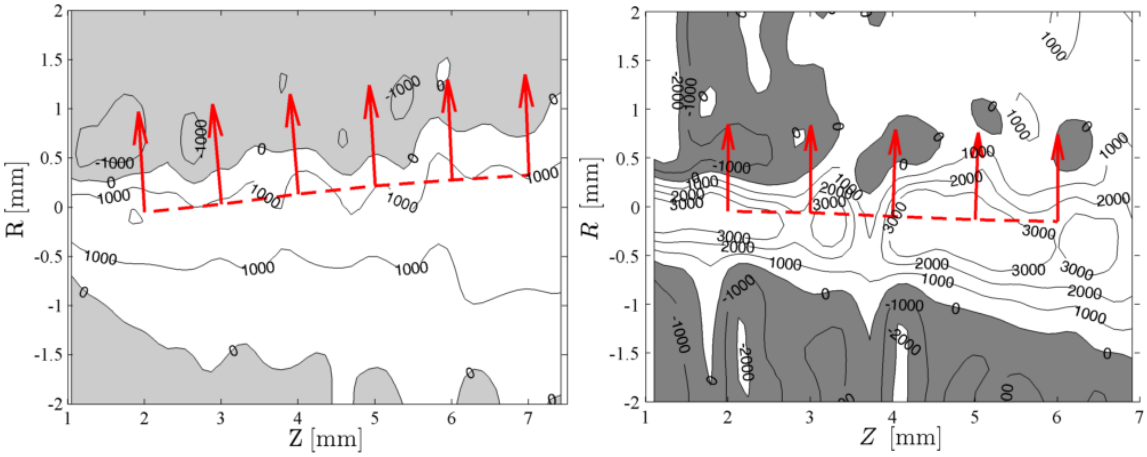

(a) $\bar{u}_{z,z}$ $[1/s]$ $(u_{pm} = 35\ m/s)$

(b) $\bar{u}_{z,z}$ $[1/s]$ $(u_{pm} = 70\ m/s)$

Figure 6.18: Mean $u_{z,z}$ strain field $[1/s]$ with mean CH-layer center line position (dashed red line) and flame normal (red arrows) overlaid ($\phi = 1.0$). Accelerating flow, $\partial u_z/\partial z > 0$, indicated by light region, decelerating region, $\partial u_z/\partial z < 0$, is shaded gray.

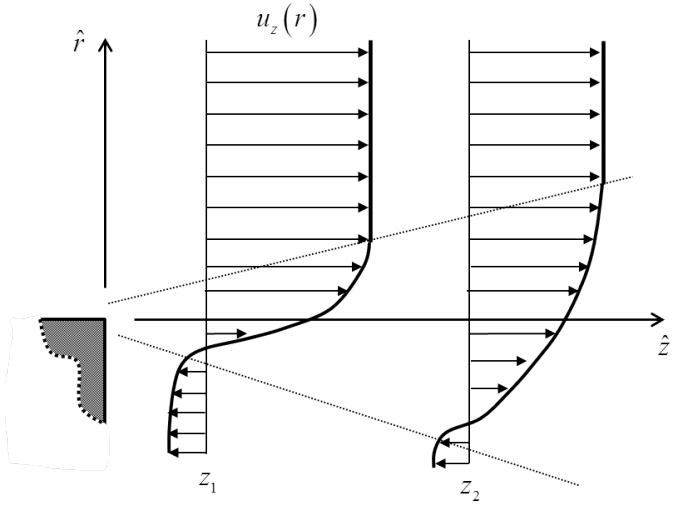

Figure 6.19: Transverse profiles of mean, axial velocity at various axial locations schematically demonstrating the strain field structure of the near field shear layer and jet.

While the first two observations are easily supported from bulk, steady state boundary layer scaling arguments, the latter trend was not expected. In fact, previous scaling work had shown mean contributions of normal strain induced stretch to be negative in flows of this nature where the flow decelerates in bulk from the high velocity annular jet into the open surroundings [127]. Indeed, experimental measurements by Zhang *et al.* [127] showed normal strain resulting in negative contributions to flame stretch. This can be primarily attributed to our previous measurements being reactant conditioned compared to the CH-layer conditioned measurements performed in this study. Indeed, the measurements in Figure 6.18a show that although the jet core is decelerating, as it must by volume flow rate considerations, the flow is actually accelerating in the region of the shear layer where the flame is stabilizing. These distinct features of the strain field within in the shear layer are shown schematically in Figure 6.19. This shows how regions in the shear layer can accelerate, even as the core flow is decelerating.

Next the time averages of the flame stretch rates at the other equivalence ratio

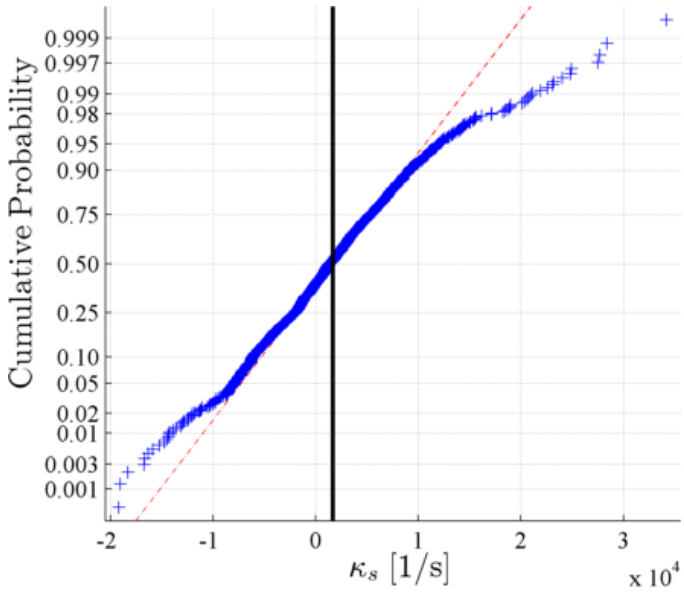

Figure 6.20: Cumulative distribution function of flame stretch measurements, κ_s^{CH}, for $\phi = 0.8$ and $u_{pm} = 35\ m/s$ at an $1mm$ axial bin centered at $Z = 6\ mm$, with the mean value shown as the black line. Gaussian probability function with same standard deviation as sample standard deviation is indicated for reference by the dashed red line.

test conditions are considered for each velocity condition. First though, the manner in which this data is presented is described. The axial profiles of time averaged quantities are produced using a spatial moving average over axial lengths of 1 mm and spaced 1 mm apart. The error bars denote the uncertainty in the mean, estimated for a Gaussian distribution from the expression:

$$\sigma_{\bar{\kappa_s}} = \sigma_{\kappa_s}/\sqrt{n} \tag{6.2}$$

where n denotes the number of realizations, varying between 900-2900, depending upon axial location and ϕ. We compare the cumulative distribution function of the measured stretch rates and a Gaussian fit in Figure 6.20. As shown in Figure 6.20, 85% of the measured stretch rates are captured by a Gaussian fit of the data ranging between probabilities of 0.05 and 0.90. In addition, the mean value, shown as a black

line, is a good metric of the center, or the median, of the measured stretch rates as it intersects the Gaussian fit line at a probability of 0.50. Similar agreement of the data to a Gaussian distribution was observed for all of the test conditions reported.

Considering Figure 6.21a and Figure 6.21b in detail now, the un-normalized results show stretch rates peaking around 4000 $1/s$ and dropping to values of 2000 $1/s$ at the end of the viewing window. The flame stretch values experienced by the flame are actually lowest with the lowest fuel/air ratio condition. This is due to the flame shifting its location slightly, apparently because of its lower flame speed, to a region with lower stretch. This response of the flame does not necessarily result in a flame that is more critically stretched, although it could. Note also how the mean stretch rates are positive throughout the measurement domain. This is contrary to results from Zhang *et al.* [127], which showed negative stretch rates close to the centerbody, transitioning to positive values downstream for an annular swirling combustor. Finally, the mean stretch rates are much less than the extinction stretch rates predicted by OPPDIF for the opposed jet configuration, as the ratio $\bar{\kappa}_s^{CH}/\kappa_{ext}^{CH}$ has a peak value of less than 0.45. Related to the point above about absolute values of the stretch rate varying with fuel/air ratio: note that the normalized flame stretch also drops with lower fuel/air ratios. In other words, Figure 6.21b *suggests that the flame is farther from extinction conditions as equivalence ratio is decreased.* Although, the opposed jet configuration does not reflect the conditions at the leading edge of the flame. Two possibilities emerge then for why the flame blows off as the equivalence ratio is further decreased. First, this trend could reverse itself and values of the $\bar{\kappa}_s^{CH}/\kappa_{ext}^{CH}$ ratio could rise as fuel/air ratio is further decreased. Alternatively, it is possible that the blowoff mechanism is not linked to local extinction, but rather that the edge flame speed or flame displacement speed cannot match the flow velocity. This point is further discussed in context of the kinematic conditions along and specifically at the leading edge of the the CH-layer. Similar behavior of mean stretch is observed

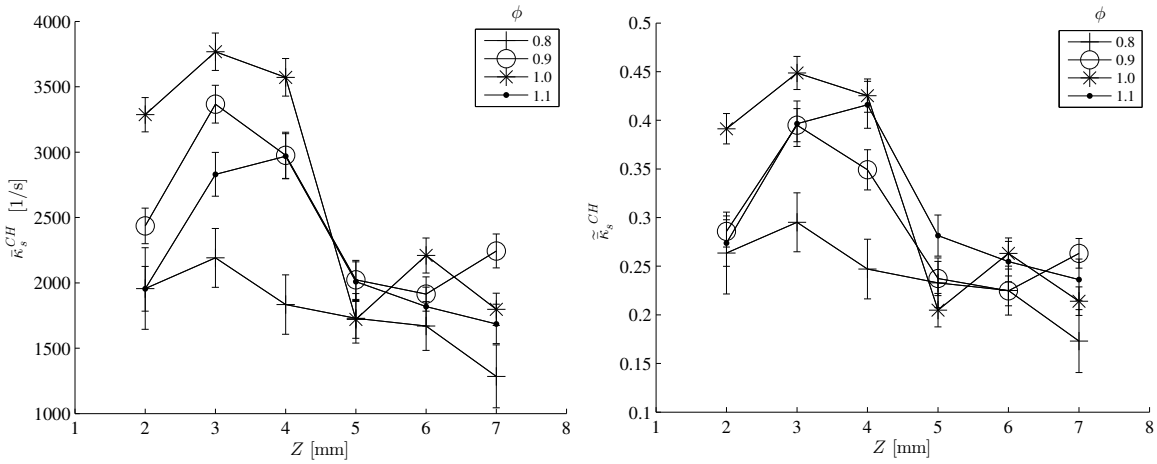

(a) $\bar{\kappa}_s^{CH}(Z)$ **(b)** $\tilde{\bar{\kappa}}_s^{CH}(Z)$

Figure 6.21: Axial dependence of mean flame stretch rates, $\bar{\kappa}_s^{CH}$ (left), and normalized mean stretch rates, $\tilde{\bar{\kappa}}_s^{CH}$, at four equivalence ratios and $u_{pm} = 35m/s$. Values were normalized by κ_{ext}^{CH} at their respective equivalence ratio.

for the $u_{pm} = 70\ m/s$ data case as shown in Figure 6.22 in that non-critical mean stretch rates are observed throughout the domain as well as a decrease in normalized mean stretch with equivalence ratio.

Finally, PDFs are presented of total stretch rate as a function of axial distance for representative 35 m/s (Figure 6.23) and 70 m/s (Figure 6.24) test cases are shown. The distributions of mean stretch rates are similar in shape for all test conditions shown appearing to be symmetric and Gaussian in nature.

6.2.2.2 Flame Kinematic Conditions

In addition to tracking the stretch conditions along the CH-layer, the velocity conditions were determined as well. Like the reported stretch values, the reported flow velocity conditions were conditioned on the centerline of the CH-layer. At each location along the CH-layer, the local velocity components in absolute coordinates of $\hat{r}$ and $\hat{z}$, were projected into local tangential, u^T, and local normal, u^N, components defined by the local and instantaneous orientation of the flame. This definition of

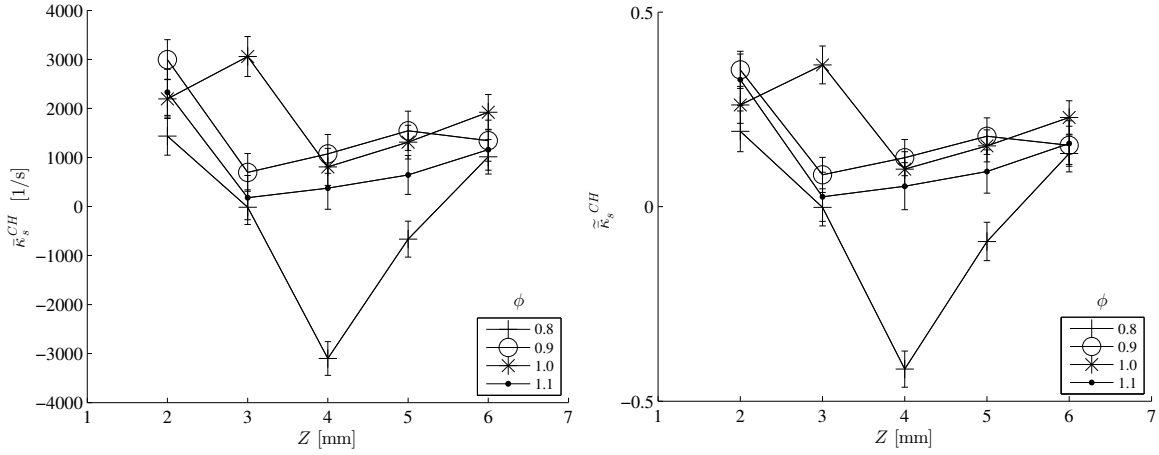

(a) $\bar{\kappa}_s^{CH}(Z)$ **(b)** $\tilde{\bar{\kappa}}_s^{CH}(Z)$

Figure 6.22: Axial dependence of mean flame stretch rates, $\bar{\kappa}_s^{CH}$ (left), and normalized mean stretch rates, $\tilde{\bar{\kappa}}_s^{CH}$, at four equivalence ratios and $u_{pm} = 70m/s$. Values were normalized by κ_{ext}^{CH} at their respective equivalence ratio.

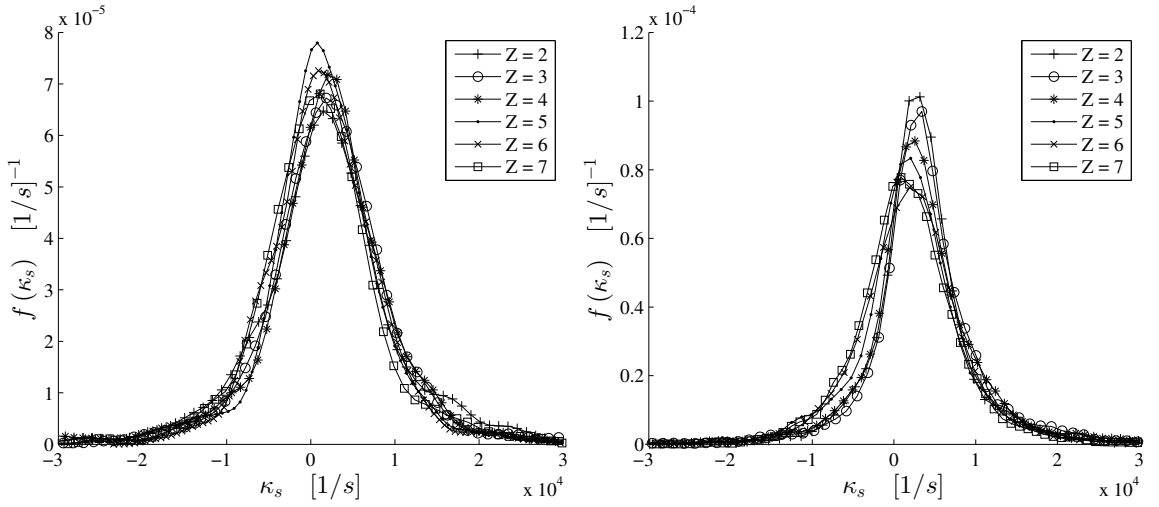

(a) $\phi = 0.8$ **(b)** $\phi = 1.0$

Figure 6.23: PDF of total flame stretch, κ_s, by axial location, shown for $\phi = 0.8$ (left) and $\phi = 1.0$ (right), for $u_{pm} = 35m/s$.

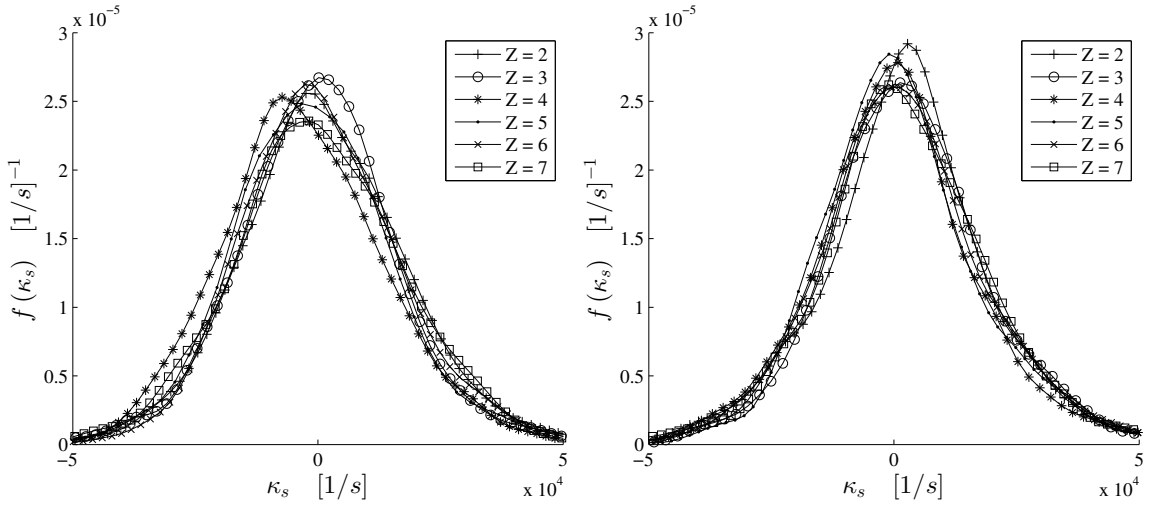

(a) $\phi = 0.8$ **(b)** $\phi = 1.0$

Figure 6.24: PDF of total flame stretch, κ_s, by axial location, shown for $\phi = 0.8$ (left) and $\phi = 1.0$ (right), for $u_{pm} = 70\ m/s$.

the velocity conditions along the CH-layer is schematically shown in Figure 6.25. The analysis of u^T and u^N velocities provides insight into the speed at which disturbances are convected along the flame front and the flow velocities opposing the normal propagation of the flame, respectively.

Figure 6.26 plots the axial dependence of the mean axial and transverse velocity at the center of the CH-layer for the $u_{pm} = 35m/s$ and $\phi = 0.9$ test case. Also shown are averages of the instantaneous local velocity projected into local flame tangential and normal directions based on instantaneous flame orientations. The radial and normal velocities are normalized by the calculated stretched displacement speed relative to the CH-layer, $S_{d,CH}$, obtained from CHEMKIN. The axial and tangential velocities are normalized by the unstretched displacement speed relative to the preheat layer, $S^o_{d,ph}$, also calculated using CHEMKIN. This different normalization is used because the tangential velocity is not directly influenced by gas expansion, as opposed to the normal velocities. In addition, measured/computed edge flame velocities in the literature are usually normalized by displacement speeds referenced to the reactants

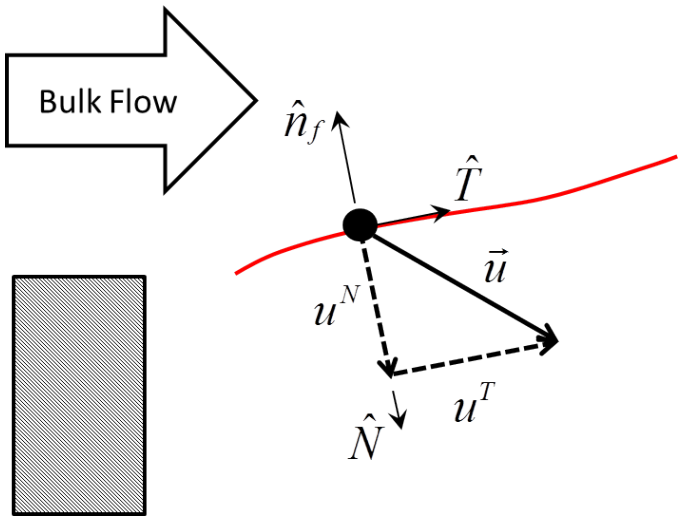

Figure 6.25: Schematic showing the decomposition of local velocity conditions along the CH-layer into tangential, u^T, and normal, u^N, components.

[29].

The magnitude of the mean axial velocity, $\tilde{u}_z$, grows with downstream distance, becoming increasingly positive with downstream distance. Due to the orientation of the flame, trends and the magnitude of mean tangential velocity, $\tilde{u}^T$, are similar to $\tilde{u}_z$. The tangential velocity along the flame starts from values of about $5 \times S^o_{d,ph}$, and quickly rises to a value of nearly $20 \times S^o_{d,ph}$, where $S^o_{d,ph}$ is the unstretched laminar flame speed relative to the initiation of the preheat layer. Prior direct measurements of non-premixed edge flame velocities show values of $v_f = 1 - 2.5 \times S^o_{d,ph}$ [4, 96]. Next, we examine trends in transverse and normal velocity profiles. The mean transverse velocity, $\tilde{u}_r$, becomes increasingly negative with downstream distance. However, given the orientation of the flame, this results in positive flow velocities normal to the flame (reactants are being convected into the flame sheet) on the order of un-stretched flame speeds, relative to the CH-layer, expected of the incoming bulk mixture. These measurements of $\tilde{u}_z$ and $\tilde{u}_r$ for this test case suggest a flame with favorable kinematic conditions along the flame front. Similar trends were observed for the $u_{pm} = 70\ m/s$ test case at the same equivalence ratio as shown in Figure 6.27. However, with the

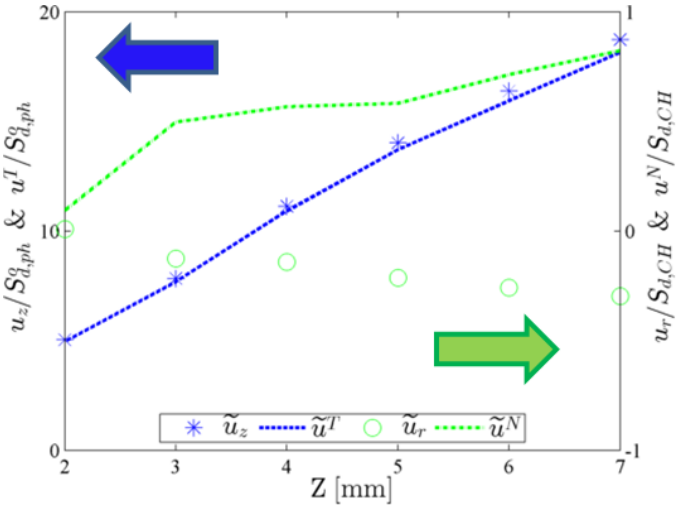

Figure 6.26: Mean velocity conditions along the CH-layer for $\phi = 0.9$, $u_{pm} = 35m/s$ case as a function of downstream distance.

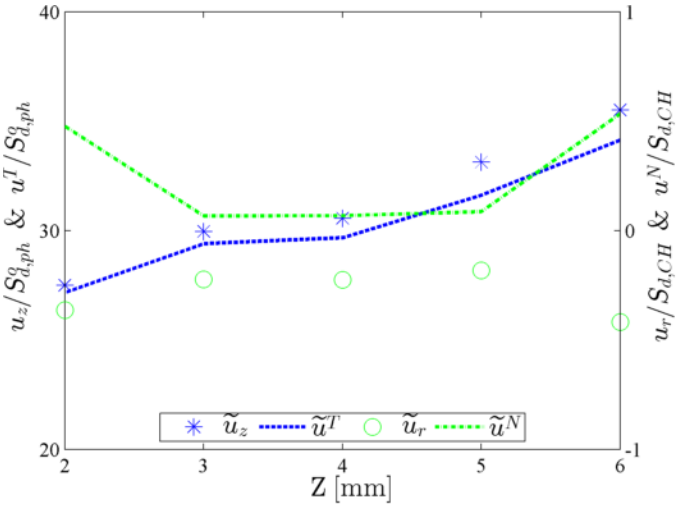

Figure 6.27: Mean velocity conditions along the CH-layer for $\phi = 0.9$, $u_{pm} = 70m/s$ case as a function of downstream distance.

increase of premixer velocity, the velocity tangent to the flame edge is much higher, and there is flat region in the normal velocity profile, likely the result of the flatter flame orientation. In addition, the velocities normal to the flame are negative, and suggest unfavorable conditions along the flame.

6.2.3 Flame Edge Conditions

The nature of the leading edge of the CH-layer is of particular interest in this study of premixed flame stabilization and for assessing the physics anchoring the flame. Most importantly, it is the hypothesis that the leading edge of the flame acts to anchor the flame throughout the combustor which is being investigated. As was pointed out in Section 2.2.3, there are two potential kinematic anchoring mechanisms which could potentially stabilize the flame: normal propagation and edge flame stabilized (Figure 2.10). Considering the observed shape of the flame from CH-PLIF images (Figure 3.13), the metrics used to characterize the flame edge conditions are formulated assuming that the flame is edge flame stabilized as shown in Figure 6.28. The flame edge at each instance in time is defined as the point farthest upstream where there is a significant intensity in the CH-PLIF images. At this point, the orientation of the flame edge with respect to the flowfield as well as the velocity conditions tangent to the flame edge is examined.

6.2.3.1 Edge Orientation

The hypothesis that the flame is edge flame stabilized is first tested by characterizing the orientation of the edge with respect to the oncoming flow. If the flame is edge flame stabilized, we would expect the flame to be oriented tangential to the oncoming flow on average. In other words, if it is the propagation of the edge of the flame which is anchoring the flame, it must as a necessary condition, be oriented appropriately with respect to the flow in order for the flame to not convect downstream. Of course, this is provided that the edge flame speed is able to oppose the local flow velocity.

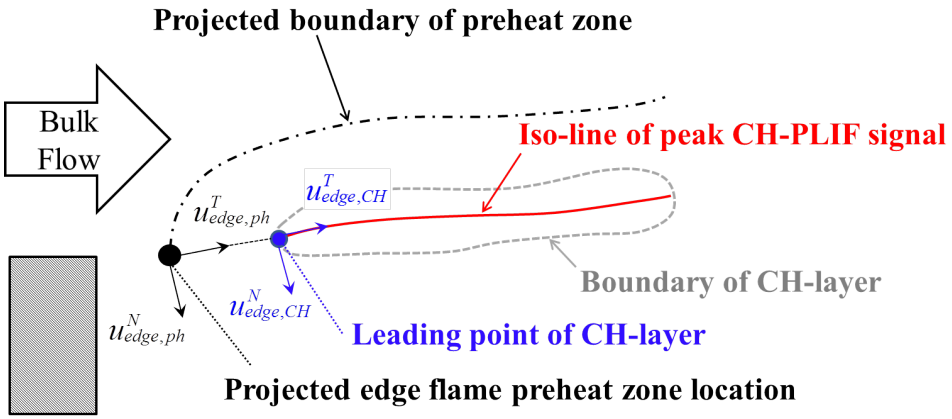

Figure 6.28: Schematic of flame structure and reference locations of interest.

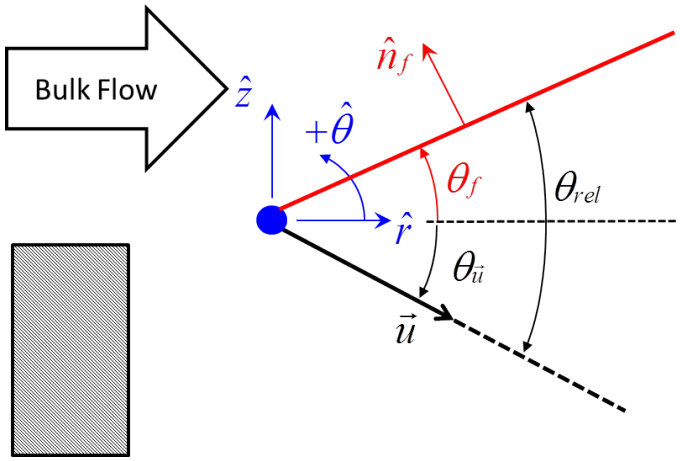

Figure 6.29: Definition of relative angle between flow and flame at the flame edge.

This is our first method of testing this hypothesis. The orientation of the flame with respect to the flow is calculated as the relative angle between the flame edge tangent and the flow direction as shown in Figure 6.29.

When the flame edge is perfectly aligned with the flow field, the relative angle between the direction of flame propagation and flow is zero. Any deviation from zero would suggest that the direction of flame edge propagation is not tangent to the flame surface in the near field. This hypothesis is confirmed by the distribution of relative angles between the flame and the flow evaluated at the upstream edge of the

CH-layer, shown in Figure 6.30, and defined as follows in eq. 6.3:

$$\theta_{rel} = \theta_f - \theta_{\vec{u}} \tag{6.3}$$

First considering the results for $\phi = 1.0$ and $u_{pm} = 35m/s$, θ_{rel} is bounded between $+/-$ $45°$ with an average value of $7°$. In fact, considering all test cases, the distributions of θ_{rel} and mean values are similar with $\bar{\theta}_{rel}$ values between -10 and $+1$ degrees and standard deviations of θ_{rel} ranging between $20° - 43°$. These results thus suggest that flame anchoring is dependent upon flame propagation tangent to the flame surface at the leading edge.

Note however, as was pointed out in Section 3.2.3, it is challenging to resolve the CH-layer. This includes resolving the orientation of the CH-layer at the leading edge. Although there may be ambiguity in the orientation of the flame at the flame leading edge, the direction which the flame must propagate in order to anchor the flame is certain based on the analysis of θ_{rel}. The question remains then what the orientation of the flame is at this leading edge. Recall from Section 3.2.3, that if the flame were to hook as a normal propagation stabilized flame would, it would result in a change in CH-layer centerline orientation from $\theta_f = 0°$ to $\theta_f = 90°$ and a displacement of the CH-layer centerline location in the transverse direction. The analysis showed that if these features existed, they would be observable from the raw data acquired, however they in fact are not observed. This provides further support to the hypothesis that this flame is edge flame propagation stabilized.

6.2.3.2 Edge Velocity

Continuing with the assumption that the leading edge of the flame in the near field is edge flame stabilized, and that the direction of edge flame propagation is tangent to the flame surface in the near field, the flow conditions at the flame edge are examined. Note, that this approach neglects azimuthal variation in the flame standoff distance,

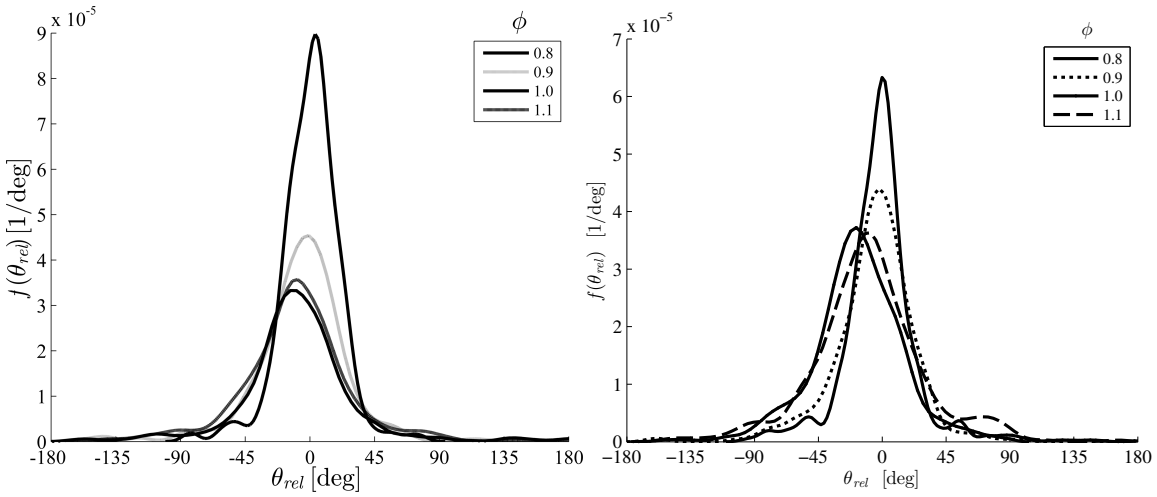

(a) $u_{pm} = 35\ m/s$ **(b)** $u_{pm} = 70\ m/s$

Figure 6.30: Probability density function of flame leading edge angle with respect to the flow, θ_{rel} for u_{pm}=35m/s and u_{pm}=70m/s test cases of varying ϕ.

and assumes that at each instant in time that the edge of the flame observed in-plane, is the absolute leading edge of the flame. In other words, it assumes there is no azimuthal component to the flame normal vector, $n_\theta = 0$, and therefore the flame is not propagating in the azimuthal direction at the leading edge. Note as well, that the temporal resolution is not enough to determine the propagation speed of the flame. However, given that the axial location of the leading edge of the flame predominantly resides within a $\approx 2mm$ range of values, as shown in Figure 6.31, two things are assumed: the orientation of the flame edge is captured in the $r - z$ plane, and that the leading edge of the flame is robust such that the mean velocity conditions at the edge reflect a the flow velocity conditions which the flame must match in order to anchor the flame.

As was done in the analysis of the velocity conditions along the CH-layer, the flow velocity at the flame edge are decomposed into components normal, $u^N_{edge,CH}$, and tangent, $u^T_{edge,CH}$, to the flame edge as shown in Figure 6.28. In this fashion, if the flame is truly edge flame stabilized, we would expect to find near zero velocities

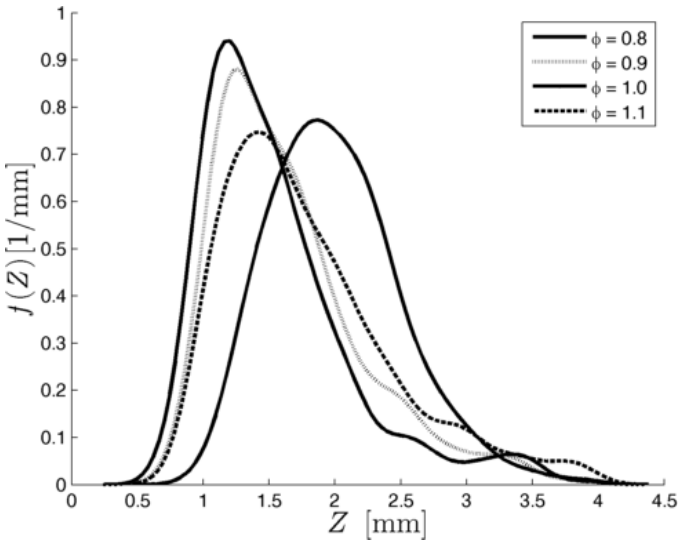

Figure 6.31: Probability density function of flame leading edge axial standoff distance, Z, for $u_{pm}=35m/s$ test cases of varying ϕ.

normal to the edge ($u^N_{edge,CH} \approx 0$) and positive velocities tangent to the edge on the order of flame speeds conditioned on the CH-layer ($u^T_{edge,CH} \approx S_{d,CH}$).

Figure 6.32a shows how the edge velocity conditions change as a function of equivalence ratio for the $u_{pm} = 35\ m/s$ test cases, where velocities at the edge have been normalized by $S^o_{d,ph}$. These velocities were calculated at the instantaneous flame edge and then time averaged. *The error bars indicate the range of velocities obtained, if the calculated edge location were to be translated one PIV interrogation window in all four directions.*

The velocity tangent to the flame edge for the low velocity test cases are relatively constant until $\phi = 0.8$ where there is a sharp increase in the mean tangent velocity. The reasons for this sharp increase are not fully understood, and possibly a reflection of the back-pressuring that the overall flame shape exerts on the approach flow field. In other words, this rise is not simply a local adjustment of the flame position –for example, detailed analysis shows that there is not a transverse shift in location of the flame edge into a higher average velocity, at least not one large enough to explain

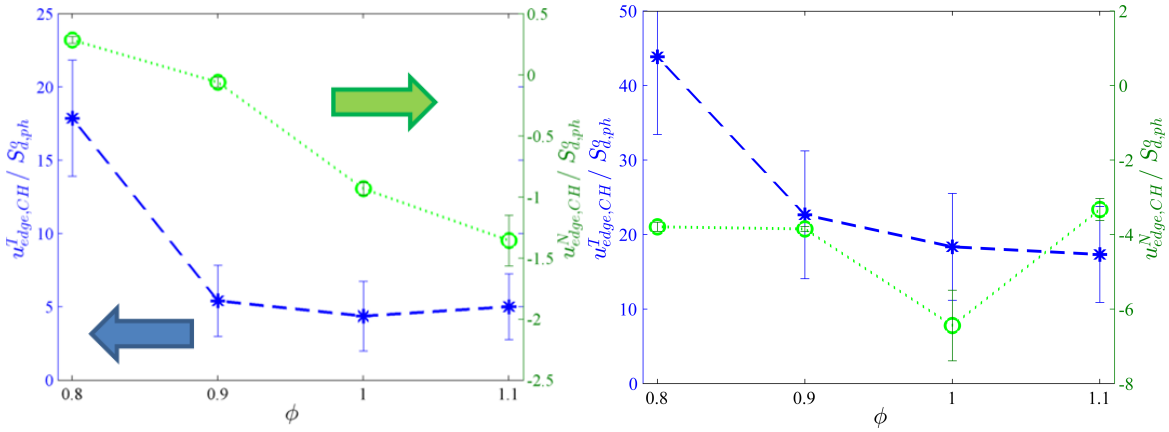

(a) $u_{pm} = 35\ m/s$ **(b)** $u_{pm} = 70\ m/s$

Figure 6.32: Normalized tangential and normal flow velocities at flame edge as a function of ϕ for u_{pm}=35m/s (left) and u_{pm}=70m/s (right).

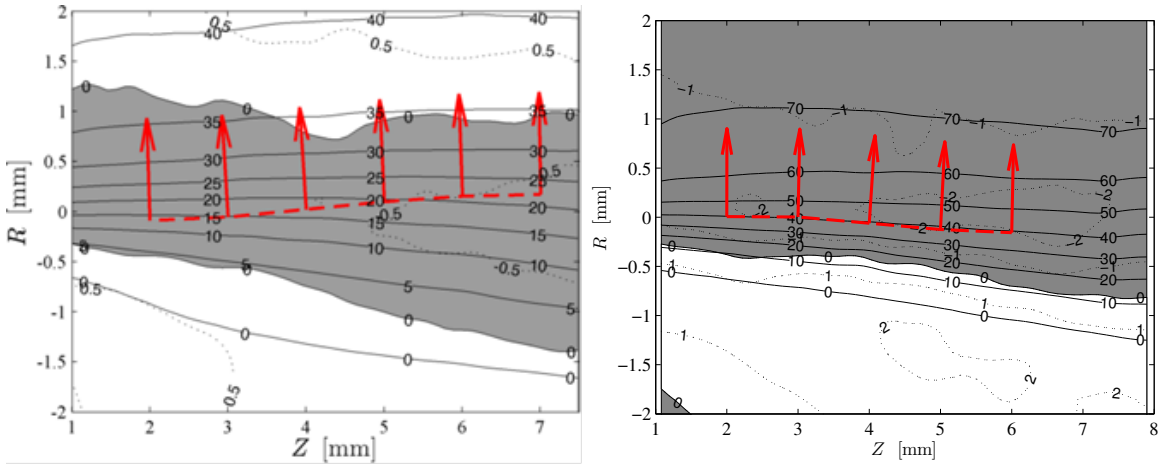

(a) $u_{pm} = 35\ m/s$ **(b)** $u_{pm} = 70\ m/s$

Figure 6.33: Mean flame position (dashed red line) and flame normal (red arrows) overlaid on top of $\bar{u}_z$ contours (solid lines) and $\bar{u}_r$ contours (dashed) with regions of $\bar{u}_r > 0$ and $\bar{u}_r \leq 0$ shown in white and gray respectively for $u_{pm} = 35\ m/s$ (left) and $u_{pm} = 70\ m/s$ (right) and ϕ=0.8.

the change in velocity. Also, the mean axial location of the leading edge shifts only slightly downstream, from 1.5 to 2.0 mm, at fuel/air ratios of 1.0 and 0.8, respectively (Figure 6.31). Since higher tangential velocities occur farther downstream, e.g., Figure 6.33a shows that the flow at $r = 0$ accelerates approximately $(1\ m/s)\,/\,(1\ mm)$, this would contribute to a 0.5 m/s rise in average velocity, a value significantly lower than required to explain the rise in tangential velocities shown in Figure 6.32a. In fact, large changes are observed in the mean flow field for the $\phi = 0.8$ test case. Overall, the flow velocity tangent to the flame is uniformly higher at comparable axial locations in the $\phi = 0.8$ case. Thus, the sharp rise in tangential velocity seen at the flame edge seems to be due to a global change in the flowfield, rather than a local adjustment of the flame as shown in Figure 6.33a.

Next, we examine the velocity conditions at the edge for the higher premixer velocity test cases, $u_{pm} = 70\ m/s$ (Figure 6.32b), focusing our discussion on the velocity component tangent to the flame edge, $u^T_{edge,CH}$. Like the low velocity test case, there is a spike in $u^T_{edge,CH}$ at $\phi = 0.8$. This again is believed to be the result of a change in the mean flow field occurring at the leanest test case (Figure 6.33b).

In fact, although stretch measurements were not obtained at the leanest equivalence of $\phi = 0.7$, similar shifts in the mean velocity field are observed for those test cases as shown in Figure 6.34 for $u_{pm} = 70 m/s$ test cases. Note the relatively good agreement in the locations of mean velocity iso-contours throughout the flow field. This further supports the idea that above a critical ϕ, the temperature rise and induced adverse pressure gradient caused by the presence of the flame results in a global change in the flow field.

6.2.4 Reactant/Product Mixing Upstream of Flame Edge

6.2.4.1 Approach

During times when the flame is locally detached from the bulkhead, mixing between the incoming reactant stream and the products in the inner recirculation zone can

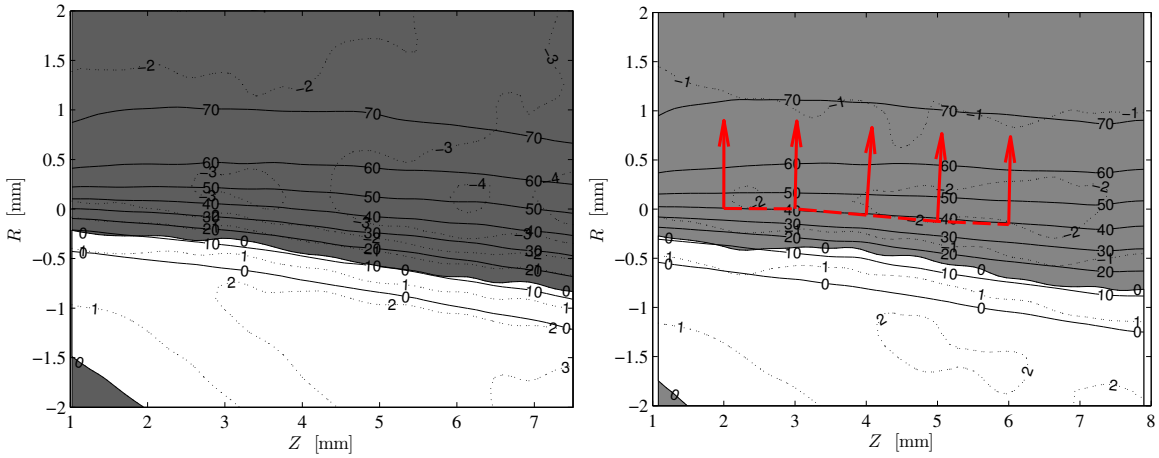

(a) $\phi = 0.7$ **(b)** $\phi = 0.8$

Figure 6.34: Mean flame position (dashed red line) and flame normal (red arrows) overlaid on top of $\bar{u}_z$ contours (solid lines) and $\bar{u}_r$ contours (dashed) with regions of $\bar{u}_r > 0$ and $\bar{u}_r \leq 0$ shown in white and gray respectively for $\phi = 0.7$ (left) and $\phi = 0.8$ (right) and $u_{pm} = 70m/s$.

occur. Reactants diluted with products will increase the temperature of the reactant mixture, while decreasing the concentrations of fuel and oxidizer. Increases in reactant temperature will increase the reactivity of the mixture while dilution of the reactant concentrations will act to do the opposite. However, due to the high temperature sensitivity of reactions, it is presumed that the overall effect of mixing is to enhance the reactivity of the mixture. Numerical studies of opposed jet flames subject to reaction dilution are discussed in Section 7.2 and demonstrate its effect on key flame stabilization parameters such as κ_{ext} and S_d. That being said, the goal of this section is assess the likelihood that mixing, or reactant stream dilution, occurs upstream of the flame attachment point.

The approach to quantify mixing upstream of the attachment point is shown in Figure 6.35. At each instance in time, a control line is defined from the corner of the center body to the leading edge of the flame located at (z_{edge}, r_{edge}), shown as the

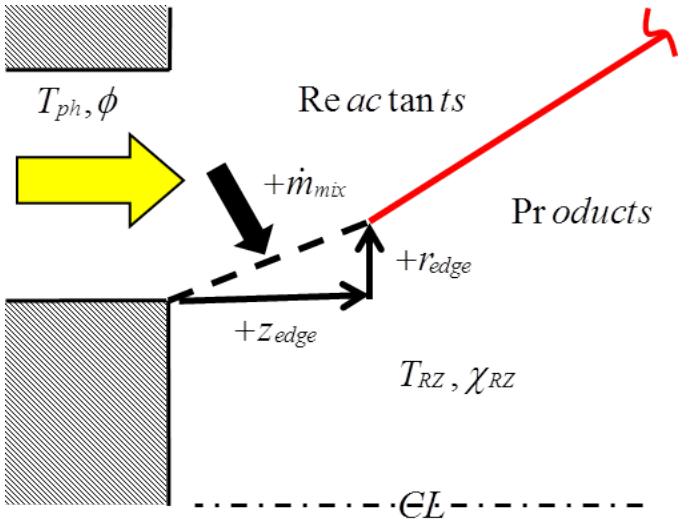

Figure 6.35: Control surface definition for attachment point mixing calculations

dashed line. Along the mixing line, the net volumetric flow rate per unit length, $\dot{V}'$, is determined for all time instances:

$$\dot{V}'(t_j) = \sum_{i=1}^{n_j} u^N(s_i)\, ds_i \tag{6.4}$$

where s_i is the location along the mixing surface, ds_i is the incremental length at s_i, $u^N(s_i)$ is the velocity normal to the mixing surface at location s_i, and n_j is the number of points along the mixing surface. Note that $u_N(s_i)$ is positive in the direction from the jet to the recirculation zone as shown in Figure 6.35. This metric will serve as an indicator of the degree to which the composition of the reactant mixture at the attachment point is being altered by mixing with the recirculation zone.

6.2.4.2 Results

The volumetric flux per unit length, or $\dot{V}'$, was determined at each time instant when a flame was observed. Note that positive values of $\dot{V}'$ as defined in Figure 6.35 indicate transport across the mixing surface from the reactant stream to the recirculation zone, whereas negative values indicate transport from the the recirculation zone to

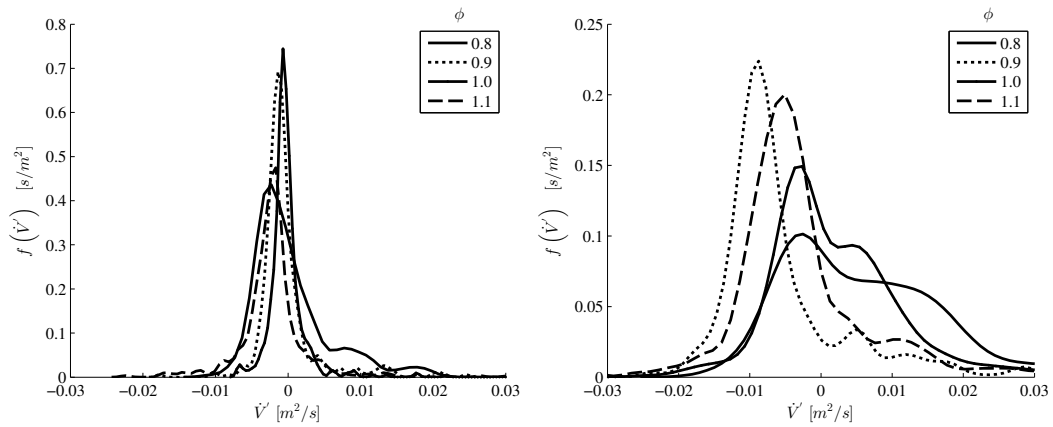

(a) $u_{pm} = 35\ m/s$ **(b)** $u_{pm} = 70\ m/s$

Figure 6.36: Normalized PDF of volumetric flow rate per unit length, $\dot{V}'$, positive for transport from reactants to products, for $u_{pm} = 35\ m/s$ (left) and $u_{pm} = 70\ m/s$ test cases.

the reactant stream, indicative of reactant stream dilution. The PDFs for the $u_{pm} = 35\ m/s$ test cases, shown in Figure 6.36a, are relatively symmetric with the exception of the $\phi = 0.8$ test case. In addition, there was not a strong trend in ϕ for the time averaged value of $\dot{V}'$ or the net value, summed over all time instances, $\sum_{j=1}^{t_{tot}} \dot{V}'(t_j)$. Although again, note the appearance of a slight asymmetry in the PDF for $\phi = 0.8$ near $\dot{V}' = 0.01$ and the overall widening of the PDF. These asymmetries in the PDF become even more noticeable and apparent in the high velocity test cases, $u_{pm} = 70\ m/s$ (Figure 6.36b).

Clearer insight into the mixing behavior upstream of the attachment point was obtained by investigating the correlation between $\dot{V}'$ and the transverse coordinate of the flame edge, r_{edge}. In fact, $\dot{V}'$ was observed to correlate well with the transverse location of the leading point of the flame as shown for 35 m/s test cases (Figure 6.37) and 70 m/s test cases (Figure 6.38). The correlation of $\dot{V}'$ with r_{edge} is more clearly shown in Figure 6.39 and Figure 6.40 which show PDFs of $\dot{V}'$ at fixed values of r_{edge}. Returning to Figure 6.37 and Figure 6.38, note as well, the preference of

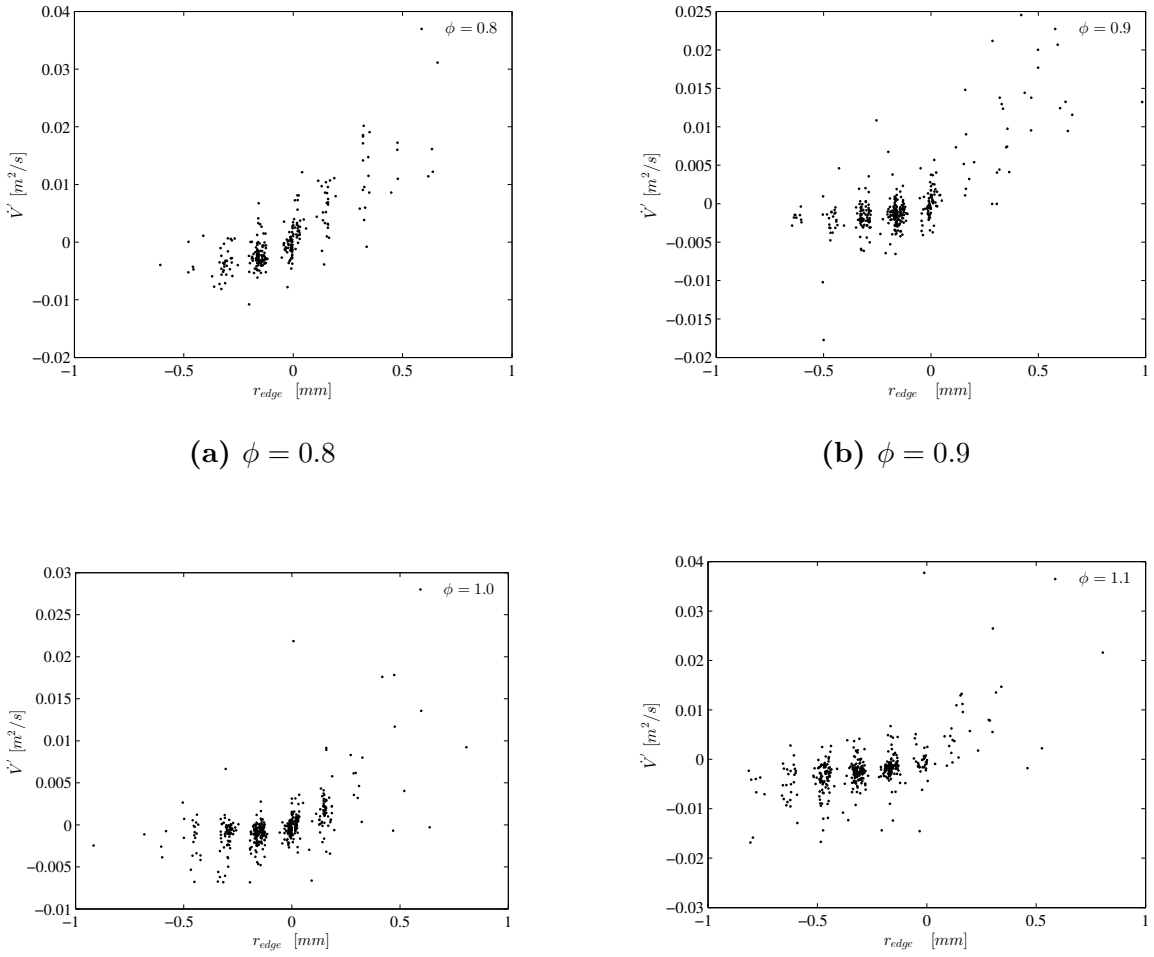

(a) $\phi = 0.8$ **(b)** $\phi = 0.9$

(c) $\phi = 1.0$ **(d)** $\phi = 1.1$

Figure 6.37: Scatter plot of $\dot{V}'$ as a function of radial edge location, r_{edge}, for $u_{pm} = 35\ m/s$ test cases and various ϕ ranging from 0.8 to 1.1.

the leading edge of the flame to anchor in regions where reactant dilution is more likely to occur for both velocity conditions ($\dot{V}' < 0$). However, for the leanest test condition, $\phi = 0.8$, the likelihood of reactant dilution decreases, another indication of degraded flame stability as blowoff conditions are approached. Thus it seems likely that reactant dilution is occurring and potentially influencing the burning properties of the flame at the flame anchor.

Lastly, the transverse location of the flame edge, r_{edge}, was uncorrelated with the axial location of the flame edge, z_{edge} as shown in Figure 6.41 and Figure 6.42.

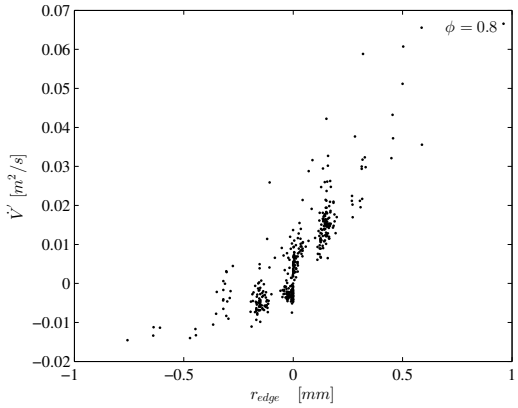

(a) $\phi = 0.8$

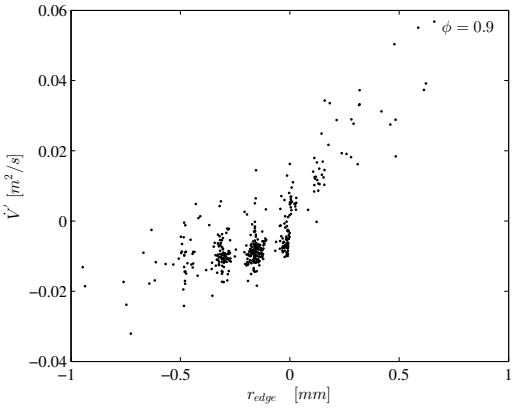

(b) $\phi = 0.9$

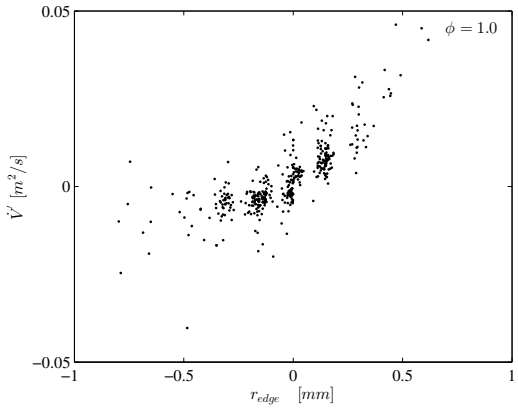

(c) $\phi = 1.0$

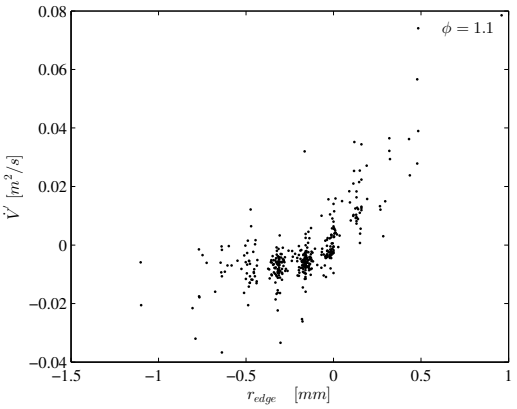

(d) $\phi = 1.1$

Figure 6.38: Scatter plot of $\dot{V}'$ as a function of radial edge location, r_{edge}, for $u_{pm} = 70\ m/s$ test cases and various ϕ ranging from 0.8 to 1.1.

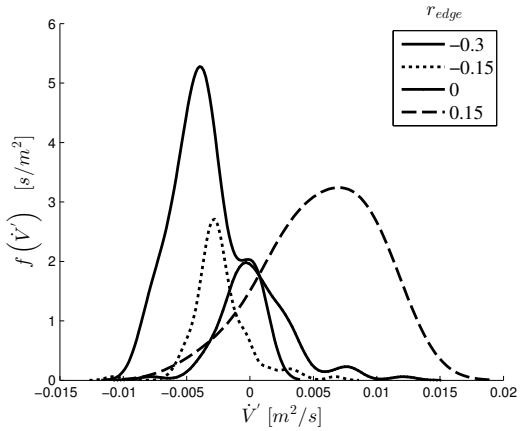

(a) $\phi = 0.8$

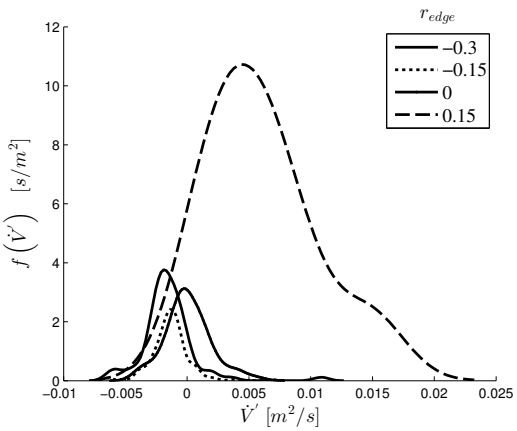

(b) $\phi = 0.9$

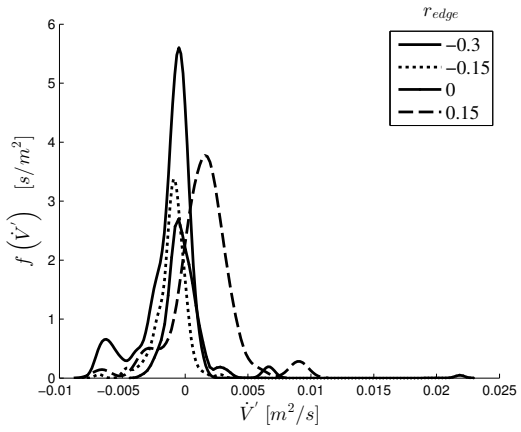

(c) $\phi = 1.0$

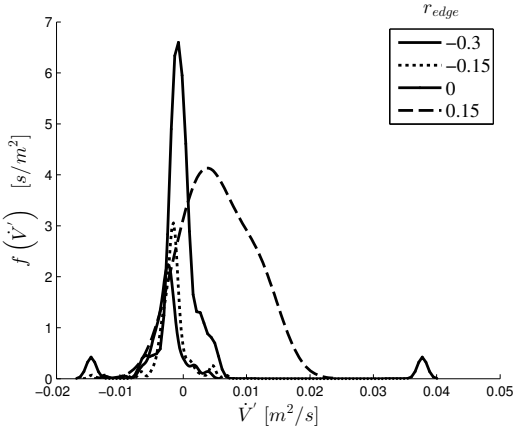

(d) $\phi = 1.1$

Figure 6.39: PDFs of $\dot{V}'$ grouped by radial edge location, r_{edge}, for $u_{pm} = 35\ m/s$ test cases and various ϕ ranging from 0.8 to 1.1.

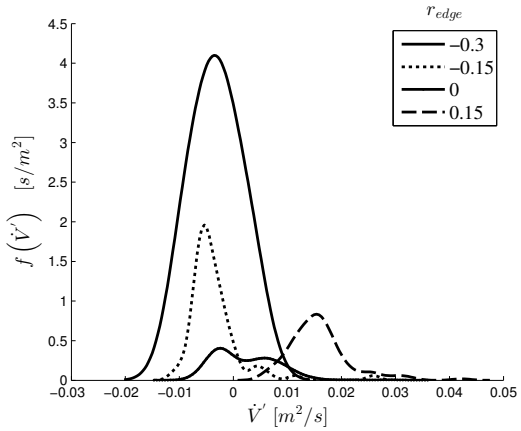

(a) $\phi = 0.8$

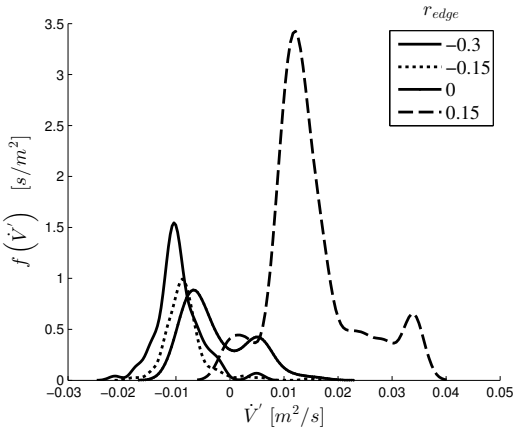

(b) $\phi = 0.9$

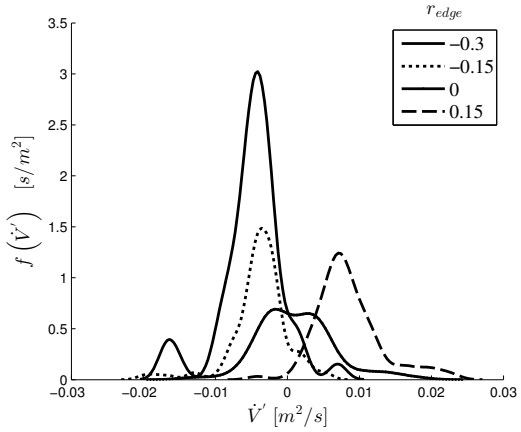

(c) $\phi = 1.0$

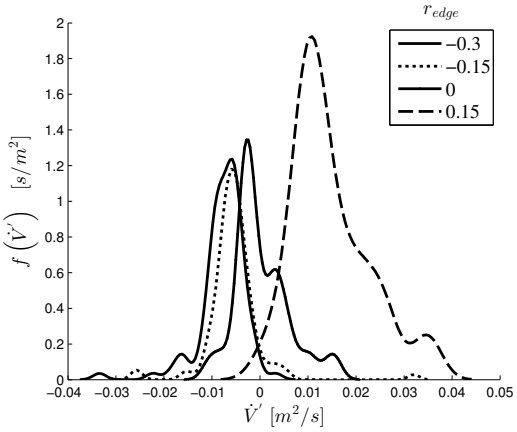

(d) $\phi = 1.1$

Figure 6.40: PDFs of $\dot{V}'$ grouped by radial edge location, r_{edge}, for $u_{pm} = 70\ m/s$ test cases and various ϕ ranging from 0.8 to 1.1.

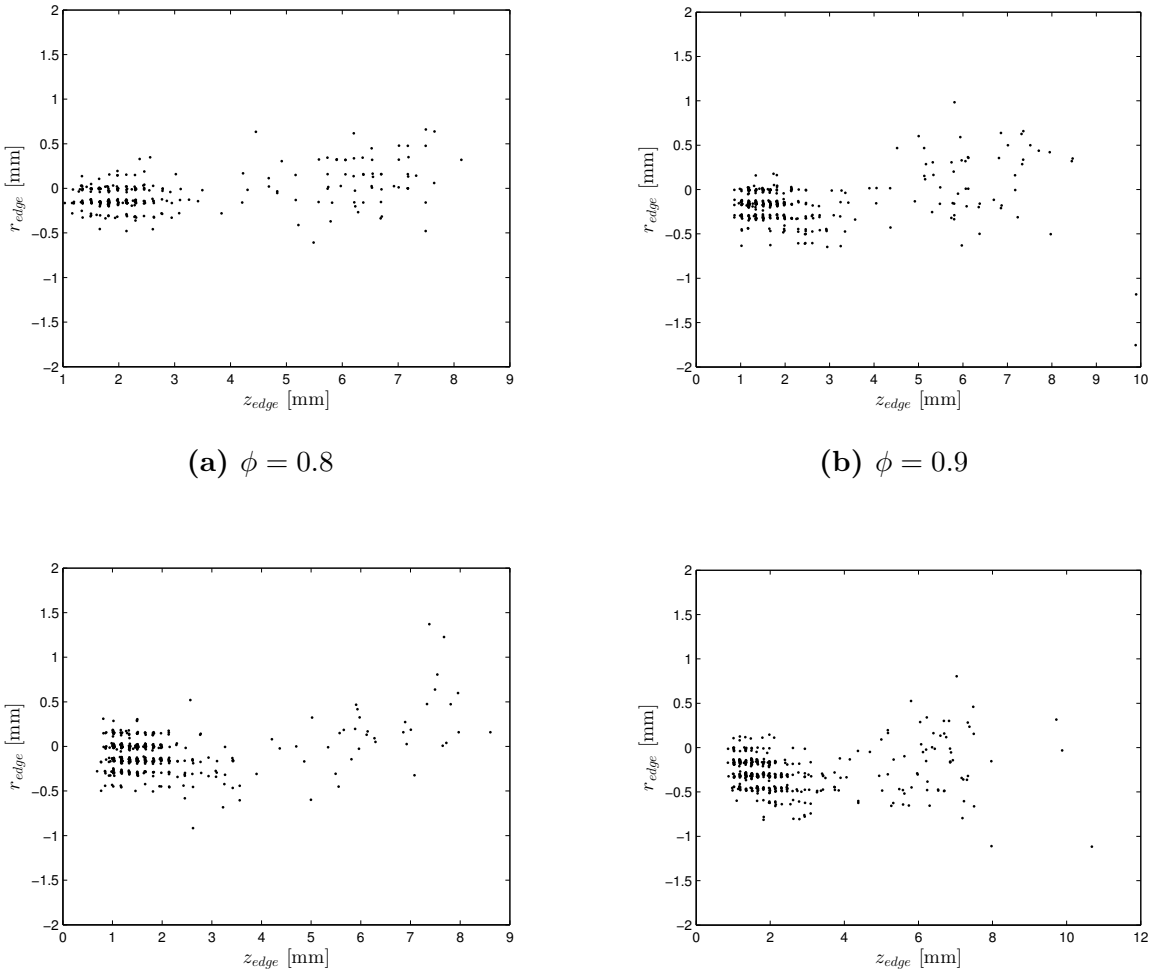

(a) $\phi = 0.8$ **(b)** $\phi = 0.9$

(c) $\phi = 1.0$ **(d)** $\phi = 1.1$

Figure 6.41: Scatter plot of flame edge locations for $u_{pm} = 35\ m/s$ test cases and ϕ ranging from 0.8 to 1.1.

Thus, the transverse edge location is the key parameter determining the likelihood of reactant dilution upstream of the flame leading edge.

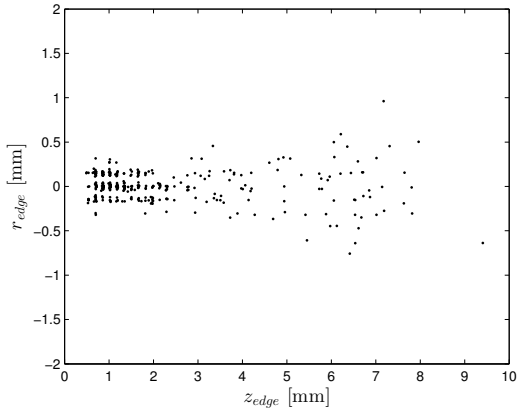

(a) $\phi = 0.8$

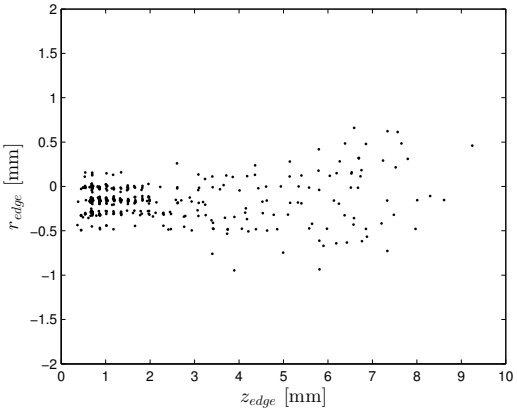

(b) $\phi = 0.9$

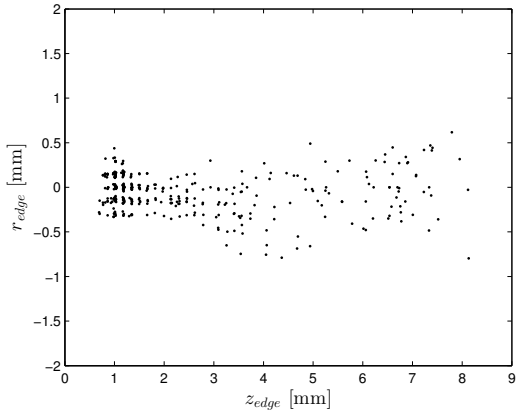

(c) $\phi = 1.0$

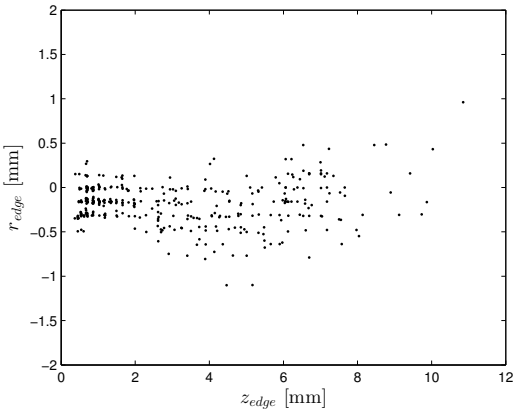

(d) $\phi = 1.1$

Figure 6.42: Scatter plot of flame edge locations for $u_{pm} = 70\ m/s$ test cases and ϕ ranging from 0.8 to 1.1.

CHAPTER VII

RESULTS: NUMERICAL MODELING OF RECIRCULATION ZONE PHYSICS

In the experimental results chapter, Chapter 6, the measured stretch along the CH-layer was compared to extinction stretch rates calculated using CHEMKIN's symmetric opposed-jet model. As was presented in Section 5.2 of the "Numerical Modeling Approaches" chapter, there are additional physics which are not included which could substantially alter the stretched flame behavior. As such, models which account for *non-adiabatic effects* and *reactant dilution* were proposed. The proposed model for the current studies of *non-adiabatic effects* has been used in previous experimental and numerical studies [33, 121, 28, 78]. In addition to the effect of heat loss for the product opposed jet configuration , Coriton *et al.* [27] explored the sensitivity of flame stability to the product stream composition. The model proposed for the study of *reactant dilution* studies the effect of reactant/product mixing. The details of the models used in the study of recirculation zone physics and the corresponding results are presented in this chapter in which non-adiabatic and attachment point mixing effects on flame response to stretch is quantified, and the implications on flame stability are discussed.

7.1 Flame Sensitivity to Heat Losses

As one might suspect, the direct effect of heat loss is to decrease the flame temperature, decreasing the reactivity of the flame and resulting in decreases flame speed and the extinction stretch limit. The asymmetric opposed-jet model of Figure 5.7, a reactant stream opposed by a product stream, was used to study the effect of heat

loss on stretched flames. These calculations were performed for varying levels of heat loss from the flame to the product side by varying the fixed product side temperature for each test case. Each product temperature was defined relative to the extinction temperature for the symmetric test configuration through a temperature ratio, $T_r = T_{RZ}/T_{ext}^{ad}$, where T_{RZ} is the temperature of the product or recirculation zone stream and T_{ext}^{ad} is the extinction temperature from the adiabatic or symmetric opposed-jet model, for which both jets are identical, pre-mixed reactant mixtures (Figure 5.1). Calculations were performed for $T_{reac} = 533K$ and values of ϕ and T_r outlined in Table 5.1.

The effect of heat loss on stretched flames is clearly observed in Figure 7.1 which shows flame temperature response to stretch for test cases subject to varying degrees of heat loss. Note, for the range of positive stretch, $\kappa_s^{ph} > 0$, where all three flames exist, the maximum flame temperature, T_{max}, decreases with increasing heat loss for both equivalence ratios shown. In addition, note how the response of $T_{max}\left(\kappa_s^{ph}\right)$ for the $T_r = 1.0$ and $T_r = 1.05$ flames do not abruptly extinguish; flame temperature gradually and monotonically decreases with flame stretch, asymptotically approaching the product jet temperature. It is also interesting to note, that the temperature at which abrupt extinction happens for the $T_r = 0.8$ test case, nearly matches that of the extinction temperature for the symmetric, or adiabatic flame calculations as shown in Table 7.1. This is in fact why product side temperatures for the non-adiabatic studies were chosen relative to T_{ext}^{ad} as the demarcation between abrupt and gradual extinction occurs for $T_{RZ} \approx T_{ext}^{ad}$.

Flame speed is also drastically altered by the presence of heat loss at high stretch rates as evident in Figure 7.2. The displacement flame speed, $S_{d,ph}$, is defined by the local minimum in velocity normal to the flame in the preheat layer of the flame (Figure 5.3). The deviation in $S_{d,ph}$ between the test cases of varying T_r, becomes more apparent at higher stretch rates, where higher degrees of heat loss, result in

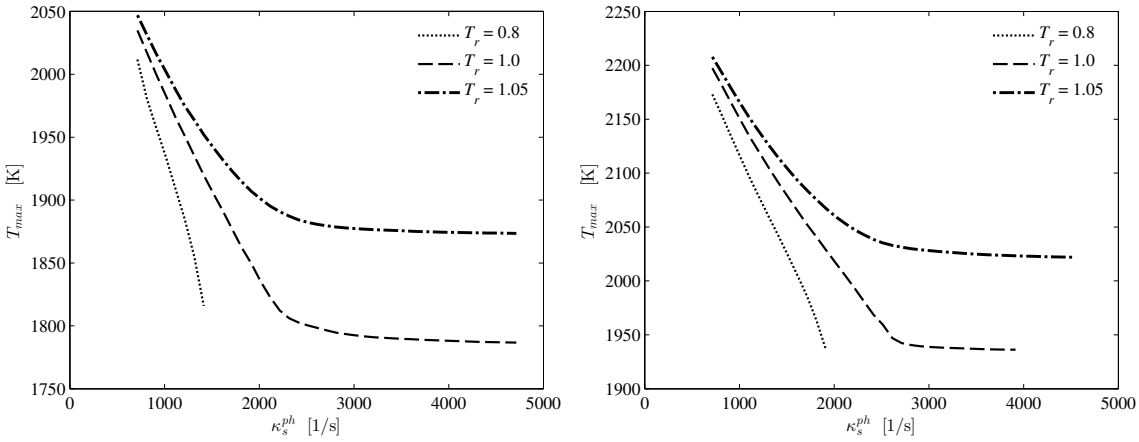

(a) $\phi = 0.8$ **(b)** $\phi = 1.0$

Figure 7.1: Flame temperature response of a non-adiabatic, asymmetric, opposed jet methane-air flame at a $T_{ph} = 533K$, with varying normalized product side temperatures, T_r, for $\phi = 0.8$, left, and $\phi = 1.0$, right.

Table 7.1: Comparison of flame temperature at extinction between symmetric, adiabatic and asymmetric, non-adiabatic opposed jet flames. Non-adiabatic results are for a $T_r = 0.8$.

	T_{ext} [K]	
ϕ	Symmetric	$T_r = 0.8$
0.7	1698.7	1689.9
0.8	1775.2	1776.3
0.9	1844.7	1830.5
1.0	1906.7	1898.1
1.1	1957.8	1936.1

lower flame speeds. Similar to the response of flame temperature to heat loss, $S_{d,ph}$ asymptotically approaches a limit value at high stretch for the $T_r = 1.0$ and $T_r = 1.05$ test cases, although the physicality of a displacement based flame speed in this region is questioned. In the high stretch limit where the flame temperature and flame speed approach their asymptotes, the flame is no longer self supporting, as suggested by the lack of temperature rise above the product side temperature, but relies on any partial consumption of the reactant stream from diffusion of heat across the stagnation plane. Thus, although abrupt extinction is not observed in the stretched flame temperature for cases with $T_r > 1.0$, a consumption based flame speed provides a clear indication when a flame is no longer self-supporting, as defined by Equation 7.1 for the consumption of methane.

$$S_{c,CH_4}^{HD} = -\frac{1}{\rho_{reac} Y_{CH_4}} \int_{z_{reac}}^{z_{SP}} \dot{\omega}_{CH_4} dz \tag{7.1}$$

The bounds of the integral were chosen to be the reactant jet exit, z_{reac}, and the stagnation surface, z_{SP}, such that $S_{c,CH_4}^{HD} > 0$ only when methane is consumed on the reactant side of the stagnation surface. Figure 7.3 shows the same test cases as Figure 7.2 but for S_{c,CH_4}^{HD}. Note the steep drop off in S_{c,CH_4}^{HD} at high stretch indicating incomplete consumption of methane and the point at which the flame is no longer self-sustaining. Any consumption of methane beyond that point is the result of methane diffusion across the stagnation plane.

There are two conclusions from these studies. Namely, that recirculation zones of high enough temperature, $T_r > 1.0$, will prevent abrupt, extinction based events, and therefore decrease the possibility of flame holes, although variations in burning intensity and reaction rate would certainly be expected. Second, that the extinction stretch rate drastically decreases in the presence of heat loss from the flame to the recirculation zone ($T_r < 1.0$).

Given the ambiguity in the extinction limit for asymmetric stagnation flames with $T_r \geq 1.0$, we compare the stretched flame response for the symmetric configuration

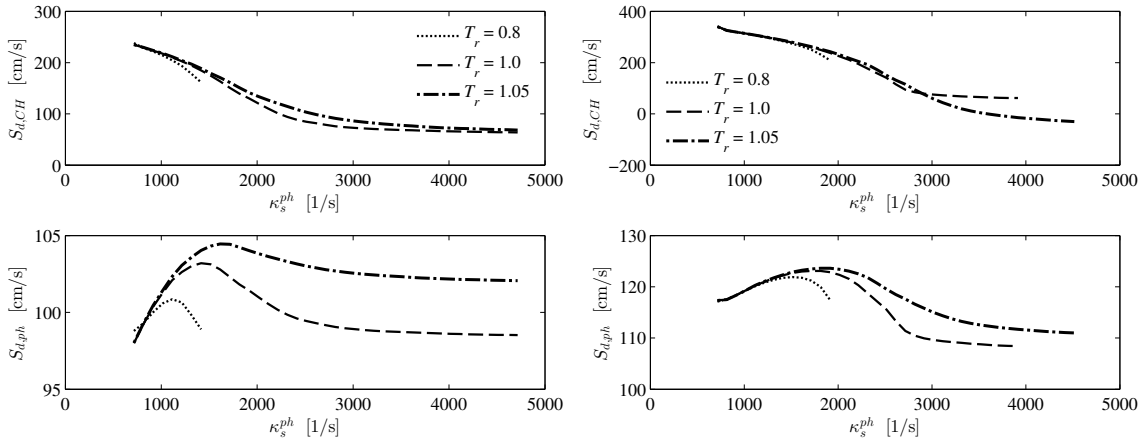

(a) $\phi = 0.8$ **(b)** $\phi = 1.0$

Figure 7.2: Stretched displacement flame speeds of a non-adiabatic, asymmetric, opposed jet methane-air flame at a $T_{ph} = 533K$, with varying normalized product side temperatures, T_r, for $\phi = 0.8$, left, and $\phi = 1.0$, right.

with the $T_r = 0.8$ test case, which also abruptly extinguishes, allowing for a κ_{ext}^{ph} to be quantified. Figure 7.4 shows the laminar flame speed stretch response, $S_{d,ph}\left(\kappa_s^{ph}\right)$, for these two test cases at $\phi = 0.8$, Figure 7.4a, and $\phi = 1.0$, Figure 7.4b. It is clear for both equivalence ratios, that κ_{ext}^{ph}, is much lower with heat loss. In fact, κ_{ext}^{ph} is consistently lower both in reference to the preheat zone, left, and CH-layer, right, as shown in Figure 7.5. In addition, $S_{d,ph}$ is also consistently lower for the $T_r = 0.8$ test case. Thus in the limit where $T_r < 1.0$, we expect the stability of the flame to be drastically influenced by heat loss as both $S_{d,ph}$ and κ_{ext}^{ph} strongly deviate from symmetric/adiabatic conditions.

7.2 Flame Sensitivity to Reactant Dilution

As abrupt extinction for the asymmetric opposed-jet configuration only occurred when the flame was subject to heat loss, $T_r < 1$, the effect of reactant dilution was studied for a single T_r of 0.8 for the test conditions shown in Table 5.2. The asymmetric model used to study the effect of heat losses was modified as shown in

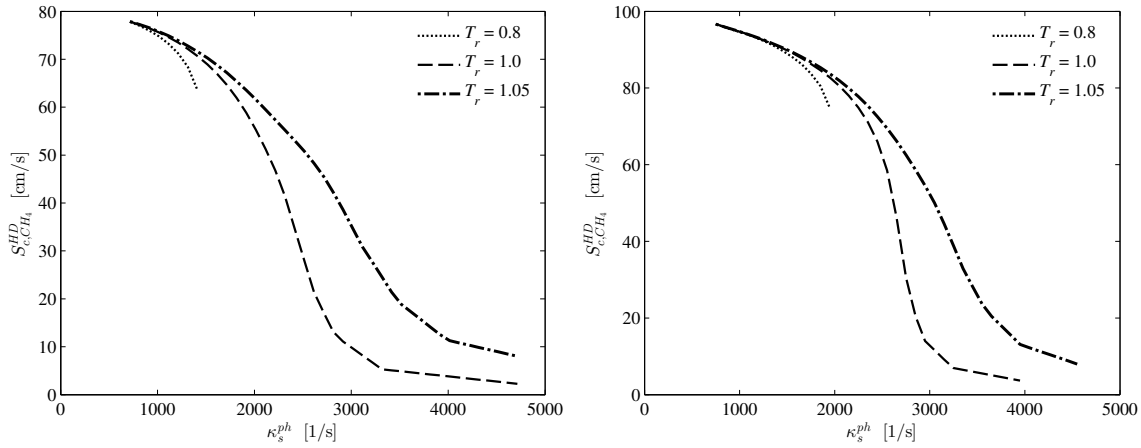

(a) $\phi = 0.8$ **(b)** $\phi = 1.0$

Figure 7.3: Stretched methane consumption flame speeds, S^{HD}_{c,CH_4}, of a non-adiabatic, asymmetric, opposed jet methane-air flame at a $T_{ph} = 533K$, with varying normalized product side temperatures, T_r, for $\phi = 0.8$, left, and $\phi = 1.0$, right.

Figure 5.8 to account for reactant dilution by mixing with the product or recirculation zone jet which has been cooled ($T_r < 1$). The mass fraction of products in the reactant stream, Y_{EGR}, was varied from no dilution to 30%. There were four quantities of interest that were used to quantify the effect of reactant dilution on the flame: T_{max}, $S_{d,ph}$, S_{c,CH_4} and κ_{ext}. The first three parameters are indicators of changes in the flame's response to stretch and the last an indicator of a change in the stretch space in which a flame can exist.

Figure 7.6 plots the maximum temperature response of the flame to stretch, $T_{max}\,(\kappa_s)$, shown for mixtures of varying reactant dilution. Note, these results are shown for varying ranges of stretch, terminating at the upper limit of flame stretch, κ_{ext}, for each respective test case. Clearly, increasing reactant dilution leads to increasingly lower flame temperatures at a fixed κ^{ph}_s, presumably the result of decreasing heat of combustion counteracting increases of reactant sensible enthalpy.

Next, the sensitivity of the stretched flame speed, $S_{d,ph}\,(\kappa_s)$, to reactant dilution, shown in Figure 7.7 is discussed. Contrary to flame temperature, flame speed increases

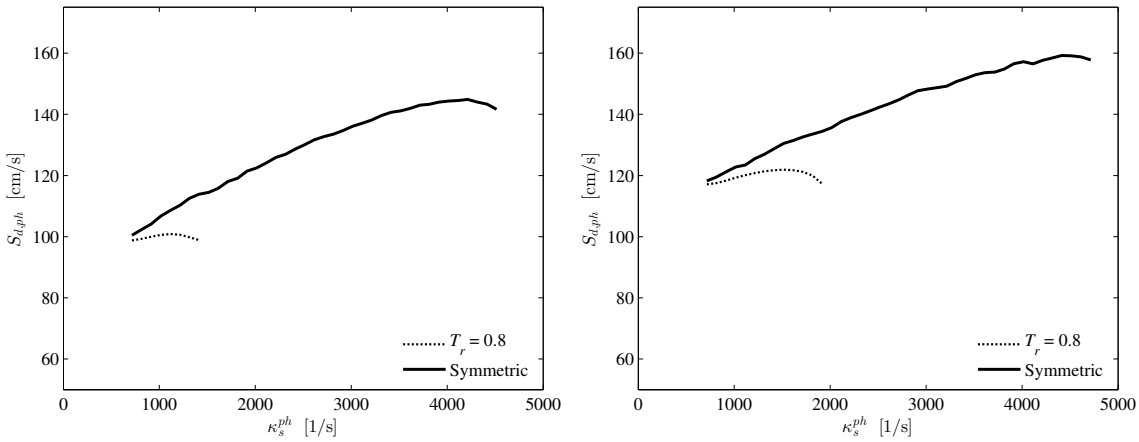

(a) $\phi = 0.8$ **(b)** $\phi = 1.0$

Figure 7.4: Effect of heat loss on the response of flame speed to stretch rate demonstrated from a comparison of symmetric opposed-jet calculations for the adiabatic case and asymmetric opposed-jet calculations with a $T_r = 0.8$ for the non-adiabatic test case. Flame speed and stretch is reported relative to the preheat zone, $S_{d,ph}\,(\kappa_s)$, for $\phi = 0.8$, left, and $\phi = 1.0$, right, for methane-air mixtures at a $T_{ph} = 533K$.

with Y_{EGR} and thus the flame benefits slightly from reactant dilution. For instance, at a $\phi = 0.8$ and $Y_{EGR} = 0.3$, Figure 7.7a, and at low stretch rates, $S_{d,ph}$ increases by $\approx 15\%$ while the $\kappa_{ext,ph}$ decreases by $\approx 26\%$. So long as the flame is far from being critically stretched, these results suggest a mechanism by which the attachment point location is resistant to downstream advection resulting from a kinematic imbalance between flow and flame speed. Assuming Y_{EGR} increases with standoff distance, local flame speed would increase as well and counteract the further displacement of the flame downstream. Note however, that the physics of edge flames are not captured by the opposed jet model.

The effect of EGR on methane based consumption speed, S_{c,CH_4}^{FD}, is similar to those observed for $S_{d,ph}$ as shown in Figure 7.8. Note that S_{c,CH_4}^{FD} was evaluated over the entire opposed-jet domain as defined by Equation 7.2, where z_{EGR} is the location of the reactant jet exit and z_{RZ} the location of the product or recirculation zone jet exit.

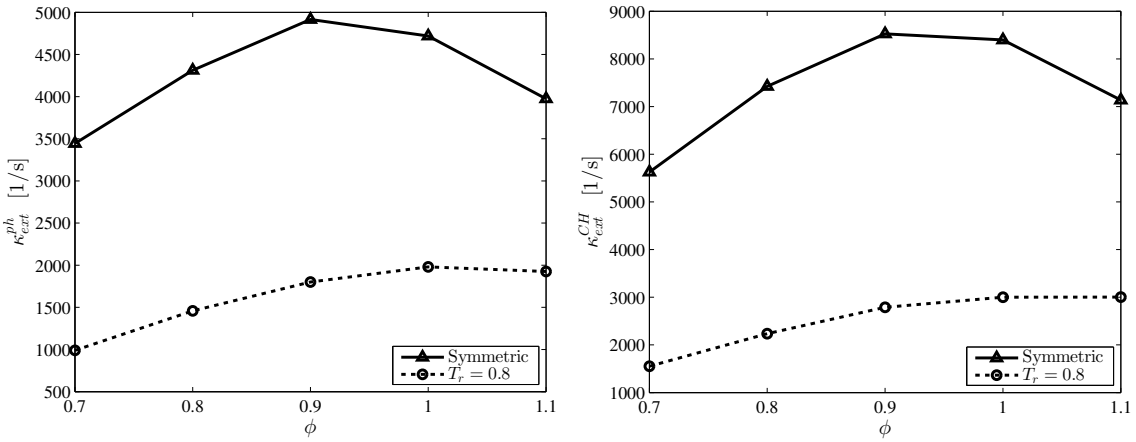

(a) $\kappa_{ext}^{ph}(\phi)$ **(b)** $\kappa_{ext}^{CH}(\phi)$

Figure 7.5: Effect of heat loss on the extinction stretch rate demonstrated from a comparison of symmetric opposed-jet calculations for the adiabatic case and asymmetric opposed-jet calculations with a $T_r = 0.8$ for the non-adiabatic test case. Extinction stretch rates are reported for κ_{ext}^{ph}, left, and κ_{ext}^{CH}, right, for methane-air mixtures at a $T_{ph} = 533K$.

Values of S_{c,CH_4} calculated over only the EGR side of the domain, $z_{EGR} < z < z_{SP}$, were equal to values calculated for the full domain, S_{c,CH_4}^{FD}, thus confirming that even with EGR, the consumption of methane remains confined to the EGR side of the domain and the abrupt nature of extinction for these mixtures.

$$S_{c,CH_4}^{FD} = -\frac{1}{\rho_{EGR} Y_{CH_4}} \int_{z_{EGR}}^{z_{RZ}} \dot{\omega}_{CH_4} dz \tag{7.2}$$

Lastly, Figure 7.9 summarizes the effect of Y_{EGR} on κ_{ext}^{ph}, Figure 7.9a, and κ_{ext}^{CH}, Figure 7.9b, for all test cases. Note, that while there is expected to be a upper limit in Y_{EGR} which would support a flame, that limit was not observed for the range of Y_{EGR} explored in these studies. Note as well, that reactant dilution is expected to occur only in the near field and at locations downstream where a flame hole might be present. Clearly though, the limit in flame stretch is influenced by the reactant

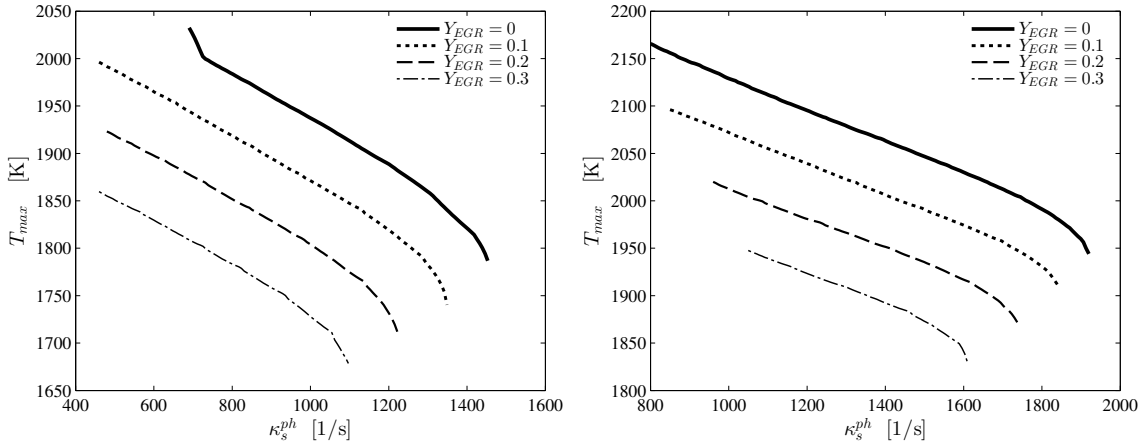

(a) $\phi = 0.8$ **(b)** $\phi = 1.1$

Figure 7.6: Flame temperature response, $T_{max}\,(\kappa_s)$, of a non-adiabatic, asymmetric, opposed jet methane-air flame at a $T_{ph} = 533K$, subject to varying degrees of reactant dilution, Y_{EGR}, with a fixed normalized product side temperatures, $T_r = 0.8$, for $\phi = 0.8$, left, and $\phi = 1.0$, right.

dilution.

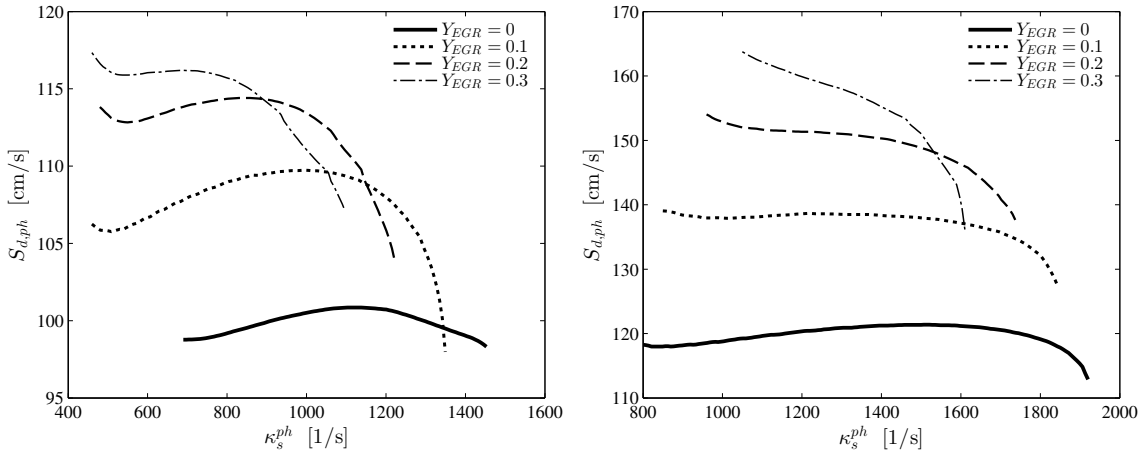

(a) $\phi = 0.8$ **(b)** $\phi = 1.0$

Figure 7.7: Stretched displacement flame speeds of a non-adiabatic, asymmetric, opposed jet methane-air flame at a $T_{ph} = 533K$, subject to varying degrees of reactant dilution, Y_{EGR}, with a fixed normalized product side temperatures, $T_r = 0.8$, for $\phi = 0.8$, left, and $\phi = 1.0$, right.

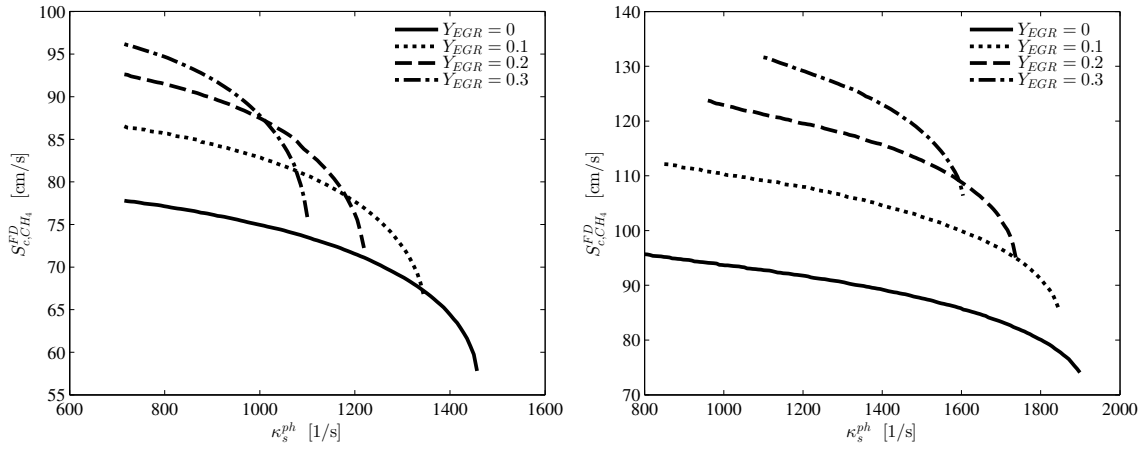

(a) $\phi = 0.8$ **(b)** $\phi = 1.1$

Figure 7.8: Stretched, methane consumption flame speeds, $S_{c,CH_4}^{FD}(\kappa_s)$, of a non-adiabatic, asymmetric, opposed jet methane-air flame at a $T_{ph} = 533K$, subject to varying degrees of reactant dilution, Y_{EGR}, with a fixed normalized product side temperatures, $T_r = 0.8$, for $\phi = 0.8$, left, and $\phi = 1.0$, right.

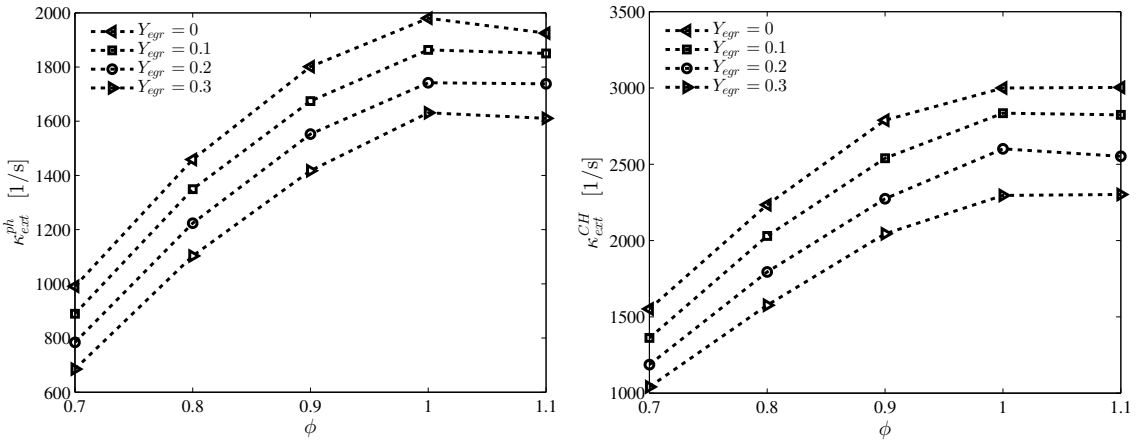

(a) $\kappa_{ext}^{ph}(\phi)$ **(b)** $\kappa_{ext}^{CH}(\phi)$

Figure 7.9: Effect of reactant dilution, Y_{EGR} , on extinction stretch rate, κ_{ext}, using an asymmetric opposed-jet configuration with a $T_r = 0.8$. Extinction stretch rates are reported for κ_{ext}^{ph}, left, and κ_{ext}^{CH}, right, for methane-air mixtures at a $T_{ph} = 533K$.

CHAPTER VIII

CONCLUSION

The major results and conclusions of this thesis are summarized in this chapter. Then recommendations for future studies related to this thesis are presented.

8.1 Reduced–Order Modeling of Flame Stabilization

A successful stretch based scaling of OSL flame stabilization in a swirl stabilized combustor was developed. This scaling was formulated on the hypothesis that shear layer stabilized flame transitions, either blowoff or attachment, are the result of a critical flame stretch limit. Assuming the extinction stretch rate, κ_{ext}, as the fundamental chemical kinetic parameter of interest, separate parameters were defined for scaling attachment and blowoff, $\kappa_{ext}\left(\phi, T_{ph}\right)$ and $\kappa_{ext,a}\left(\phi, T_{ref}\right)$ respectively. These parameters successfully collapsed OSL attachment/blowoff sensitivity to bulkhead temperature, equivalence ratio, and preheat temperature. Thus, this work demonstrated the applicability and relevance of κ_{ext} as a fundamental chemical parameter of interest to a practical combustor, which can be calculated from the reduced–order model of the opposed–jet configuration in CHEMKIN.

8.2 Experimental Measurements of Stretched Flames

The experimental studies and analysis performed provide invaluable data in the attachment point region of a shear layer stabilized flame. The experimental studies produced high spatial resolution measurements of CH-PLIF and PIV, which enabled the flame and flow field to be characterized. From this data set, stretch rate in the attachment point region was calculated, the physics of the flame at the attachment point were evaluated, and mixing upstream of the attachment point was estimated.

The major takeaways from each of these studies are presented next.

8.2.1 Flame Stretch Measurements

Flame stretch measurements performed at $u_{pm} = 35m/s$, showed that on average, these flames experienced stretch conditions that were favorable for these mixtures (positive flame stretch) and that were far from the stretch extinction limit predicted from OPPDIF calculations in CHEMKIN. However, the maximum mean stretch rate was observed for the stoichiometric test case and any deviation from stoichiometric conditions resulted in a decrease in the mean measured stretch rate resulting in flames that were less critically stretched. In fact, at the leanest equivalence ratio of $\phi = 0.8$, the condition closest to lean blowoff, the mean flame stretch rate was the smallest compared to the other test cases with $0.8 < \phi \leq 1.1$ (Figure 6.21). This would suggest, that OSL blowoff is not the result of local stretch induced extinction downstream of the leading edge in the nearfield. However, it should be pointed out that the opposed–model used to calculate κ_{ext} (OPPDIF in CHEMKIN) is a one-dimensional reduced–order model, which does not reflect the highly non-1D flame physics at the leading edge. As a result, there is uncertainty in concluding whether the stretch conditions at the leading edge become more or less critical without knowing the appropriate value of κ_{ext} at the leading edge.

Similar results were observed in the stretch measurements for the higher velocity test case, $u_{pm} = 70m/s$ with one exception (Figure 6.22). While the mean stretch rate was observed to be positive for $0.8 < \phi \leq 1.1$, at $\phi = 0.8$ the mean stretch rate was negative at several axial locations. This was a result of the mean flame angle becoming negative at those locations, presumably the result of a local imbalance between flame speed and flow speed advecting the flame front away from the incoming reactant jet. This in turn causes negative flame stretch contributions from the shear strain term, $\partial u_z/\partial r$, and a potential change in flame stability, as the flame has to recover from an

orientation and location where the flame stretch is now negative.

8.2.2 Attachment Point Orientation and Kinematics

The centerline of the CH-layer was observed to be near horizontal throughout the measurement domain and up to the leading edge of the flame, suggesting that the flame is *edge flame stabilized*. Analysis of the relative angle between the direction of flame propagation and flow, θ_{rel}, demonstrated the tangential alignment of flame with respect to the flow, supporting the edge flame hypothesis. Finally, analysis of the raw data also demonstrated the ability of this technique to observe the orientation and position at the leading edge of the flame which provided greater confidence in our conclusion that since normal propagation features were not observed, the flame is *edge flame stabilized*.

The CH-PLIF images obtained of the flame in the attachment point region provided a unique insight into the flame anchoring physics, challenging the classical concept of normal propagation stabilization at the attachment point. With respect to the CH-layer, the flow velocities tangent to the flame edge were calculated. Although the tangential velocity conditions at the edge of the CH-layer are higher than expected stretched flame speeds, the mean tangential velocity at the flame edge was relatively constant with respect to each mixture's unstretched flame speed for $\phi = 0.9 - 1.1$. However, there was a sharp increase in the mean tangential velocity at the flame edge for $\phi = 0.8$. This behavior, along with the noted alignment of the flame edge with the flow, further indicates that the flame is anchored by flame propagation tangent to the flame surface downstream of the leading edge. The measured trend of higher edge velocities and lower stretch rates at decreasing ϕ suggest that blowoff potentially occurs as a result of a local kinematic imbalance between flow velocity and edge flame speed, rather than local extinction. These studies motivate the further study and inclusion of edge flame physics in the evaluation of flame stabilization in shear

layers.

8.2.3 Attachment Point Reactant Composition

The burning properties of mixtures are highly sensitive to reactant composition and temperature. Therefore, even slight mixing between the incoming reactant stream and the recirculation zone upstream of the flame attachment point, could potentially alter the burning properties at the leading edge, and therefore, flame stability. For this study, the volumetric flow rate per unit length, $\dot{V}'$, was calculated along a line from the corner of the centerbody to the edge of the flame. These calculations showed a preference of the flame edge, r_{edge}, to reside in regions where reactant dilution was more likely to occur, $r_{edge} < 0$ (Figure 6.37). In fact, $\dot{V}'$ and r_{edge} positively correlate with each other. These results suggest that reactant dilution is occurring with a positive net effect on flame stability such that the attachment point preferentially sits in locations where the reactant stream is diluted with products.

8.3 Numerical Modeling of Recirculation Zone Physics

The calculations performed using the non-adiabatic opposed-jet model (Figure 5.7) and non-adiabatic opposed jet model with EGR (Figure 5.8) provided insight into the effect of heat losses from the flame to the recirculation zone and reactant dilution on flame stability. The results can be summarized as follows as two main conclusions. Abrupt flame extinction is only possible when there are heat losses from the flame. Second, product dilution up to $Y_{EGR} = 30\%$ increases the flame speed with a slight decrease in the extinction stretch rate. The first point explains the ability of the flame to withstand high stretch rates in regions supported by the recirculation of hot products downstream of the attachment point. The second point provides initial insight on potentially how the flame is able to withstand velocity fluctuations at the attachment point. Note, that in order to further validate the effect of reactant dilution, the experimental results strongly suggest the use an edge flame modeling

approach to calculate stretch limits and burning velocities.

8.4 Future Work Recommendations

There are two aspects related to this thesis that are addressed in this section: PIV measurements, and edge flame behavior.

8.4.1 PIV measurements

The PIV measurements could benefit from improvements in the accuracy of the velocity measurements and the temporal resolution. As was demonstrated in the analysis of error presented in the Appendix, Chapter A, the accuracy in instantaneous stretch rates suffered greatly from inaccuracies in velocity as estimated using PIV uncertainty analysis. Given the challenges of a swirling flow field, performing stereo-PIV would improve the optimization of the laser sheet thickness. With the measurement of the out-of-plane velocity component, the sheet thickness could be set at minimal thickness with acceptable loss of pairs. A thinner sheet would improve velocity measurements by minimizing variation of particle displacement within the thickness of the sheet. Time resolved PIV measurements would also improve the velocity measurements as spectral filtering of the velocity field measurements could be applied.

The cross-correlation used to calculate the PIV vectors was limited in its ability to only determine the displacement and resulting velocities in two orthogonal directions. Generalized digital particle image velocimetry (DPIV) algorithms have been developed which provide direct calculation of velocity, vorticity, and in-plane shear rates [79, 35, 40]. For example, Duncan *et al.* [35] demonstrated the superior ability of DPIV to characterize the velocity field of an Oseen vortex.

8.4.2 Edge flame behavior

The study of premixed edge flames, especially in the context of flame stabilization in practical combustors, is relatively immature. While configurations have been developed for the experimental study of edge flames, such as the angled-opposed jet burner [114, 113, 74], these experimental studies lack detailed flame and flow measurements in order to understand the flame stretch and velocity conditions with respect to the edge of the flame. Given the observed characteristics of the flame structure in the attachment point consistent with an edge propagation stabilization, additional fundamental studies of premixed edge flames and characterization of flame edge speeds would be beneficial. While numerical studies have been performed by Daou and Linan [29], these studies lack detailed chemical kinetics.

APPENDIX A

ERROR ANALYSIS

The section below will discuss various sources of error which influence the accuracy and precision of velocity and stretch measurements performed in this work using Particle Image Velocimetry (PIV). This analysis will address particle physics related to the ability of the particle to track the flow field when subject to thermophoretic forces, flow unsteadiness, and swirl induced centrifugal forces. In addition, the limitations of the PIV algorithm to precisely and accurately characterize the velocity field are addressed by a discussion of PIV velocity resolution and uncertainty analysis using cross-correlation statistics [124]. Velocity gradients are approximated using a finite differencing scheme, and as such, introduce sources of error which are discussed especially related to fields subject to vortex induced strain. Finally, a propagation of error analysis will then performed relating the various quantifiable sources of error in velocity measurements to parameters and metrics of interest for these studies. Namely flow velocities along and at the leading edge of the CH-layer, and the stretch conditions along the CH-layer. In conclusion, suggestions for improvements on the discussed measurement techniques are made.

A.1 Velocity Measurements

First and foremost, there are sources of error directly related to the physics governing particles suspended in a fluid medium. Ideally, the particle motion will very closely follow the flowfield. However, the particle size, and density affect its ability to follow the flowfield in reacting flowfields due to temperature gradient induced

thermophoretic forces. These same particle properties will affect its response to fluctuating flow conditions, and fluid rotation in the form of vortices or on a bulk scale through swirl. As is demonstrated, there is a compromise between particle responsiveness and resistance to thermophoretic forces when selecting particles for velocity field diagnostics. Second, errors related to the technique PIV are discussed. Errors in this sense are essentially related to ability of the PIV algorithm to report physically relevant velocities. This can be reduced to an analysis of particle retention within the laser plane, at a minimum, or within the PIV interrogation window size. Regions of large velocity gradients within an interrogation window can also introduce errors in the reported velocities in the form of bias error. Lastly, error estimates of the reported velocities are reported based on PIV resolution, as well using DaVis's uncertainty analysis toolbox based on cross-correlation statistics developed by Wieneke *et al.* [124].

A.1.1 Particle Error Sources

A.1.1.1 Particle Lag

Particle lag is a concern for LDV of PIV techniques in any flow where the material derivative of velocity is non-zero:

$$\frac{D\vec{u}}{Dt} \neq 0 \tag{A.1}$$

In other words, once the drag forces equilibrate the flow and particle velocity, fluid flow acceleration at any point in the flow field will potential reintroduce an imbalance between particle and flow velocity. How quickly the flow particle accelerates to the flow velocity depends on the particle lag time, or particle Stokes time, τ_s [6]:

$$\tau_s \equiv \frac{\rho_p d_p^2}{18\mu} \tag{A.2}$$

Bergthorson *et al.* [6] analyzed the effect of particle lag on particle velocity, u_p, providing this relationship for a particle in a uniformly accelerating flow field with a

constant velocity gradient, $du_f/dx = \sigma$:

$$\frac{u_p}{u_f} \cong \frac{1}{1 + C_{KW}\tau_s\sigma} \tag{A.3}$$

In this very simple example, we can understand the major factors influencing discrepancies between u_p and u_f, namely particle diameter, d_p, and velocity gradient magnitude, σ. Inspecting eqn. A.2, and eqn. A.3, it becomes clear that increasing d_p or σ results in larger relative differences between u_p and u_f, both very physically intuitive results.

In order to extend beyond this rather simple example, and into a more general framework of understanding particle lag, studies have been carried out to understand particle lag of particles subject to harmonic fluctuations [80, 81]. Melling's analysis of tracer particle dynamics in a harmonically oscillating flow environment produced the following expression for the ratio of the time averaged particle and fluid energy ($\bar{u_p^2}/\bar{u_f^2}$):

$$\frac{\bar{u_p^2}}{\bar{u_f^2}} = \left(1 + \frac{\omega_c}{C}\right)^{-1} \tag{A.4}$$

where Melling defines the characteristic frequency of the particle motion, C, as:

$$C = \frac{18\mu}{\rho_p d_p^2} \tag{A.5}$$

Equations A.4 and A.5 can be then used to establish cut-off frequencies, $1/\omega_c$, above which the mean energy of the particle is less than a defined threshold. Likewise, these equations can be used in order to determine the required particle size, d_p in order to achieve a specified f_c. For instance, alumina oxide particles, Al_2O_3, in a flame environment with a temperature of $1800K$, must be smaller than $2.46\mu m$ and $0.78\mu m$ to achieve f_c of 1 kHz and 10 kHz respectively.

A.1.1.2 Thermophoretic Forces

Thermophoretic forces could potentially influence the motion of seeding particles within the flow field, and thereby alter the calculated velocity field from PIV. These

forces are proportional to $\nabla T/T$ and act in the opposite direction of the temperature gradient. In the presence of a flame, thermophoretic forces will act to slow particles down as they pass through the flame. Brock's analysis of thermophoretic forces [10] provides the following relationship for modeling this force as cited by Bergthorson *et al.* [6]:

$$F_T = -\frac{6\pi\mu\nu d_p C_s \left(\frac{k_f}{k_p} + C_t Kn\right)}{(1 + 3C_m Kn)(1 + 2k_f/k_p + 2C_t Kn)} \frac{\nabla T}{T} \tag{A.6}$$

Note the direct dependence on particle material properties such as particle diameter, d_p, and particle thermal conductivity, k_p, as well as through the Kn number. So long as $Kn << 1$, decreasing d_p will decrease the thermophoretic force, F_T, acting on the particle. In addition, the higher the particle thermal conductivity, the smaller the F_T. However, although F_T may decrease, this may lead to larger discrepancies between particle and flow velocity as the mass of the particle is proportional to d_p^3. In addition, Stokes drag must also be taken into account in order to understand the net effect on the particle velocity.

Several investigations have been performed to quantify the effect of thermophoretic forces on measured particle velocities [115, 46, 109]. For instance, Sung *et al.* [109] performed experimental velocity measurements on a counterflow test geometry comparing them to calculations of the particle velocity subject to Stokes and thermophoretic forces. They observed particle velocity lag resulting in velocity bias as high as 15 cm/s within the flame zone. However, interesting enough, the particle velocity profiles for particle diameters of $5\mu m$ and $0.3\mu m$ are indistinguishable from one another within the flame. As such, we assume velocity errors due to thermophoretic forces, σ_u^{TP}, to be $\approx 15 cm/s$.

A.1.1.3 Centrifugal Effects

Given the swirling nature of this flow field, centrifugal effects could influence the path of the particles considerably. In fact, a significant change in the radial seeding

density at the dump plane was observed when $1-2\ \mu m$ diameter seeding particles were used rather than 5 μm diameter seeding particles. The $1-2\ \mu m$ diameter particles produced a uniform density of seeding in the annular jet entering the combustor while the 5 μm were located mainly in the outer shear layer with considerably less particles entering the combustor in the jet. Particle lag, or the ability of the particle to follow the flow changes, is responsible for this observed difference in seeding density, the smaller particles following the flow better than the larger ones. Given enough time, all particles are removed from the center of the swirling flow field, with particles distributed radially by increasing particle diameter.

A.1.2 PIV Error Sources

A.1.2.1 Loss of Pairs

The laser sheet optics and data acquisition settings require special attention in order to ensure that loss of pairs via out of plane motion does not invalidate the velocity fields acquired. To reduce the probability of loss of pairs, the laser sheet thickness ($1mm$) and shot separation times ($5\mu s$ & $2\mu s$) were chosen such that the maximum in plane movement would be 20% of the sheet thickness assuming maximum out of plane velocities, , on the order of the bulk flow velocities (35 & 70 m/s). The interrogation window size used to determine the PIV vector field were 32 x 32 sq. pixels in size with 50% overlap. An overlap of 50% was chosen in order to provide the highest spatial resolution of the flow field while limiting the possibility of a noisy local region in the Mie-scattering images leading to two invalid, neighboring vectors. After the PIV vector fields are calculated, they are then smoothed by a local 3x3 median filter before the strain fields are calculated.

A.1.2.2 High Flow Gradients

High flow gradients pose challenges for PIV in determining accurate and unbiased velocity vectors. Velocity bias is likely to occur with more lower velocity particles than

higher velocity particles staying in the interrogation window between shots for fixed interrogation window calculations. However, with the implementation of multiple passes, initial calculations of particle movement can be used to displace the relative location of interrogation windows between image pairs resulting in lower loss-of-pairs and decreased measurement bias. The accuracy of PIV velocities is also sensitive to velocity gradients. As discussed by Raffel *et al.* [92], rms uncertainties in velocities increase with velocity gradient. They also point out that smaller interrogation windows are less sensitive to velocity gradients and have lower uncertainties. In addition, the use of interrogation windows which deform based on the surrounding strain field will also improve the accuracy of the PIV vectors.

A.1.2.3 Seeding Density Gradients

Variations in seeding density can result from poor introduction of seed into the flow field, from the inability of seed to track fluid mechanic features of the flow field, such as vortices, or from temperature induced variations of the fluid density. Spatial variations in seeding density can adversely affect the accuracy of PIV through a bias error, as the velocity calculated is preferentially biased towards regions within an interrogation window with higher seeding densities [108, 82]. The seeding density is clearly higher in the non-reacted or reactant region, and although the location of the CH-layer centerline did exist at times in regions of uniform seeding, there were certainly times where it was close enough to the Mie-edge to be affected by seeding density gradients.

Next, estimates of particle density induced bias errors are provided. Note, that this error source only is present in regions where there is both a gradient in particle seeding density and velocity. Figure A.1 shows the representative velocity field and density field used in this analysis. The seeding density, ρ_{seed}, was assumed to vary

linearly over the temperature based flame thickness, δ_f^T:

$$\rho_{seed}(r) = \rho_{seed}^{prod} + \frac{\partial \rho_{seed}}{\partial r} r \approx \rho_{seed}^{prod} + \frac{\rho_{seed}^{reac} - \rho_{seed}^{prod}}{\delta_f^T} r \tag{A.7}$$

which is valid for $0 < r < \delta_f^T$ and where ρ_{seed}^{prod} is the seeding density in the product region, ρ_{seed}^{reac} is the seeding density in the reactant region, and δ_f^T is the temperature based flame thickness. A linear gradient in axial velocity was assumed as well:

$$u_z(r) = \frac{\partial u_z}{\partial r} r \approx \frac{0.9 u_{bulk}}{\delta_{bl}} r \tag{A.8}$$

where the transverse gradient in axial velocity was approximated by the bulk velocity, u_{bulk}, and boundary layer thickness, δ_{bl}. Since velocities are biased towards higher seed density regions, the center of particle mass within an PIV interrogation window, $\bar{r}$, is determined using Equation A.7. The difference in velocity at the center of the interrogation window, r_c, and at $\bar{r}$ is determined:

$$\Delta u_z = u_z(\bar{r}) - u_z(r_c) \approx (\bar{r} - \Delta_{PIV}) \frac{0.9 u_{bulk}}{\delta_{bl}} \tag{A.9}$$

where Δu_z is the bias error in velocity caused by variations in particle seeding density and Δ_{PIV} is the PIV vector spacing. Δu_z increases with velocity gradients in the seeding gradient direction and with seeding density gradients. It is also sensitive to the ratio of seeding density in the reactants to that in the products. In the estimates of seeding density bias errors in these studies, the ratio of average intensity in the reactant and product regions was used as an indicator of seeding particle density with values ranging from 2.5 to 2.8. Note that Δu_z is not a function of the absolute velocity within an interrogation window and it is assumed that in-plane and out-of-plane loss of pairs are not present.

For the $u_{bulk} = 35 m/s$ test case, Δu_z ranged from $1.8 m/s$ to $1.4 m/s$ with larger bias errors present towards the product side of the flow field. These values are upwards of $\approx 40\%$ of the mean velocity conditions at the leading edge of the flame for the $0.8 < \phi < 1.1$ test cases but decrease relative to the mean velocity conditions for the

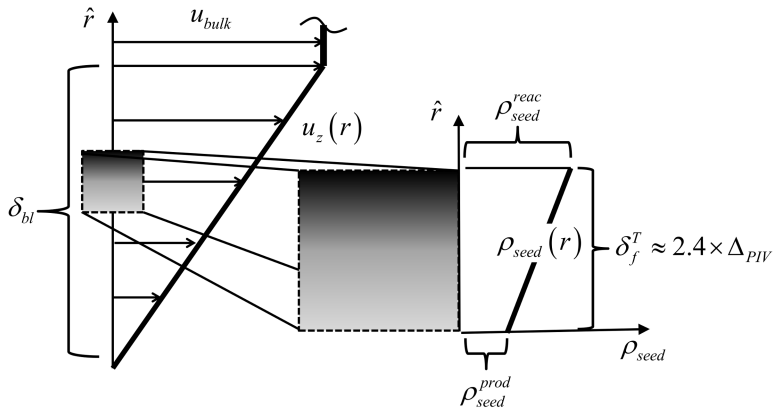

Figure A.1: Schematic representing seed density variation within shear layer.

$\phi = 0.8$ test cases to $\approx 10\%$. These values are high compared to other velocity error sources, however, the transition from high to low density seeding in the measurements was observed to occur over distances of $\approx 1mm$ rather than $\delta_f^T \approx 0.26mm$. This larger transition from low to high seeding density results in considerably lower velocity bias errors of $\approx 0.7m/s$, which are on the order of the other sources of error expected.

A.1.3 PIV Velocity Error Estimation

The error in measured velocities using PIV is discussed in this section. There are two approaches of error estimation that are discussed, one related to the limitations of the cross-correlation PIV algorithm to determine the actual displacement of the particles and the second related to direct error estimation of velocity uncertainties. The first approach which is discussed quantifies a velocity uncertainty based on PIV's limitation of particle displacement resolution on the sub-pixel scale. This approach to velocity uncertainty quantification is referred to as sub-pixel resolution error. There have been many methods developed for the second approach to directly quantify velocity uncertainty. These methods have the potential to directly quantify velocity uncertainty resulting from physical sources as well as from PIV limitations. Four such direct estimation methods are introduced followed by a more in depth discussion of the *correlation statistics* method.

A.1.3.1 Sub-Pixel Resolution Error

Random uncertainty in the velocity vectors caused by particle displacement resolution limitations of the PIV algorithm was determined by estimating the precision of the sub-pixel interpolation algorithm in locating the peak of the particle displacement, cross correlation map. This was carried out using the guidelines and equation provided by Raffel *et al.* [92]:

$$\sigma_u^{PIV} = u\frac{\delta_d}{d} = \frac{\delta_d}{\Delta t \cdot p_{res}} \tag{A.10}$$

where u, d, δ_d, Δt, and p_{res} are the local velocity, corresponding movement in pixel space, sub-pixel interpolation precision, shot separation time, and pixels per unit length. Using the second expression for σ_u, velocity uncertainties are estimated for the two bulk velocity test conditions:

$$\sigma_{u=35m/s}^{PIV} = \frac{0.04\ pixels}{(5e-6s)\cdot(1/0.007\frac{pixels}{mm})} \tag{A.11}$$

$$\sigma_{u=35m/s}^{PIV} = 0.6m/s \tag{A.12}$$

$$\sigma_{u=70m/s}^{PIV} = 0.1m/s \tag{A.13}$$

Note, that the decrease in velocity error for the higher velocity case is driven by the shorter shot separation times used ($\Delta t^{70\ m/s} < \Delta t^{35\ m/s}$).

Improvement upon PIV resolution error is a balance between other limitations of the technique. For instance, increasing particle size is one method to decreasing δ_d, however as discussed, larger particles have higher particle flow lags and will not follow the flow as precisely. Furthermore, increasing the field resolution by zooming in, will increase p_{res} and decrease δ_d, but will result in lower Δt in order to prevent in-plane loss-of-pairs, assuming that the same interrogation window size is used.

A.1.3.2 Methods of Error Quantification

A relatively new advancement in the field of PIV is the development of methods to directly calculate local estimates of the error in an instantaneous velocity vector. Four methods are presented which have been proposed to quantify velocity uncertainty by the PIV community as summarized by Sciacchitano *et al.* [102]. They are the *uncertainty surface* method [116], *particle disparity* method [103], *peak ratio* method [14], and the *correlation statistics* method [123]. These development of these methods are a critical first step towards quantitative error estimation of PIV data.

While the objective of these error quantification methods are the same, they differ in their approach and ability to do so. The most straightforward is the *peak ratio* method which empirically determines the uncertainty in the velocity magnitude as a function of the ratio of the magnitudes of the peak and second peak of the cross-correlation map, or peak to peak ratio, PPR [14]:

$$\sigma_{|u|} = 0.402 PPR^{-0.84} \tag{A.14}$$

While the PPR is easily obtainable, the coefficients of Equation A.14 are empirical and must be determined from analysis of synthetic or artificially produced velocity fields.

The *uncertainty surface method* offers an approach which allows for the sensitivity to various sources of error to be accounted for in a lookup table [116]. This lookup table or uncertainty surface is generated by using synthetic images which vary parameters of interest and determine the error in reported velocity components. In their work, Timmins *et al.* applied this technique to error from particle image diameter, particle seeding density, particle displacement, and velocity gradient. This method is limited by its ability to only assess errors caused by the PIV algorithm and has only been utilized in the study of a laminar flow field.

The last two methods provide the most direct and robust approach to determining

the error in PIV measurements. Both the *particle disparity* method and the *correlation statistics* method determine error by comparing the actual particle displacement field with the particle displacement field predicted from the PIV algorithm. With the *particle disparity* method, the predicted particle displacement field is determined by shifting the first particle image field by the local displacement field calculated. Ideally, the predicted particle displacement field and the second particle image field would be identical with the absence of noise. Using the PIV algorithm, the difference between between predicted and actual particle image fields is determined as an estimate of local error for each particle. Instead of analyzing the individual contributions of particles to the error in each velocity vector reported, the *correlation statistics* method relies on analysis of the shape of the correlation map of the predicted and actual particle fields, with the assumption that the correlation map is symmetric when there is no error. Through analysis of the sources of asymmetries in the correlation map, the overall error, resulting from the PIV algorithm as well as physical sources is determined. Wieneke and Prevost [123] and Wieneke [124] explore the sensitivity of PIV error to various flow field, particle, and image quality characteristics.

The generality of the *correlation statistics* technique make it an attractive choice for evaluating PIV errors which has been implemented into commercial PIV software, such as DaVis. The details of this method as well as estimates of error in the measurements used in these studies is discussed in greater detail in the following section.

A.1.3.3 Uncertainty Analysis: Cross-Correlation Statistics

The *correlationstatistics* method of PIV error quantification developed by Wieneke and Prevost [123, 124] and implemented in DaVis 8.2, was used to provide estimates of the error in the PIV measurements used in these studies. This technique allows for random and bias errors to be determined for each component of velocity. Figure

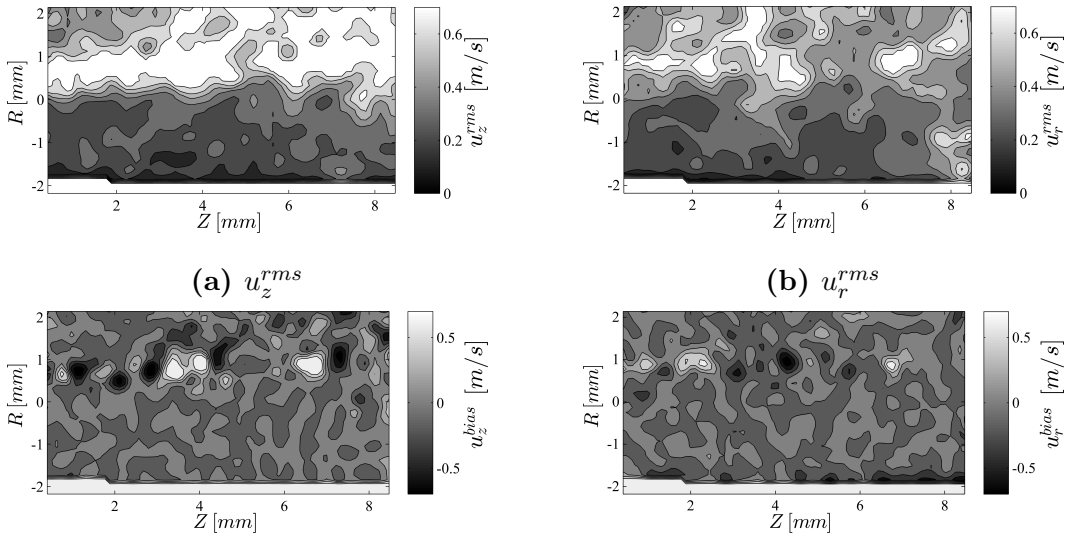

(a) u_z^{rms} **(b)** u_r^{rms}

(c) u_z^{bias} **(d)** u_r^{bias}

Figure A.2: Instantaneous PIV vector error fields for $\phi = 0.9$ and $u_{pm} = 35m/s$ test case obtained from DaVis.

A.2 shows representative instantaneous error fields for the $\phi = 0.9$, $u_{pm} = 35m/s$ test case.

Certainly these fields suggest that the total error, from random and bias sources, is highly dependent on the spatial location within the flow field and specifically the fluid features present in the flow field. Based on the fields shown, we expect that the distribution of velocity error to be different in the *jet*, *shear layer*, and *recirculation* zone regions of the flow field. For instance, it appears as if the highest random errors occur within the jet and shear layer while the highest bias errors are present in the shear layer. In other words, the local physics of the flow field appear to be causing a variation in the local velocity uncertainties such that the error is not spatially uniform. This is evident from the mean velocity uncertainty fields in Figure A.3 and further supported by a comparison of the PDFs of the random and bias error for the three regions identified in this flowfield (Figure A.4). Certainly the shear layer is a challenging region of the flow field to perform PIV velocity measurements in with its

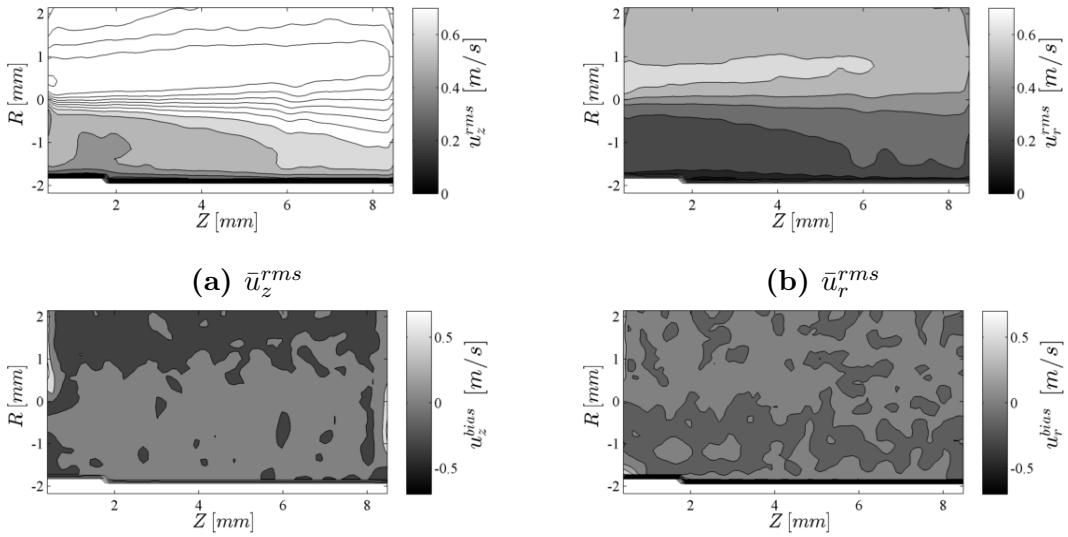

(a) $\bar{u}_z^{rms}$ **(b)** $\bar{u}_r^{rms}$

(c) $\bar{u}_z^{bias}$ **(d)** $\bar{u}_r^{bias}$

Figure A.3: Time averaged PIV vector error fields for $\phi = 0.9$ and $u_{pm} = 35m/s$ test case obtained from DaVis.

large spatial gradients in flow velocity; the challenges of which have been discussed in a previous section. Inspecting the PDFs of Figure A.4, it becomes clear that the region of greatest interest in these studies, the shear layer, has the highest mean rms velocity uncertainties, and the largest range of bias errors amongst the three regions. Given this information, we are interested in how these uncertainties in velocity impact our ability to calculate accurate strain rates from PIV velocity vectors.

We next examine the uncertainty in the calculated strain for a representative location within the shear layer. This location is held fixed for the span of equivalence ratios for the $u_{pm} = 35\ m/s$ test cases. In our calculation of the uncertainty in an instantaneous strain measurement, we have chosen a central difference estimate of the strain. As such, error in an instantaneous strain rate from random and bias sources is estimated as:

$$\sigma_{u_{i,x}}^{rms}(x_0, t) = \sqrt{\frac{\sigma_{u_i^{rms}}(x_1, t)^2 + \sigma_{u_i^{rms}}(x_{-1}, t)^2}{2\Delta x^2}} \tag{A.15}$$

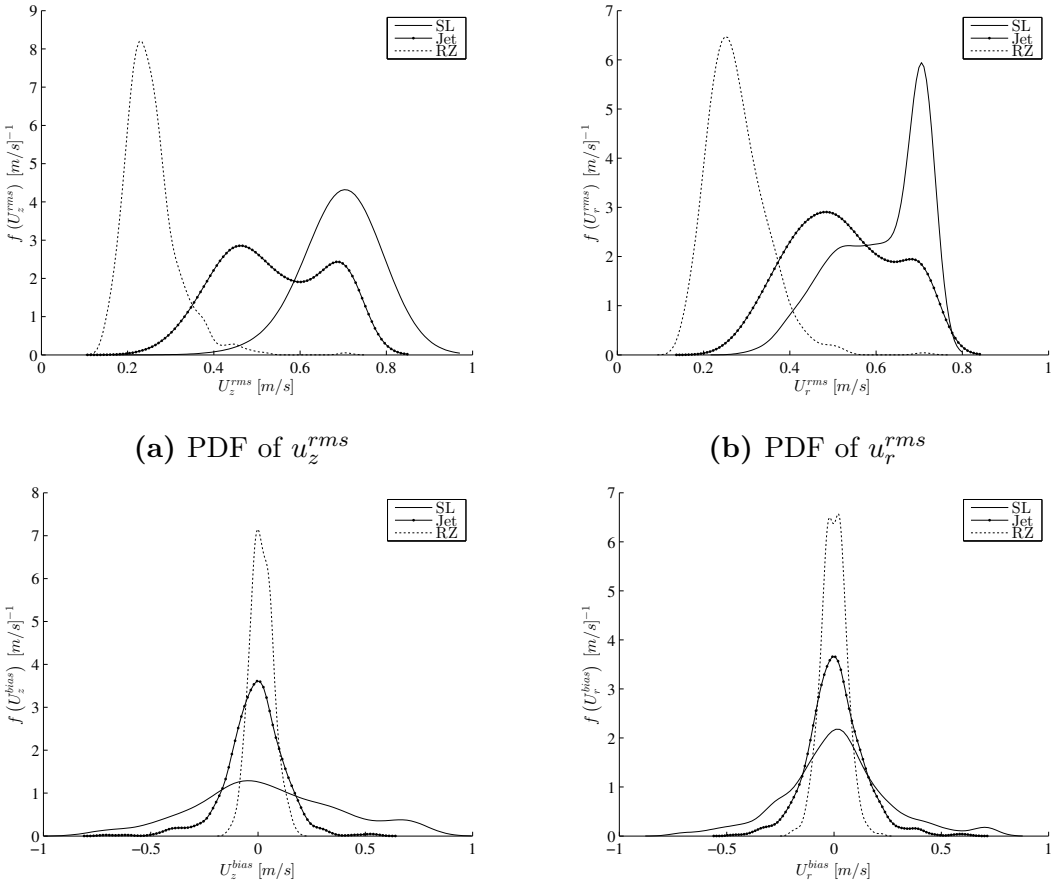

(a) PDF of u_z^{rms}

(b) PDF of u_r^{rms}

(c) PDF of u_z^{bias}

(d) PDF of u_r^{bias}

Figure A.4: PDFs of velocity *rms* and *bias* uncertainties in velocity by flow field region for the $\phi = 0.9$ and $u_{pm} = 35m/s$ test case.

$$\sigma_{u_{i,x}}^{bias}(x_0,t) = \frac{\sigma_{u_i^{bias}}(x_1,t) - \sigma_{u_i^{bias}}(x_{-1},t)}{2\Delta x} \tag{A.16}$$

where $\sigma_{u_{i,x}}$ is the spatial derivative of the velocity component in direction i with respect to the spatial direction x, σ_{u_i} is the instantaneous uncertainty of the velocity component in direction i, and Δx is the separation distance between point measurements (*e.g.*, $\Delta_x = x_1 - x_0$). Figure A.5 shows the PDFs of the computed strain uncertainties resulting from random and bias sources of velocity uncertainties for the strain terms largely responsible for flame stretch for these particular studies of a shear layer stabilized flame, $u_{z,r}$ and $u_{z,z}$. Note that the average bias induced strain uncertainty is much less than the average rms induced strain uncertainty. In fact, bias induced strain uncertainty is on the order of strain uncertainties resulting from PIV resolution uncertainties. Strain uncertainty from rms sources is much higher on the order of 10^3 s^{-1}. Note as well that while the distribution of $\sigma_{u_{z,z}}^{rms}$ seems symmetric, the distribution of $\sigma_{u_{z,r}}^{rms}$ is clearly not although the ranges of these parameters are comparable. With calculated mean stretch rates on the same order of these strain uncertainties, instantaneous measurements would have relative uncertainties on the order of the reported value, and would be very inaccurate.

A.2 Propagation of Error

A.2.1 Edge Velocity Measurements

The error in edge velocities from uncertainties in the velocity measurement as well as uncertainties in flame angle are addressed. We will take into consideration error in velocity measurements caused by thermophoretic forces, PIV resolution limitations, and the error estimated from cross-correlation statistics. Below are expressions for the measurement uncertainty of u^T and u^N:

$$\sigma_{u^T} = \left[\sigma_u^2 + \left(u_r cos\theta_f - u_z sin\theta_f\right)^2 \sigma_{\theta_f}^2\right]^{1/2} \tag{A.17}$$

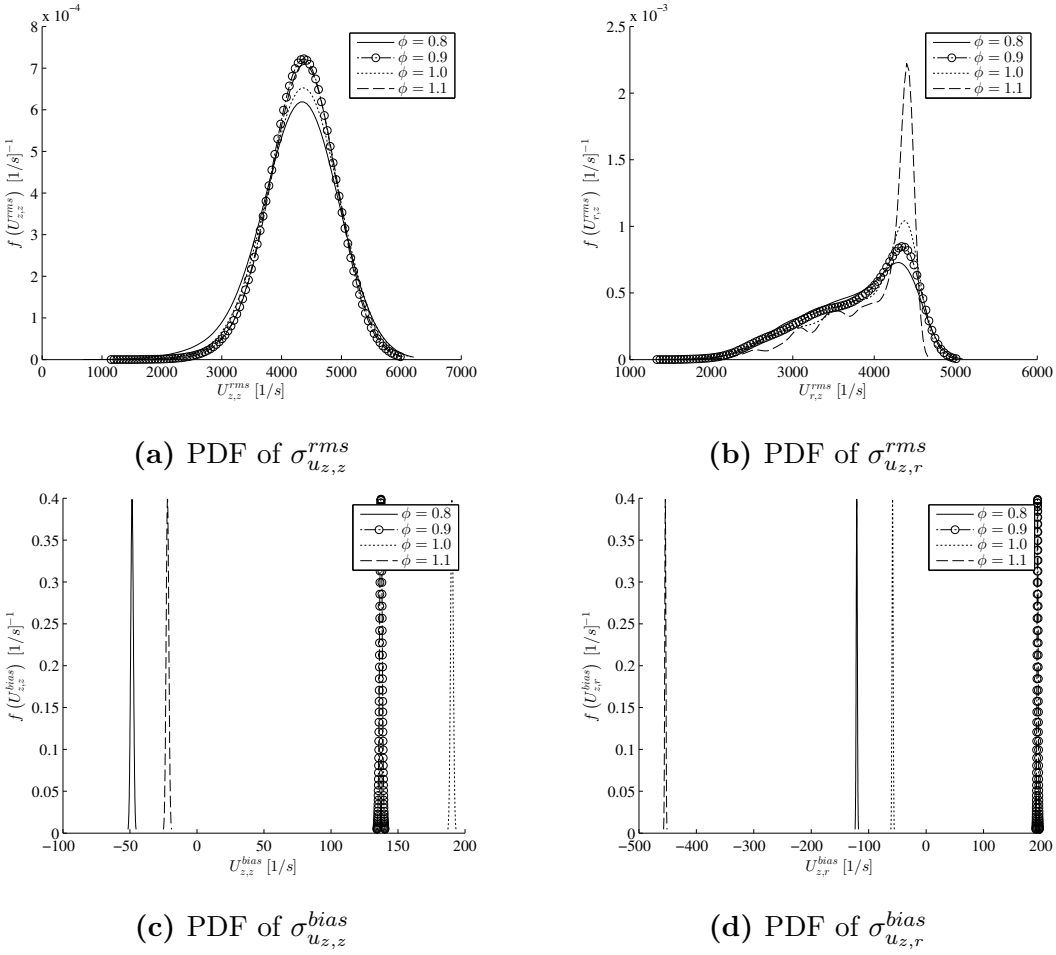

(a) PDF of $\sigma_{u_{z,z}}^{rms}$

(b) PDF of $\sigma_{u_{z,r}}^{rms}$

(c) PDF of $\sigma_{u_{z,z}}^{bias}$

(d) PDF of $\sigma_{u_{z,r}}^{bias}$

Figure A.5: PDFs of strain errors with the shear layer resulting from *rms* and *bias* uncertainties in velocity for the dominant strain sources of flame stretch, $u_{z,r}$ and $u_{z,z}$, for the $u_{pm} = 35m/s$ test cases.

$$\sigma_{u^N} = \left[\sigma_u^2 + \left(u_z cos\theta_f - u_r sin\theta_f\right)^2 \sigma_{\theta_f}^2\right]^{1/2} \tag{A.18}$$

Uncertainty in an instantaneous measurement of both velocities is dependent on the velocity components and the flame angle at that point in time. As a worst case bound, we calculate the edge velocity uncertainty for $u_z = 10 \times u_r = 10m/s$ and $\theta_f = 45°$. In addition, we combine the error contributions from thermophoretic effects, PIV resolution, and cross-correlation estimates as follows:

$$\sigma_u = \sqrt{\sigma_u^{PIV^2} + \sigma_u^{TP^2} + \sigma_u^{UA^2}} \tag{A.19}$$

where σ_u^{PIV}, σ_u^{TP}, and σ_u^{UA} are velocity uncertainties from PIV resolution limits, thermophoretic effects, and cross-correlation estimates. Note, although we include thermophoretic induced velocities as a general contribution to uncertainty in velocity, it physically only impedes particle motion normal to the flame front or parallel to the direction of the temperature gradient. Also, compared to other sources of error, thermophoresis is negligible within the shear layer with total error dominated by σ_u^{UA}, presumably the result of physical sources of error such as particle tracking, loss of pairs, the presence of high strain rates, and in-plane variation of the flow field. Note, within the shear layer, the uncertainty in velocity magnitude is estimated as a worst case to be $\approx 1.7m/s$ for the $u_{pm} = 35m/s$ test case with dominant contributions from $u_{z,rms}$ and $u_{r,rms}$, and negligible contributions from $u_{z,bias}$ and $u_{r,bias}$, on average.

This results in velocity uncertainties of $\approx 1.7m/s$ for both σ_{u^T} and σ_{u^N} with dominant contributions coming from the uncertainty of and sensitivity to the velocity measurement. These uncertainties are insignificant relative to the tangential velocities measured but certainly significant compared to the mean normal velocities and expected flame speeds for these mixtures.

A.2.2 Flame Stretch Measurements

Derivatives of the velocity field were approximated using a centered difference scheme. Truncation error for this scheme is $O(\Delta x^2$ and therefore minimized as grid spacing is decreased. However, as grid spacing is decreased, error from measurement noise becomes increasingly large and, at a small enough grid spacing, can dominate leading to increasing error with decreasing grid size. The strain field was also smoothed by locally averaging the nearest three strain measurements to the point of interest. This treatment of the strain field is consistent with that taken by Filatyev *et al.* [41]. Finally, a linear propagation of error analysis was carried out in order to calculate the uncertainty in an instantaneous measurement of flame stretch,σ_{κ_s}, as shown below:

$$\begin{aligned}\sigma_{\kappa_s} = &\left(\frac{\partial \kappa_s}{\partial u_r}\sigma_{u_r}\right)^2 + \left(\frac{\partial \kappa_s}{\partial u_{r,r}}^2 + \frac{\partial \kappa_s}{\partial u_{z,z}}^2 + \frac{\partial \kappa_s}{\partial u_{z,r}}^2 + \frac{\partial \kappa_s}{\partial u_{z,r}}^2 + \frac{\partial \kappa_s}{\partial u_{r,z}}^2\right)\sigma_{\overline{\overline{S}}}^2 \\ &+ \left(\frac{\partial \kappa_s}{\partial r}\sigma_r\right)^2 + \left(\frac{\partial \kappa_s}{\partial \theta_f}\sigma_{\theta_f}\right)^2\end{aligned} \tag{A.20}$$

Note the second grouping of the sensitivities of flame stretch to each of the sources of 2D flame strain as a result of the uncertainty being the same for all strain terms. This expression can be further simplified by first examining the sensitivity of flame stretch to the independent variables:

$$\begin{aligned}&\frac{\partial \kappa_s}{\partial u_r} = \frac{1}{r},\ \frac{\partial \kappa_s}{\partial r} = -\frac{u_r}{r^2} \\ &\frac{\partial \kappa_s}{\partial u_{r,r}} = sin^2\theta_f,\ \frac{\partial \kappa_s}{\partial u_{z,z}} = cos^2\theta_f \\ &\frac{\partial \kappa_s}{\partial u_{z,r}} = \frac{\partial \kappa_s}{\partial u_{r,z}} = -cos\theta_f sin\theta_f \\ &\frac{\partial \kappa_s}{\partial \theta_f} = +2u_{r,r}sin\theta_f - 2u_{z,z}cos\theta_f - (u_{z,r} + u_{r,z})\left(2cos^2\theta_f - 1\right)\end{aligned}$$

Expanding the each term, the following simplification to the flame strain sensitivity terms can be carried out:

$$\begin{aligned}\left(\frac{\partial \kappa_s}{\partial u_{r,r}}^2+\frac{\partial \kappa_s}{\partial u_{z,z}}^2+\frac{\partial \kappa_s}{\partial u_{z,r}}^2+\frac{\partial \kappa_s}{\partial u_{r,z}}^2\right) &= sin^4\theta_f+cos^4\theta_f+2cos^2\theta_f sin^2\theta_f \\ &= sin^4\theta_f+cos^2\theta_f sin^2\theta_f+cos^4\theta_f+cos^2\theta_f sin^2\theta_f \\ &= sin^2\theta_f\left(sin^2\theta_f+cos^2\theta_f\right)+cos^2\theta_f\left(cos^2\theta_f+sin^2\theta_f\right) \\ &= sin^2\theta_f+cos^2\theta_f \\ &= 1\end{aligned}$$

σ_{κ_s} is simplified to the following expression:

$$\sigma_{\kappa_s}=\left[\begin{array}{c}\frac{1}{r^2}\sigma_{u_r}^2+\frac{u_r^2}{r^4}\sigma_r^2+\sigma_{\frac{\partial}{S}}^2 \\ +(2u_{r,r}sin\theta_f-2u_{z,z}cos\theta_f-\left(u_{z,r}+u_{r,z}\right)^2\left(2cos^2\theta_f-1\right))^2\sigma_{\theta_f}^2\end{array}\right]^{1/2} \tag{A.21}$$

Taking into account the orientation of the flame in this particular flow field, ($\theta_f \approx 0°$), removing terms with small error sources, (σ_{u_r} & σ_r), and based on inspection of the strain field leaving only the dominant strain terms, $u_{z,z}$ & $u_{z,r}$, and further confirmed by inspection of the contributions to flame stretch, eqn. (A.21) can be further reduced to:

$$\sigma_{\kappa_s} \approx \left[\sigma_{\frac{\partial}{S}}^2+\left(-2u_{z,z}-u_{z,r}\right)^2\sigma_{\theta_f}^2\right]^{1/2} \tag{A.22}$$

The uncertainty in the flame angle was assumed to be 5° based on the observed flame angles distributed in groupings 2.5° apart, presumably the resolution of flame angle measurements. The sensitivity of flame stretch to flame angle is a function of the instantaneous strain conditions. Therefore we present a worst case result based on the maximum observed sensitivity to flame angle:

$$\max\left(\left|\frac{\partial \kappa_s}{\partial \theta_f}\right|\right)\sigma_{\theta_f} \approx 900\ s^{-1} \tag{A.23}$$

where:

$$\frac{\partial \kappa_s}{\partial \theta_f} \approx -2u_{z,z} - u_{z,r} \tag{A.24}$$

Given the uncertainty in the velocity measurements, from each of the sources of error, the overall uncertainty in the stretch measurements can be calculated. For instance, upon inspection of the PDFs of strain errors, Figure A.5, the uncertainty in strain rate, $\overline{\overline{S}}$, is assumed to be $\approx 4500\ 1/s$. Comparing these two sources of flame stretch uncertainty, it is clear that the maximum uncertainty in stretch measurements is dominated by sensitivity to and uncertainty in velocity conditions.

Note, that the uncertainty in an instantaneous stretch measurement is on the order of the reported mean values. These values are typical of PIV measurement techniques which are very noisy. However, given the number of samples, and as reported in Chapter 6, the uncertainty in the reported mean values of stretch are a fraction of the mean values. Thus, although there is low relative confidence in reported instantaneous stretch measurements, the uncertainty in the reported mean stretch values is low for all test cases.

APPENDIX B

SUPPLEMENTAL MATERIAL: SWIRL FLAME SENSITIVITY TEST CASES

Table B.1: Line fits of $\phi\,(T_{bhd})$ for OSL attachment and blowoff transitions for centerbody diameter, d_{cb}, sensitivity test cases. Fits are valid for range of bulkhead temperatures, T_{bhd}, indicated in table.

	Case A					**Case B**				
Case No.	m_{attach}	b_{attach}	$m_{blowoff}$	$b_{blowoff}$	T_{bhd}, [K]	m_{attach}	b_{attach}	$m_{blowoff}$	$b_{blowoff}$	T_{bhd}, [K]
1	-3.95E-04	0.820	-5.03E-04	0.776	500→625	-2.65E-04	0.745	-9.55E-05	0.580	500→675
2	-1.27E-04	0.587	-7.12E-04	0.864	475→600	-3.13E-04	0.682	-5.11E-04	0.721	475→625
3	-6.92E-07	0.649	-1.55E-04	0.626	350→525	-5.11E-05	0.649	-3.91E-04	0.697	375→525

Table B.2: Line fits of $\phi\,(T_{bhd})$ for OSL attachment and blowoff transitions for combustor diameter, d_{comb}, sensitivity test cases. Fits are valid for range of bulkhead temperatures, T_{bhd}, indicated in table.

	Case A					**Case B**				
Case No.	m_{attach}	b_{attach}	$m_{blowoff}$	$b_{blowoff}$	T_{bhd}, [K]	m_{attach}	b_{attach}	$m_{blowoff}$	$b_{blowoff}$	T_{bhd}, [K]
4	-1.27E-04	0.587	-7.12E-04	0.864	475→600	-2.53E-04	0.623	-2.60E-04	0.629	450→650
5	-6.92E-07	0.649	-1.55E-04	0.626	400→525	-7.98E-05	0.618	-4.51E-05	0.601	350→475

Table B.3: Line fits of $\phi(T_{bhd})$ for OSL attachment and blowoff transitions for combustor length, l_{comb}, sensitivity test cases. Fits are valid for range of bulkhead temperatures, T_{bhd}, indicated in table.

	Case A					Case B				
Case No.	m_{attach}	b_{attach}	$m_{blowoff}$	$b_{blowoff}$	T_{bhd}, [K]	m_{attach}	b_{attach}	$m_{blowoff}$	$b_{blowoff}$	T_{bhd}, [K]
6	-2.88E-04	0.645	-2.38E-04	0.618	475→650	-2.53E-04	0.623	-2.60E-04	0.629	425→650
7	-2.96E-04	0.748	-3.52E-04	0.738	325→575	-7.98E-05	0.618	-4.51E-05	0.601	375→475
8	-2.69E-04	0.639	-2.78E-04	0.643	450→675	-1.99E-04	0.594	-2.02E-04	0.594	450→675
9	-2.94E-04	0.761	-2.06E-04	0.673	350→575	-3.93E-04	0.794	-1.50E-04	0.652	375→575

Table B.4: Line fits of $\phi(T_{bhd})$ for OSL attachment and blowoff transitions for swirler vane angle, θ_{vane}, sensitivity test cases. Fits are valid for range of bulkhead temperatures, T_{bhd}, indicated in table.

	Case A					Case B				
Case No.	m_{attach}	b_{attach}	$m_{blowoff}$	$b_{blowoff}$	T_{bhd}, [K]	m_{attach}	b_{attach}	$m_{blowoff}$	$b_{blowoff}$	T_{bhd}, [K]
10	-1.63E-04	0.627	-2.04E-04	0.635	475→725	-1.26E-04	0.595	-1.49E-04	0.591	475→725
11	-2.88E-04	0.645	-2.38E-04	0.618	475→650	-2.69E-04	0.639	-2.78E-04	0.643	450→675
12	-2.96E-04	0.748	-3.52E-04	0.738	325→575	-2.94E-04	0.761	-2.06E-04	0.673	350→575
13	-2.53E-04	0.623	-2.60E-04	0.629	425→650	-1.99E-04	0.594	-2.02E-04	0.594	450→675
14	-7.98E-05	0.618	-4.51E-05	0.601	375→475	-3.93E-04	0.794	-1.50E-04	0.652	375→575
15	-6.39E-05	0.695	-6.79E-04	0.910	350→550	-8.53E-05	0.785	-2.43E-04	0.700	425→625
16	-3.13E-04	0.682	-5.38E-04	0.736	475→625	-3.08E-04	0.690	-3.12E-04	0.626	475→600
17	-1.13E-05	0.632	-3.76E-04	0.688	375→525	-3.60E-04	0.827	-3.66E-04	0.701	350→525

Table B.5: Line fits of $\phi(T_{bhd})$ for OSL attachment and blowoff transitions for preheat temperature, T_{ph}, sensitivity test cases. Fits are valid for range of bulkhead temperatures, T_{bhd}, indicated in table.

	Case A					Case B				
Case No.	m_{attach}	b_{attach}	$m_{blowoff}$	$b_{blowoff}$	T_{bhd}, [K]	m_{attach}	b_{attach}	$m_{blowoff}$	$b_{blowoff}$	T_{bhd}, [K]
18	-6.39E-05	0.695	-6.79E-04	0.910	350→550	-2.47E-04	0.736	-3.06E-04	0.720	500→675
19	-1.13E-05	0.632	-3.76E-04	0.688	375→525	-3.13E-04	0.682	-5.38E-04	0.736	475→625
20	-3.60E-04	0.827	-3.66E-04	0.701	350→525	-3.08E-04	0.690	-3.12E-04	0.626	475→600
21	-7.98E-05	0.618	-4.51E-05	0.601	350→475	-2.53E-04	0.623	-2.60E-04	0.629	425→650
22	-3.93E-04	0.794	-1.50E-04	0.652	375→575	-1.99E-04	0.594	-2.02E-04	0.594	450→675
23	-2.96E-04	0.748	-3.52E-04	0.738	325→575	-2.88E-04	0.645	-2.38E-04	0.618	475→650
24	-2.94E-04	0.761	-2.06E-04	0.673	350→575	-2.69E-04	0.639	-2.78E-04	0.643	450→675
25	-8.02E-06	0.655	-3.14E-04	0.701	400→525	-1.81E-04	0.617	-7.35E-04	0.877	475→600

Table B.6: Line fits of $\phi(T_{bhd})$ for OSL attachment and blowoff transitions for premixer velocity, u_{pm}, sensitivity test cases. Fits are valid for range of bulkhead temperatures, T_{bhd}, indicated in table.

	Case A					Case B				
Case No.	m_{attach}	b_{attach}	$m_{blowoff}$	$b_{blowoff}$	T_{bhd}, [K]	m_{attach}	b_{attach}	$m_{blowoff}$	$b_{blowoff}$	T_{bhd}, [K]
26	-3.13E-04	0.682	-5.38E-04	0.736	475→625	-2.47E-04	0.736	-3.06E-04	0.720	500→675
27	-1.13E-05	0.632	-3.76E-04	0.688	375→525	-6.39E-05	0.695	-6.79E-04	0.910	350→550
28	-3.60E-04	0.827	-3.66E-04	0.701	325→525	-8.53E-05	0.785	-2.43E-04	0.700	425→625
29	-2.88E-04	0.645	-2.38E-04	0.618	475→650	-1.63E-04	0.627	-2.04E-04	0.635	475→725
30	-2.69E-04	0.639	-2.78E-04	0.643	450→675	-1.26E-04	0.595	-1.49E-04	0.591	475→725
31	-1.81E-04	0.617	-7.35E-04	0.877	475→600	-3.39E-04	0.792	-3.78E-04	0.702	500→625

Table B.7: Line fits of $\phi\,(T_{bhd})$ for OSL attachment and blowoff transitions for thermoacoustic sensitivity test cases. Fits are valid for range of bulkhead temperatures, T_{bhd}, indicated in table.

	Case A					**Case B**				
Case No.	m_{attach}	b_{attach}	$m_{blowoff}$	$b_{blowoff}$	T_{bhd}, [K]	m_{attach}	b_{attach}	$m_{blowoff}$	$b_{blowoff}$	T_{bhd}, [K]
32	-2.96E-04	0.748	-3.52E-04	0.738	325→575	-7.98E-05	0.618	-4.51E-05	0.601	375→475
33	-2.94E-04	0.761	-2.06E-04	0.673	350→575	-3.93E-04	0.794	-1.50E-04	0.652	375→575

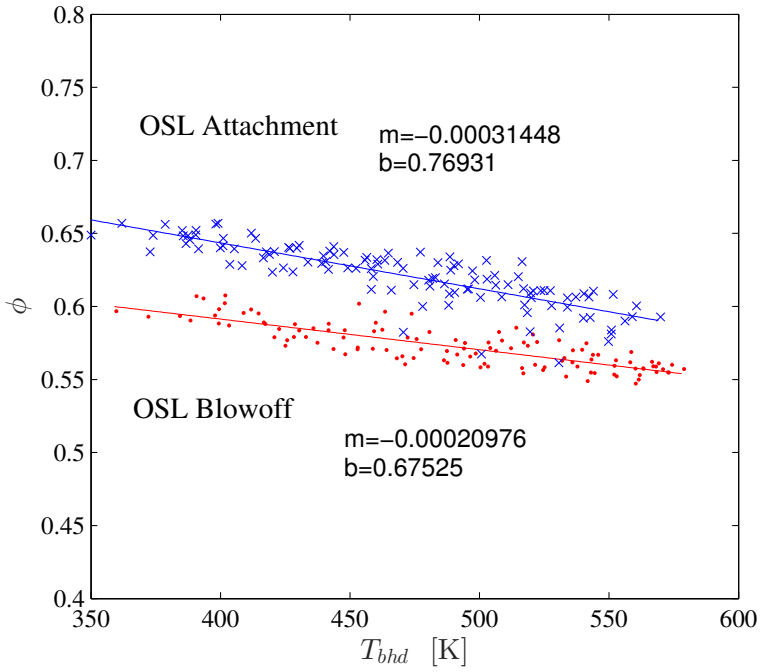

Figure B.1: Flame configuration map for test cases 9A, 12B, 24A, and 33A, performed without acoustic measurements.

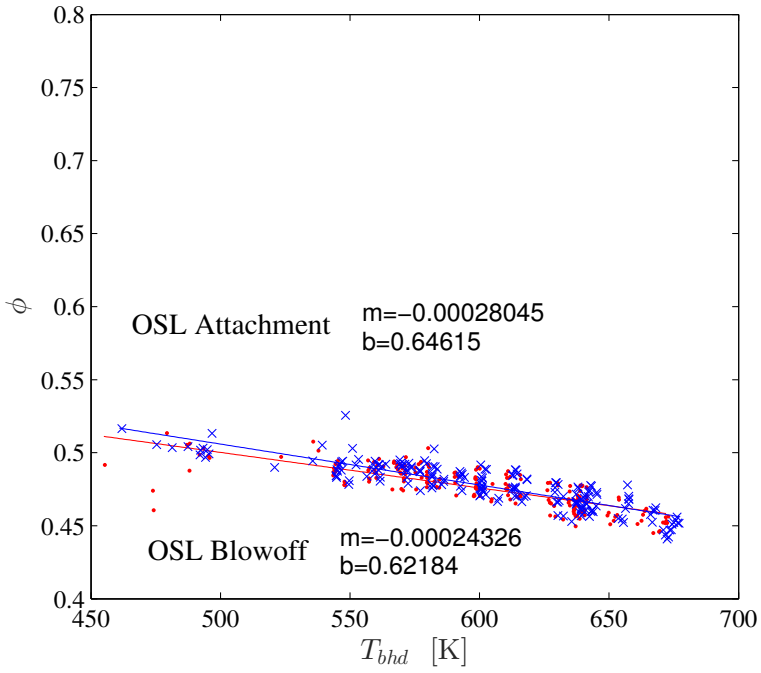

Figure B.2: Flame configuration map for test cases 8A, 11B, 24B, and 30A, performed without acoustic measurements.

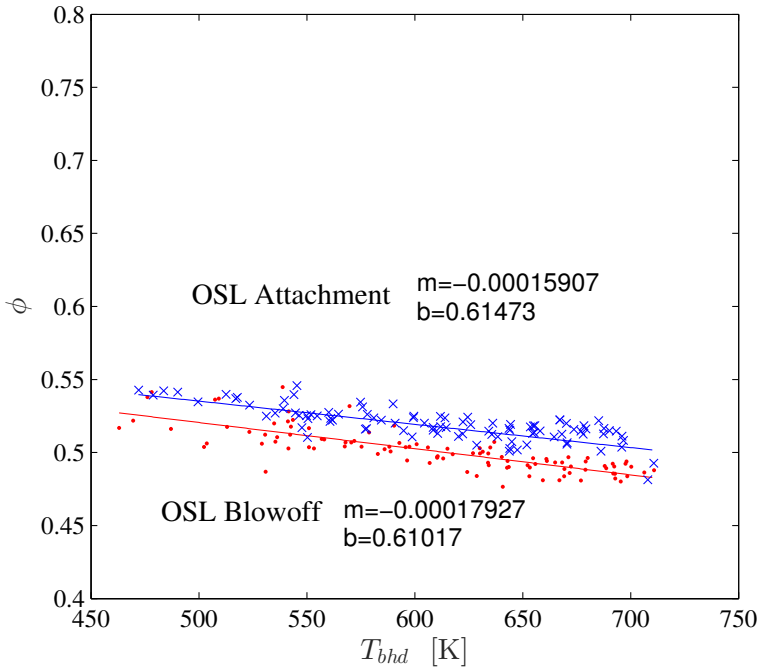

Figure B.3: Flame configuration map for test cases 10B and 30B, performed without acoustic measurements.

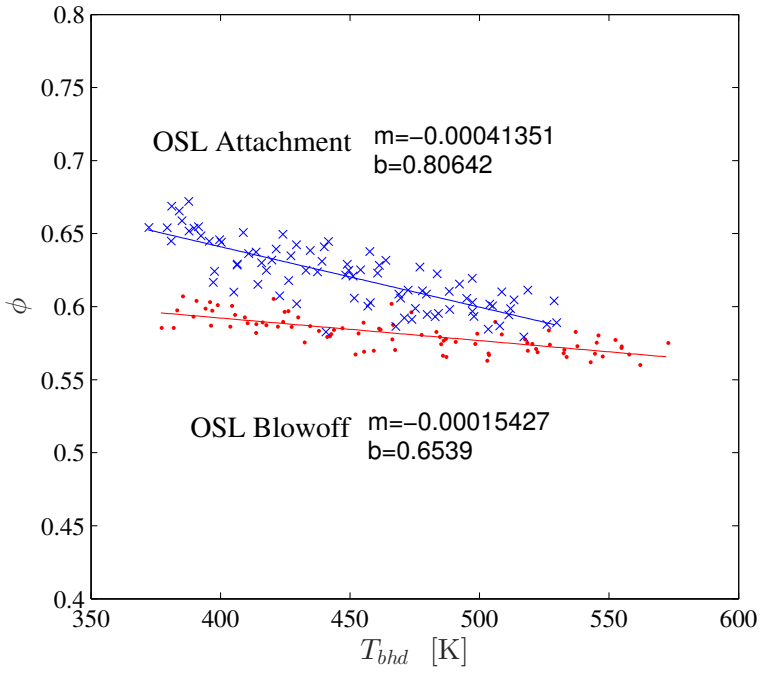

Figure B.4: Flame configuration map for test cases 9B, 14B, 22A, and 33B, performed without acoustic measurements.

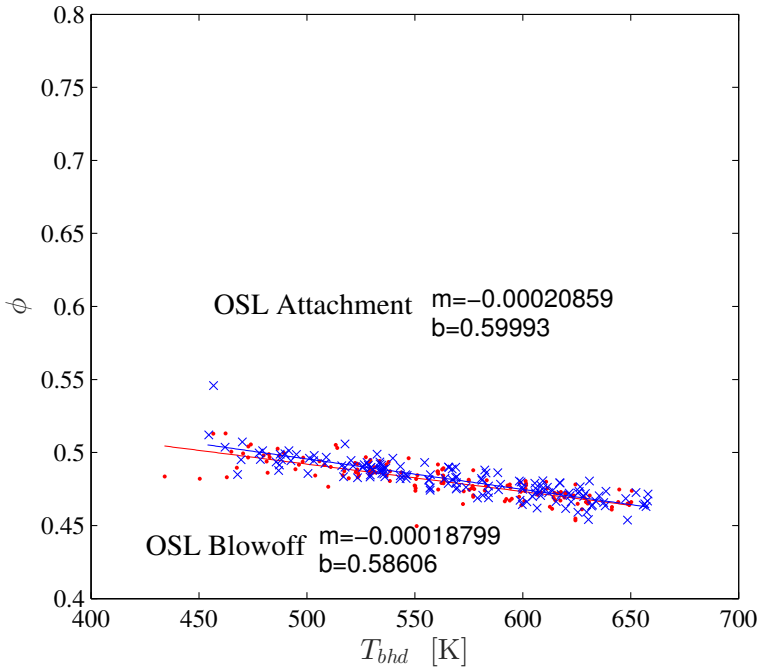

Figure B.5: Flame configuration map for test cases 8B, 13B, and 22B, performed without acoustic measurements.

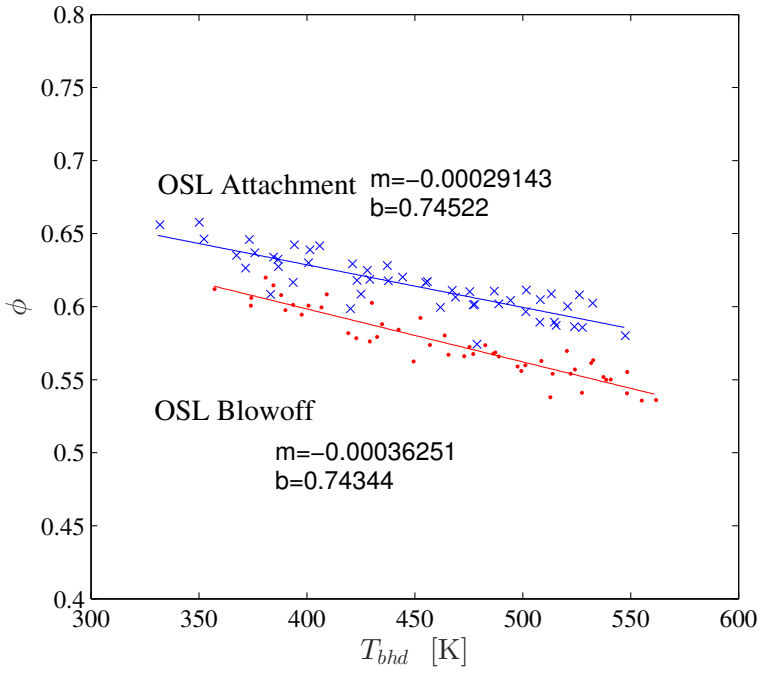

Figure B.6: Flame configuration map for test cases 7A, 12A, 23A, and 32A, performed without acoustic measurements.

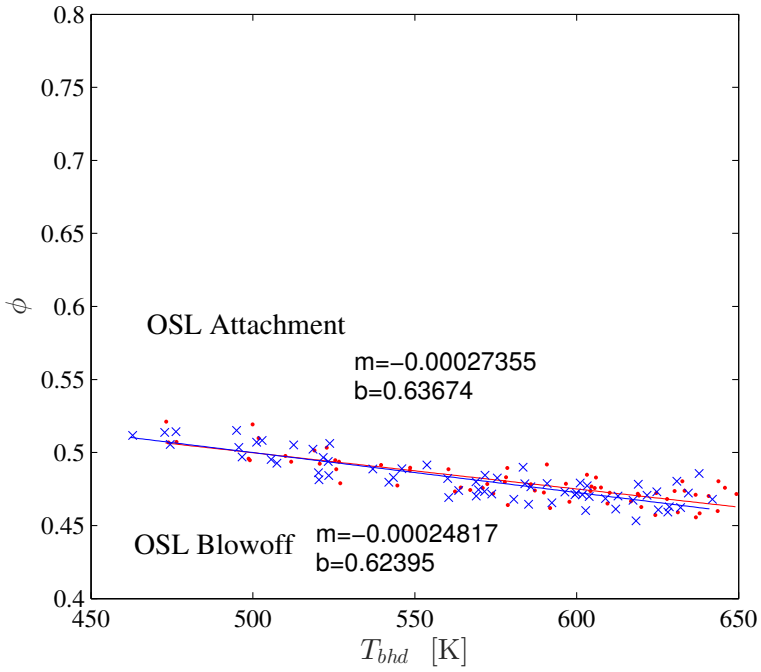

Figure B.7: Flame configuration map for test cases 6A, 11A, 23B, and 29A, performed without acoustic measurements.

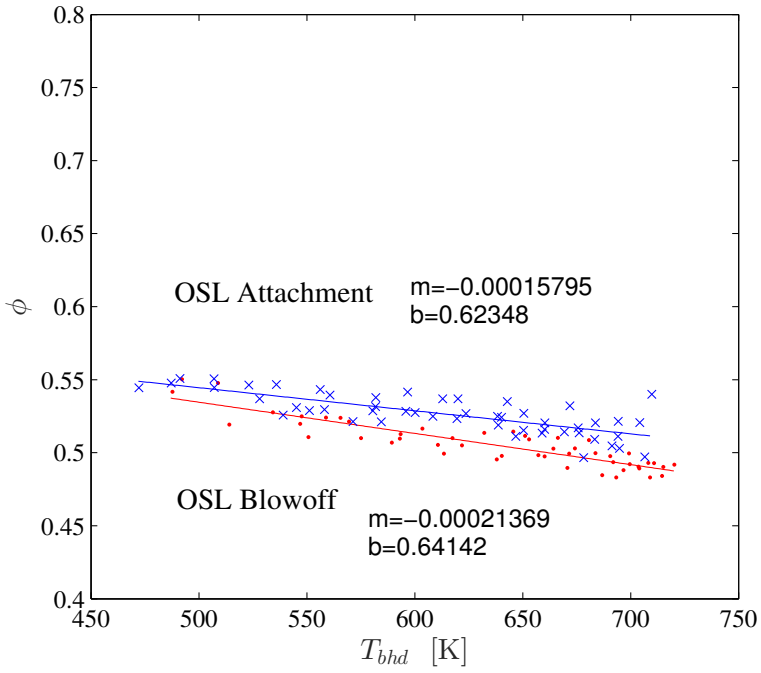

Figure B.8: Flame configuration map for test cases 10A and 29B, performed without acoustic measurements.

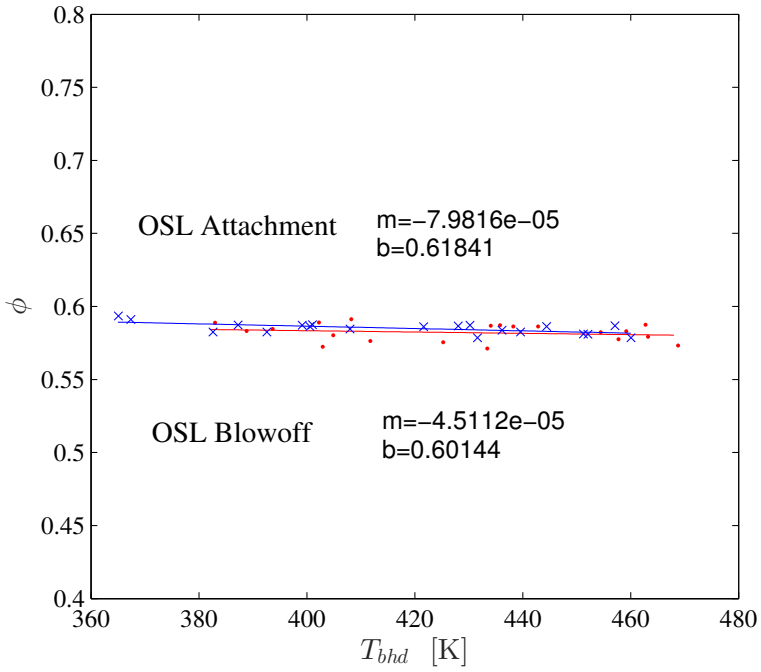

Figure B.9: Flame configuration map for test cases 5B, 7B, 14A, 21A, and 32B, performed without acoustic measurements.

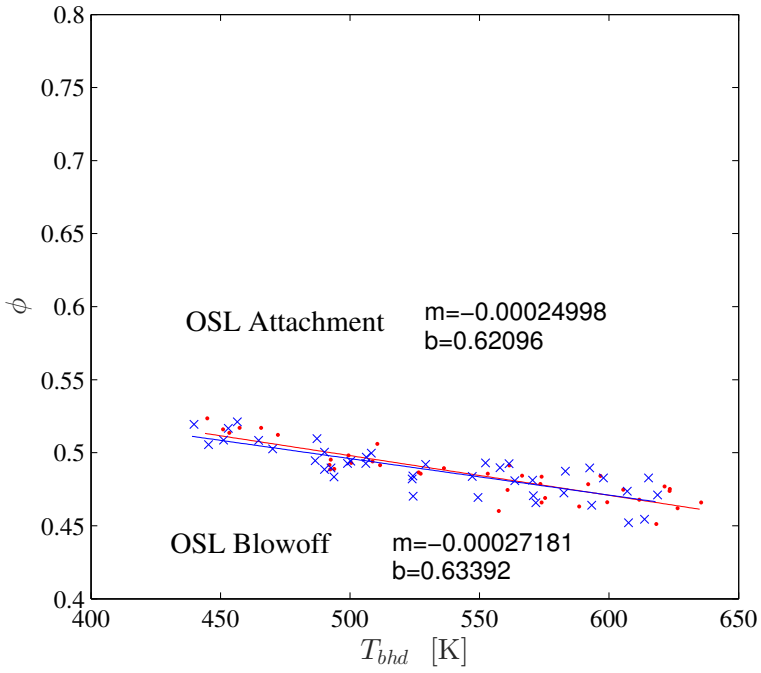

Figure B.10: Flame configuration map for test cases 4B, 6B, 13A, and 21B, performed without acoustic measurements.

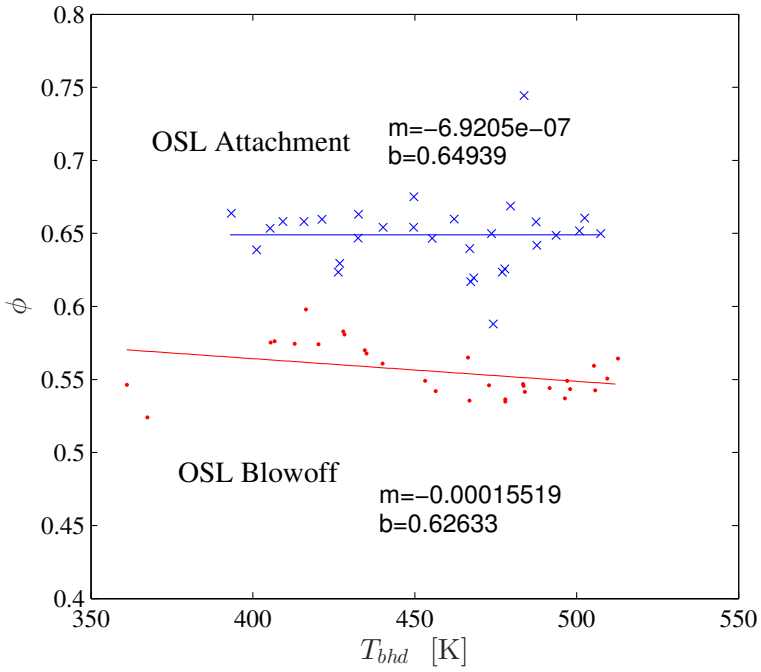

Figure B.11: Flame configuration map for test cases 3A, 5A, and 25A performed without acoustic measurements.

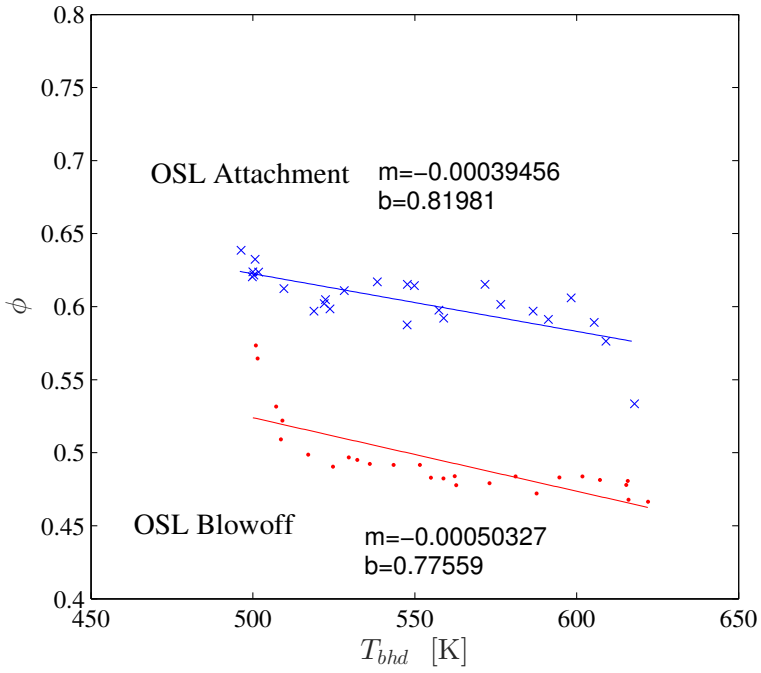

Figure B.12: Flame configuration map for test cases 1A and 31B, performed without acoustic measurements.

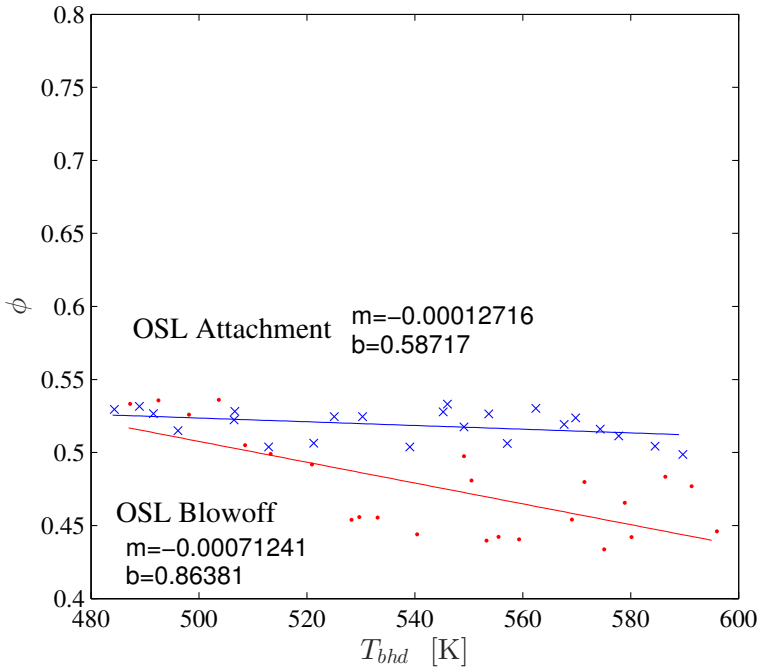

Figure B.13: Flame configuration map for test cases 2A, 4A, 25B, and 31A, performed without acoustic measurements.

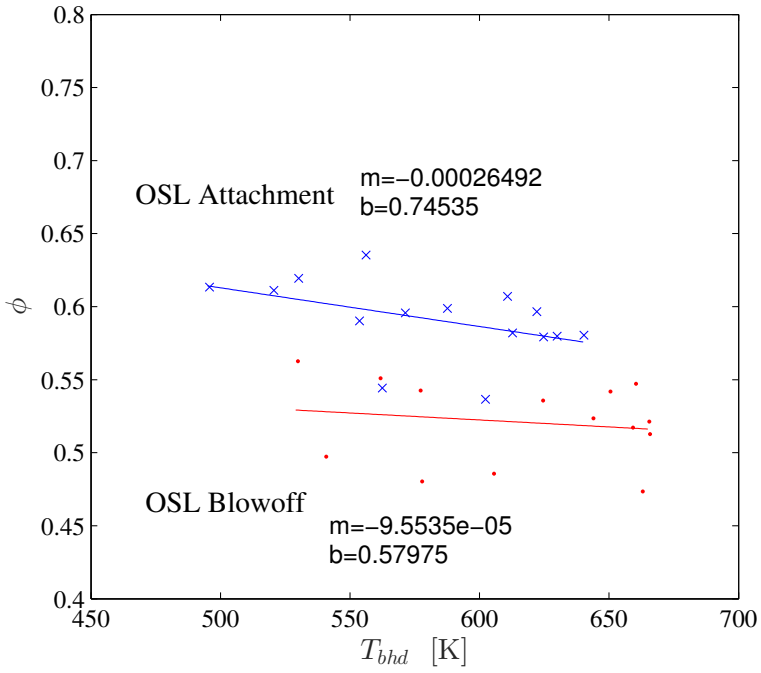

Figure B.14: Flame configuration map for test cases 1B, 19B, and 26B, performed without acoustic measurements.

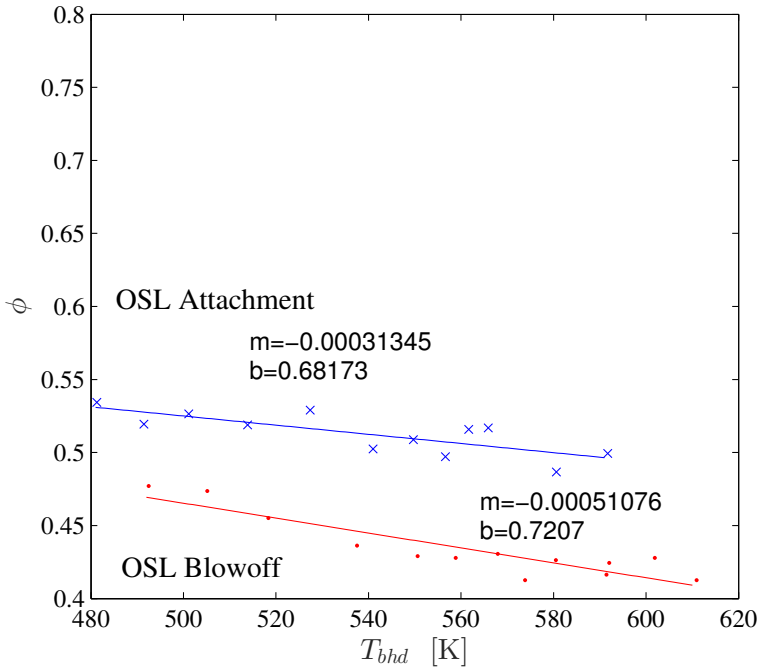

Figure B.15: Flame configuration map for test cases 2B, 16A, 19B, and 26A, performed without acoustic measurements.

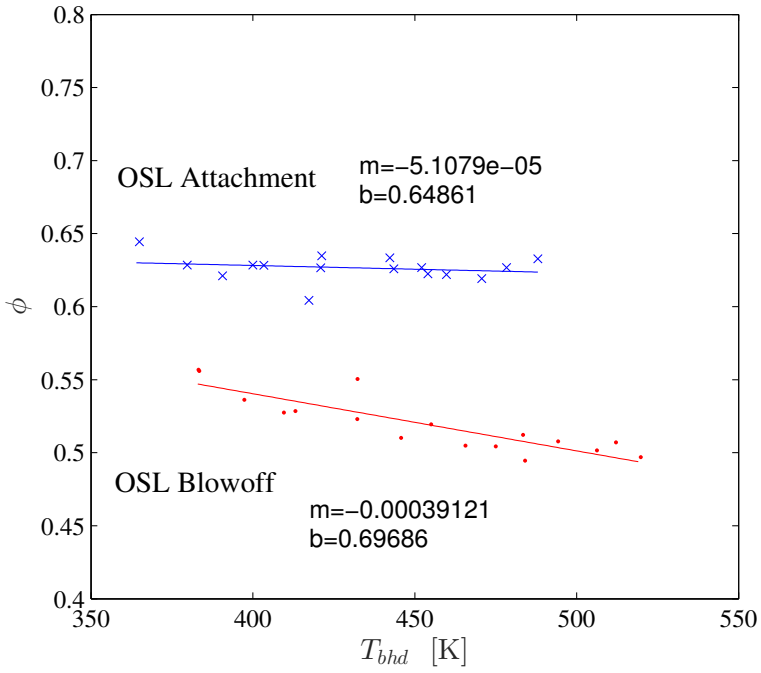

Figure B.16: Flame configuration map for test cases 3B, 17A, 19A, and 27A, performed without acoustic measurements.

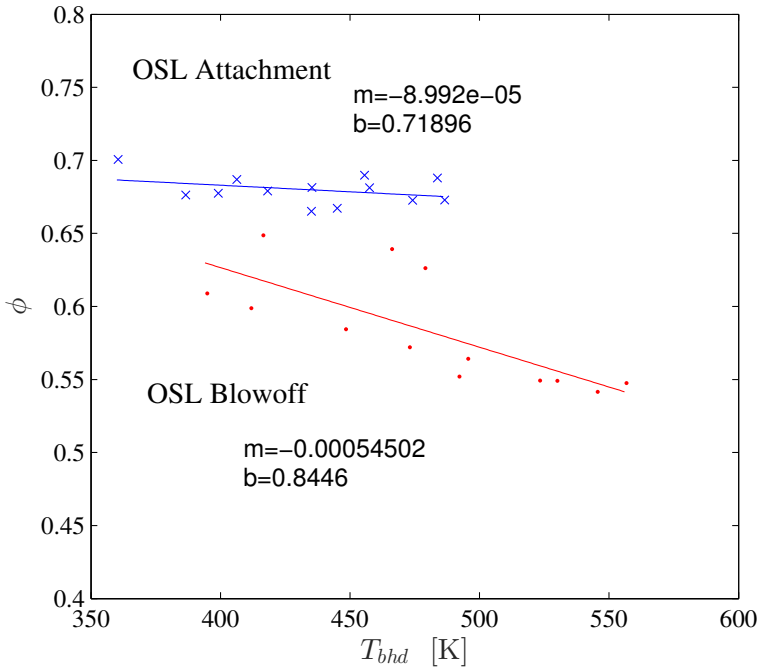

Figure B.17: Flame configuration map for test cases 15A, 18A, and 27B, performed without acoustic measurements.

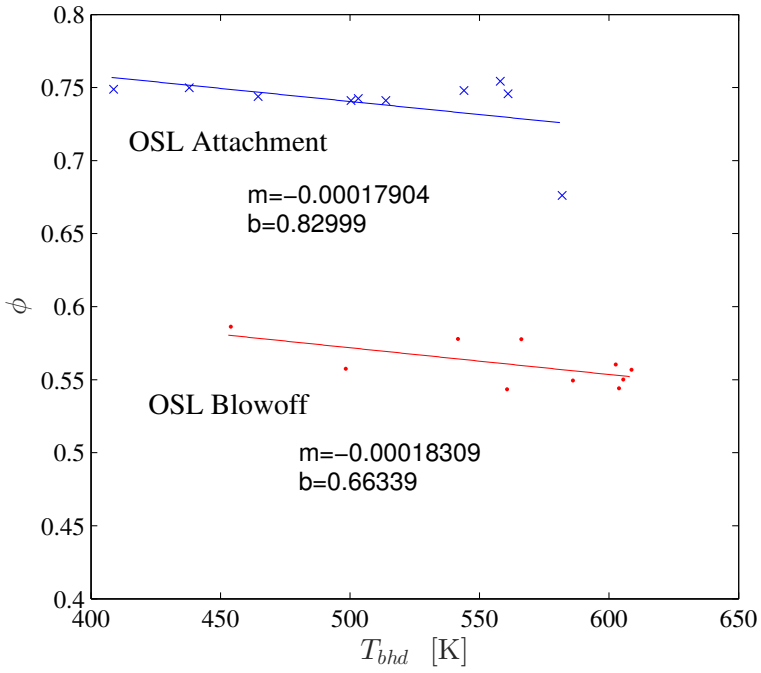

Figure B.18: Flame configuration map for test cases 15B and 28B, performed without acoustic measurements.

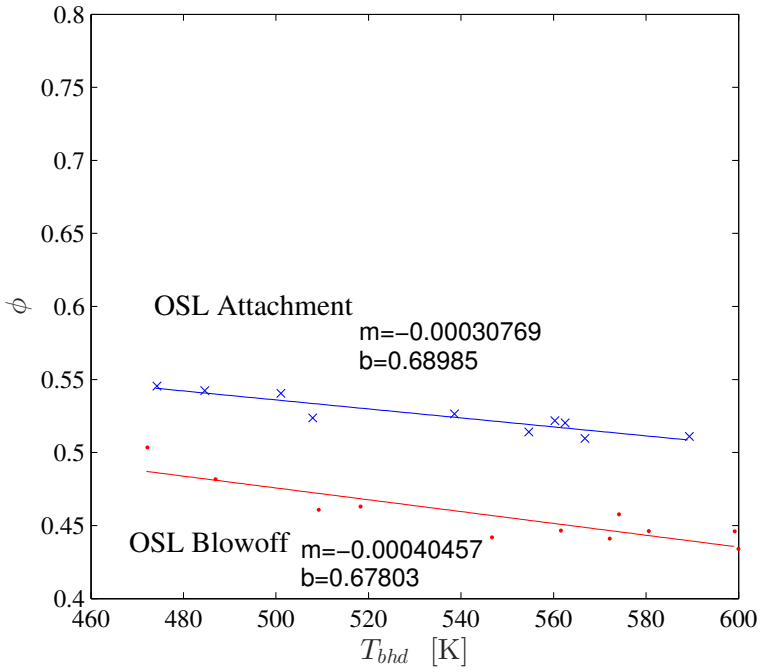

Figure B.19: Flame configuration map for test cases 16B and 20B, performed without acoustic measurements.

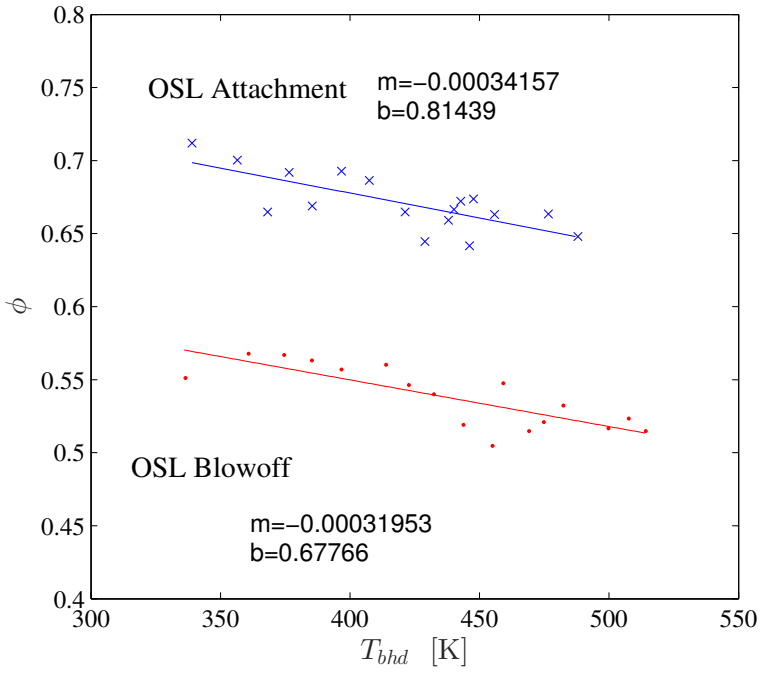

Figure B.20: 20) Flame configuration map for test cases 17B, 20A, and 28A, performed without acoustic measurements.

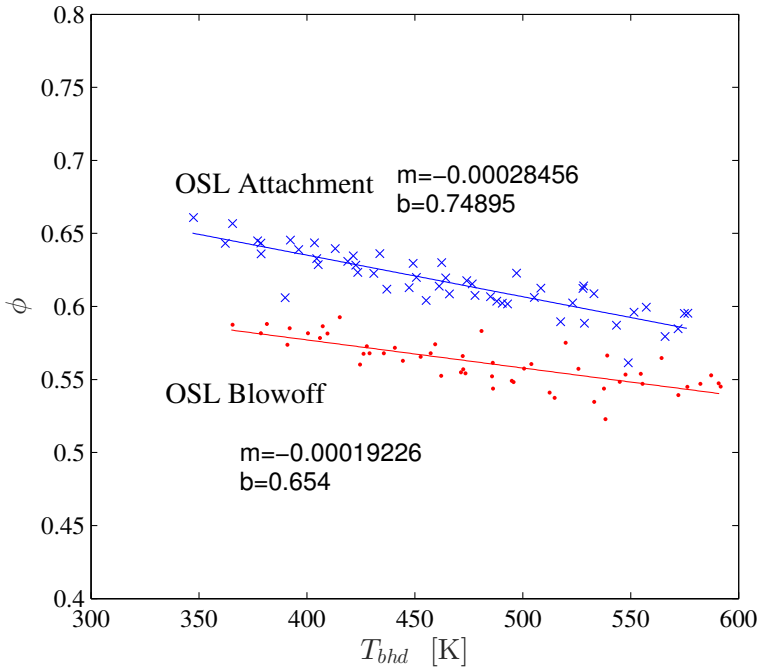

Figure B.21: Flame configuration map for test cases 9A, 12B, 24A, and 33A, performed with acoustic measurements.

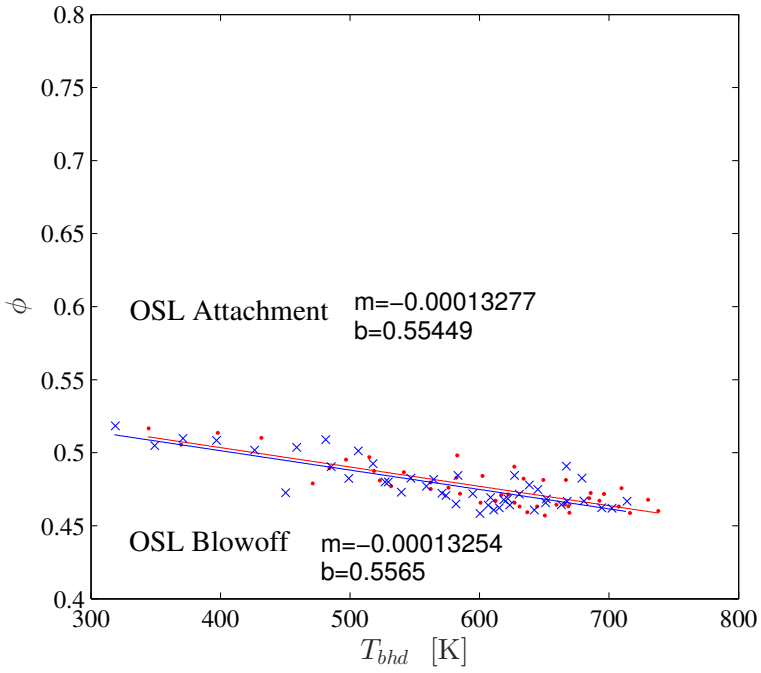

Figure B.22: Flame configuration map for test cases 8A, 11B, 24B, and 30A, performed with acoustic measurements.

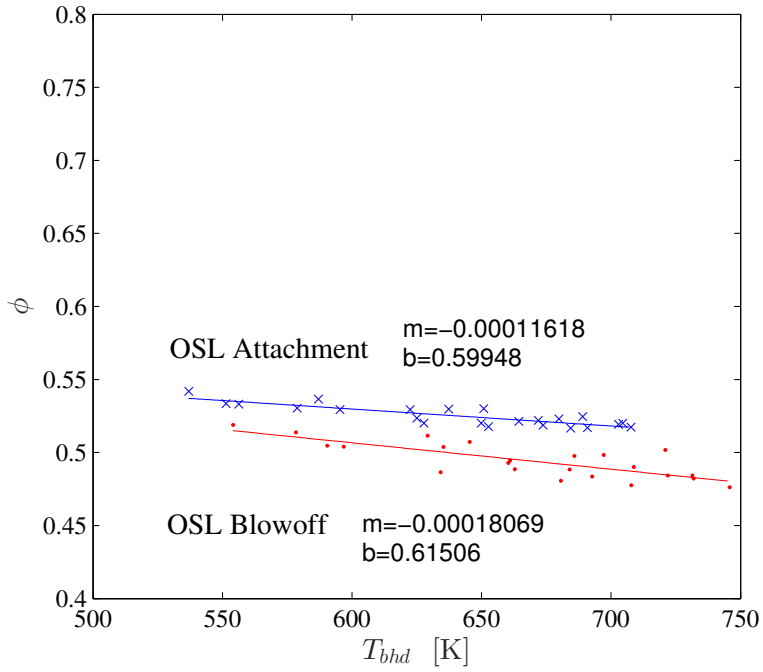

Figure B.23: Flame configuration map for test cases 10B and 30B, performed with acoustic measurements.

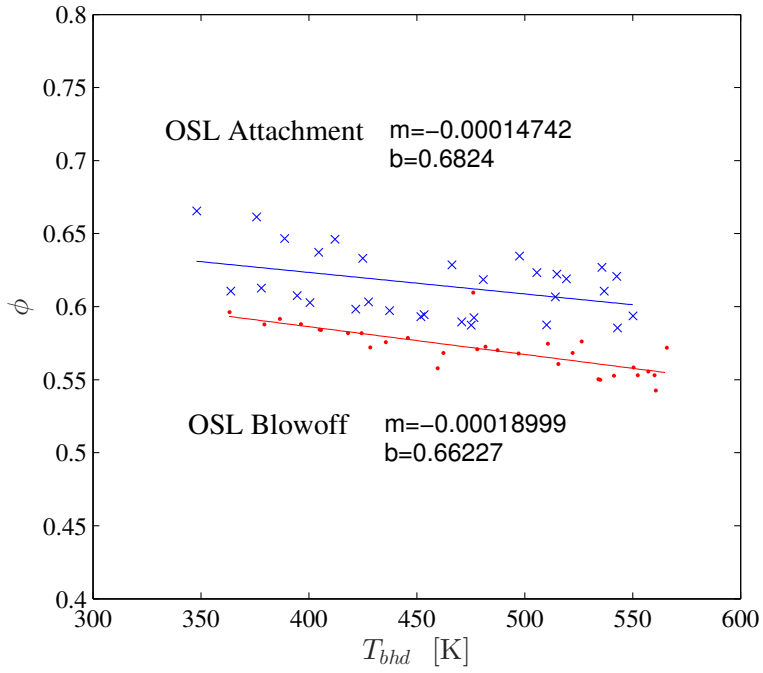

Figure B.24: Flame configuration map for test cases 9B, 14B, 22A, and 33B, performed with acoustic measurements.

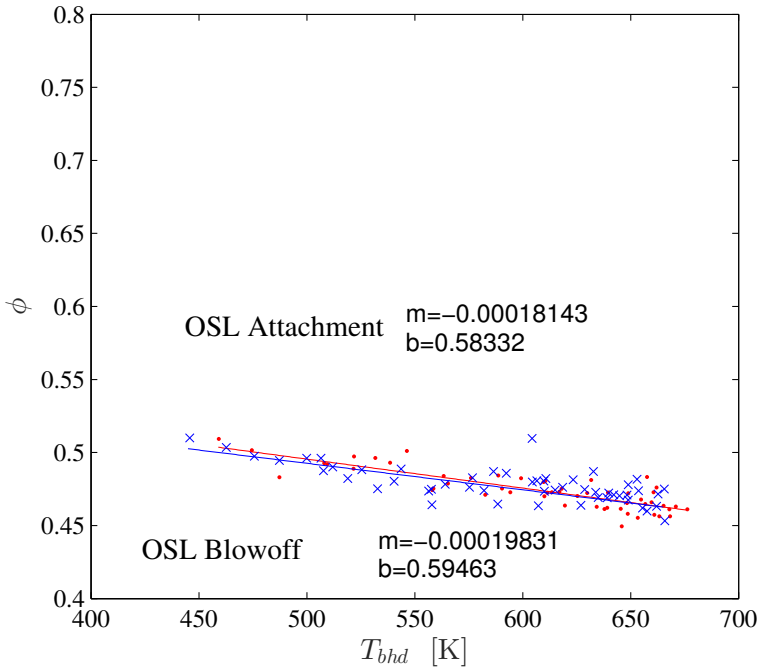

Figure B.25: Flame configuration map for test cases 8B, 13B, and 22B, performed with acoustic measurements.

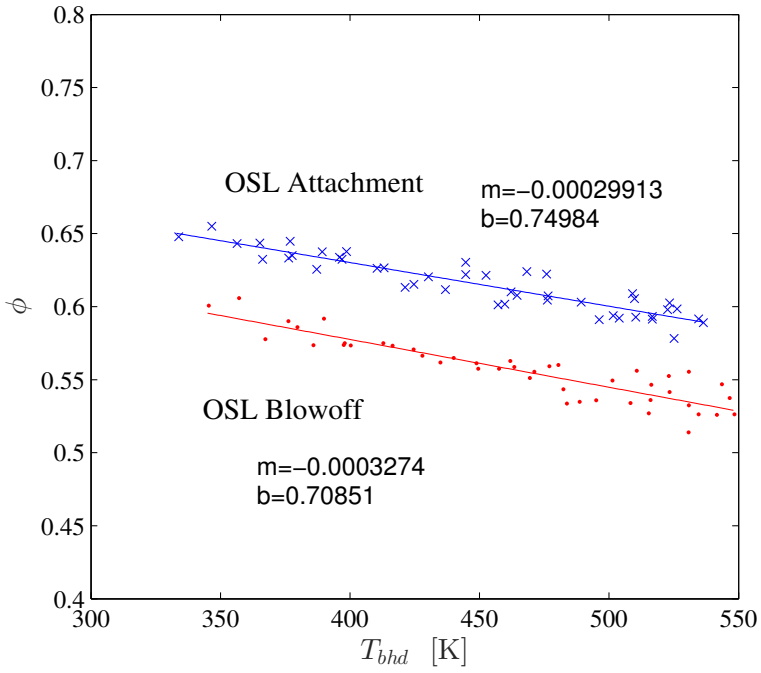

Figure B.26: Flame configuration map for test cases 7A, 12A, 23A, and 32A, performed with acoustic measurements.

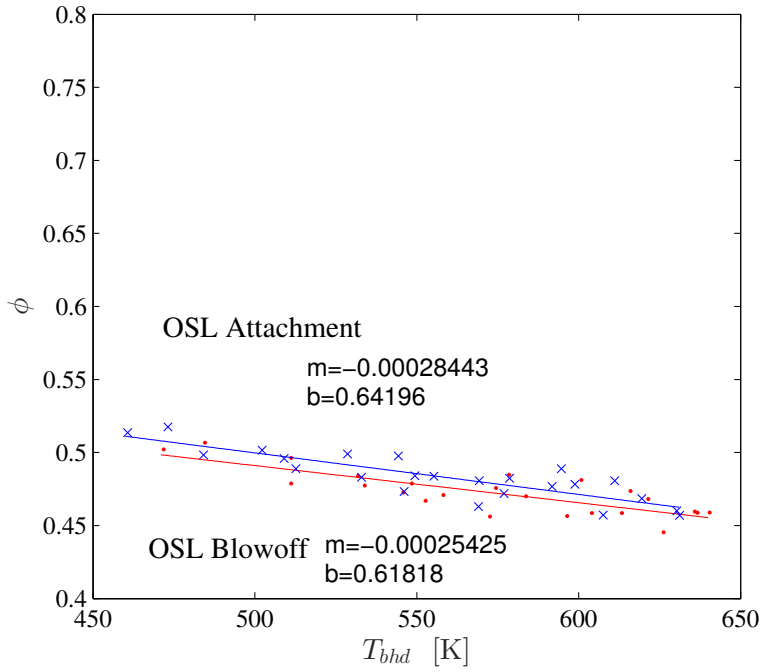

Figure B.27: Flame configuration map for test cases 6A, 11A, 23B, and 29A, performed with acoustic measurements.

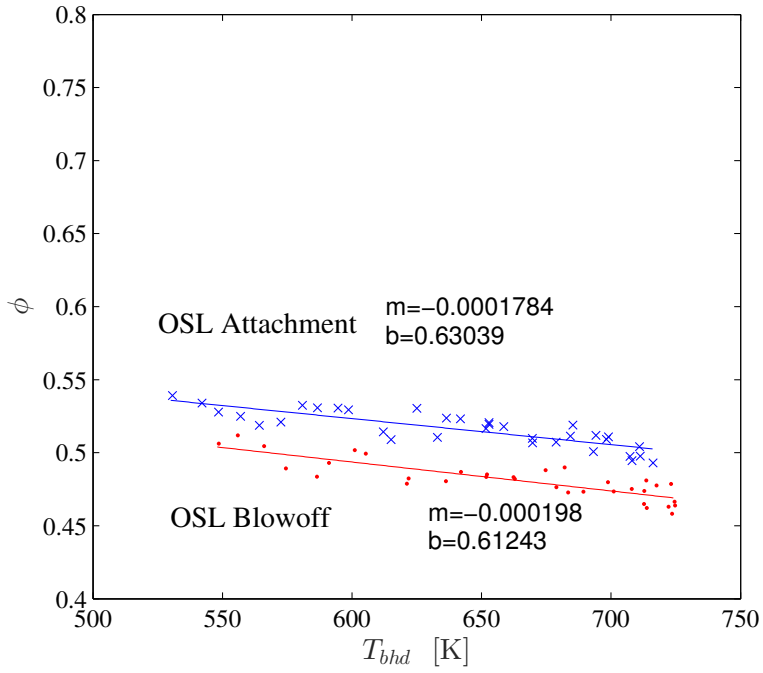

Figure B.28: 10P) Flame configuration map for test cases 10A and 29B, performed with acoustic measurements.

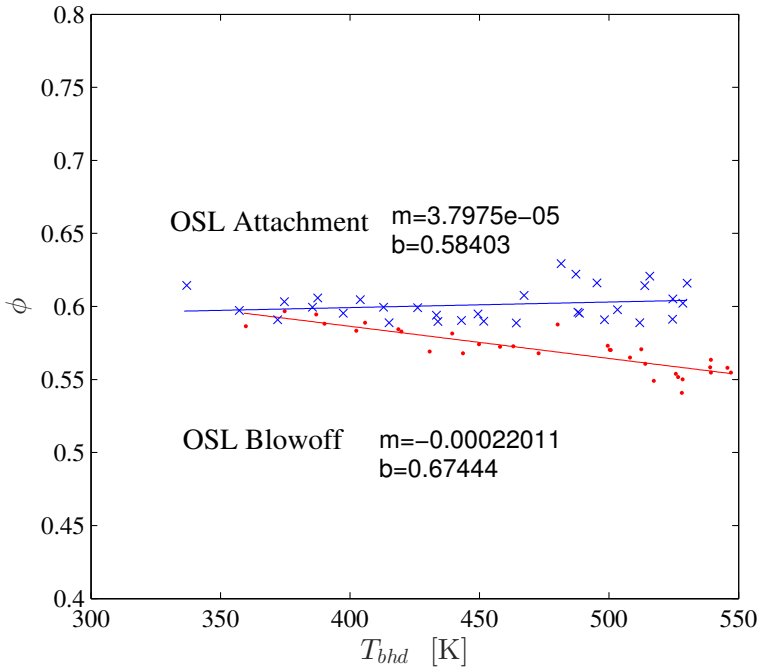

Figure B.29: 11P) Flame configuration map for test cases 5B, 7B, 14A, 21A, and 32B, performed with acoustic measurements.

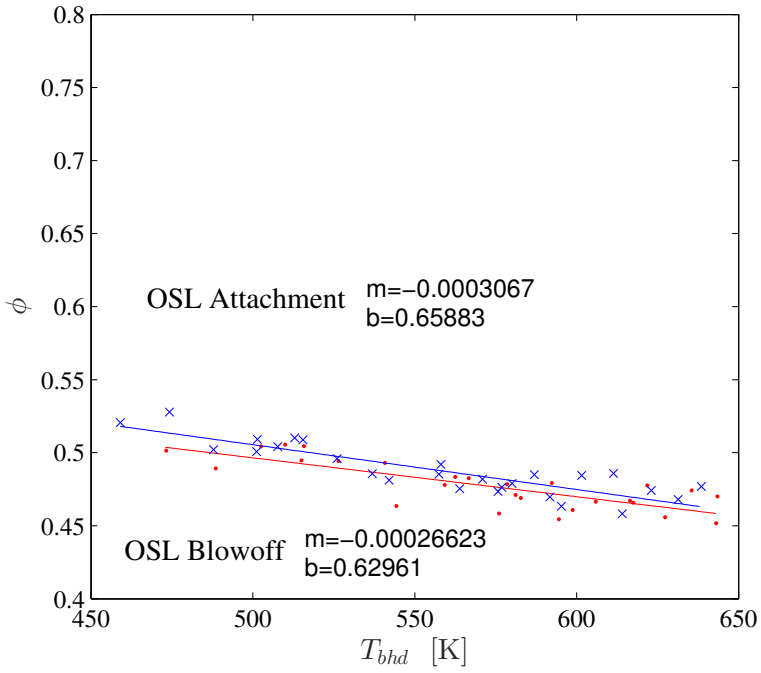

Figure B.30: 12P) Flame configuration map for test cases 4B, 6B, 13A, and 21B, performed without acoustic measurements.

APPENDIX C

SUPPLEMENTAL MATERIAL: EXPERIMENTAL RESULTS

C.1 Shear Layer Characteristics

C.1.1 Flow Field Characteristics

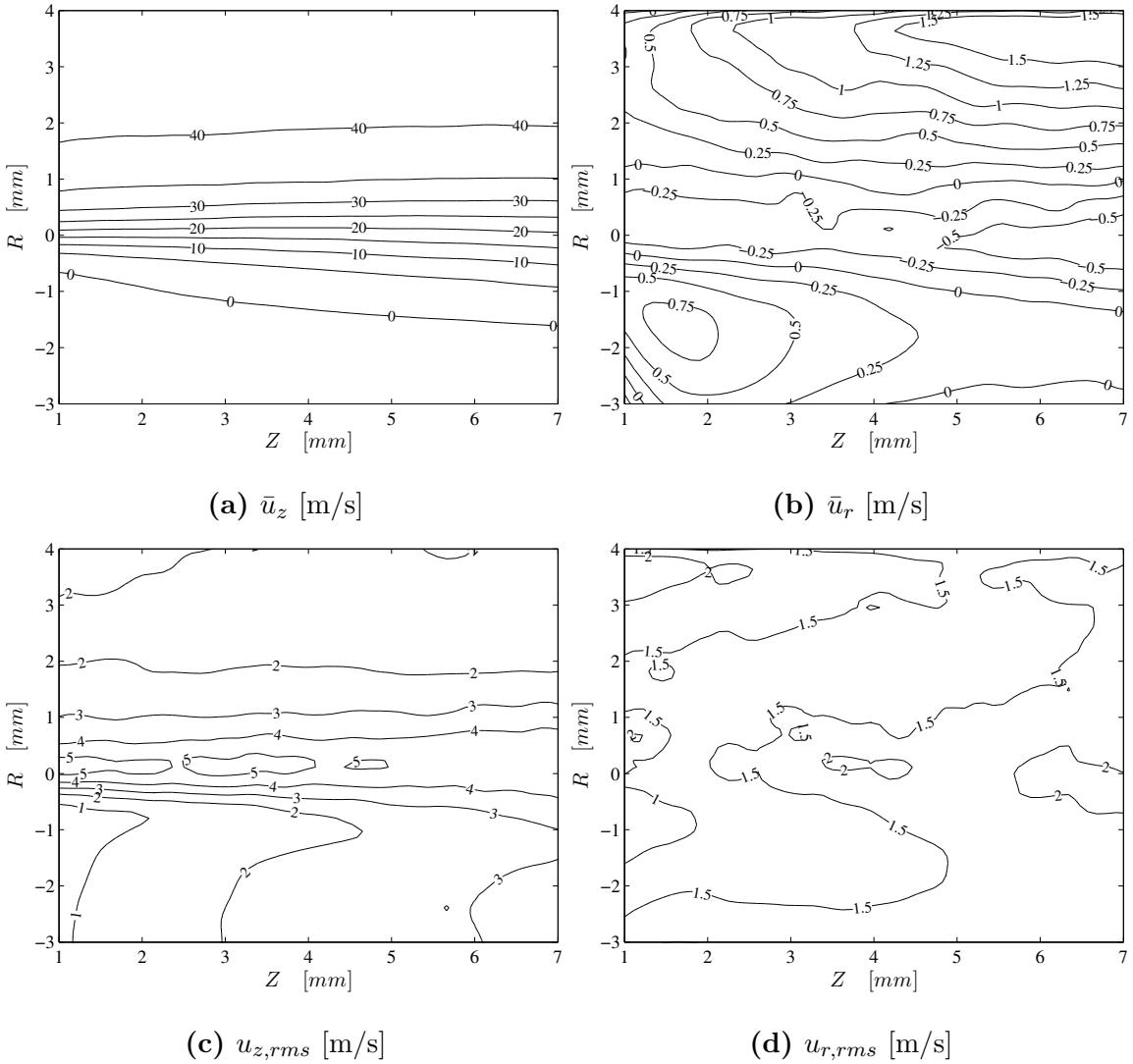

(a) $\bar{u}_z$ [m/s] **(b)** $\bar{u}_r$ [m/s]

(c) $u_{z,rms}$ [m/s] **(d)** $u_{r,rms}$ [m/s]

Figure C.1: Mean and rms velocity fields for $\phi = 0.8$ and $u_{pm} = 35 m/s$.

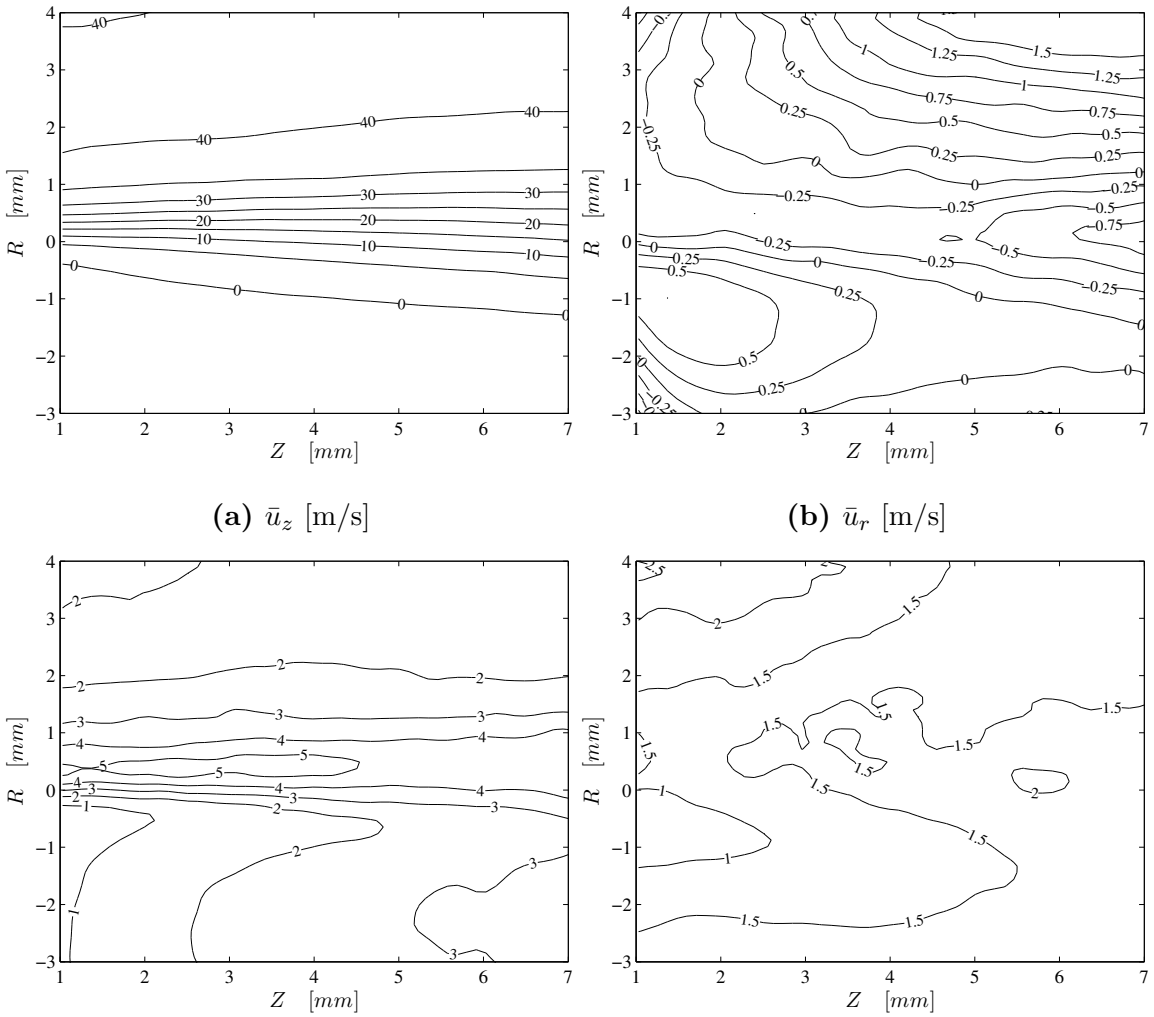

(a) $\bar{u}_z$ [m/s]

(b) $\bar{u}_r$ [m/s]

(c) $u_{z,rms}$ [m/s]

(d) $u_{r,rms}$ [m/s]

Figure C.2: Mean and rms velocity fields for $\phi = 0.9$ and $u_{pm} = 35 m/s$.

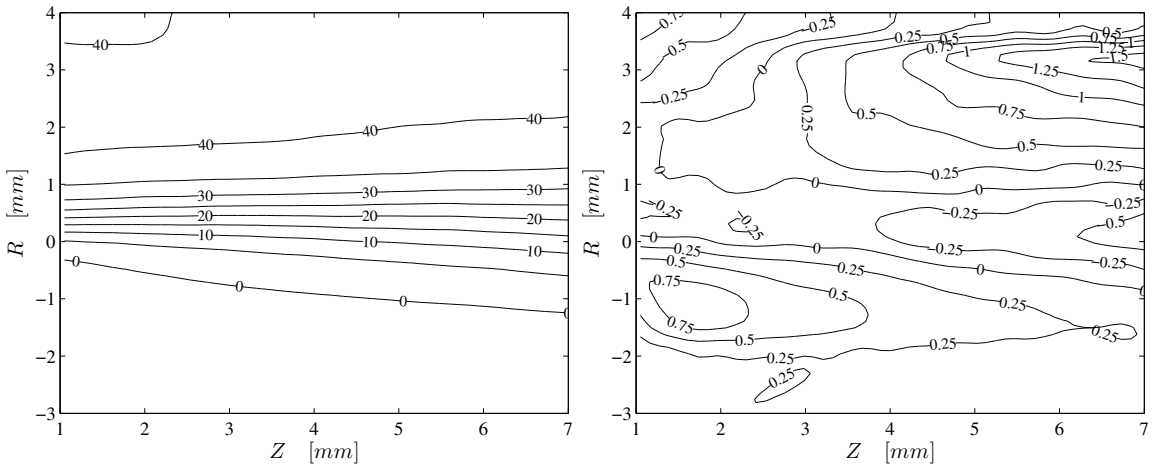

(a) $\bar{u}_z$ [m/s] **(b)** $\bar{u}_r$ [m/s]

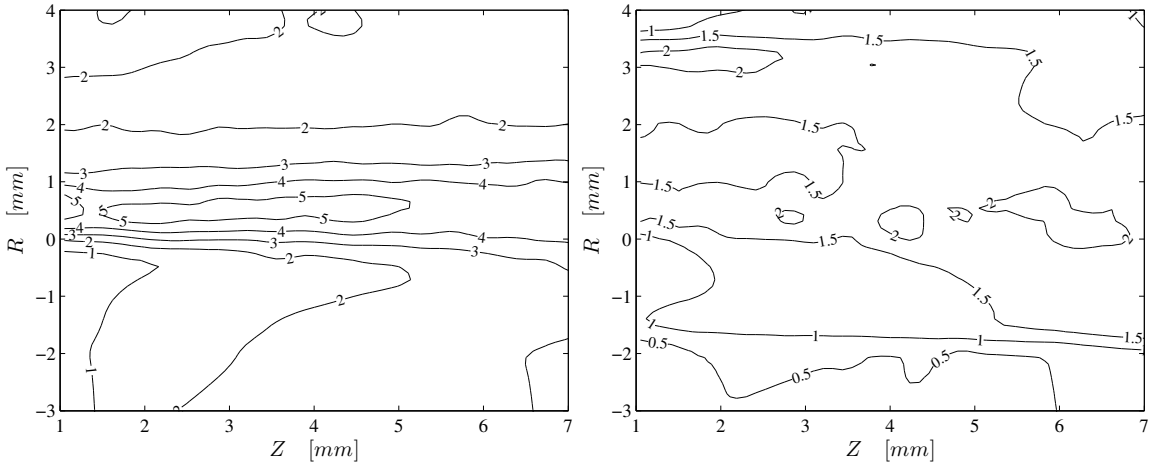

(c) $u_{z,rms}$ [m/s] **(d)** $u_{r,rms}$ [m/s]

Figure C.3: Mean and rms velocity fields for $\phi = 1.0$ and $u_{pm} = 35 m/s$.

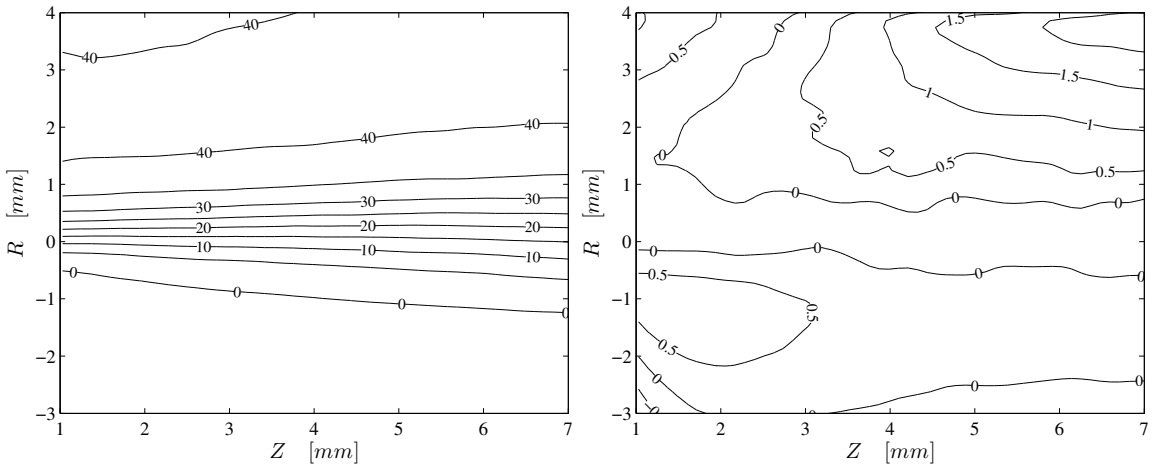

(a) $\bar{u}_z$ [m/s]

(b) $\bar{u}_r$ [m/s]

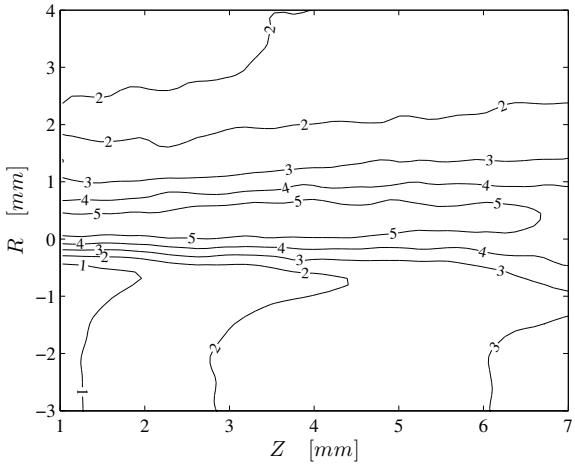

(c) $u_{z,rms}$ [m/s]

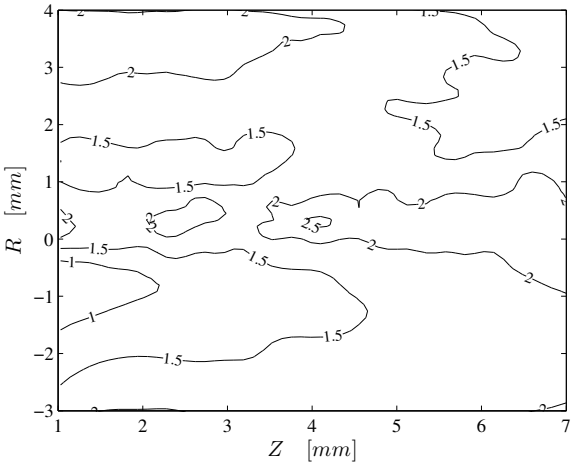

(d) $u_{r,rms}$ [m/s]

Figure C.4: Mean and rms velocity fields for $\phi = 1.1$ and $u_{pm} = 35 m/s$.

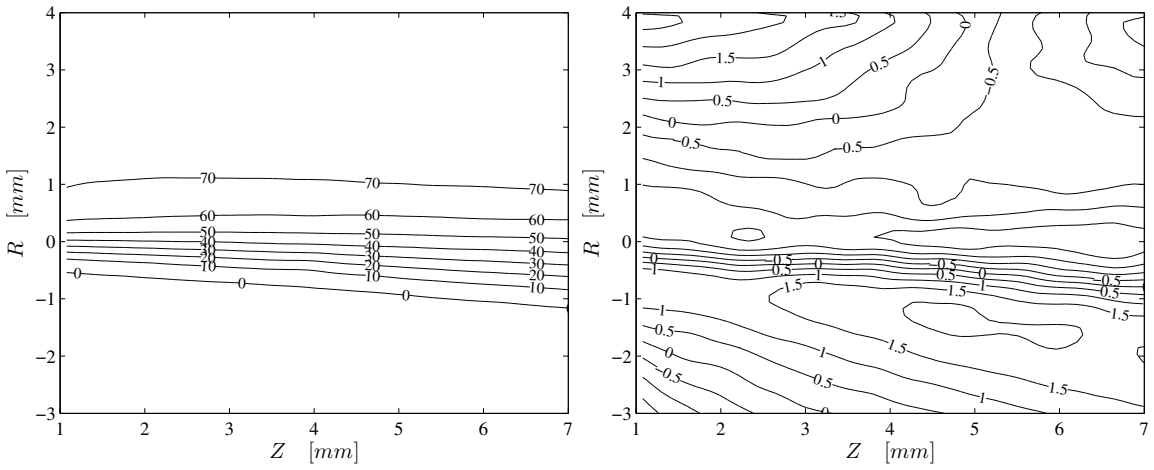

(a) $\bar{u}_z$ [m/s]

(b) $\bar{u}_r$ [m/s]

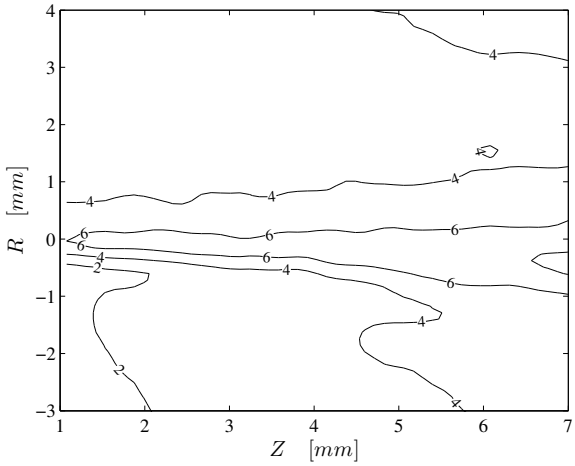

(c) $u_{z,rms}$ [m/s]

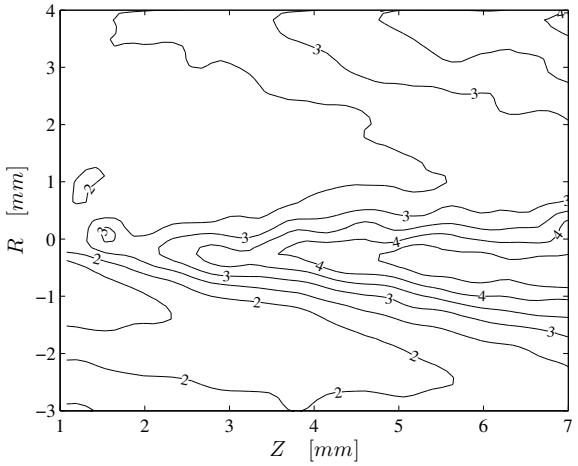

(d) $u_{r,rms}$ [m/s]

Figure C.5: Mean and rms velocity fields for $\phi = 0.8$ and $u_{pm} = 70 m/s$.

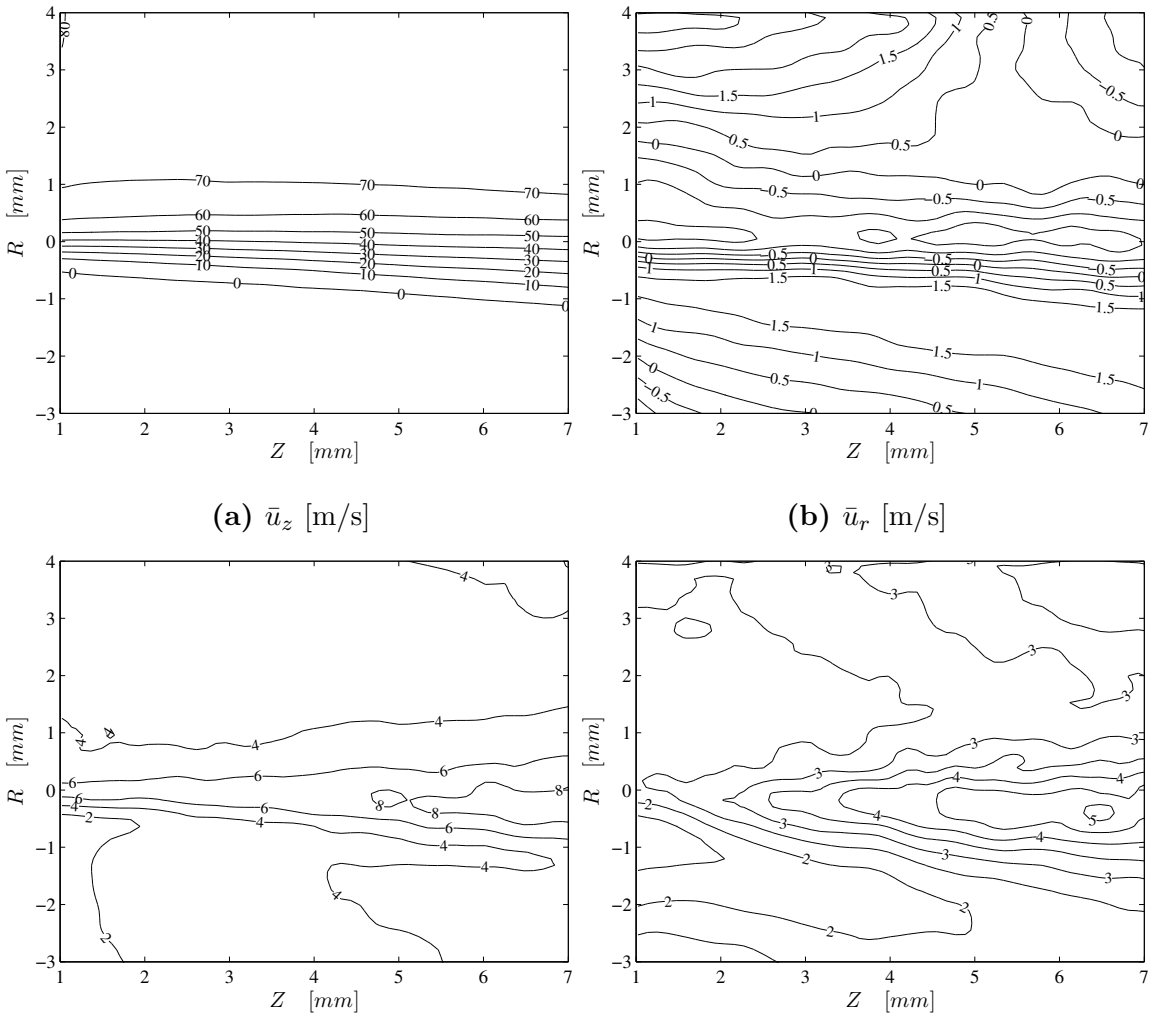

(a) $\bar{u}_z$ [m/s]

(b) $\bar{u}_r$ [m/s]

(c) $u_{z,rms}$ [m/s]

(d) $u_{r,rms}$ [m/s]

Figure C.6: Mean and rms velocity fields for $\phi = 0.9$ and $u_{pm} = 70 m/s$.

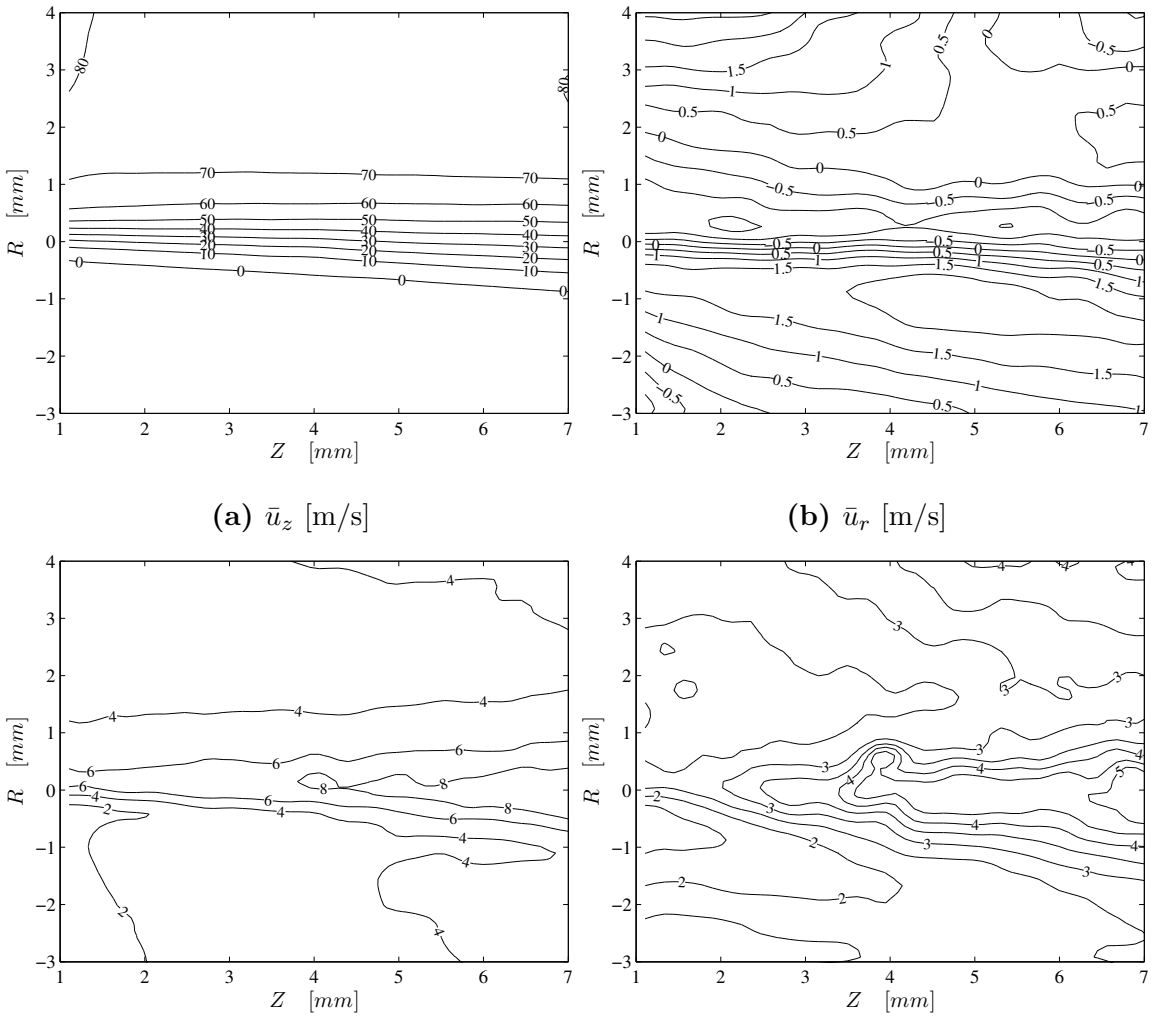

(a) $\bar{u}_z$ [m/s]

(b) $\bar{u}_r$ [m/s]

(c) $u_{z,rms}$ [m/s]

(d) $u_{r,rms}$ [m/s]

Figure C.7: Mean and rms velocity fields for $\phi = 1.0$ and $u_{pm} = 70 m/s$.

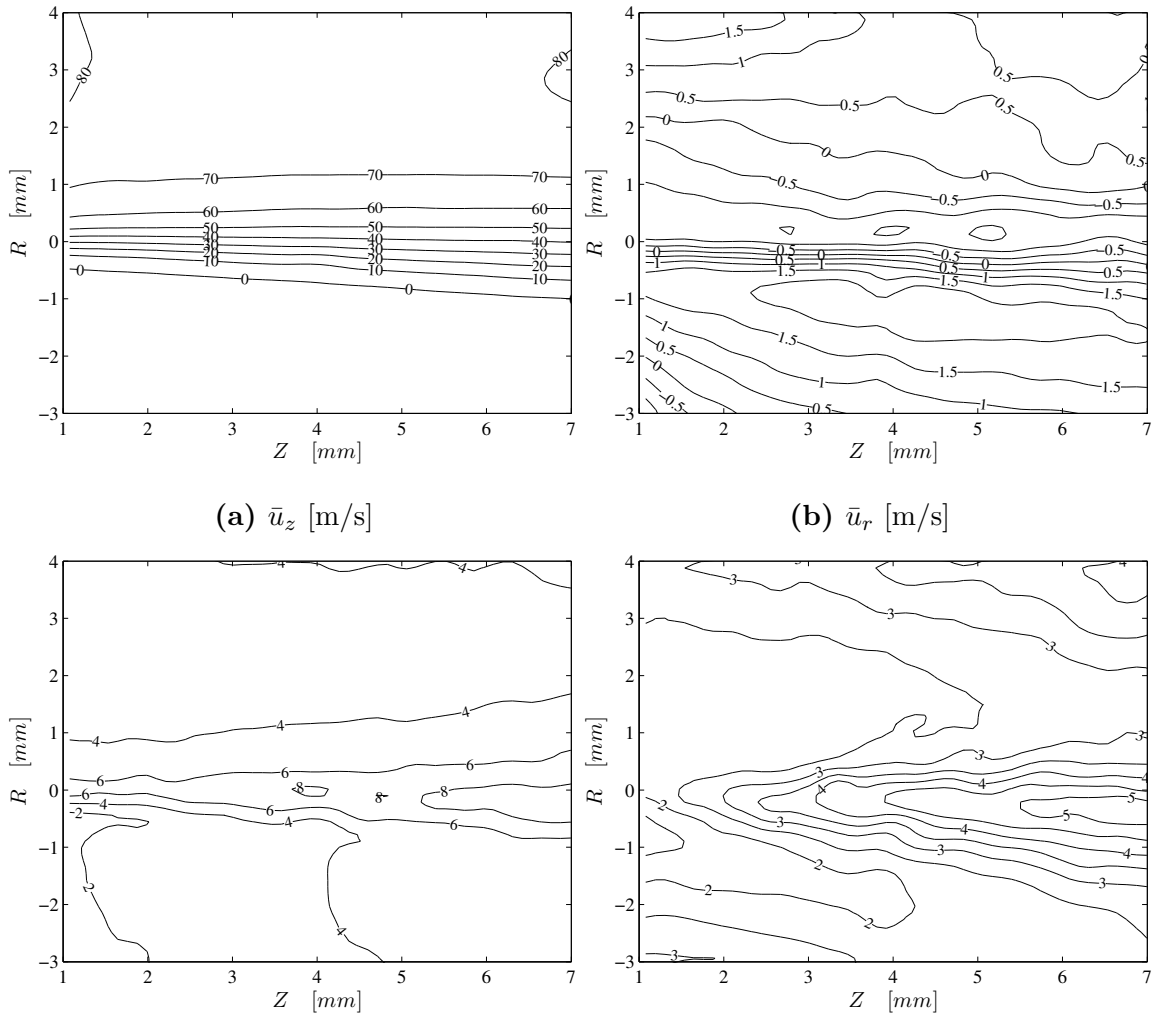

(a) $\bar{u}_z$ [m/s]

(b) $\bar{u}_r$ [m/s]

(c) $u_{z,rms}$ [m/s]

(d) $u_{r,rms}$ [m/s]

Figure C.8: Mean and rms velocity fields for $\phi = 1.1$ and $u_{pm} = 70 m/s$.

C.1.2 Strain Field Characteristics

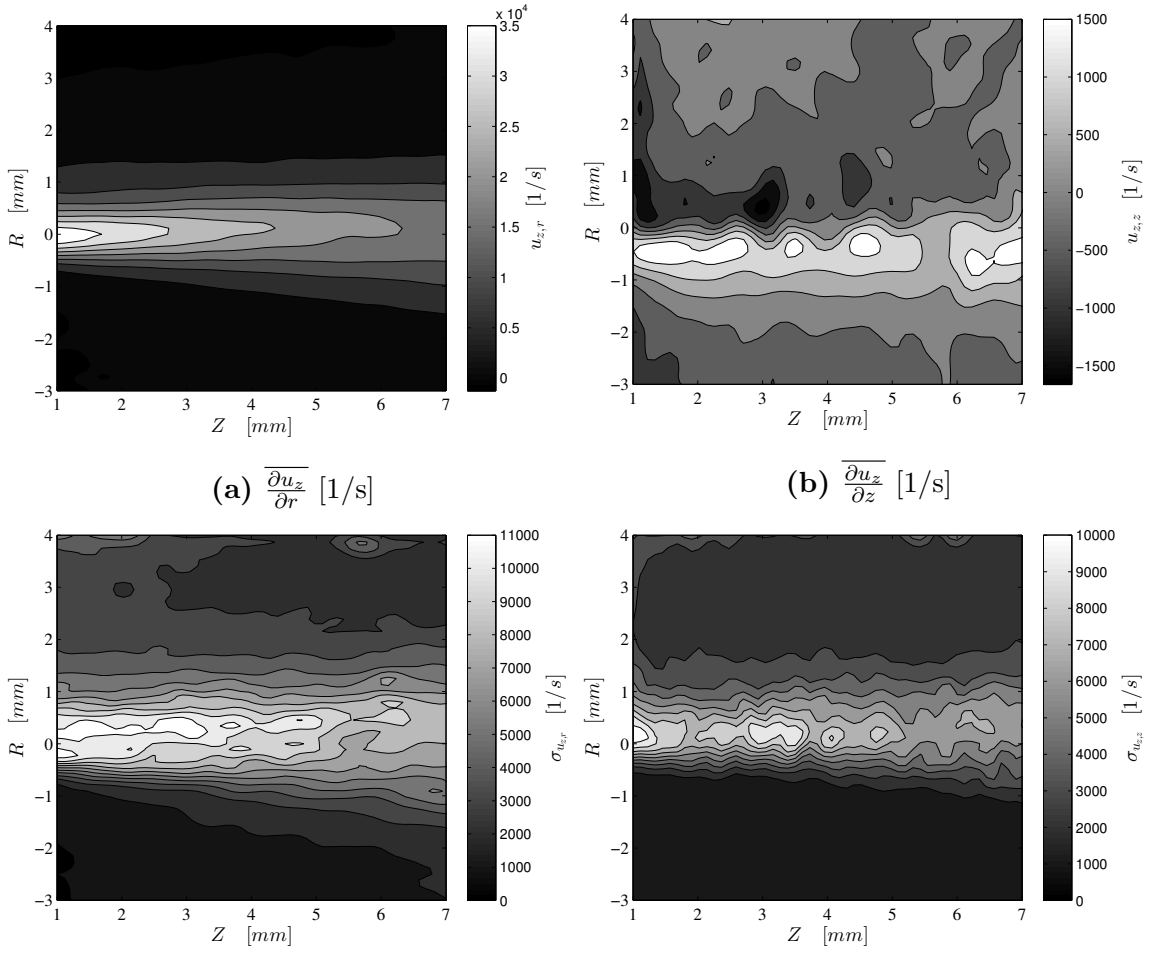

(a) $\overline{\frac{\partial u_z}{\partial r}}$ [1/s]

(b) $\overline{\frac{\partial u_z}{\partial z}}$ [1/s]

(c) $\sigma_{u_{z,r}}$ [1/s]

(d) $\sigma_{u_{z,z}}$ [1/s]

Figure C.9: Mean and standard deviation of strain fields for $\phi = 0.8$ and $u_{pm} = 35m/s$.

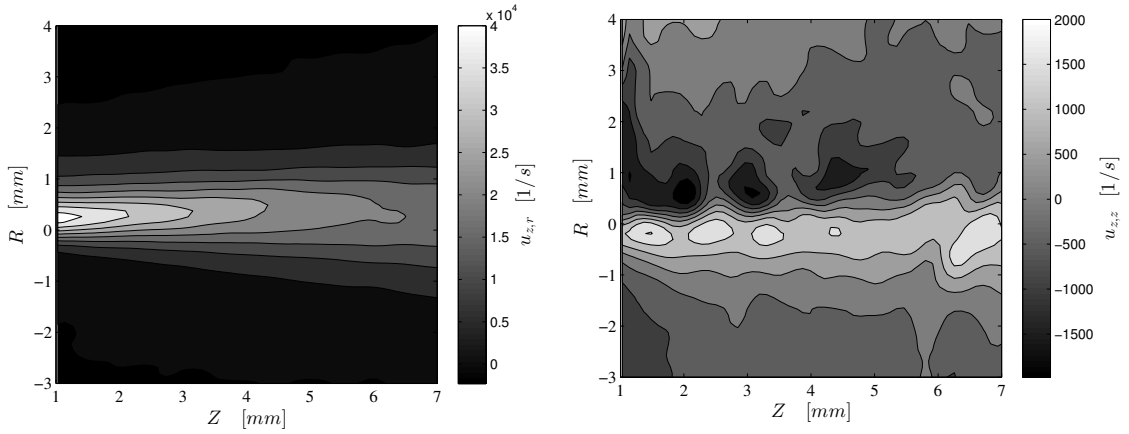

(a) $\overline{\frac{\partial u_z}{\partial r}}$ [1/s]

(b) $\overline{\frac{\partial u_z}{\partial z}}$ [1/s]

(c) $\sigma_{u_{z,r}}$ [1/s]

(d) $\sigma_{u_{z,z}}$ [1/s]

Figure C.10: Mean and standard deviation of strain fields for $\phi = 0.9$ and $u_{pm} = 35m/s$.

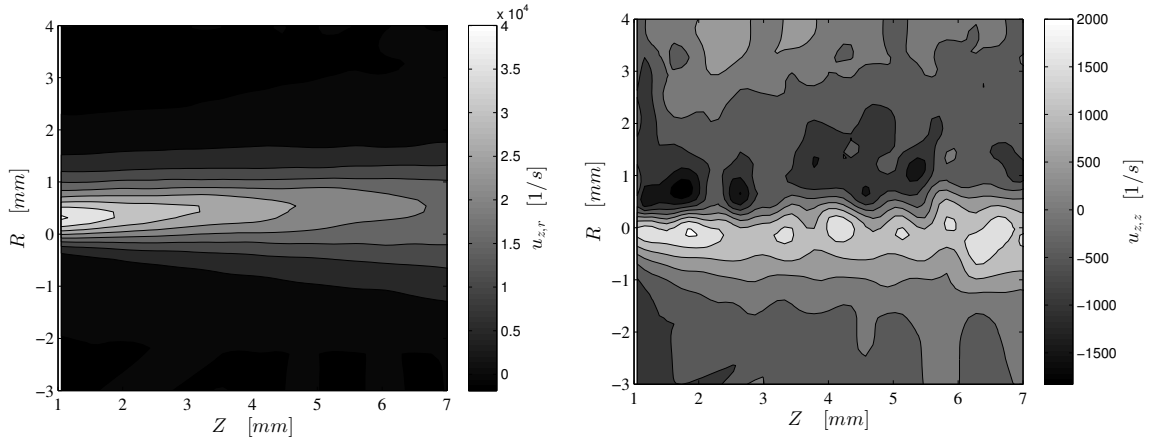

(a) $\overline{\frac{\partial u_z}{\partial r}}$ [1/s]

(b) $\overline{\frac{\partial u_z}{\partial z}}$ [1/s]

(c) $\sigma_{u_{z,r}}$ [1/s]

(d) $\sigma_{u_{z,z}}$ [1/s]

Figure C.11: Mean and standard deviation of strain fields for $\phi = 1.0$ and $u_{pm} = 35m/s$.

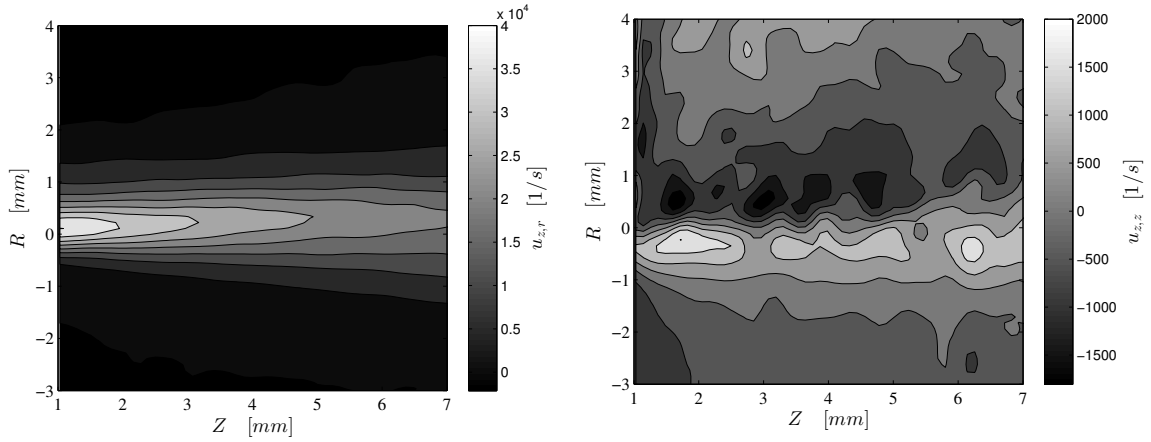

(a) $\overline{\frac{\partial u_z}{\partial r}}$ [1/s] **(b)** $\overline{\frac{\partial u_z}{\partial z}}$ [1/s]

(c) $\sigma_{u_{z,r}}$ [1/s] **(d)** $\sigma_{u_{z,z}}$ [1/s]

Figure C.12: Mean and standard deviation of strain fields for $\phi = 1.1$ and $u_{pm} = 35m/s$.

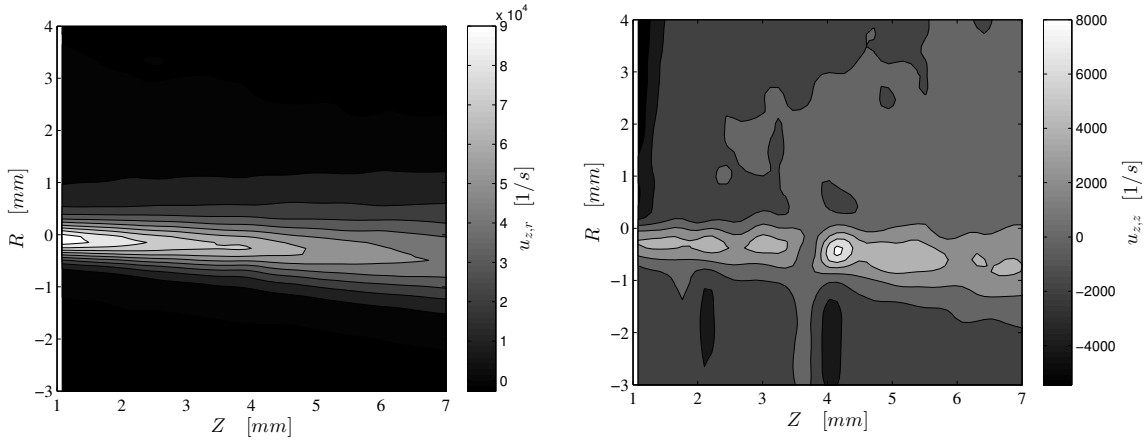

(a) $\overline{\frac{\partial u_z}{\partial r}}$ [1/s]

(b) $\overline{\frac{\partial u_z}{\partial z}}$ [1/s]

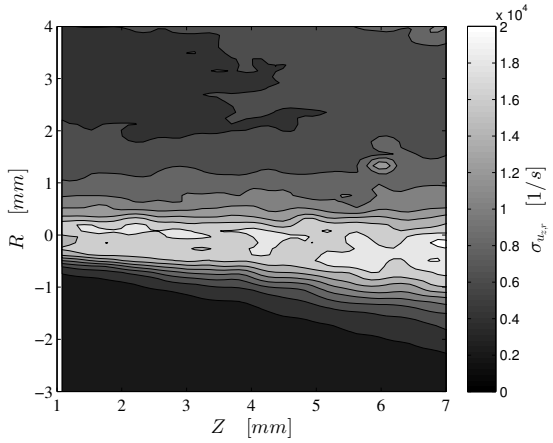

(c) $\sigma_{u_{z,r}}$ [1/s]

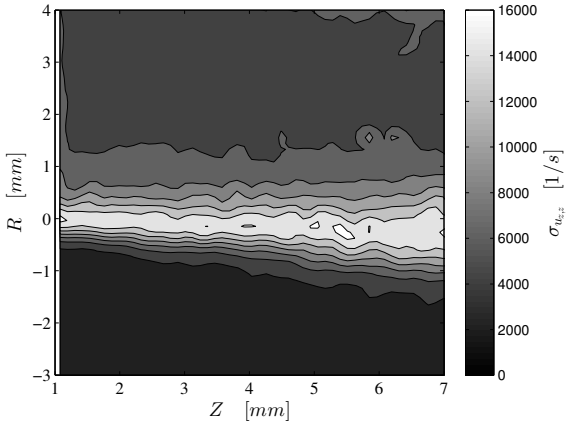

(d) $\sigma_{u_{z,z}}$ [1/s]

Figure C.13: Mean and standard deviation of strain fields for $\phi = 0.8$ and $u_{pm} = 70m/s$.

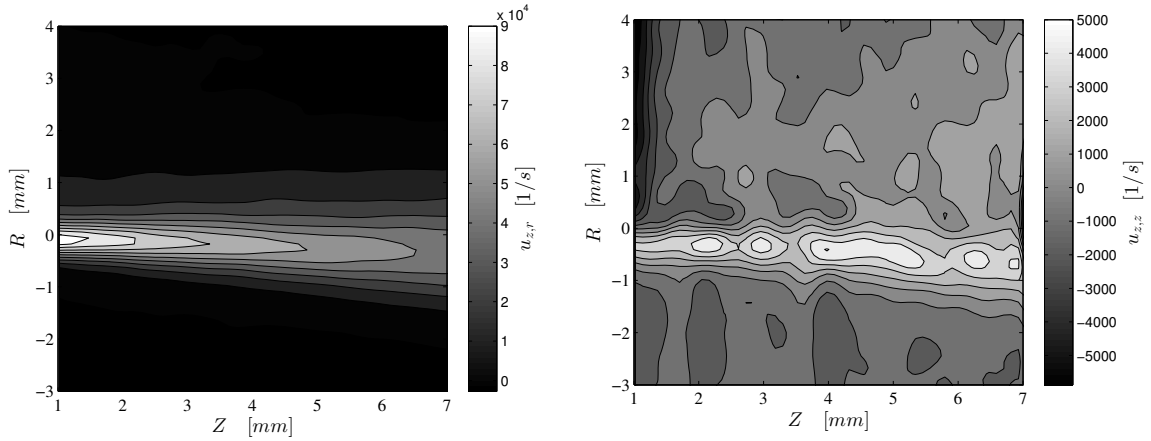

(a) $\overline{\frac{\partial u_z}{\partial r}}$ [1/s]

(b) $\overline{\frac{\partial u_z}{\partial z}}$ [1/s]

(c) $\sigma_{u_{z,r}}$ [1/s]

(d) $\sigma_{u_{z,z}}$ [1/s]

Figure C.14: Mean and standard deviation of strain fields for $\phi = 0.9$ and $u_{pm} = 70m/s$.

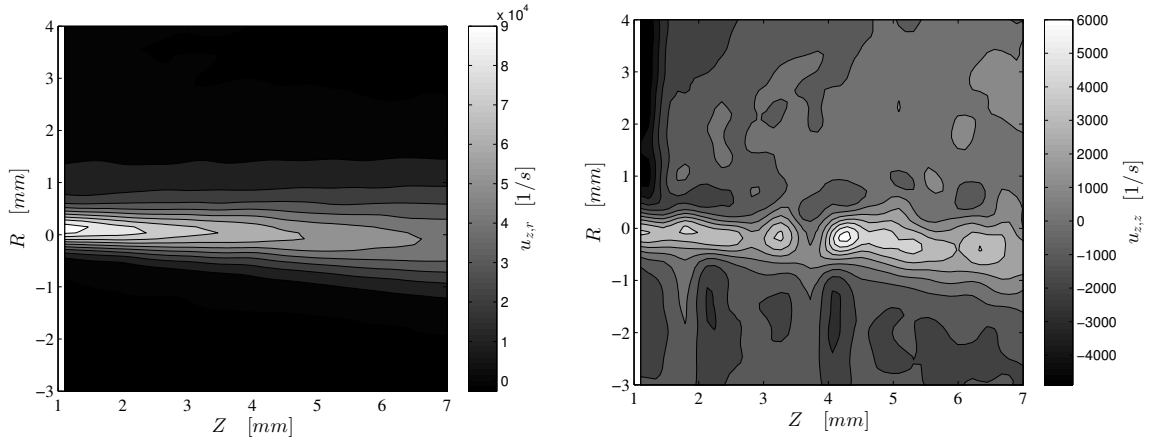

(a) $\overline{\frac{\partial u_z}{\partial r}}$ [1/s] **(b)** $\overline{\frac{\partial u_z}{\partial z}}$ [1/s]

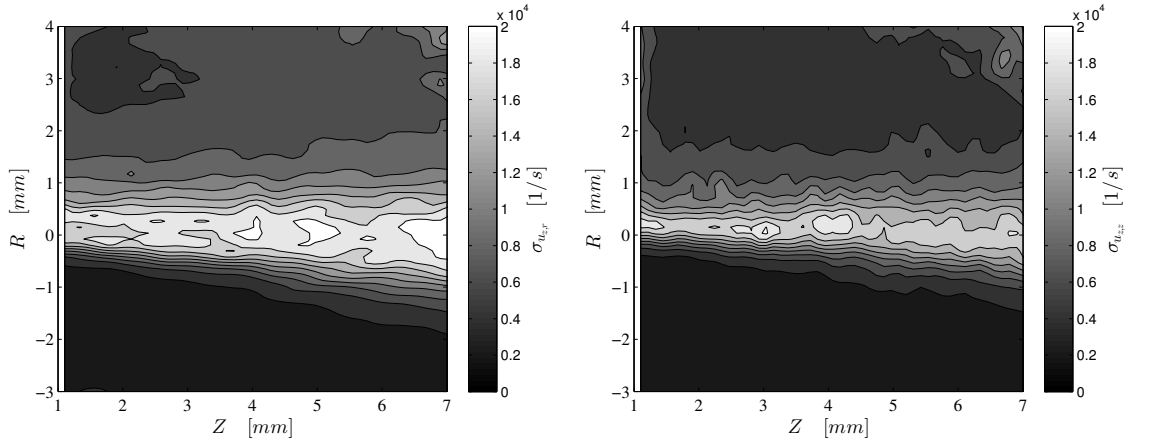

(c) $\sigma_{u_{z,r}}$ [1/s] **(d)** $\sigma_{u_{z,z}}$ [1/s]

Figure C.15: Mean and standard deviation of strain fields for $\phi = 1.0$ and $u_{pm} = 70m/s$.

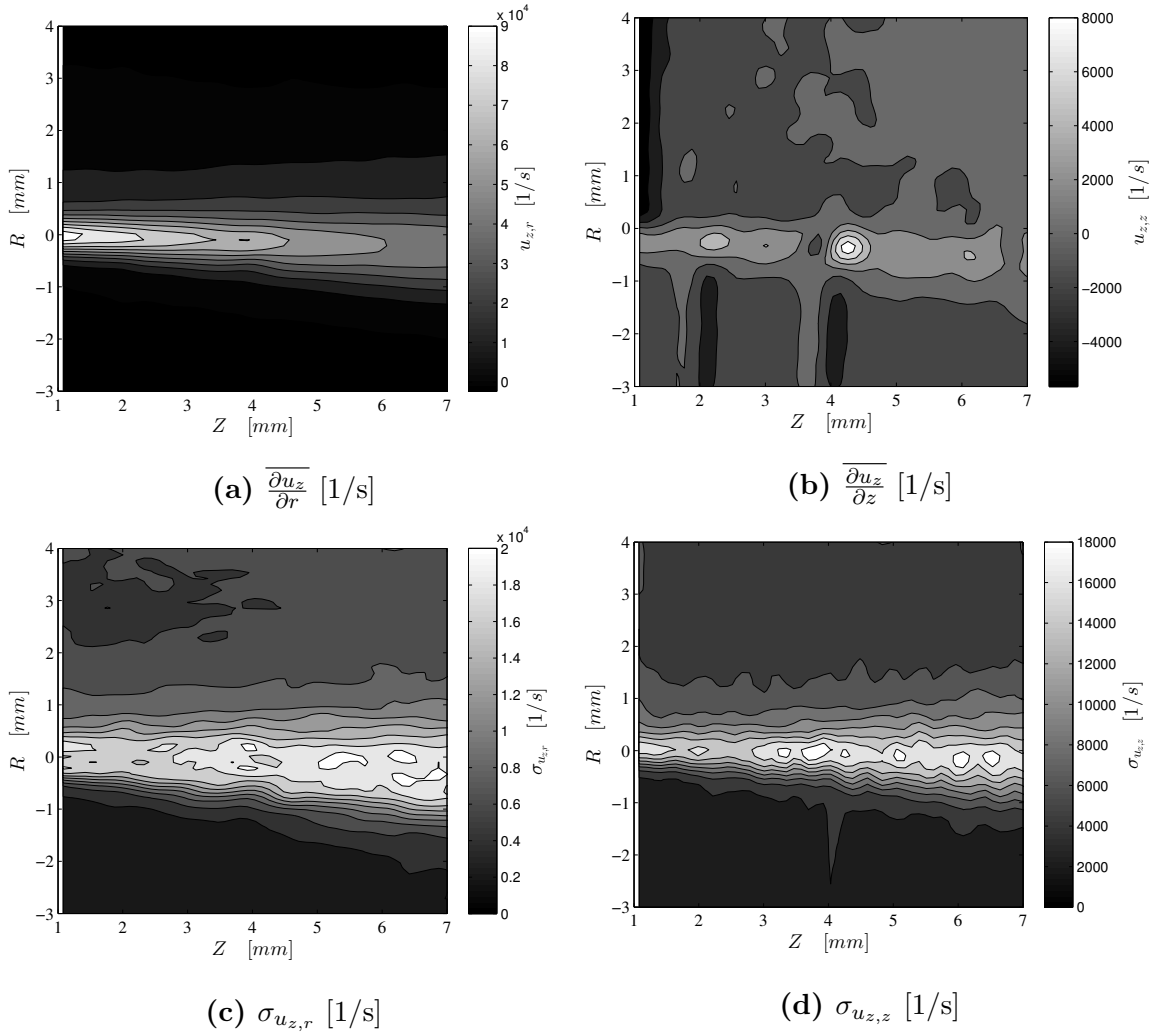

(a) $\overline{\frac{\partial u_z}{\partial r}}$ [1/s]

(b) $\overline{\frac{\partial u_z}{\partial z}}$ [1/s]

(c) $\sigma_{u_{z,r}}$ [1/s]

(d) $\sigma_{u_{z,z}}$ [1/s]

Figure C.16: Mean and standard deviation of strain fields for $\phi = 1.1$ and $u_{pm} = 70m/s$.

C.2 Flame Measurements

C.2.1 PIV and CH-PLIF

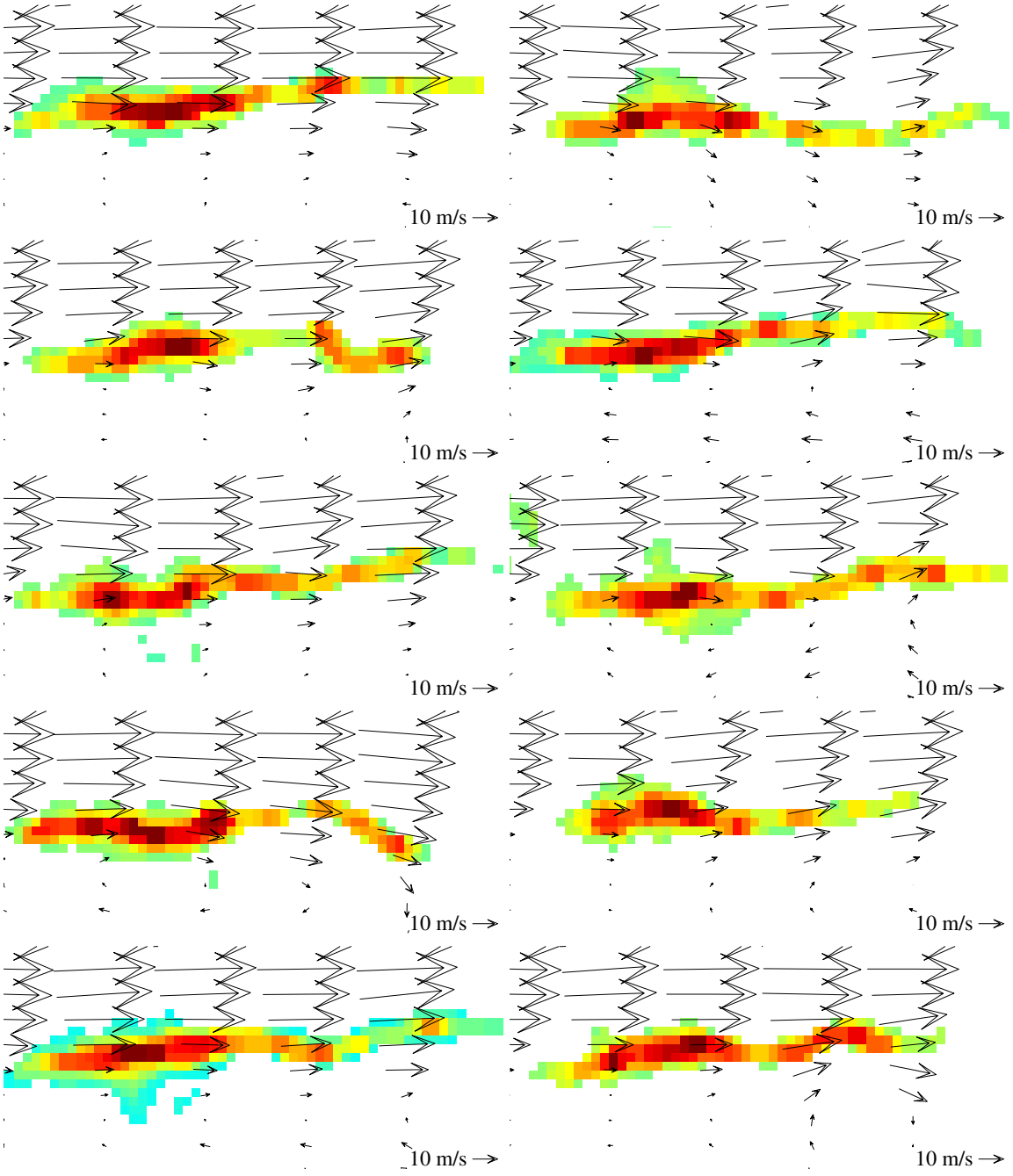

Figure C.17: Sample instantaneous images of CH-PLIF and velocity vectors for ϕ=0.8 and u_{pm}=35m/s.

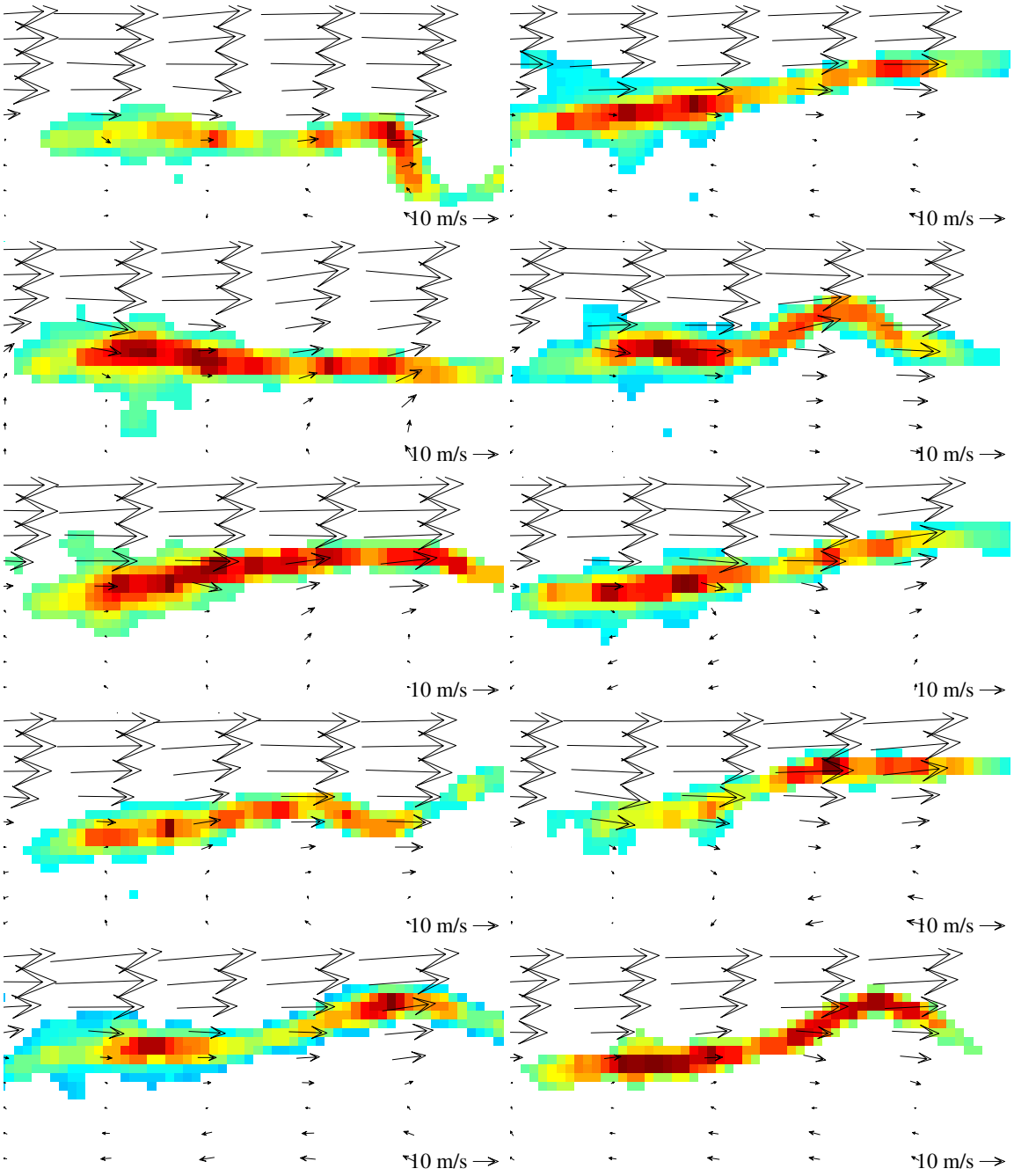

Figure C.18: Sample instantaneous images of CH-PLIF and velocity vectors for $\phi = 0.9$ and $u_{pm} = 35 m/s$.

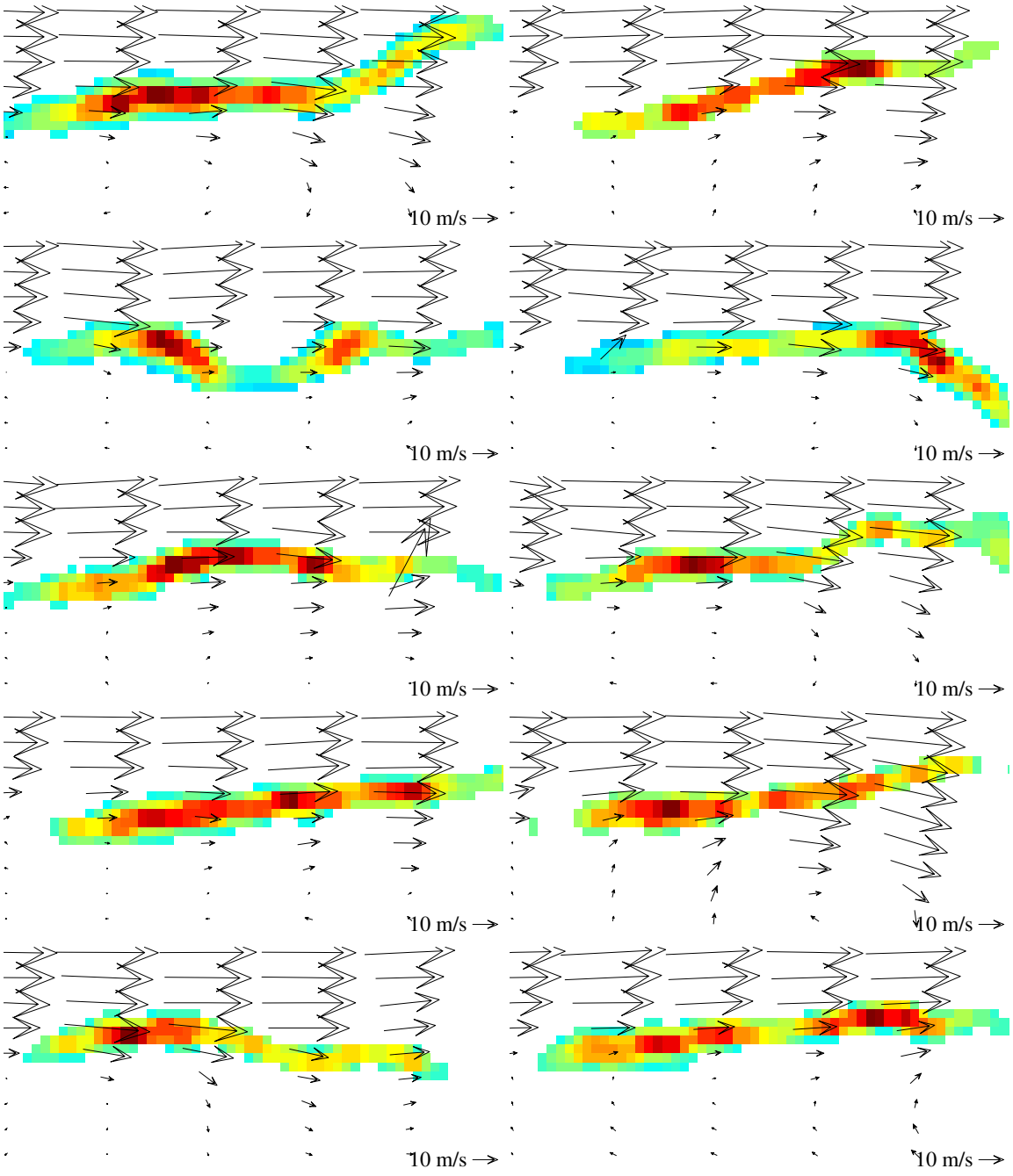

Figure C.19: Sample instantaneous images of CH-PLIF and velocity vectors for $\phi = 1.0$ and $u_{pm} = 35 m/s$.

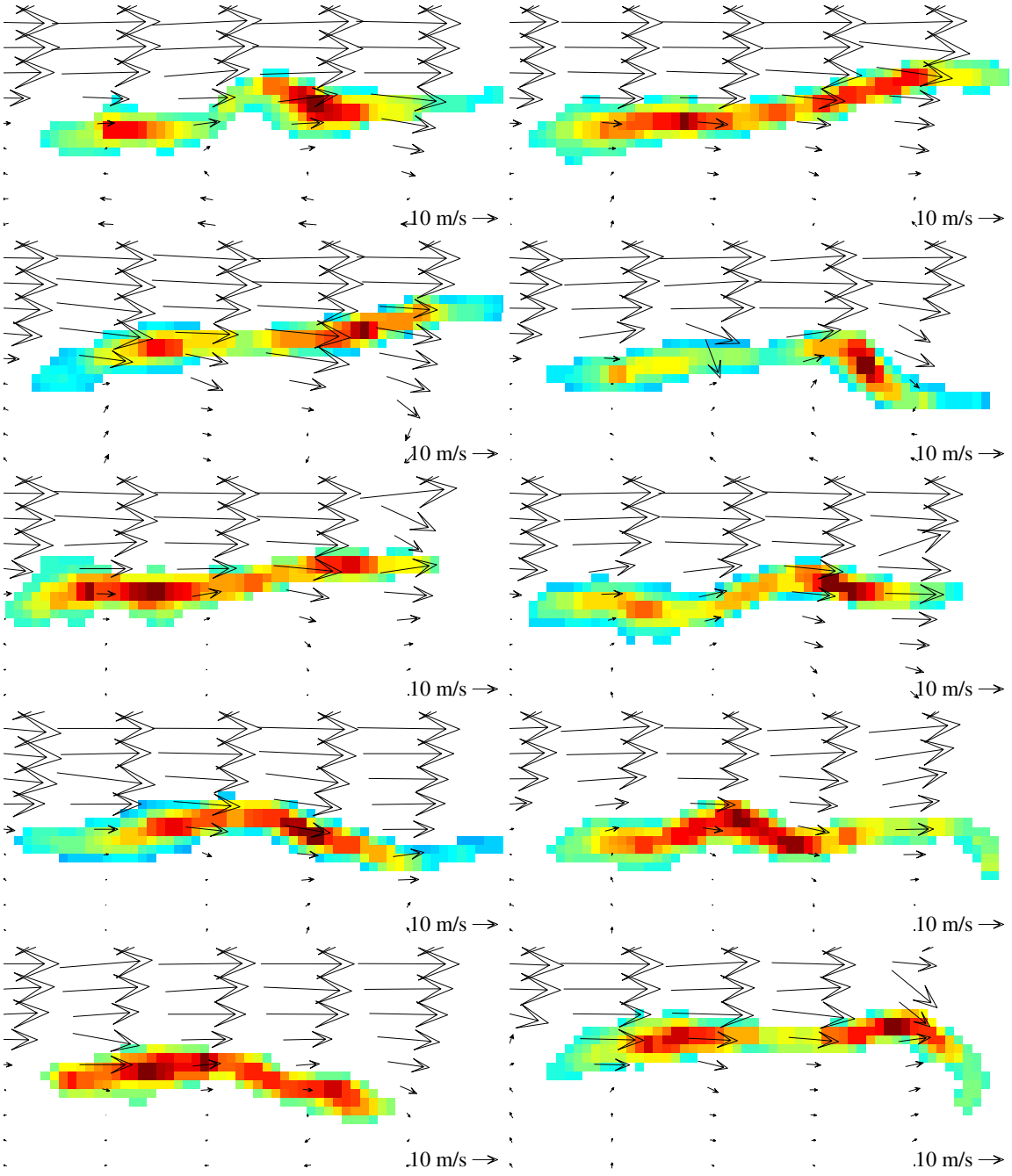

Figure C.20: Sample instantaneous images of CH-PLIF and velocity vectors for $\phi = 1.1$ and $u_{pm} = 35 m/s$.

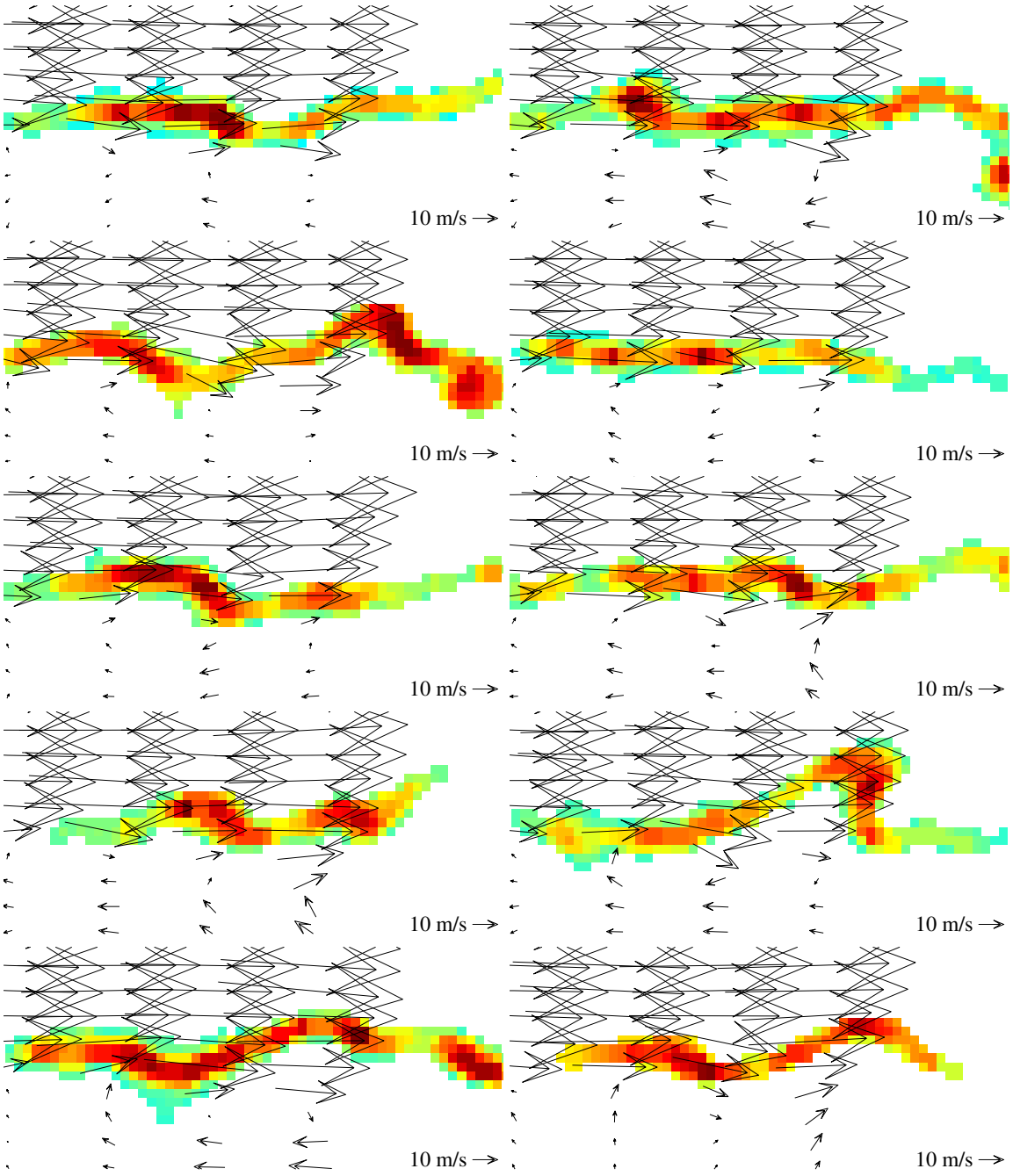

Figure C.21: Sample instantaneous images of CH-PLIF and velocity vectors for $\phi = 0.8$ and $u_{pm} = 70 m/s$.

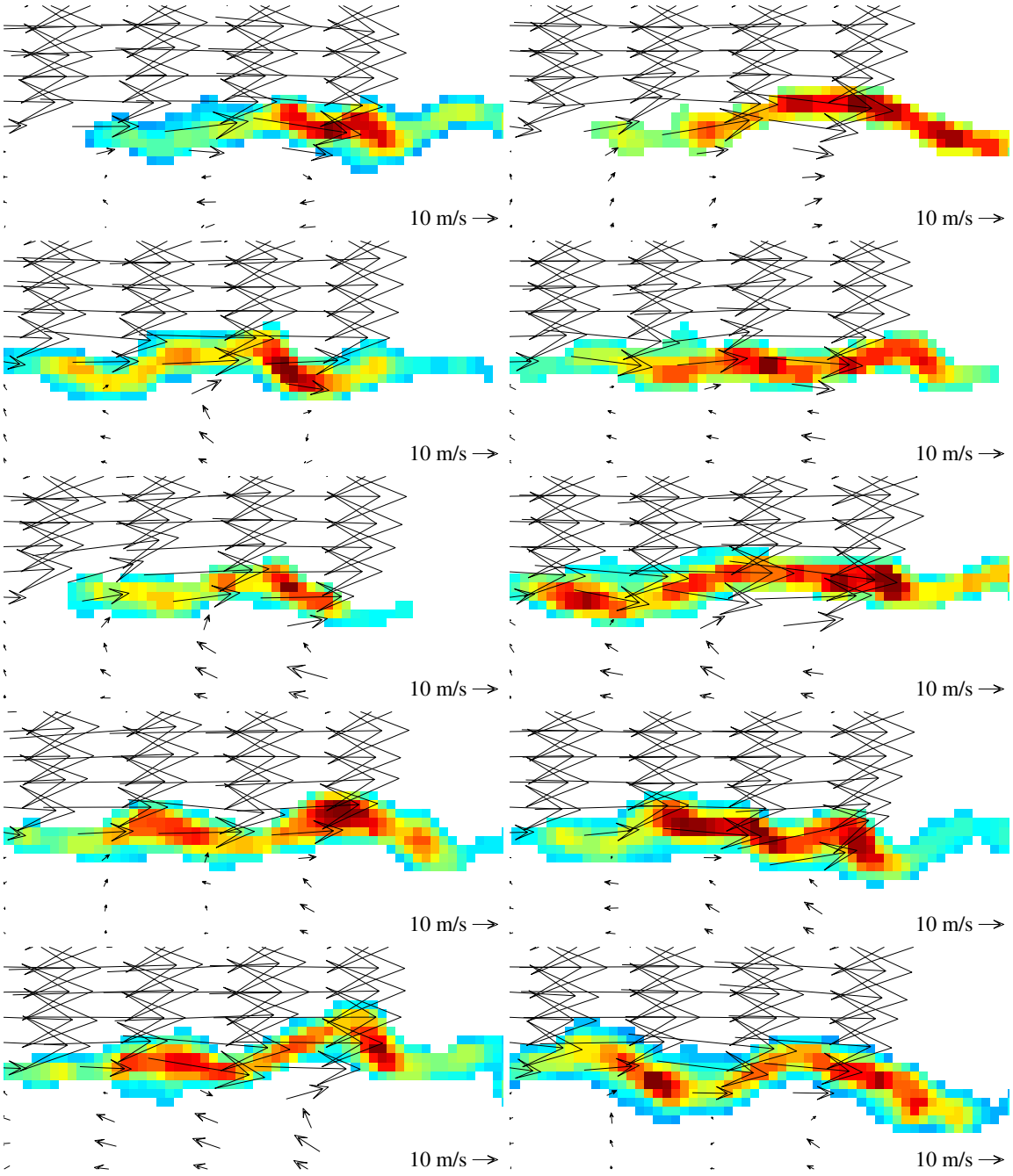

Figure C.22: Sample instantaneous images of CH-PLIF and velocity vectors for $\phi = 0.9$ and $u_{pm} = 70 m/s$.

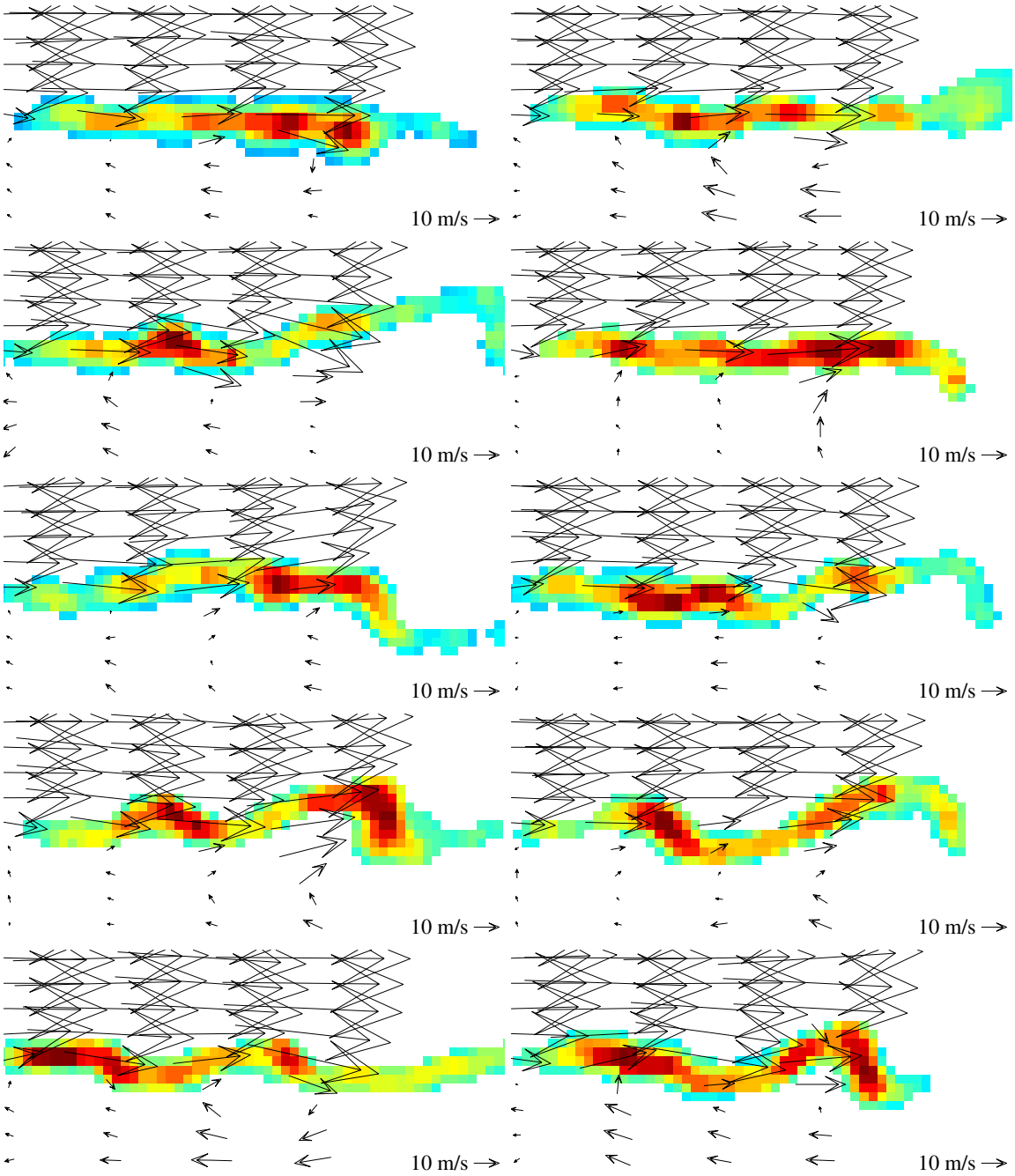

Figure C.23: Sample instantaneous images of CH-PLIF and velocity vectors for $\phi = 1.0$ and $u_{pm} = 70 m/s$.

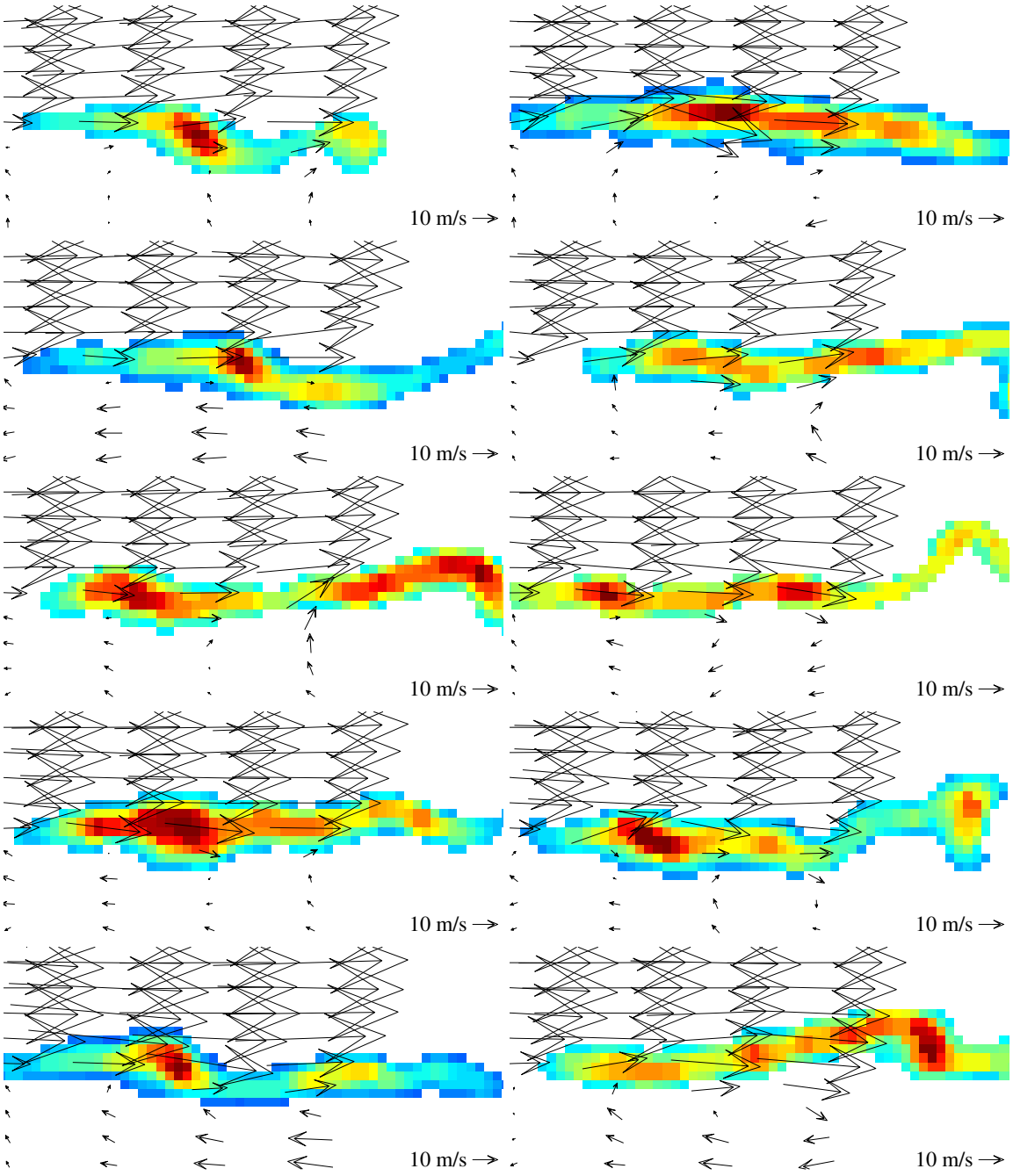

Figure C.24: Sample instantaneous images of CH-PLIF and velocity vectors for $\phi = 1.1$ and $u_{pm} = 70 m/s$.

C.2.2 Flame Stretch Measurements

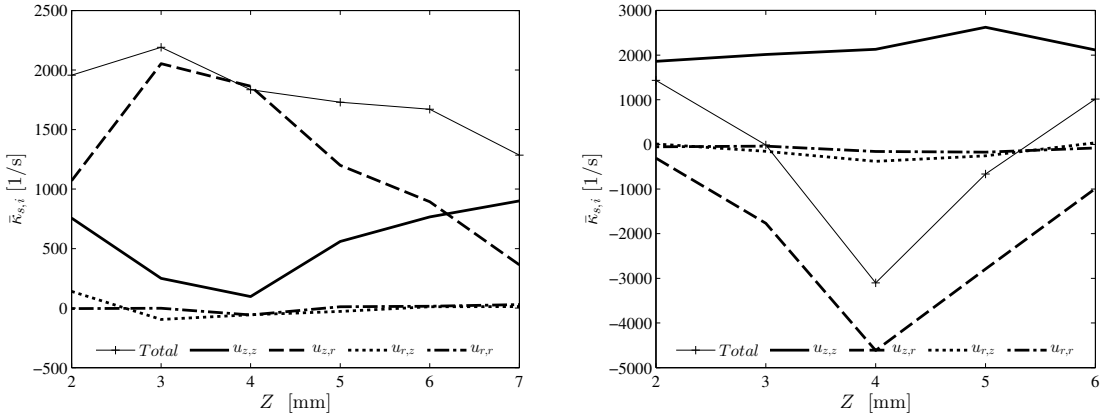

(a) $u_{pm}=35m/s$ **(b)** $u_{pm}=70m/s$

Figure C.25: Mean flame stretch as a function of Z by source for $\phi = 0.8$ and $u_{pm}=35m/s$ (left) and $u_{pm}=70m/s$ (right).

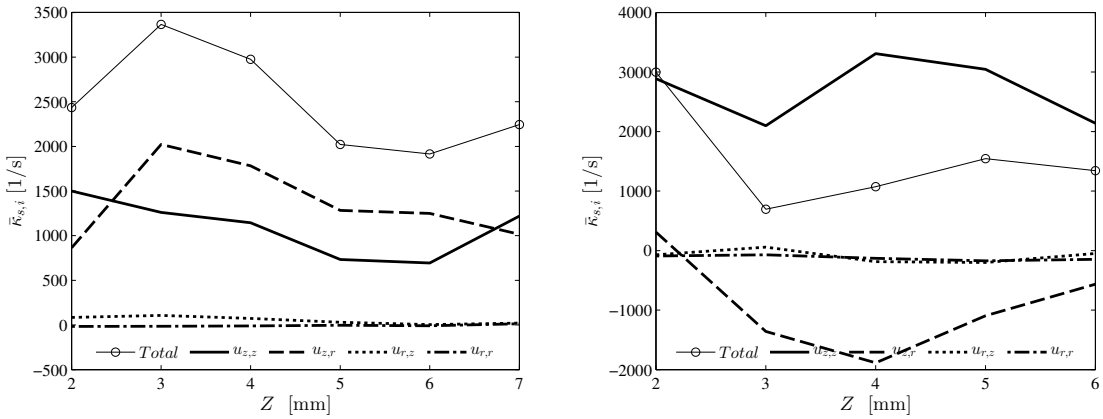

(a) $u_{pm}=35m/s$ **(b)** $u_{pm}=70m/s$

Figure C.26: Mean flame stretch as a function of Z by source for $\phi = 0.9$ and $u_{pm}=35m/s$ (left) and $u_{pm}=70m/s$ (right).

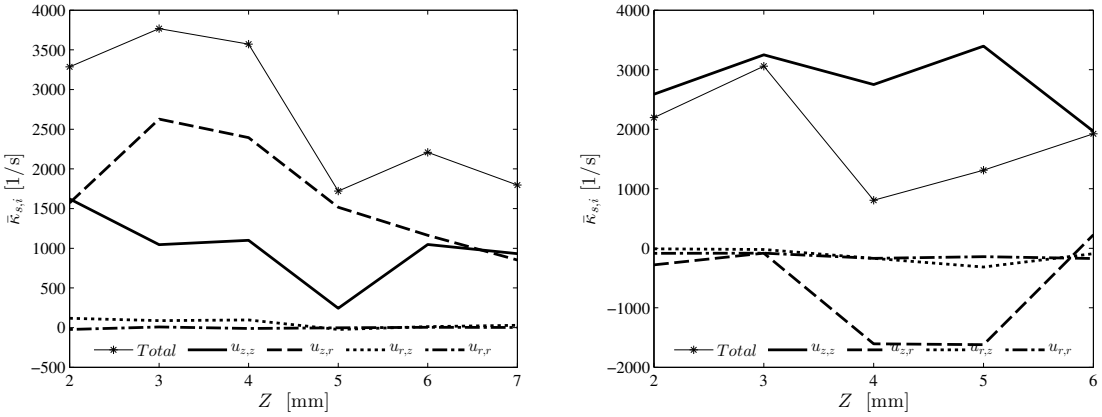

(a) $u_{pm}=35m/s$ **(b)** $u_{pm}=70m/s$

Figure C.27: Mean flame stretch as a function of Z by source for $\phi = 1.0$ and $u_{pm}=35m/s$ (left) and $u_{pm}=70m/s$ (right).

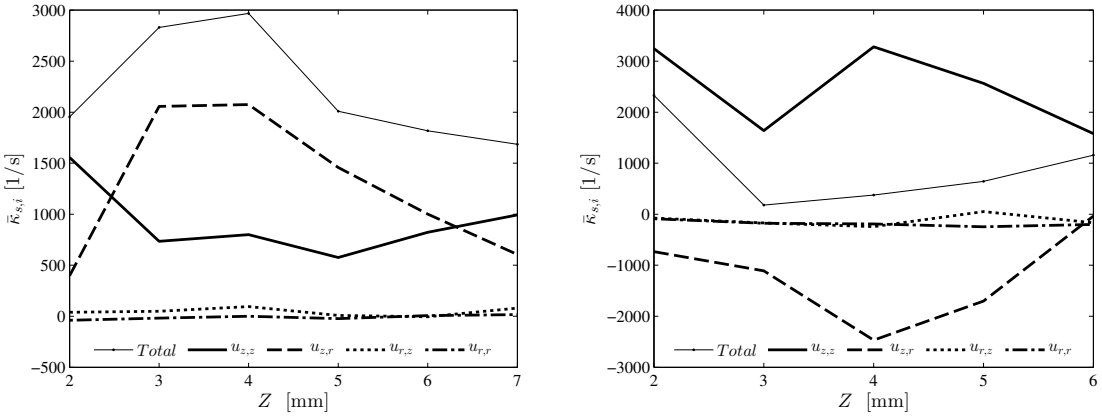

(a) $u_{pm}=35m/s$ **(b)** $u_{pm}=70m/s$

Figure C.28: Mean flame stretch as a function of Z by source for $\phi = 1.1$ and $u_{pm}=35m/s$ (left) and $u_{pm}=70m/s$ (right).

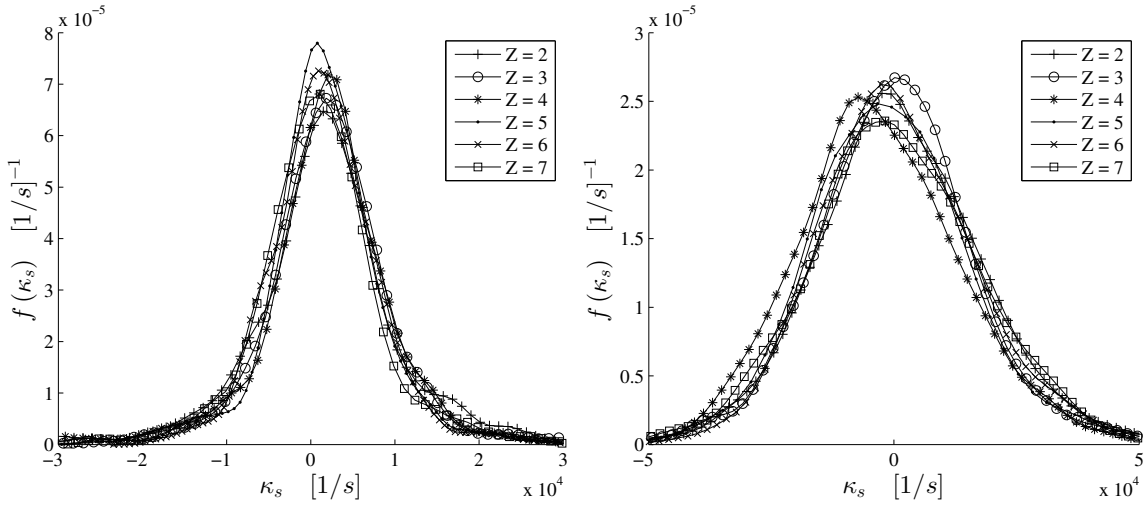

(a) $u_{pm} = 35m/s$ **(b)** $u_{pm} = 70m/s$

Figure C.29: PDF of mean flame stretch as a function of Z for $\phi = 0.8$ and $u_{pm} = 35m/s$ (left) and $u_{pm} = 70m/s$ (right).

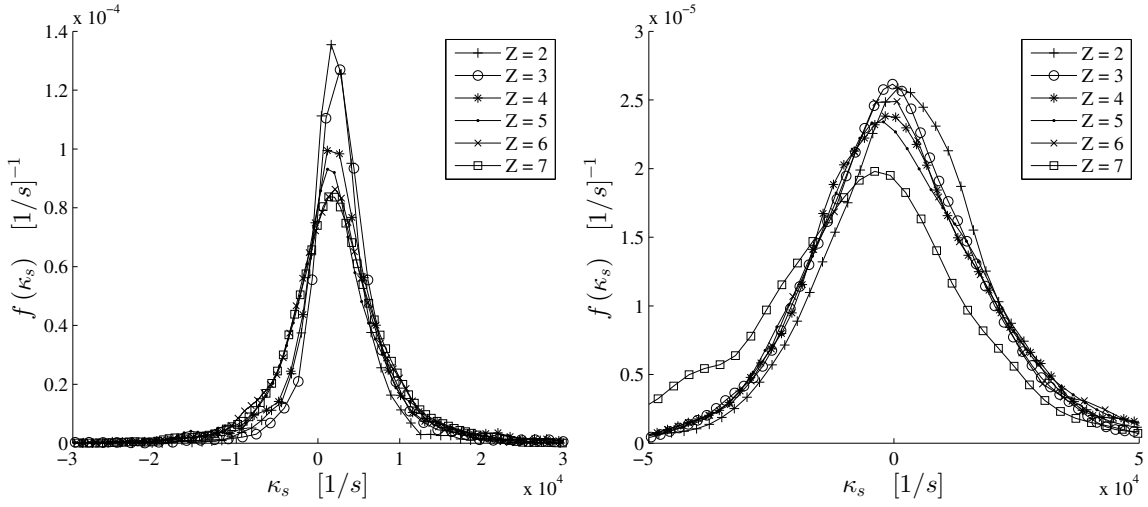

(a) $u_{pm} = 35m/s$ **(b)** $u_{pm} = 70m/s$

Figure C.30: PDF of mean flame stretch as a function of Z for $\phi = 0.9$ and $u_{pm} = 35m/s$ (left) and $u_{pm} = 70m/s$ (right).

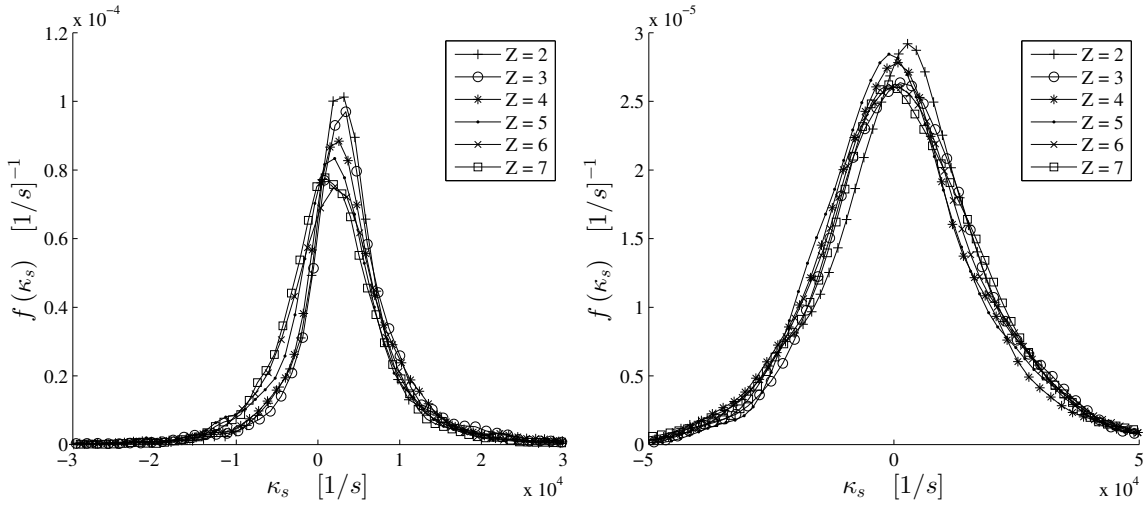

(a) $u_{pm} = 35m/s$ **(b)** $u_{pm} = 70m/s$

Figure C.31: PDF of mean flame stretch as a function of Z for $\phi = 1.0$ and $u_{pm} = 35m/s$ (left) and $u_{pm} = 70m/s$ (right).

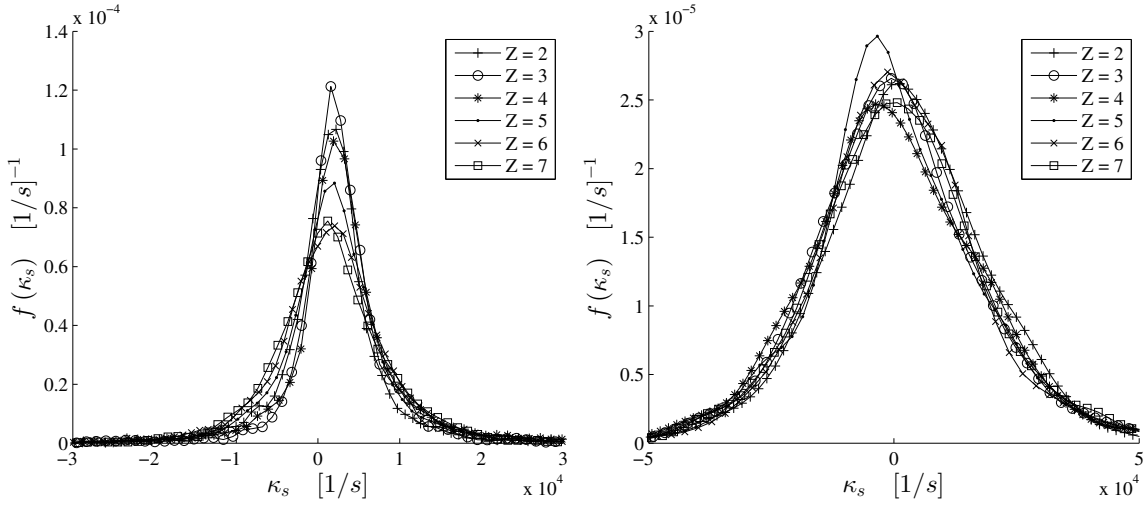

(a) $u_{pm} = 35m/s$ **(b)** $u_{pm} = 70m/s$

Figure C.32: PDF of mean flame stretch as a function of Z for $\phi = 1.1$ and $u_{pm} = 35m/s$ (left) and $u_{pm} = 70m/s$ (right).

REFERENCES

[1] "CHEMKIN-PRO 15131," 2013.

[2] Abdel-Gayed, R. G., Bradley, D., and Lung, F. K. K., "Combustion regimes and the straining of turbulent premixed flames," *Combustion and Flame*, vol. 76, pp. 213–218, May 1989.

[3] Aggarwal, S. K., "Extinction of laminar partially premixed flames," *Progress in Energy and Combustion Science*, vol. 35, pp. 528–570, Dec. 2009.

[4] Amantini, G., Frank, J., and Gomez, A., "Experiments on standing and traveling edge flames around flame holes," *Proceedings of the Combustion Institute*, vol. 30, no. 1, pp. 313–321, 2005.

[5] Amato, A., *Leading points concepts in turbulent premixed combustion modeling*. Dissertation, Georgia Institute of Technology, May 2014. Ph.D.

[6] Bergthorson, J. M. and Dimotakis, P. E., "Particle velocimetry in high-gradient/high-curvature flows," *Experiments in Fluids*, vol. 41, pp. 255–263, May 2006.

[7] Besbes, S., Mhiri, H., Palec, G. L., and Bournot, P., "Numerical and experimental study of two turbulent opposed plane jets," *Heat and Mass Transfer*, vol. 39, pp. 675–686, Sept. 2003.

[8] Bhm, B., Heeger, C., Boxx, I., Meier, W., and Dreizler, A., "Time-resolved conditional flow field statistics in extinguishing turbulent opposed jet flames using simultaneous highspeed PIV/OH-PLIF," *Proceedings of the Combustion Institute*, vol. 32, no. 2, pp. 1647–1654, 2009.

[9] Borghi, R., "On the Structure and Morphology of Turbulent Premixed Flames," in *Recent Advances in the Aerospace Sciences* (Casci, P. I. C. and Bruno, C., eds.), pp. 117–138, Springer US, 1985.

[10] Brock, J. R., "On the theory of thermal forces acting on aerosol particles," *Journal of Colloid Science*, vol. 17, pp. 768–780, Oct. 1962.

[11] Buckmaster, J., "Edge-flames," *Progress in Energy and Combustion Science*, vol. 28, no. 5, pp. 435–475, 2002.

[12] Buckmaster, J., "Edge-flames," *Progress in Energy and Combustion Science*, vol. 28, no. 5, pp. 435–475, 2002.

[13] Cha, M. S. and Ronney, P. D., "Propagation rates of nonpremixed edge flames," *Combustion and Flame*, vol. 146, pp. 312–328, July 2006.

[14] Charonko, J. J. and Vlachos, P. P., "Estimation of uncertainty bounds for individual particle image velocimetry measurements from cross-correlation peak ratio," *Measurement Science and Technology*, vol. 24, pp. 65301–65316, June 2013.

[15] Chaudhuri, S., Kostka, S., Renfro, M. W., and Cetegen, B. M., "Blowoff dynamics of bluff body stabilized turbulent premixed flames," *Combustion and Flame*, vol. 157, pp. 790–802, Apr. 2010.

[16] Chaudhuri, S., Kostka, S., Renfro, M. W., and Cetegen, B. M., "Blowoff mechanism of harmonically forced bluff body stabilized turbulent premixed flames," *Combustion and Flame*, vol. 159, pp. 638–640, Feb. 2012.

[17] Chen, J. H. and Im, H. G., "Correlation of flame speed with stretch in turbulent premixed methane/air flames," vol. 27, pp. 819–826, Elsevier, 1998. 1.

[18] Chen, J. and Im, H., "Stretch effects on the burning velocity of turbulent premixed hydrogen/air flames," *Proceedings of the Combustion Institute*, vol. 28, no. 1, pp. 211–218, 2000.

[19] Cho, P., Law, C. K., Hertzberg, J. R., and Cheng, R. K., "Structure and propagation of turbulent premixed flames astabilized in a stagnation flow," *Symposium (International) on Combustion*, vol. 21, no. 1, pp. 1493–1499, 1988.

[20] Cho, Y., Kim, J.-H., Cho, T., Moon, I., Yoon, Y., and Lee, C., "Analysis of turbulent premixed flame structure using simultaneous PIV-OH PLIF," *Journal of Visualization*, vol. 7, pp. 43–54, Mar. 2004.

[21] Chong, L. T. W., Komarek, T., Zellhuber, M., Lenz, J., Hirsch, C., and Polifke, W., "Influence of strain and heat loss on flame stabilization in a non-adiabatic combustor," 2009.

[22] Chterev, I., Foley, C. W., Foti, D., Kostka, S., Caswell, A. W., Jiang, N., Lynch, A., Noble, D. R., Menon, S., Seitzman, J. M., and Lieuwen, T. C., "Flame and Flow Topologies in an Annular Swirling Flow," *Combustion Science and Technology*, vol. 186, no. 8, pp. 1041–1074, 2014.

[23] Chterev, I., Foley, C., Noble, D., Ochs, B., Seitzman, J., and Lieuwen, T., "Shear layer flame stabilization sensitivities in a swirling flow," June 2012.

[24] Chung, S., DH, C., and Cho, P., "Local extinction Karlovitz number for premixed flames," *Combustion and Flame*, vol. 106, no. 4, pp. 515–520, 1996.

[25] Chung, S., Kim, J., and Law, C., "Extinction of interacting premixed flames: theory and experimental comparisons," vol. 21, pp. 1845–1851, Elsevier, 1988. 1.

[26] Coppola, G., Coriton, B., and Gomez, A., "Highly turbulent counterflow flames: A laboratory scale benchmark for practical systems," *Combustion and Flame*, vol. 156, pp. 1834–1843, Sept. 2009.

[27] Coriton, B., Smooke, M., and Gomez, A., "Effect of the composition of the hot product stream in the quasi-steady extinction of strained premixed flames," *Combustion and Flame*, vol. 157, no. 11, pp. 2155–2164, 2010.

[28] Coriton, B., Frank, J. H., and Gomez, A., "Effects of strain rate, turbulence, reactant stoichiometry and heat losses on the interaction of turbulent premixed flames with stoichiometric counterflowing combustion products," *Combustion and Flame*, 2013.

[29] Daou, J. and Lin, A., "Ignition and extinction fronts in counterflowing premixed reactive gases," *Combustion and Flame*, vol. 118, pp. 479–488, Aug. 1999.

[30] Daou, J., "Strained premixed flames: Effect of heat-loss, preferential diffusion and reversibility of the reaction," *Combustion Theory and Modelling*, vol. 15, no. 4, pp. 437–454, 2011.

[31] Daou, R., Daou, J., and Dold, J., "Effect of heat-loss on flame-edges in a premixed counterflow," *Combustion Theory and Modelling*, vol. 7, no. 2, pp. 221–242, 2003.

[32] Daou, R., Daou, J., and Dold, J., "The effect of heat loss on flame edges in a non-premixed counterflow within a thermo-diffusive model," *Combustion Theory and Modelling*, vol. 8, no. 4, pp. 683–699, 2004.

[33] Dixon-Lewis, G., "Structure of laminar flames," vol. 23, pp. 305–324, Elsevier, 1991. 1.

[34] Donbar, J., Driscoll, J., and Carter, C., "Strain rates measured along the wrinkled flame contour within turbulent non-premixed jet flames," *Combustion and flame*, vol. 125, no. 4, pp. 1239–1257, 2001.

[35] Duncan, J., Bryce, T., Thomsen, H., Dabiri, D., Hove, J., and Gharib, M., "An extended study of a generalized digital particle image velocimetry (DPIV) processing technique," *Measurement Science and Technology*, vol. 20, no. 7, p. 075401, 2009.

[36] Echekki, T. and Chen, J. H., "Unsteady strain rate and curvature effects in turbulent premixed methane-air flames," *Combustion and Flame*, vol. 106, no. 1, pp. 184–202, 1996.

[37] Egolfopoulos, F. N., "Dynamics and structure of unsteady, strained, laminar premixed flames," vol. 25, pp. 1365–1373, Elsevier, 1994. 1.

[38] Emara, A., Lacarelle, A., and Paschereit, C. O., "Planar Investigation of Outlet Boundary Conditions Effect on Isothermal Flow Fields of a Swirl-Stabilized Burner," ASME, 2009.

[39] Escudier, M. and Keller, J., "Recirculation in swirling flow-a manifestation of vortex breakdown," *AIAA journal*, vol. 23, no. 1, pp. 111–116, 1985.

[40] Etebari, A. and Vlachos, P. P., "Improvements on the accuracy of derivative estimation from DPIV velocity measurements," *Experiments in Fluids*, vol. 39, no. 6, pp. 1040–1050, 2005.

[41] Filatyev, S. A., Driscoll, J. F., Carter, C. D., and Donbar, J. M., "Measured properties of turbulent premixed flames for model assessment, including burning velocities, stretch rates, and surface densities," *Combustion and Flame*, vol. 141, no. 1, pp. 1–21, 2005.

[42] Foley, C., Chterev, I., Seitzman, J., and Lieuwen, T., "Flame Configurations in a Lean Premixed Dump Combustor with an Annular Swirling Flow," 2011. 1D16.

[43] Fritsche, D., Fri, M., and Boulouchos, K., "An experimental investigation of thermoacoustic instabilities in a premixed swirl-stabilized flame," *Combustion and Flame*, vol. 151, no. 1, pp. 29–36, 2007.

[44] Giovangigli, V. and Smooke, M. D., "Extinction of Strained Premixed Laminar Flames With Complex Chemistry," *Combustion Science and Technology*, vol. 53, pp. 23–49, May 1987.

[45] Giovangigli, V. and Smooke, M., "Calculation of extinction limits for premixed laminar flames in a stagnation point flow," *Journal of Computational Physics*, vol. 68, no. 2, pp. 327–345, 1987.

[46] GOMEZ, A. and ROSNER, D. E., "Thermophoretic Effects on Particles in Counterflow Laminar Diffusion Flames," *Combustion Science and Technology*, vol. 89, pp. 335–362, Mar. 1993.

[47] Goodwin, D. G., Moffat, H. K., and Speth, R. L., "Cantera: An Object-oriented Software Toolkit for Chemical Kinetics, Thermodynamics, and Transport Processes," 2015.

[48] Gupta, A., Lilley, D., and Syred, N., *Swirl flows*, vol. 1 of *Tunbridge Wells, Kent, England, Abacus Press, 1984, 488 p.* 1984.

[49] Hawkes, E. R. and Chen, J. H., "Comparison of direct numerical simulation of lean premixed methaneair flames with strained laminar flame calculations," *Combustion and flame*, vol. 144, no. 1, pp. 112–125, 2006.

[50] Hu, S., Wang, P., and Pitz, R. W., "A structural study of premixed tubular flames," *Proceedings of the Combustion Institute*, vol. 32, no. 1, pp. 1133–1140, 2009.

[51] Huang, R. and Tsai, F., "Flow field characteristics of swirling double concentric jets," *Experimental thermal and fluid science*, vol. 25, no. 3, pp. 151–161, 2001.

[52] Huang, Y. and Yang, V., "Bifurcation of flame structure in a lean-premixed swirl-stabilized combustor: transition from stable to unstable flame," *Combustion and flame*, vol. 136, no. 3, pp. 383–389, 2004.

[53] Im, H. G. and Chen, J. H., "Effects of flow transients on the burning velocity of laminar hydrogen/air premixed flames," *Proceedings of the Combustion Institute*, vol. 28, no. 2, pp. 1833–1840, 2000.

[54] Jayachandran, J., Zhao, R., and Egolfopoulos, F. N., "Determination of laminar flame speeds using stagnation and spherically expanding flames: Molecular transport and radiation effects," *Combustion and Flame*, 2014.

[55] Ju, Y., Guo, H., Maruta, K., and Liu, F., "On the extinction limit and flammability limit of non-adiabatic stretched methaneair premixed flames," *Journal of Fluid Mechanics*, vol. 342, pp. 315–334, July 1997.

[56] Ju, Y., Masuya, G., and Ronney, P. D., "Effects of radiative emission and absorption on the propagation and extinction of premixed gas flames," *Symposium (International) on Combustion*, vol. 27, no. 2, pp. 2619–2626, 1998.

[57] Ju, Y., Matsumi, H., Takita, K., and Masuya, G., "Combined effects of radiation, flame curvature, and stretch on the extinction and bifurcations of cylindrical CH4/air premixed flame," *Combustion and Flame*, vol. 116, pp. 580–592, Mar. 1999.

[58] Kariuki, J., Dawson, J. R., and Mastorakos, E., "Measurements in turbulent premixed bluff body flames close to blow-off," *Combustion and Flame*, vol. 159, pp. 2589–2607, Aug. 2012.

[59] Karlovitz, B., Denniston, D., Knapschaefer, D., and Wells, F., "Studies on Turbulent flames: A. Flame Propagation Across Velocity Gradients B. Turbulence Measurement in Flames," vol. 4, pp. 613–620, Elsevier, 1953. 1.

[60] Kee, R. J., Miller, J. A., Evans, G. H., and Dixon-Lewis, G., "A computational model of the structure and extinction of strained, opposed flow, premixed methane-air flames," vol. 22, pp. 1479–1494, Elsevier, 1988. 1.

[61] Khosla, S., Leach, T. T., and Smith, C. E., "Flame stabilization and role of von karman vortex shedding behind bluff body flameholders," *AIAA paper*, vol. 5653, p. 2007, 2007.

[62] Korusoy, E. and Whitelaw, J., "Extinction and relight in opposed flames," *Experiments in Fluids*, vol. 33, pp. 75–89, July 2002.

[63] Kostiuk, L. W., Shepherd, I. G., and Bray, K. N. C., "Experimental study of premixed turbulent combustion in opposed streams. Part IIIspatial structure of flames," *Combustion and Flame*, vol. 118, pp. 129–139, July 1999.

[64] Kostiuk, L., Bray, K., and Cheng, R., "Experimental study of premixed turbulent combustion in opposed streams. Part IIreacting flow field and extinction," *Combustion and flame*, vol. 92, no. 4, pp. 396–409, 1993.

[65] Krmn, T. V., "ber laminare und turbulente Reibung," *ZAMM - Journal of Applied Mathematics and Mechanics / Zeitschrift fr Angewandte Mathematik und Mechanik*, vol. 1, pp. 233–252, Jan. 1921.

[66] Law, C. K. and Sung, C. J., "Structure, aerodynamics, and geometry of premixed flamelets," *Progress in Energy and Combustion Science*, vol. 26, pp. 459–505, Aug. 2000.

[67] Law, C. K., Zhu, D. L., and Yu, G., "Propagation and extinction of stretched premixed flames," *Symposium (International) on Combustion*, vol. 21, no. 1, pp. 1419–1426, 1988.

[68] Law, C. K., *Combustion physics*. Cambridge University Press, 2006.

[69] Lefebvre, A. H., *Gas Turbine Combustion*. New York: Taylor & Francis, 2nd ed., 1999.

[70] Lienhard, J. H., *Synopsis of lift, drag, and vortex frequency data for rigid circular cylinders*. 1966.

[71] Lieuwen, T., McDonell, V., Petersen, E., and Santavicca, D., "Fuel flexibility influences on premixed combustor blowout, flashback, autoignition, and stability," *Journal of Engineering for Gas Turbines & Power*, vol. 130, no. 1, p. 11506, 2008.

[72] Lieuwen, T. C., *Unsteady Combustor Physics*. Cambridge, 2012.

[73] Lilley, D. G., "Swirl Flows in Combustion: A Review," *AIAA Journal*, vol. 15, no. 8, pp. 1063–1078, 1977.

[74] LIU, J.-B. and RONNEY, P. D., "Premixed Edge-Flames in Spatially-Varying Straining Flows," *Combustion Science and Technology*, vol. 144, no. 1-6, pp. 21–45, 1999.

[75] Lu, X., Wang, S., Sung, H.-G., Hsieh, S.-Y., and Yang, V., "Large-eddy simulations of turbulent swirling flows injected into a dump chamber," *Journal of Fluid Mechanics*, vol. 527, pp. 171–195, 2005.

[76] Lucca-Negro, O. and O'Doherty, T., "Vortex breakdown: a review," *Progress in Energy and Combustion Science*, vol. 27, no. 4, pp. 431–481, 2001.

[77] Luff, D., Korusoy, E., Lindstedt, P., and Whitelaw, J. H., "Counterflow flames of air and methane, propane and ethylene, with and without periodic forcing," *Experiments in Fluids*, vol. 35, pp. 618–626, Nov. 2003.

[78] Mastorakos, E., Taylor, A., and Whitelaw, J., "Extinction of turbulent counterflow flames with reactants diluted by hot products," *Combustion and flame*, vol. 102, no. 1, pp. 101–114, 1995.

[79] Mayer, S., "A generalized processing technique in digital particle image velocimetry with direct estimation of velocity gradients," *Experiments in fluids*, vol. 33, no. 3, pp. 443–457, 2002.

[80] Mei, R., "Velocity fidelity of flow tracer particles," *Experiments in Fluids*, vol. 22, pp. 1–13, Nov. 1996.

[81] Melling, A., "Tracer particles and seeding for particle image velocimetry," *Measurement Science and Technology*, vol. 8, p. 1406, Dec. 1997.

[82] MUNGAL, M. G., LOURENCO, L. M., and KROTHAPALLI, A., "Instantaneous Velocity Measurements in Laminar and Turbulent Premixed Flames Using On-Line PIV," *Combustion Science and Technology*, vol. 106, pp. 239–265, Jan. 1995.

[83] Nair, S. and Lieuwen, T., "Acoustic detection of blowout in premixed flames," *Journal of Propulsion and Power*, vol. 21, no. 1, pp. 32–39, 2005.

[84] Nair, S. and Lieuwen, T. C., "Near-Blowoff Dynamics of a Bluff-Body Stabilized Flame," *Journal of Propulsion and Power*, vol. 23, no. 2, pp. 421–427, 2007.

[85] Patnaik, G. and Kailasanath, K., "A computational study of local quenching in flame-vortex interactions with radiative losses," *Symposium (International) on Combustion*, vol. 27, no. 1, pp. 711–717, 1998.

[86] Periagaram, K. B., "Determination of flame characteristics in a low swirl burner at gas turbine conditions through reaction zone imaging," Aug. 2012. PhD.

[87] Peters, N., "Laminar flamelet concepts in turbulent combustion," *Symposium (International) on Combustion*, vol. 21, no. 1, pp. 1231–1250, 1988.

[88] Peters, N., "The turbulent burning velocity for large-scale and small-scale turbulence," *Journal of Fluid Mechanics*, vol. 384, no. 1, pp. 107–132, 1999.

[89] Peters, N., *Turbulent Combustion*. Cambridge University Press, Aug. 2000.

[90] Poinsot, T., Veynante, D., and Candel, S., "Diagrams of premixed turbulent combustion based on direct simulation," *Symposium (International) on Combustion*, vol. 23, no. 1, pp. 613–619, 1991.

[91] Poinsot, T. and Veynante, D., *Theoretical and Numerical Combustion*. R.T. Edwards Inc., 2005.

[92] Raffel, M., Willert, C., and Kompenhans, J., *Particle Image Velocimetry; A Particle Guide*. Berlin: Springer, 1998.

[93] Richardson, E. S., Granet, V., Eyssartier, A., and Chen, J., "Effects of equivalence ratio variation on lean, stratified methaneair laminar counterflow flames," *Combustion Theory and Modelling*, vol. 14, no. 6, pp. 775–792, 2010.

[94] Roberts, W. L., Driscoll, J. F., Drake, M. C., and Goss, L. P., "Images of the quenching of a flame by a vortexTo quantify regimes of turbulent combustion," *Combustion and Flame*, vol. 94, pp. 58–69, July 1993.

[95] Sankaran, R. and Im, H., "Dynamic flammability limits of methane/air premixed flames with mixture composition fluctuations," *Proceedings of the Combustion Institute*, vol. 29, no. 1, pp. 77–84, 2002.

[96] Santoro, V. S., Lin, A., and Gomez, A., "Propagation of edge flames in counterflow mixing layers: Experiments and theory," *Proceedings of the Combustion Institute*, vol. 28, no. 2, pp. 2039–2046, 2000.

[97] Sardi, K. and Whitelaw, J. H., "Extinction timescales of periodically strained, lean counterflow flames," *Experiments in Fluids*, vol. 27, pp. 199–209, Aug. 1999.

[98] Sardi, K., Taylor, A. M. K. P., and Whitelaw, J. H., "Extinction of turbulent counterflow flames under periodic strain," *Combustion and Flame*, vol. 120, pp. 265–284, Feb. 2000.

[99] Schefer, R., Wicksall, D., and Agrawal, A., "Combustion of hydrogen-enriched methane in a lean premixed swirl-stabilized burner," *Proceedings of the combustion institute*, vol. 29, no. 1, pp. 843–851, 2002.

[100] Scheiman, J. and Brooks, J., "Comparison of experimental and theoretical turbulence reduction from screens, honeycomb, and honeycomb-screen combinations," *Journal of Aircraft*, vol. 18, no. 8, pp. 638–643, 1981.

[101] Schlichting, H., *Boundary layer theory*. New York: McGraw-Hill, 1979.

[102] Sciacchitano, A., Neal, D. R., Smith, B. L., Warner, S. O., Vlachos, P. P., Wieneke, B., and Scarano, F., "Collaborative framework for PIV uncertainty quantification: comparative assessment of methods," in *17th International Symposium on Applications of Laser Techniques to Fluid Mechanics, Lisbon, Portugal*, 2014.

[103] Sciacchitano, A., Wieneke, B., and Scarano, F., "PIV uncertainty quantification by image matching," *Measurement Science and Technology*, vol. 24, pp. 45302–45317, Apr. 2013.

[104] Shanbhogue, S. J., Husain, S., and Lieuwen, T., "Lean blowoff of bluff body stabilized flames: Scaling and dynamics," *Progress in Energy and Combustion Science*, vol. 35, pp. 98–120, Feb. 2009.

[105] Sheen, H., Chen, W., and Jeng, S., "Recirculation zones of unconfined and confined annular swirling jets," *AIAA journal*, vol. 34, no. 3, pp. 572–579, 1996.

[106] Sinibaldi, J. O., Driscoll, J. F., Mueller, C. J., Donbar, J. M., and Carter, C. D., "Propagation speeds and stretch rates measured along wrinkled flames to assess the theory of flame stretch," *Combustion and Flame*, vol. 133, pp. 323–334, May 2003.

[107] Smith, G. P., Golden, D. M., Frenklach, M., Moriarty, N. W., Eiteneer, B., Goldenberg, M., Bowman, C. T., Hanson, R. K., Song, S., and Gardiner Jr, W. C., "GRI-Mech 3.0," *URL: http://www.me.berkeley.edu/gri_mech*, 1999.

[108] Stella, A., Guj, G., Kompenhans, J., Raffel, M., and Richard, H., "Application of particle image velocimetry to combusting flows: design considerations and uncertainty assessment," *Experiments in Fluids*, vol. 30, pp. 167–180, Feb. 2001.

[109] SUNG, C. J., LAW, C. K., and L AXELBAUM, R., "Thermophoretic Effects on Seeding Particles in LDV Measurements of Flames," *Combustion Science and Technology*, vol. 99, no. 1-3, pp. 119–132, 1994.

[110] Sung, C. and Law, C., "Structural Sensitivity, Response, and Extinction of Unsteady Counterflow Flames," *AIAA paper*, pp. 98–0555, 1998.

[111] Sung, C. and Law, C., "Structural sensitivity, response, and extinction of diffusion and premixed flames in oscillating counterflow," *Combustion and flame*, vol. 123, no. 3, pp. 375–388, 2000.

[112] Syred, N. and Ber, J. M., "Combustion in swirling flows: A review," *Combustion and Flame*, vol. 23, pp. 143–201, Oct. 1974.

[113] Takita, K., Sado, M., Masuya, G., and Sakaguchi, S., "Experimental study of premixed single edge-flame in a counterflow field," *Combustion and Flame*, vol. 136, pp. 364–370, Feb. 2004.

[114] Takita, K., Sakaguchi, S., and Masuya, G., "Premixed edge flame in a counterflow field with a stretch rate gradient," *Combustion and Flame*, vol. 132, pp. 343–351, Feb. 2003.

[115] Talbot, L., Cheng, R. K., Schefer, R. W., and Willis, D. R., "Thermophoresis of particles in a heated boundary layer," *Journal of Fluid Mechanics*, vol. 101, pp. 737–758, Dec. 1980.

[116] Timmins, B. H., Wilson, B. W., Smith, B. L., and Vlachos, P. P., "A method for automatic estimation of instantaneous local uncertainty in particle image velocimetry measurements," *Experiments in Fluids*, vol. 53, pp. 1133–1147, July 2012.

[117] Valiev, D. M., Zhu, M., Bansal, G., Kolla, H., Law, C. K., and Chen, J. H., "Pulsating instability of externally forced premixed counterflow flame," *Combustion and Flame*, 2012.

[118] Vandervort, C., "9 ppm NOx/CO combustion system for F class industrial gas turbines," *Journal of engineering for gas turbines and power*, vol. 123, no. 2, pp. 317–321, 2001.

[119] Vedarajan, T. G., Buckmaster, J., and Ronney, P., "Two-dimensional failure waves and ignition fronts in premixed combustion," *Symposium (International) on Combustion*, vol. 27, no. 1, pp. 537–544, 1998.

[120] Wang, P., Wehrmeyer, J. A., and Pitz, R. W., "Stretch rate of tubular premixed flames," *Combustion and Flame*, vol. 145, pp. 401–414, Apr. 2006.

[121] Wehrmeyer, J. A., Cheng, Z., Mosbacher, D. M., Pitz, R. W., and Osborne, R., "Opposed jet flames of lean or rich premixed propane-air reactants versus hot products," *Combustion and flame*, vol. 128, no. 3, pp. 232–241, 2002.

[122] Wicksall, D., Agrawal, A., Schefer, R., and Keller, J., "The interaction of flame and flow field in a lean premixed swirl-stabilized combustor operated on H2/CH4/air," *Proceedings of the Combustion Institute*, vol. 30, pp. 2875–2883, 2005.

[123] Wieneke, B. and Prevost, R., "DIC Uncertainty Estimation from Statistical Analysis of Correlation Values," in *Advancement of Optical Methods in Experimental Mechanics, Volume 3* (Jin, H., Sciammarella, C., Yoshida, S., and Lamberti, L., eds.), Conference Proceedings of the Society for Experimental Mechanics Series, pp. 125–136, Springer International Publishing, 2014.

[124] Wieneke, B., "Generic a-posteriori uncertainty quantification for PIV vector fields by correlation statistics," in *17th International Symposium on Applications of Laser Techniques to Fluid Mechanics, Lisbon, Portugal*, 2014.

[125] Yokomori, T., Chen, Z., and Ju, Y., "Studies on the flame curvature effect on burning velocity," 2006.

[126] Yoshida, A., "Structure of opposed jet premixed flame and transition of turbulent premixed flame structure," *Symposium (International) on Combustion*, vol. 22, no. 1, pp. 1471–1478, 1989.

[127] Zhang, Q., Shanbhogue, S., Shreekrishna, Lieuwen, T., and O'Connor, J., "Strain Characteristics Near the Flame Attachment Point in a Swirling Flow," *Combustion Science and Technology*, vol. 183, no. 7, pp. 665–685, 2011.

[128] Zukoski, E. E., *Flame stabiliztion on bluff bodies at low and intermediate Reynolds numbers*. PhD thesis, California Institute of Technology, 1954.